Hybrid Perovskite Nanocrystals: Synthesis, Stability and Defect Tolerance

Madeeha Tabassum

SUBMITTED IN PARTIAL FULFILLMENT OF THE REQUIREMENTS

OF THE DEGREE OF DOCTOR OF PHILOSOPHY

School of Engineering and Materials Science,

Queen Mary University of London,

London, UK

May 2024

Declaration

I, Madeeha Tabassum, confirm that the research included within this thesis is my work or that where it has been carried out in collaboration with, or supported by others, this is duly acknowledged below, and my contribution is indicated. Previously published material is also acknowledged below.

I attest that I have exercised reasonable care to ensure that the work is original and does not to the best of my knowledge break any UK law, infringe any third party's copyright or other Intellectual Property Rights, or contain any confidential material.

I accept that the school has the right to use plagiarism detection software to check the electronic version of the thesis.

I confirm that this thesis has not been previously submitted for the award of a degree by this or any other university.

Date: 29/05/2024

Acknowledgements

First, I am indeed grateful to my supervisor Dr. Lei Su, who provided me with complete support scientifically, academically, and emotionally throughout my Ph.D. journey. Without his support and guidance, I would not be able to finish my Ph.D. I would like to thank Prof. Michael Reece for his academic advice to make sure I finish my Ph.D. on time.

I am thankful to my research group members and other colleagues who were a source of inspiration through their friendliness, assistance, and advice and worthy to mention in no special order are Jinshuai Zhang, Yongfeng Zhou, Yufei Wang, and Dr. Hangfeng Zhang. Special thanks to Prof. William Gillin and Dr. Huanqing Ye for their help in Time-resolved PL spectroscopy and data analysis.

I would like to acknowledge the Higher Education Commission (HEC) of Pakistan and Queen Mary University of London (QMUL) for their mutual financial support in providing me with an opportunity to study abroad. I gratefully acknowledge the facilities and support offered by the School of Engineering and Materials Science. I appreciate Dr. Richard Whiteley, Dr. Dongsheng Wu, Dr. Qasim Zia, Dr. Subash Rai, and Dr. Shoghik Hakobyan for their technical support.

I would like to dedicate this thesis to my parents, sisters, brothers, husband Dr. Qasim Zia, and daughter Eileen Qasim whose unconditional love, support, and prayers have always been the motivation behind my success.

Abstract

This thesis aims to fabricate doped halide perovskite materials (HPM) by using targeted elements, which have provided a dimension beyond structural and compositional modification to achieve desired properties. The doping of alkali metal ions (Li^+, Na^+, K^+, Rb^+, and Cs^+) in three-dimensional HPM is reviewed to lay a particular focus on advances in synthesis, doping-induced changes in optical and electrical properties, and their optoelectronic applications. In addition, advancements in wearable perovskite devices (e.g., solar cells, photodetectors, and light-emitting diodes) concerning their device structures, working mechanisms, and fabrication techniques have been discussed. In our first study**,** we study the doping of Cs and Rb cations into $MAPbBr_3$ PeNCs to optimize their morphology, crystal structure, and optical properties. It is found that rubidium cations doping can greatly enhance the photoluminescence intensity of the $MAPBBr_3$ PeNCs, whereas cesium cations can improve structural stability owing to the increased valance bond intensity. Secondly, we demonstrated the self-passivation method for the surface defects by introducing potassium (K) or rubidium (Rb) during the colloidal fabrication of PeNCs, leading to much-improved crystallinity, photoluminescence, and improved radiative efficiency. Thirdly, poly (L-lactic acid) (PLLA) nanofibrous membranes embedded with $FAPbBr_3$ perovskite nanocrystals by electrospinning the perovskite and PLLA precursor solution were examined. The resultant PLLA-$FAPbBr_3$ nanofibrous membranes exhibited stability and remained in the water for about 45 days while maintaining their PL peak intensity at 50% of the initial value. Finally, a brief study about flexible photoelectric devices based on halide perovskite NCs was conducted. The future development of perovskite devices based on existing innovative display and lighting technologies was also stated.

Table of Contents

Declaration **2**

Acknowledgements **3**

Abstract **4**

Table of Contents **5**

List of Notations and Abbreviations **10**

List of Figures **13**

List of Tables **23**

Chapter 1 Introduction **24**

1.1 Background 24

1.2 Research Objectives 27

1.3 Scope of the thesis 28

1.4 Thesis outline 30

Chapter 2 Literature Review **31**

2.1 Halide perovskite materials (HPM) 31

2.2 Goldschmidt tolerance factor (T) for 3D structures 33

2.3 Octahedral factor (μ) 35

2.4 Synthesis of metal halide perovskite (MHP) nanocrystals 36

2.4.1 Ligand-assisted reprecipitation (LARP) method 36

2.4.2 Hot injection (HI) method 37

2.5 Methods beyond LARP and hot injection 39

2.5.1 Sonication 39

2.5.2 Solvothermal 40

2.6 Defects in metal halide perovskite nanocrystals 41
2.6.1 Ball milling 43
2.7 Strategies for defects passivation and stability of perovskite nanocrystals 45
2.7.1 Compositional engineering 45
2.7.2 Surface ligand modifications 47
2.7.3 Coating strategies 49
2.8 Applications of MHP nanocrystals 51
2.8.1 Solar cells 51
2.8.2 Light emitting diodes 52
2.8.3 Photodetectors (PDs) 53
2.9 Advances in doping with alkali metals in halide perovskite materials 55
2.9.1 Overview 55
2.9.2 Influence of cesium ions doping in HPM 56
2.9.3 Role of incorporating rubidium ions in HPM 64
2.9.4 Incorporating other alkali metal ions (K^+, Na^+, and Li^+) for enhanced performance of HPM 69
2.9.5 Conclusion and outlook 75
2.10 Recent Developments in Smart Textiles Based on Perovskite Materials 76
2.10.1 Overview 76
2.10.2 Introduction 77
2.10.3 Perovskite Device structures and working mechanism. 79
2.10.4 Manufacturing Techniques 82
2.10.5 Textile-based perovskite optoelectronic applications 88
2.10.6 Challenges and future perspectives 99
Chapter 3 Tuning the Optical Properties of Perovskite Nanocrystals 102

3.1 Overview 102
3.2 Introduction 103
3.3 Experimental 105
3.3.1 Materials 105
3.3.2 Material synthesis 105
3.3.3 Characterizations 106
3.4 Results and discussion 106
3.5 Conclusion 110
3.6 Preliminary data 111
Chapter 4 Fabrication of Potassium- and Rubidium-doped Formamidinium Lead Bromide Nanocrystals for Surface Defects Passivation and Improved Photoluminescence Stability 122
4.1 Overview 122
4.2 Introduction 123
4.3 Experimental section 126
4.3.1 Materials 126
4.3.2 Synthesis of $FAPbBr_3$ NCs 126
4.3.3 Fabrication of K^+/Rb^+ doped $FAPbBr_3$ NCs 127
4.3.4 Characterizations 127
4.4 Results and discussion 128
4.4.1 Structural and optical characteristics 129
4.4.2 Dynamics of photoexcited charge carriers 136
4.4.3 Passivation mechanism of alkali metal ions for stable PeNCs 138
4.4.4 Effects of K^+/Rb^+ on the colloidal stability of PeNCs 139
4.5 Comparison of effects of alkali metal ions on MA and FA-based nanocrystals 141

4.6 Conclusion 142

4.7 Preliminary data 144

Chapter 5 $FAPbBr_3$ perovskite nanocrystals embedded in poly (L–lactic acid) nanofibrous membranes for enhanced air and water stability. 151

5.1 Overview 151

5.2 Introduction 152

5.3 Experimental 155

5.3.1 Materials: 155

5.3.2 Fabrication of nanocrystals embedded PLLA electrospun NFs: 155

5.3.3 Synthesis of $FAPbBr_3$ perovskite NCs: 156

5.3.4 Characterization: 156

5.4 Results and discussion 157

5.4.1 Morphology of $FAPbBbr_3$ NCs-PLLA nanofibres 158

5.4.2 The crystallinity of $FAPbBbr_3$ NCs-PLLA nanofibrous membranes 161

5.4.3 Surface chemistry of the $FAPbBr_3$ NCs-PLLA nanofibres 162

5.4.4 Air and water stability of composite membranes 165

5.5 Conclusion 168

5.6 Preliminary Data 170

Chapter 6 Hybrid organic-inorganic perovskite nanocrystals for flexible photoelectric applications 171

6.1 Introuction 171

6.1.1 Experimental 172

6.1.2 Materials and Method 172

6.1.3 Characterizations 172

6.2 Results and discussion 173

6.3 Conclusion 179

Chapter 7 Conclusions and Future work 180

References 185

List of publications 221

List of Notations and Abbreviations

HPM	Halide perovskite materials
MHP	Metal halide perovskites
LEDs	Light emitting diodes
PDs	Photodetectors
PeLEDs	Perovskite LEDs
PSCs	Perovskite solar cells
PCE	Power conversion efficiency
PeLEDs	Perovskite light-emitting diodes
NCs	Nanocrystals
QDs	Quantum dots
NPLs	Nanoplatelets
PeNCs	Perovskite nanocrystals
PLQY	Photoluminescence quantum yields
EQE	External quantum efficiency
PL	Photoluminescence
LARP	Ligand-assisted reprecipitation
ETL	Electron transport layer
HTL	Hole transport layers
EML	Perovskite emissive layer
PNFs	Polymer nanofibres
EQE	External quantum efficiency

EL	Electroluminescence
T	Goldschmidt tolerance factor
MOFs	Metal-organic frameworks
$MAPbI_3$	Methylammonium lead triiodide
$CsPbX_3$	Cesium lead halide (X=Br, Cl, I)
RbI	Rubidium iodide
$PbBr_2$	Lead bromide
FABr	Formamidinium bromide
CsAc	Cesium acetate
TOPO	Trioctylphosphine oxide
TEOS	Tetraethoxysilane
DMF	N, N-Dimethylformamide
DMSO	Dimethylsulfoxide
GBL	γ-butyrolactone
PLLA	Poly (L-lactic acid)
PET	Polyethylene terephthalate
PEN	Poly (ethylene 2,6-naphthalate)
PI	Polyimide
PVP	Poly(vinylpyrrolidone)
PAN	Polyacrylonitrile
PS	Polystyrene
PMMA	Poly (methyl methacrylate
PVDF	Poly (vinylidene fluoride

PAN/PU	Poly(acrylonitrile)/ Polyurethane
PEOXA	Poly(2-ethyl-2-oxazoline)
TiO_2	Titanium dioxide
Ag	Silver
FWHM	Full width at half-maxima
TEM	Transmission electron microscopy
XRD	X-ray diffraction
UV-Vis	Ultraviolet-Visible
SEM	Scanning electron microscopy
FTIR	Fourier transform infrared spectroscopy
XPS	X-ray photoelectron spectroscopy
°C	Degree Celsius
K	Kelvin
Å	Angstrom
nm	Nanometre
ns	Nanoseconds
µm	Micrometre
mA/cm^2	Milliampere per square centimetre
Cd/m^2	Candela per square metre

List of Figures

Figure 1:1: Current research directions of colloidal halide perovskite nanocrystals. 25

Figure 1:2: Flow chart of the thesis outline. 30

Figure 2:1: A typical perovskite crystal structure. Reproduced from [25]. 32

Figure 2:2: Perovskite crystal structure and Goldschmidt tolerance factor. Reproduced from [49], copyright 2022, John Wiley and Sons. 35

Figure 2:3: Octahedral versus tolerance factor for different metal halide perovskite structures. Reproduced from [53]. 36

Figure 2:4: (a) Schematic illustration of the LARP method. (b) Precursor materials and shape of perovskite NCs. (c) The solution contains a dispersion of $CH_3NH_3PbBr_3$ NCs. Reproduced from [55], copyright 2015, American Chemical Society. 37

Figure 2:5: Schematic of hot injection method to fabricate perovskite nanostructures. Reproduced from [60]**.** 38

Figure 2:6: Production of Cs-based perovskite NCs using single-step sonication technique and photographs of $CsPBX_3$ NCs dispersions with different halide compositions. Reproduced from [62], copyright 2016, Wiley-VCH Verlag GmbH & Co. KGaA, Weinheim. 39

Figure 2:7: The top-down synthetic method to synthesize $CH_3NH_3PbX_3$ PeNCs. Two precursors usually $PbBr_2$ and MABr are mixed under ultrasonication with capping ligands to form bulk $MAPbBr_3$ which is then broken into NCs under continuous ultrasonication. Reproduced from [63], copyright 2017, Wiley-VCH Verlag GmbH & Co. KGaA, Weinheim. 40

Figure 2:8: Schematic illustration of Mn-doped $CsPbCl_3$ NCs. Reproduced from [64], copyright 2018, The Royal Society of Chemistry. 40

Figure 2:9: (a) Different types of defects in metal halide perovskites. (b) Schematic illustration of the perovskite nanocrystal surface capped by ligands and an enlarged view of the nanocrystal surface with defects and different types of ligands such as alkylammonium ions, carboxylic acid, and zwitterions. Reproduced from [68], copyright 2021, Wiley-VCH GmbH. 42

Figure 2:10: Photographs of the (a) planetary ball mill (b) zirconia bowl filled with zirconia balls (c) bulk $CsPbBr_3$ used as starting materials (d) working mechanism of the planetary ball mill (e) schematic of processes occurring during the mechanochemical production of PeNCs (f) just after the ball milling (g) NCs dispersion in toluene (h) TEM image of the resulting PeNCs. Reproduced from [71]**,** copyright 2018, American Chemical Society. 44

Figure 2:11: Surface chemistry and defect passivation of halide perovskite nanocrystals. (a) Schematic of the formation of surface defects on pristine NCs surface with well-capped ligands. (b) Types of ligands used to passivate NCs. Reproduced from [68], copyright 2021, Wiley-VCH GmbH. 48

Figure 2:12: Schematic illustration of the synthesis of SiO_2-coated $CsPbBr_3$ NCs by one-pot technique. Reproduced from [101]**,** copyright 2020, Elsevier. 50

Figure 2:13: Perovskite LEDs structure and work mechanism. The perovskite emission layer is sandwiched between HTL and ETL. Reproduced from [8], copyright 2019, Elsevier. 52

Figure 2:14: Classification of photodetectors. Reproduced from [107], copyright 2017, The Royal Society of Chemistry..... 54

Figure 2:15: (a) SEM images of perovskite films deposited on FTO substrates with 0, 0.4, 0.8, 1.2, and 1.6 mol% CsAc alloying (left-right). (b) Time-resolved PL of perovskite films wo/w CsAc alloying. (c) Stable output curves of current densities and efficiencies of the best-performing PSCs wo/w CsAc alloying. Adapted with permission from ref. [127], copyright

2019, WILEY-VCH. (d) Time-resolved PL (e) and photovoltaic performance of perovskite thin films doped with different proportions of Rb^+ and Cs^+ ions. Adapted with permission from ref.[128], copyright 2020, Elsevier..... 59

Figure 2:16 (a) Photographs of different perovskite NCs in solution. (b) XRD patterns of $FA_{(1-x)}Cs_xPbBr_3$ (x = 0–0.6). (c) Lattice fringe and peak position (≈15°) as a function of Cs content, x, in $FA_{(1-x)}CsxPbBr_3$. (d) Absorption spectra and (e) PL spectra of $FA_{(1-x)}CsxPbBr_3$ (x = 0–0.6). (f) J–V (g) luminance–voltage, (h) EQE–current density, and (i) current efficiency–current density characteristics of perovskite LEDs, based on $FA_{(1-x)}Cs_xPbBr_3$ (x = 0. 0.1, 0.2, and 0.3). Adapted with permission from ref. [82] , copyright 2017, WILEY-VCH 61

Figure 2:17: (a) TEM image of the $MA_{0.7}Cs_{0.3}PbBr_3$ NCs. (b) The absorption spectra, (c) PL spectra, (d) XRD patterns, (e) EQE vs. current density and (f) luminance vs. voltage, of $MA_{1-x}CsxPbBr_3$ (x = 0 to 0.4). Adapted with permission from ref. [83] , copyright 2017, The Royal Society of Chemistry 63

Figure 2:18: (a) SEM images, (b) contact angle images and (c) charge-carrier lifetimes, (d) electron−hole sum mobilities from optical-pump terahertz-probe (OPTP) measurements, (e) charge-carrier diffusion lengths considering front face excitation as a function of the RbBu concentration. Adapted with permission from ref. [144], copyright 2020, American Chemical Society 66

Figure 2:19 (a) TEM images of synthesized $RbxCs_{1-x}PbBr_3$ nanocubes (b) Photoluminescence (solid line) and absorption (dashed line) spectra of the synthesized solution. Inset is a picture of various solutions, illuminated by a UV-LED source (λ = 374 nm) displaying the tunable emission. (c) Current density (J) is displayed by squares and luminance (L) is displayed by circles. (d) External quantum efficiency as a function of applied bias. (e) Devices that exhibited

the largest luminance at their peak EQEs. Adapted with permission from ref. [85],copyright 2019, WILEY-VCH 68

Figure 2:20: SEM images of (a) without, or with (b) NaI (c) KI doping (d) The X-ray diffraction patterns (e) the enlarged comparison of (110) diffraction peak (f) the steady-state photoluminescence (PL) (g) the current density–voltage characteristics and (h) external quantum efficiency (EQE) spectra with Na^+, K^+ doped and the control sample without doping (i) The J–V curve of champion PSCs with 1.0 mol% Na^+ doping measured at the AM 1.5G solar spectra of 100mWcm^{-2} at a reverse scan. Adapted with permission from ref. [137], copyright 2017, WILEY-VCH. 69

Figure 2:21: (a) XRD patterns of perovskite films with different x values and standard XRD patterns of $CsPbBr_3$ and $CsPbCl_3$. (b and c) TEM images of pristine and K^+ based (4.0% in terms of nominal K^+ ratio) NCs and size distribution analysis; the insets show the corresponding high-resolution TEM images. (d) Schematic illustration of potassium passivation. (e) Current density–voltage–luminance curves and (f) EQE-luminance curve for LED device based on x = 4.0%. Adapted with permission from ref [156], copyright 2020, WILEY-VCH..... 72

Figure 2:22: Schematic diagram showing the four typical layered structures of perovskite solar cells. (a) n-i-p mesoscopic (b) n-i-p planar (c) p-i-n planar (d) p-i-n mesoscopic. Reproduced from ref. [192], copy right 2018, Springer nature. 80

Figure 2:23: Deposition technique for halide perovskite thin films at laboratory scale and large scale. (a) Spin coating (b) Thermal evaporation (c) Blade coating (d) Slot-die coating (e) Inkjet printing (f) Spray coating. Reproduced from ref. [215], copy right 2021, Oxford university press. 86

Figure 2:24: Application and performance of perovskite solar cell textile. (a) Photograph of perovskite solar cell (scale bar = 1cm). (b) Power conversion efficiency with a bending angle of 45° of solar cell textile (c-d) I-V curves of fibre-shaped perovskite solar cells connected in parallel and in series, respectively (e) Textile perovskite solar cell powering an electronic watch at room temperature (scale bar = 2cm) (f) A textile perovskite solar cell frozen in ice powering an electronic clock (g) Testing of textile perovskite solar cells placed at charcoal powering an electronic clock (scale bar = 4cm). Reproduced from ref. [164], copyright 2020, Royal society of chemistry. 90

Figure 2:25: Photoelectric characteristics of perovskite photodetectors. (a) I-V curves in dark and light exposure with different power densities of the photodetectors. (b) Time-dependant (I-t) curves under light illumination with different power densities at a bias voltage of 5V. (c) Photo-response with light switch On and Off at a fixed light power density of 80mW/cm^2 and a bias voltage of 5V. (d) Photoresponsivity and detectivity are the functions of light intensity. (e) Illustration of the fabrication process of quasi-spring-like network structured photodetectors. Reproduced from ref. [240], copyright 2019, Royal society of chemistry. ... 94

Figure 2:26: Device structure and electric behavior of light-emitting perovskite fibre. (a) Illustration of the working mechanism of light-emitting perovskite fibres. (b) Schematic of the perovskite fibre. Inset, cross-sectional SEM image of fibre. (c) Luminance and current-density curves of perovskite fibres. (d-e) Electroluminescent spectra of green and red perovskite fibre. Insert, a photograph of the red and green perovskite fibre. (e) Photographs of the bend perovskite fibre and its electroluminescent behavior under bending position. Reproduced from ref. [246] , copyright 2020, Springer nature. 96

Figure 2:27: Photograph of stretchable perovskite light-emitting diodes. (a) Current density-voltage and luminance-voltage characteristics of perovskite light-emitting diodes with stretchable electrodes. (b) A durability test before and after pressure was applied on flexible electrodes under a voltage of 3V. (d) Change in luminance characteristics after repetitive stretching cycles at strains of 20%. (e-f) Bending behavior of stretchable perovskite light-emitting diodes, touched by wrench and finger at the voltage of 7V. Reproduced from ref [247], copyright 2020, American chemical society..... 98

Figure 3:1: (a) TEM image of the $MAPbBr_3$ PeNCs (b-c) Morphology of $MAPbBr_3$ PeNCs with mixed-cations Cs/Rb (d) Histogram of as-prepared $MAPbBr_3$ PeNCs (e) Histogram of $MA_{1-x}Cs_xPbBr_3$ when x=0.3 for Cs cations (f) Histogram of $MA_{1-x}Rb_xPbBr_3$ PeNCs when x=o.4 for Rb ions..... 107

Figure 3:2: a) The absorption spectra of $MAPbBr_3$ and alkali metal ions (Cs and Rb) substituted PeNCs. (b) Optical band gap energy calculation (Tauc's plot) of the untreated and treated PeNCs. 108

Figure 3:3: (a) PL spectra as a function of alkali metal cations content in $MAPbBr_3$ PeNCs. (b) X-ray-diffraction patterns of alkali metal cations treated $MAPbBr_3$ PeNCs..... 110

Figure 3:4: Photographs of the precipitates obtained in toluene solution. (a) Ligand assited repricipitation of $MAPbI_3$, $MAPbI_2Br$, $Cs0.3MA0.7PbI_3$ in toluene. (b) photographs of Dnanocrystals under ambient light. (c) photographs of nanocrystals under UV-irradation.. 112

Figure 3:5: Absorption spectra of $MAPbI_3$ (C1), MAPbI2Br (C2), Cs0.3MA0.7PbI3 (C3) nanocrystals. 113

Figure 3:6: Photographs of precursor solution and precipitates in toluene solution. (a)Precursor solution in acetonitrile solvent and precipitation in toluene. (b) Photographs of cesium doped nanocrystals under ambient light and UV-irradiation. 114

Figure 3:7: Absorption spectra of (a) $MAPbI_2Br$ and (b) Cs_xMA_{1-x} PbI_2Br (x=0 to 0.6) nanocrystals 114

Figure 3:8: PL spectra of $MAPbI_2Br$ and $CsxMA_{1-x}PbI_2Br$ (x=0 to 0.6) nanocrystals..... 115

Figure 3:9: TEM micrograph of the $MAPbI_2Br$ nanocrystals. (a) $MAPbI_2Br$ (b)-(c) HRTEM micrograph of $Cs_{0.1}MA_{0.9}$ PbI2Br (d) $Cs_{0.2}MA_{0.8}$ PbI_2Br (e) HRTEM micrograph of $Cs_{0.2}MA_{0.8}PbI_2Br$ (f) $Cs_{0.3}MA_{0.7}PbI_2Br$ (g) HRTEM micrograph of $Cs_{0.3}MA_{0.7}$ PbI_2Br. 116

Figure 3:10: FTIR spectra of $MAPbI_2Br$ and Cs_xMA_{1-x} PbI_2Br (x=0 to 0.6)..... 117

Figure 3:11: The X-ray diffraction (XRD) patterns obtained for the $MAPbI_2Br$ and Cs_xMA_{1-x} PbI_2Br nanocrystals. 118

Figure 3:12: Absorption spectra of $MAPbBr_3$ and RbxMA1-x PbBr3 (x=0 to 0.4) nanocrystals 119

Figure 3:13: PL spectra of MAPbBr3 and RbxMA1-x PbBr3 (x=0 to 0.4) nanocrystals.... 120

Figure 3:14: The X-ray diffraction (XRD) patterns obtained for the RbxMA1-xPbBr3 and MAPbBr3 nanocrystals. 121

Figure 4:1. Schematic illustration of potassium and rubidium passivation..... 128

Figure 4:2. (a) UV–vis absorption and PL spectra. (b-d) TEM images of undoped $FAPbBr_3$ NCs, K-doped NCs, and Rb-doped NCs respectively. The inset shows the high-resolution TEM images of the corresponding samples. 132

Figure 4:3. XRD pattern of (a) freshly prepared thin films on the glass substrate. (b-c) XRD patterns of all samples exposed to a humid environment for the stated times. The features are

assigned as stated; we assign the feature marked * to be the non-perovskite phase of $RbPbBr_3$. (d) Peak position and (e) FWHM for the perovskite NCs over time. (f) Basic cubic crystal structure of $FAPbBr_3$ NCs at room temperature. 132

Figure 4:4. FTIR spectra of undoped, K-passivated, and Rb-passivated $FAPbBr_3$ NCs..... 134

Figure 4:5. (a) Pb4f and Br3d XPS spectra and (c) N/Pb ratio (d) (O/Pb) ratio of all samples of $FAPbBr_3$ NCs. 136

Figure 4:6. Time-resolved PL spectra for colloidal undoped, K-doped, and Rb-doped FAPbBr3 NCs 137

Figure 4:7. Stability test of the perovskite NCs. (a-c) Recorded PL spectra of the dispersion solution of undoped and doped FAPbBr3 NCs for 30 days. (d) Optical image of corresponding perovskite NCs dispersed in hexane under 365 nm UV excitation. 141

Figure 4:8: PL and UV–vis absorption spectra of $FAPbBr_3$ NCs solutions. (a) Sodium ion (b) potassium ion and (c) rubidium ion passivated NCs. Tauc plot showing the band gap calculation for (d) Na^+ (e) K^+ (f) Rb^+ treated NCs. 145

Figure 4:9: Fourier-transform infrared spectroscopy *(*FTIR*) of* $FAPbBr_3$ NCs. (a) Sodium ion (b) potassium ion and (c) rubidium ion passivated NCs. (d) Schematic illustration of potassium passivation. Adapted with permission from ref [156],copyright © 2020, WILEY-VCH 147

Figure 4:10: The X-ray diffraction (XRD) patterns obtained for the FAPbBr3 nanocrystals (a) Sodium ions (b) potassium ions and (c) rubidium ions passivated $FAPbBr_3$ NCs. (d) Crystal structure of $FAPbBr_3$ 148

Figure 4:11: Digital photographs of FAPbBr3 NCs under room light. 149

Figure 4.12: PL spectra of $FAPbBr_3$ NCs solutions. (a) potassium ion (b) rubidium ion (c) Sodium ion and passivated NCs. 150

Figure 5:1: Schematic of electrospinning set-up for the fabrication of perovskite NCs-PLLA nanofibres. 157

Figure 5:2: SEM images of the electrospun perovskite-polymer membranes. (a)-(b) Morphology of pristine PLLA nanofibres with different magnifications. (c)-(d) SEM image $FAPbBr_3$ NCs@PLLA nanofibres (e)-(f) Confocal fluorescence microphotographs of perovskite-polymer membranes with a 488 nm laser as the light source. 160

Figure 5:3:(a) UV-VIS absorption and PL spectra of $FAPbBr_3$ NCs. (b) TEM images of $FAPbBr_3$ NCs. 160

Figure 5:4: (a) X-ray diffraction pattern of pure $FAPbBr_3$ NCs, PLLA, and PeNCs-PLLA nanofibres; * indicates the peaks belonging to $FAPbBr_3$. (b) The cubic crystal structure of $FAPbBr_3$ NCs at room temperature. 161

Figure 5:5: FTIR spectra of PLLA nanofibres, pure $FAPbBr_3$ NCs, and perovskite nanocrystals encapsulated by PLLA nanofibres. 163

Figure 5:6: XPS analysis of (a) PLLA and PeNCs- PLLA nanofibres. (b-c) Pb 4f and Br 3d XPS spectra of composite nanofibres 164

Figure 5:7: PL intensity variation spectra of $FAPbBr_3$ NCs-PLLA nanofibres with storage time (a) in air and (b) in water. (c) Summary of PL intensity ratio for the composite films as a function of storage time in air and water. (d) Photograps of PLLA nanofibres and $FAPbBr_3$ NCs-PLLA nanofibres. (e) Photographs of $FAPbBr_3$ NCs-PLLA nanofibres after immersion in water after 10 and 45 days. 166

Figure 5:8: Trials images of Electrospun membranes. 170

Figure 6:1. (a) Schematic diagram of synthesis of FAPbBr3 NCs. (b-c) UV-VIS absorption of polyester-PeNCs and TEM of $FAPbBr_3$ NCs, respectively (d) Schematic diagram of the photoelectric device using a FAPbBr3 NCs. 174

Figure 6:2. (a) SEM images of the polyester knitted structure. (b) SEM image of polyester-PeNCs sample. (c-d) Confocal fluorescence microphotographs of polyester-PeNCs with a 488 nm laser as the light source 175

Figure 6:3. X-ray diffraction pattern of pure $FAPbBr_3$ NCs, polyester, and polyester-PeNCs samples. 176

Figure 6:4. (a) XPS analysis of (a) PeNCs and polyester-PeNCs. (b) Pb 4f spectra of composite flexible structure 177

Figure 6:5. FTIR spectra of PeNCs and polyester coated PeNCs. 178

Figure 6:6: (a) Photograph of the device (b) I-V characteristics in dark. 179

List of Tables

Table 2.1: Perovskites and their crystal structures 34

Table 2.2: Summary of alkali metal ions doped perovskite solar cell performance..... 60

Table 2.3: Summary of alkali metal-doped ions perovskite light-emitting diode 71

Table 2.4: Radiative lifetime analysis for the alkali-doped halide perovskite materials 73

Table 2.5: Summary of the textile-based perovskite solar cells performance [a] 92

Table 3.1: Different levels of reactants for Cesium doped MAI_2Br samples 111

Table 4.1. Summary of characterization of all $FAPbBr_3$ perovskite NCs samples. 130

Table 4.2. PL lifetime of undoped, potassium, and rubidium passivated FAPbBr3 NCs. 137

Table 4.3: Comparison of alkali metal ions treated perovskite nanocrystals. 141

Table 4.4: PLQY of $FAPbBr_3$ Nanocrystals treated with different additives..... 142

Table 4.5: PL and absorption values of $FAPbBr_3$ NCs for different concentrations of Na, K, and Rb ions 146

Table 5:1: Comparison of the FAPbBr3 perovskite NCs incorporated in poly (L–lactic acid) nanofibers with some other materials..... 167

Chapter 1 Introduction

1.1 Background

Optoelectronics is a major area of interest for a wide range of scientific and industrial applications. It has emerged as a quickly growing technology field that consists of applying electronic devices to detect, source, and control light. These devices can be a part of many applications such as automatic access control systems, military services, telecommunication, medical equipment, and more. The range of devices that fall under optoelectronics is broad, including light-emitting diodes (LEDs), information displays, sensing systems, photodiodes, solar cells, and optical communication systems [1].

Halide perovskite materials (HPM) have emerged as a class of excellent semiconductors, which have shown remarkable performance in solution-processed optoelectronic and photonic device applications. These materials generally show a type of crystal structure with the chemical formula ABX_3, in which A and B are alkali and metal cations, respectively, and X is an anion. The solid-state physics perspectives of HPM have been studied in detail regarding their optoelectronic properties, charge carrier dynamics and defect-related charge recombination. Photovoltaic applications have been mainly focused on 3D HPM that perform isotropic carrier transport advantageous for power generation. Unlike conventional materials, HPM are ionic crystals and allows the easy tuning of bandgap and optical characteristics by varying the halide anions. Strong bandgap absorption at the edge wavelength and broad flat absorption covering visible light wavelength make the HPM a strong candidate for sunlight absorption [2].

Perovskite solar cells (PSCs) have demonstrated incredible progress in recent years with a rapid increase in power conversion efficiency (PCE) from about 3% in 2006 to over 25% today. Solar

energy is important in decarbonising the world's energy supply and is expected to generate 50% of global electricity demand by 2050. Therefore, perovskites as the light-harvesting layer has considered one of the most attractive options for solar cells because of their flexibility, lightweight, and cheap scale-up process [3]–[5]. In addition, perovskite materials have promising optoelectronic properties (**Figure 1:1**) suitable for light-emitting applications. Over the past few years, the development of perovskite light-emitting diodes (PeLEDs) has increased rapidly with external quantum efficiency over 30% [6].

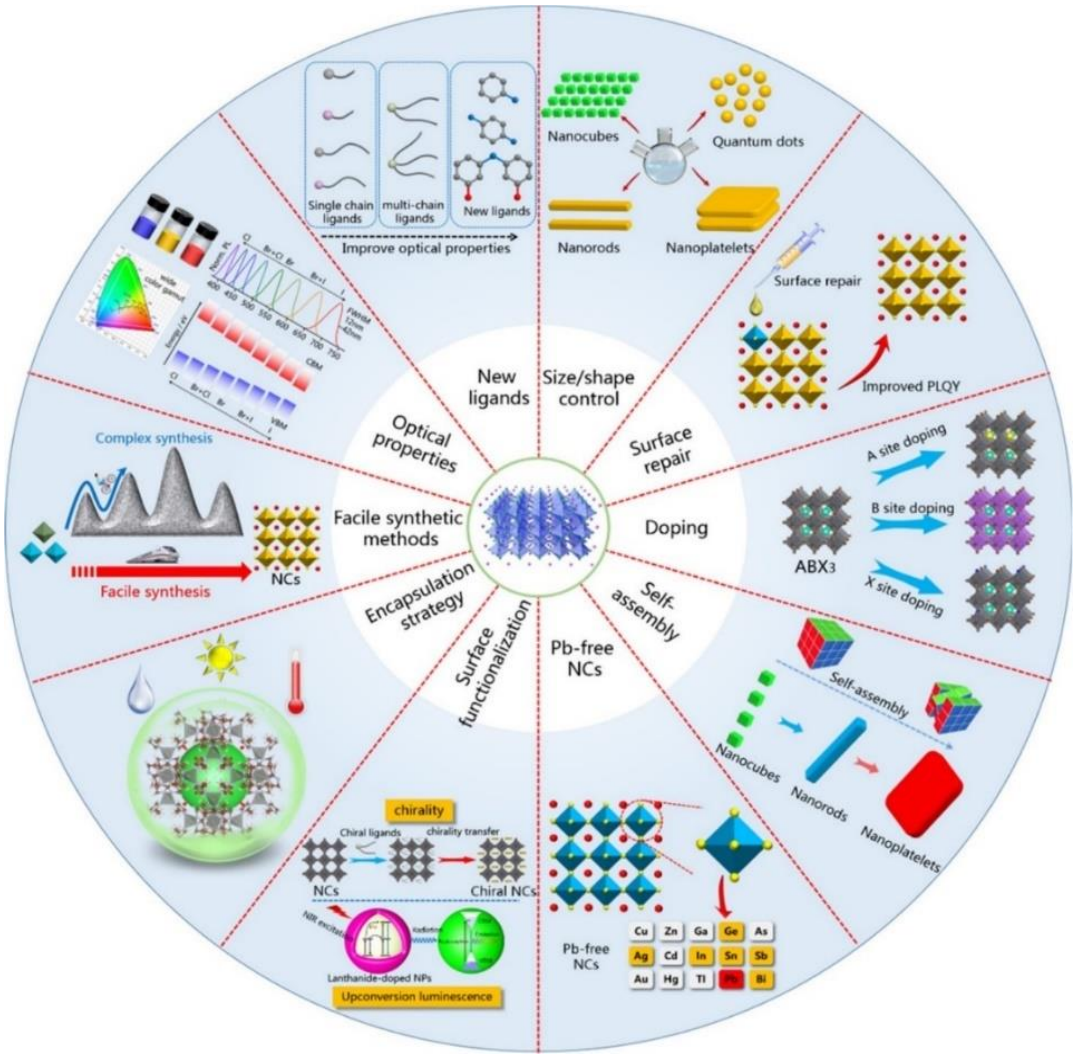

Figure 1:1: Current research directions of colloidal halide perovskite nanocrystals. Reproduced from [7], copyright 2021, American Chemical Society.

Halide perovskite nanocrystals (NCs) have emerged as efficient light emitters with near-unity PLQY. The early studies on solution-processed perovskite nanocrystals (PeNCs) were reported in 2012-2014. These fine PeNCs exhibit much improved emissivity as demonstrated by a PLQY of 20% for $MAPbBr_3$ NCs. In January 2015, Protesescu et al. achieved a breakthrough in monodisperse $CsPbBr_3$ NC synthesis exhibiting PLQY values up to 100% and a quantum-size effect similar to traditional QDs. In March 2015, Zhang et al. reported the ligand-assisted reprecipitation (LARP) technique for the room-temperature fabrication of MA-based NCs with colour-tunable wavelength and PLQY up to 70%. Over the years, numerous reports have been published focusing on ligands, temperature, surface chemistry, and precursors. A wide variety of morphologies including nanocubes, nanowires, nanosheets, nanoplatelets, and quantum dots have been synthesized [2].

The unique properties of PeNCs make them promise for various applications:

1. **Optoelectronics**: PeNCs show great potential in the development of light-emitting diodes (LEDs), displays, and lasers. Their tunable emission wavelength allows for the fabrication of efficient optoelectronic devices [8].
2. **Photovoltaics**: PeNCs can be used in photovoltaic devices to convert sunlight into power and offer the potential for low-cost solar energy solutions [9].
3. **Sensing and imaging**: Perovskite-based 3D imaging sensors are known to have an extremely high angular resolution with a unique angle to colour conversion principle, allowing to detect light field from x-ray to visible wavelength [10] .
4. **Catalysis**: Perovskite-assisted photocatalysis is a convenient approach to modulating chemical transformations with light. The ease of synthesis and ability to tune their bandgap makes them potential candidates for catalysis applications [11].

1.2 Research Objectives

The main objectives of this research can be summarized as follows:

1. To fabricate the perovskite nanocrystals ($FAPbBr_3$ NCs, $MAPbBr_3$ NCs) and rational control of NCs surface defects via alkali metal ions and polymeric materials.
2. To study the incorporation of Cs and Rb cations into $MAPbBr_3$ PeNCs to optimize their morphology, crystal structure, and optical properties. The RbBr and CsBr are used to partially replace the MA cations. Band-gap engineering of mixed-cation PeNCs has been demonstrated during the fabrication process, by replacing the MA cations with alkali metal ions (Cs and Rb), with different concentrations.
3. To study the effects of introducing potassium cations (K^+) and rubidium cations (Rb^+) during the ligand-assisted reprecipitation (LARP) process for the fabrication of formamidinium lead bromide ($FAPbBr_3$) nanocrystals. The introduced alkali metal cations (K^+/Rb^+) act as new passivating agents, which not only occupy the places of dangling organic ligands but also reduce the density of surface defects of PeNCs.
4. To fabricate the $FAPbBr_3$ NCs-PLLA nanofibers with high surface area by using electrospinning, which is low-cost, versatile, and allows the control of NFs composition. The in-situ room temperature fabrication method has been developed for the synthesis of $FAPbBr_3$ NCs-PLLA nanofibres with $FAPbBr_3$ NCs as an emitter and PLLA as the matrix. It is a straightforward and low-cost method to prepare the composite film of $FAPbBr_3$ NCs-PLLA for strong stability in air and water.
5. To study the $FAPbBr_3$ NCs and knitted polyester fabric as a flexible substrate. Confocal laser scanning is used to study the fundamental understanding of the optical properties of the directly formed NCs in highly flexible knitted structures.

6. To comprehensively characterize the perovskite NCs either encapsulated by PLLA nanofibres or treated by alkali metal ions by using advanced characterization techniques including TEM, XRD, and XPS, ultraviolet-visible (UV-Vis), and photoluminescence (PL) spectra.

1.3 Scope of the thesis

This research study has been reported for impressive progress in the development of halide perovskite nanocrystals. Different strategies have been reported to reduce surface defects and trap densities.

Chapter 2 gives a comprehensive review of the halide perovskite materials (HPM) and their doping strategies to enhance their performance without affecting their structure and inherent properties. **Chapter 3** describe the Cs and Rb cations doping into $MAPbBr_3$ PeNCs to optimize their morphology, crystal structure, and optical properties. **Chapter 4** describes the effects of introducing potassium cations (K^+) and rubidium cations (Rb^+) during the ligand-assisted reprecipitation (LARP) process for the fabrication of formamidinium lead bromide ($FAPbBr_3$) nanocrystals. The introduced alkali metal cations (K^+/Rb^+) act as new passivating agents, which not only occupy the places of dangling organic ligands but also reduce the density of surface defects of PeNCs. This study, therefore, set out to suppress the nonradiative recombination of the $FAPbBr_3$ NCs, and, consequently, K^+/Rb^+ based $FAPbBr_3$ NCs showed long-term colloidal stability of more than 1 month that indicates the strong bond between the NCs and new metal ligands. **Chapter 5** presents the fabrication of the poly (L-lactic acid) (PLLA) nanofibrous membrane embedded with $FAPbBr_3$ perovskite nanocrystals by electrospinning the perovskite and PLLA precursor solution. This is a simple and low-cost technique for the direct confinement of nano-sized functional materials in continuous polymer nanofibres. PLLA as a

polymer matrix provided a high surface framework to fully encapsulate the perovskite NCs. **Chapter 6** presents the properties of the directly formed NCs in highly flexible knitted structures. Finally, **Chapter 7** summarizes the findings of this research, the outlook some potential applications, and some suggestions for future research.

1.4 Thesis outline

The outline of the current thesis is described as a brief flow chart in **Figure 1:2**.

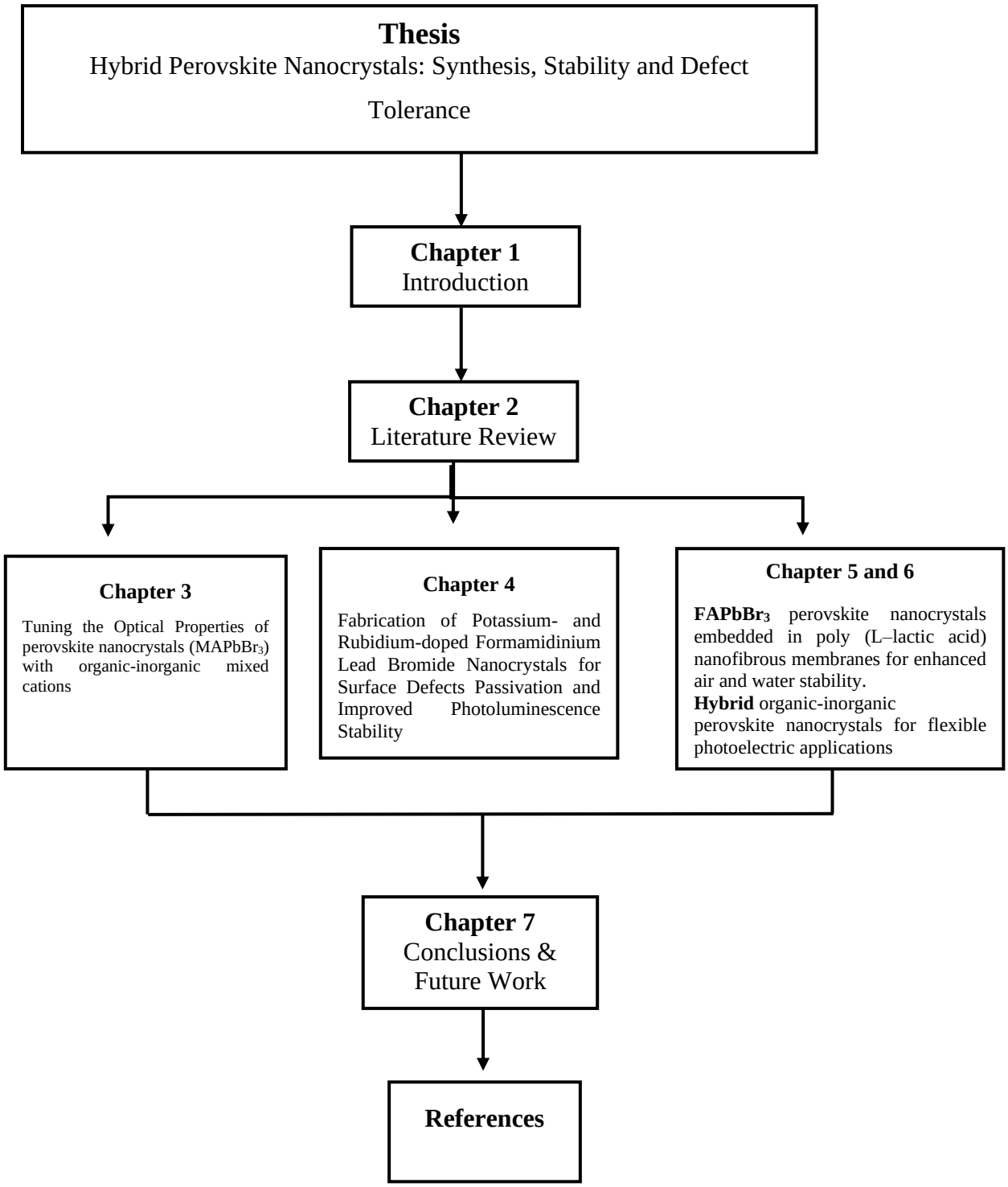

Figure 1:2: Flow chart of the thesis outline.

Chapter 2 Literature Review

2.1 Halide perovskite materials (HPM)

Halide perovskite materials (HPM) have emerged as a class of excellent semiconductors in high-performance optoelectronic applications. In 1839, the term "perovskite" was first coined by Gustav Rose for the $CaTiO_3$ mineral, who named it after nobleman Count Lev Alekseyevich von Perovski. These materials demonstrate unique optical and electrical properties such as tunable bandgap, high photoluminescence quantum yields (PLQYs), high light absorption coefficient, and efficient charge carrier mobility, hence could exhibit a promising future for next-generation electronic devices [12], [13]. The potential to combine all the listed properties in one material with low-cost solution processability has emerged HPM as a focus of current research. In recent years, perovskite materials have been used as a functional layer in light-emitting diodes (LEDs) with external quantum efficiency (EQE) up to 28.2% [14], highly sensitive photodetectors with low noise in photon detections, lasers with an ultralow lasing threshold of 220nJ/cm^2, and perovskite solar cells (PSCs) achieving certified power conversion efficiency (PCE) over 25% [15]–[17]. The remarkable performance of perovskite materials has been made possible by the general perovskite structure ABX_3, where A is a monovalent cation (that can be either organic (e.g., $CH_3NH_3^+$ (methylammonium/MA^+), $CH(NH_2)_2^+$ (formamidinium/FA^+)) or inorganic e.g., Cs^+ (cesium)), B is a divalent cation mostly Pb^{2+} (lead), Sn^{2+} (tin) and trivalent cation Bi^{3+} (bismuth) or their co-alloying with Ge^{2+} (germanium) and Mn^{2+} (manganese), and X is a halide anion (Cl^-, Br^-, I^- or their mixtures) [18]–[20].

The crystal structure of ABX_3 (**Figure 2:*1***) type perovskite consists of a network of corner-shared lead halide octahedra $[BX_6]^{-4}$ with a 12-fold coordinated large size A-site cation

fulfilling the voids to balance the charge. These materials can form multiple structural polymorphs from cubic to hexagonal complex phases depending on the connectivity to the $[BX_6]^{-4}$ octahedra [21]–[23]. HPM with such unique structures possesses excellent photoelectric properties, low exciton binding energy, and solar light absorbance [24].

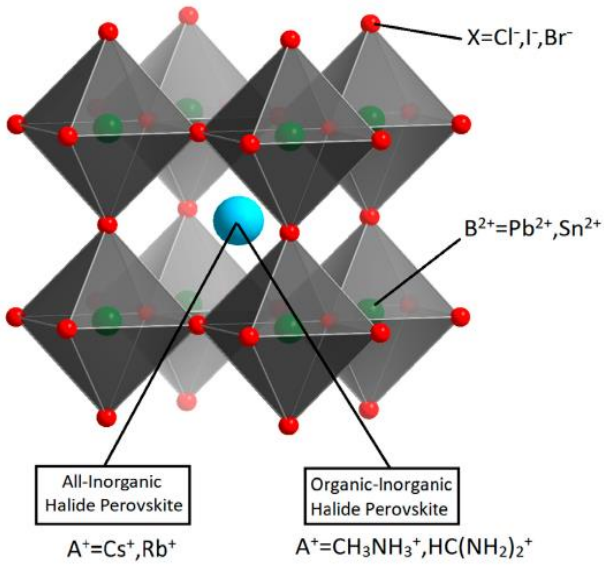

Figure 2:1: A typical perovskite crystal structure. Reproduced from [25].

Doping engineering, a method to introduce impurity atoms into the target crystal lattice can optimize the perovskite materials performance without affecting their structure and inherent properties [26], [27]. Taking into account the inherent HPM-related issues such as their long-term stability, defect states, and performance has attracted the doping strategy [28]–[30]. To fill these gaps, researchers [9], [31]–[33] have been working on the incorporation of various ions into the HPM to study their effects. Only a small concentration of dopants can modify the required characteristics of halide perovskites to the required level without introducing deep energy levels. In addition, doping elements usually do not give rise to the quenched emission due to the surface defect states as reported in conventional II-VI, III-V, and IV-VI inorganic

semiconductors [34], [35]. Therefore, the strategy to dope heteroatoms into the perovskite structure increases the ability to optimize the structural parameters and efficiency. Doping of A-site cation has been mostly reported to tune the bandgap, and the ability to make the host perovskite more stable [36]. Moreover, B-site doping is used to reduce the toxicity of lead ions and extend the charge carrier lifetime of solar power conversion and light absorption process [37], [38]. Furthermore, the mixing of X-site halide anions not only serves the purpose of desired shift in the absorption band but also optimizes the electroluminescence (EL) spectrum of perovskites [39]. Hence, compared with pristine halide perovskites, doped HPM can improve the performances of solar cells, lasers, LEDs, photodetectors, and field-effect transistors [40].

2.2 Goldschmidt tolerance factor (T) for 3D structures

To predict the structural stability and lattice distortion of ABX_3-type perovskite materials, the Goldschmidt tolerance factor (T) has been widely used in applied studies. Also, for a stable doped perovskite structure, the ionic radii of all constituent elements should match well. The T is determined by the ratios of effective ionic radii of the cation A (R_A), the cation B (R_B), and the X (R_X) anion using the following expression:

$$T = R_A + R_X/\sqrt{2}(R_B + R_X)$$

The perfect symmetry of perovskite compounds adopts a cubic close-packed crystal structure with T = 1, with the boundary conditions for stable cubic perovskite structures being $0.9 \leq T \leq 1$. When the value of constituent ionic radii deviates from the ideal case ($T \neq 1$) (**Figure 2:*2*),** crystal distortion and structural strain occur. As this deviation arises, the crystal adopts a lower symmetry leading to tetragonal or orthorhombic structures [41], [42]. When the ionic radii of the A-site cation are smaller than the ideal value, then T becomes smaller than 1, and as a result,

BX_6 octahedra will be distorted to fill space. However, non-perovskite structures are formed as the size of the A-site cation becomes too large (T > 1) to form a nonperovskite phase. **Table 2.1** shows the different perovskites and their stable crystal structures at ambient conditions.

Table 2.1: Perovskites and their crystal structures

Perovskite type	**Temperature (K)**	**Crystal structure**	**Room Temp crystal phase**	**Ref.**
$MAPbBr_3$	>236.9	Cubic (α phase)	Cubic	[43]
	155.1-236.9	Tetragonal (β phase)		
	149.5-155.1	Tetragonal		
	<144.5	Orthorhombic (γ phase)		
$MAPbCl_3$	>178.8	Cubic	Cubic	[43]
	172.9-178.8	Tetragonal		
	<172.9	Orthorhombic		
$MAPbI_3$	>327.4	Cubic		[43]
	162.2-327.4	Tetragonal	Tetragonal	
	<162.2	Orthorhombic		
$CsPbBr_3$	403	Cubic		[44]
	361	tetragonal		
		Orthorhombic		
$CsPbI_3$	298.15/room Tem	Orthorhombic black α / cubic phase	Orthorhombic	[45]
$CsPbCl_3$	320	tetragonal phase		[46]
	316	orthorhombic		
	310	monoclinic phase		
$FAPbI_3$	298.15/room Tem	Hexagonal δ/yellow phase/non photoactive	Hexagonal (non-perovskite)	[47]
	390	Trigonal, cubic symmetry/ α /black /photoactive phase		
$FAPbBr_3$	>275	Cubic	Cubic	[48]
	175	Tetragonal		
	100	Orthorhombic		

The definition of the Goldschmidt tolerance factor has been used to determine whether a combination of ions can form a stable perovskite structure for organic-inorganic halide perovskite materials. Though, there are too many exceptions that cannot completely fit into the

concept of the Goldschmidt tolerance factor. Consequently, another numerical parameter is introduced to anticipate the substituted perovskite crystal structures.

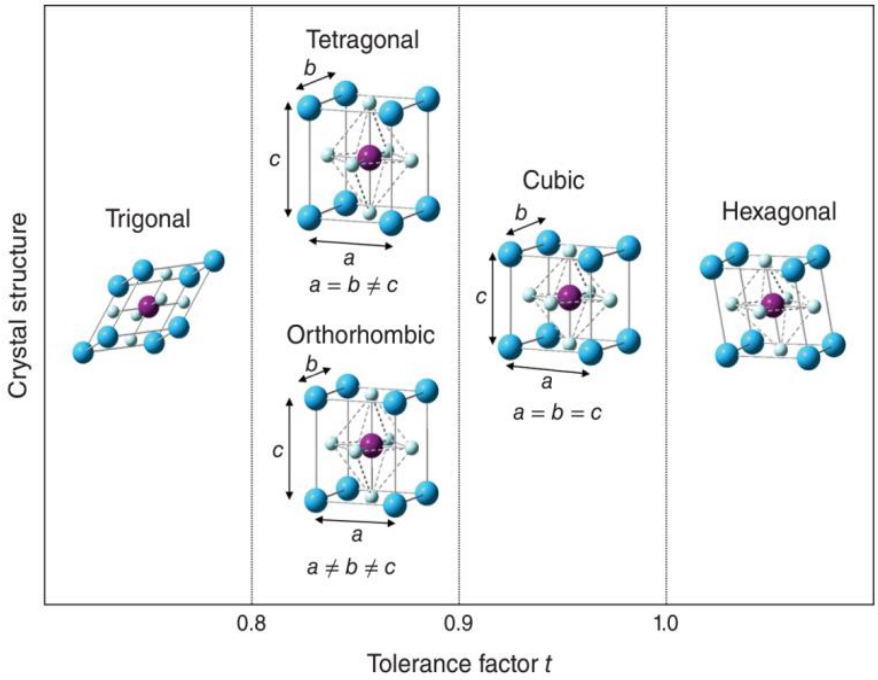

Figure 2:2: Perovskite crystal structure and Goldschmidt tolerance factor. Reproduced from [49], copyright 2022, John Wiley and Sons.

2.3 Octahedral factor (μ)

To describe the threshold of perovskite compounds stability, an additional octahedral factor (μ) that is defined as the ratio of the ionic radii of the B-site cation R_B and the halide X anion R_X in the general formula ABX_3 [50]–[52].

$$\mu = RB/Rx$$

This numerical expression shows the structural stability of the BX_6 octahedron. When it is in the range of $0.44 \leq \mu \leq 0.9$, it generally forms a stable perovskite structure. Along with the Goldschmidt tolerance factor (T), the octahedral factor is intended to choose ions and

combinations to consider the number of theoretically possible configurations for stable halide perovskites as shown in **Figure 2:*3***.

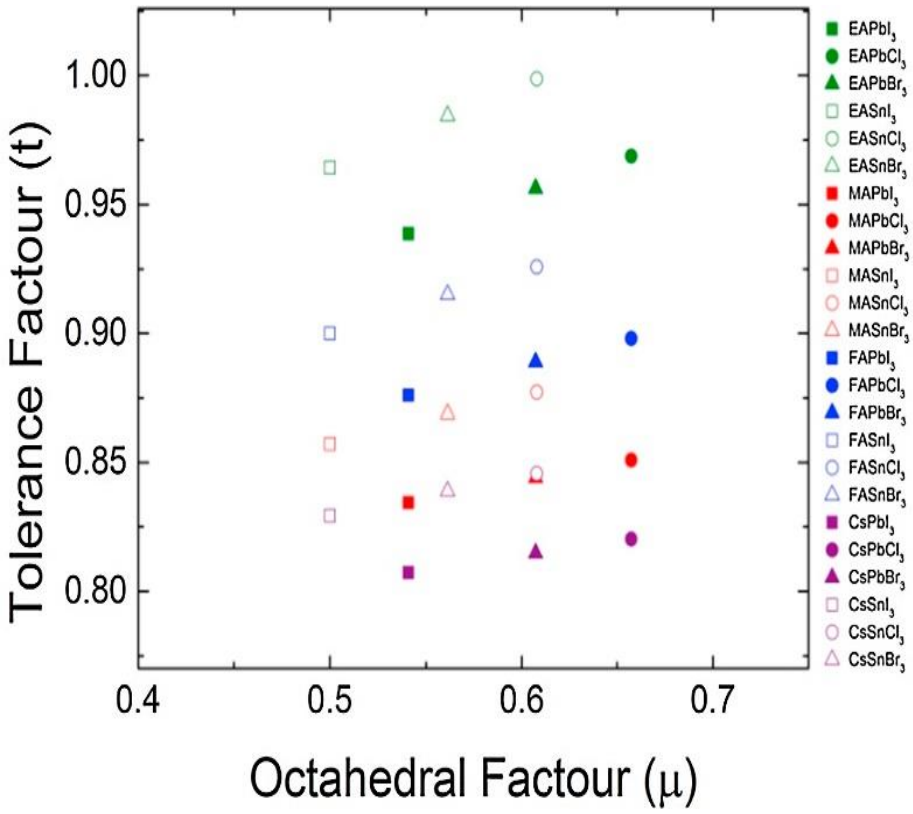

Figure 2:3: Octahedral versus tolerance factor for different metal halide perovskite structures. Reproduced from [53].

2.4 Synthesis of metal halide perovskite (MHP) nanocrystals

2.4.1 Ligand-assisted reprecipitation (LARP) method

Ligand-assisted reprecipitation (**Figure 2:*4***a) is one of the most well-known techniques for the synthesis of halide perovskite nanocrystals. It is a powerful approach to fabricate perovskite NCs (**Figure 2:*4***b,c) via mixing of precursor salts of CsX, MX_2, etc. where M = Pb, Sn or Bi, etc., and X=Cl, Br, or I dissolved into the solvent (such as dimethylformamide or nonpolar solvents such as hexane or toluene) with the presence of the ligands. The mixing of two solvents

starts the nucleation and accelerates the growth of MHP NCs. The simple and versatile LARP method is conducted under air and, hence, can be realized for the large-scale production of MHP NCs [54].

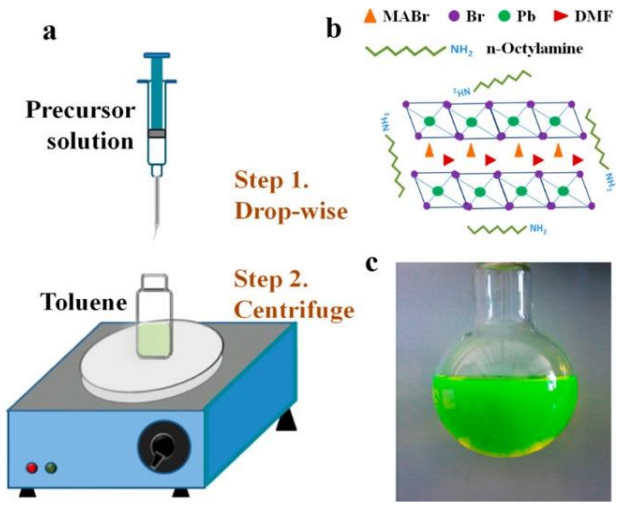

Figure 2:4: (a) Schematic illustration of the LARP method. (b) Precursor materials and shape of perovskite NCs. (c) The solution contains a dispersion of $CH_3NH_3PbBr_3$ NCs. Reproduced from [55], copyright 2015, American Chemical Society.

In 2012, G.C. Papavassiliou's research group first-ever synthesized the $CH_3NH_3PbBr_3$ NCs from the LARP technique [56]. After that, the LARP method has been extended by many researchers have for the synthesis of $FAPbX_3$ perovskite NCs (size 20-44 nm), inorganic halide perovskite NCs using CsX precursor (size 2-6nm) [57], alkali metal-doped halide perovskite (such as $Cs_{1-x}MA_xPbX_3$, Cs1-xFA_xPbX_3, etc.) NCs (size 6-10nm) [58], and lead-free $MA_3Bi_2Br_9$ nanosized perovskites [59].

2.4.2 Hot injection (HI) method

The hot injection (HI) method (**Figure 2:5**) is performed at high temperatures and in the absence of air for the synthesis of halide perovskite NCs. The quick injection of the precursor (such as A-cation) into the hot solution that contains the solvent with suitable ligands and the

remaining precursor (i.e., MX_3), resulting in the formation of small NCs with narrow size distribution. It was found that the size and shape of MHP NCs can be controlled by (1) precursor solution injection temperature (2) ligands to precursor ratio (3) reaction time and (4) precursor concentration [6].

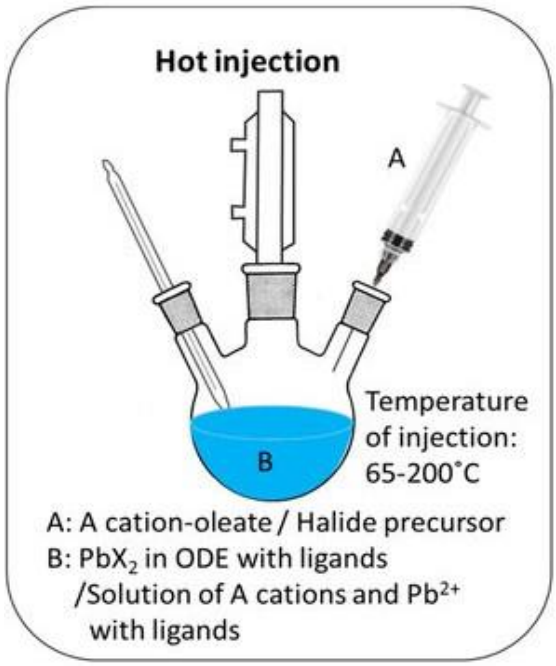

Figure 2:5: Schematic of hot injection method to fabricate perovskite nanostructures. Reproduced from [60]**.**

Protesecu et al. were the first to fabricate $CsPbX_3$ NCs (size 8 nm) with a high degree of band gap engineering in the temperature range of 140°C to 200°C [61]. They were fabricated as single crystalline nanocubes with edge lengths of 4-15 nm by using the precursor of Cs-oleate and Pb-halide in octadecene. The colloidal synthesis of mixed-halide perovskite NCs such as $PbI_2/PbBr_2$ or $PbCl_2/PbBr_2$ could also be produced by the HI method.

2.5 Methods beyond LARP and hot injection

2.5.1 Sonication

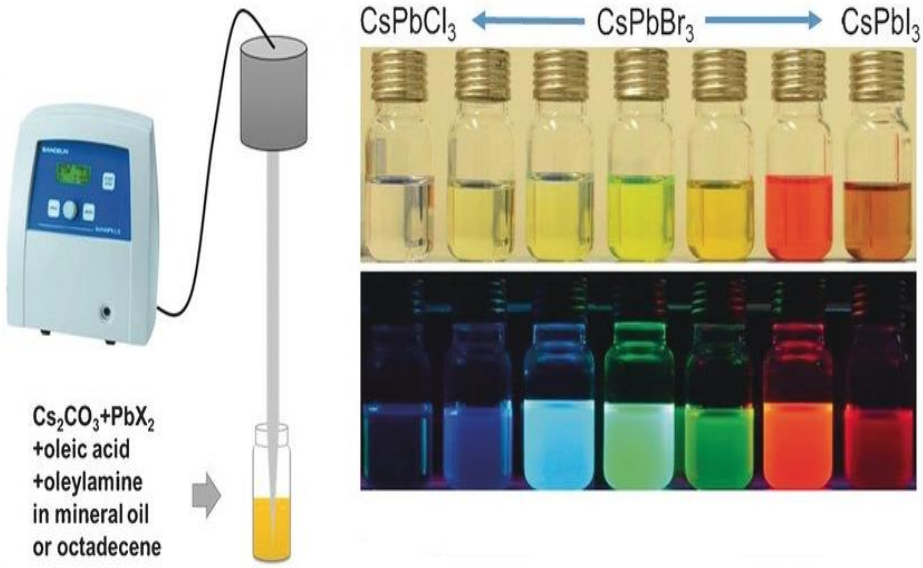

Figure 2:6: Production of Cs-based perovskite NCs using single-step sonication technique and photographs of $CsPBX_3$ NCs dispersions with different halide compositions. Reproduced from [62], copyright 2016, Wiley-VCH Verlag GmbH & Co. KGaA, Weinheim.

Sonication is the large-scale tip-ultrasonication technique for the production of $CsPbX_3$ NCs and nanoplatelets (NPLs). Tong et al. [62] reported this method as shown in **Figure 2:6** for the synthesis of nanowires, cutting nanowires for nanorods and NPLs. Huang et al. [63] adapted this approach (**Figure 2:*7***) for the synthesis of $CH_3NH_3PbX_3$ nanocrystals by using oleic acid and oleic amine as coordinating solvents. One advantage of the tip-ultrasonication is that it avoids the use of polar solvents and reduces the reaction time by using one-step ultrasonic treatment of precursor solution for the fabrication of monodisperse red, green (PLQY ≈ 70%), and blue emitting NCs.

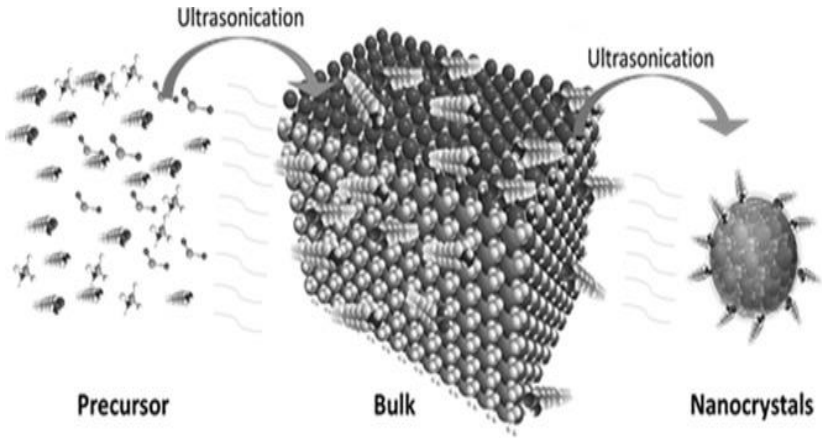

Figure 2:7: The top-down synthetic method to synthesize $CH_3NH_3PbX_3$ PeNCs. Two precursors usually $PbBr_2$ and MABr are mixed under ultrasonication with capping ligands to form bulk $MAPbBr_3$ which is then broken into NCs under continuous ultrasonication. Reproduced from [63], copyright 2017, Wiley-VCH Verlag GmbH & Co. KGaA, Weinheim.

2.5.2 Solvothermal

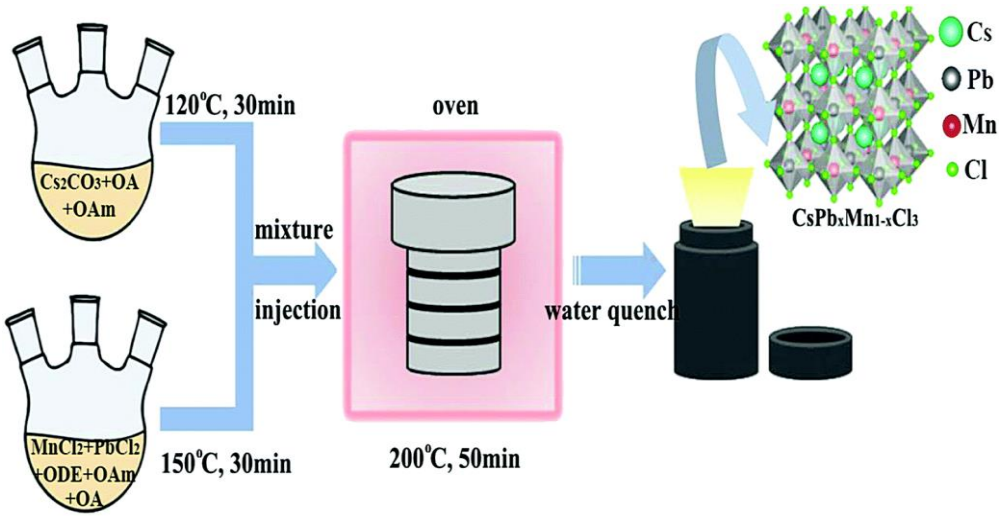

Figure 2:8: Schematic illustration of Mn-doped $CsPbCl_3$ NCs. Reproduced from [64], copyright 2018, The Royal Society of Chemistry.

Min et al. presented a solvothermal approach to preparing the all-inorganic $CsPbX_3$ perovskite NCs with tunable and high PLQY up to 80%, controllable morphology, and composition. In addition, ultrathin mixed-halide $CsPbX_3$ nanowires with a diameter of ≈ 2.6 nm can be synthesized with high morphological yield [65]. Li et al. successfully fabricated the Mn-doped $CsPbCl_3$ NCs by solvothermal reaction (**Figure 2:*8***) and the as-prepared NCs were demonstrated to be used as colour converters for LEDs [64].

2.6 Defects in metal halide perovskite nanocrystals

Metal halide perovskite nanocrystals with large specific surface areas increase the likelihood of surface defects compared to that bulk single crystals or polycrystalline thin films. Defects have been considered an important part of semiconductor crystals, controlling their electric, optical, and structural properties, and hence affect a wide range of optoelectronic applications. Although defects give rise to many advantages, the traps they introduce in the bandgap are detrimental to the optoelectronic performance of the HPM. Therefore, it is essential to comprehend and control the defect population to recognize the potential of perovskite NCs [66] [67].

In generally classified semiconductors such as Si, GaAs, CdTe, CdSe, InP, and metal chalcogenides, a small number of defects can severely affect their inherit PLQY, carrier mobility, and stability. However, there is a specific class of semiconductors like lead halide perovskites that are defect tolerant, so it is possible to achieve low non-radiative recombination despite a high population of defects in the bandgap [68].

Like in semiconductors, two main types of defects in HPM are atomic scale and structural defects. Atomic scale defects are vacancies, interstitial defects, and anti-site defects (**Figure 2:9**a)**.** Structural defects are generally classified into dislocation and grain boundary defects.

Furthermore, defect complexes like Schottky and Frenkel defects can occur. The common point defects (A and X-site vacancies) in perovskites are usually shallow-level defects and are not detrimental to the device's efficiency. Point defects with deep traps such as interstitial or anti-site are almost absent in the HMP since they have high formation energy. Hence, the main defects which we consider during the fabrication process are uncoordinated lead ions and surface-charged defects [68].

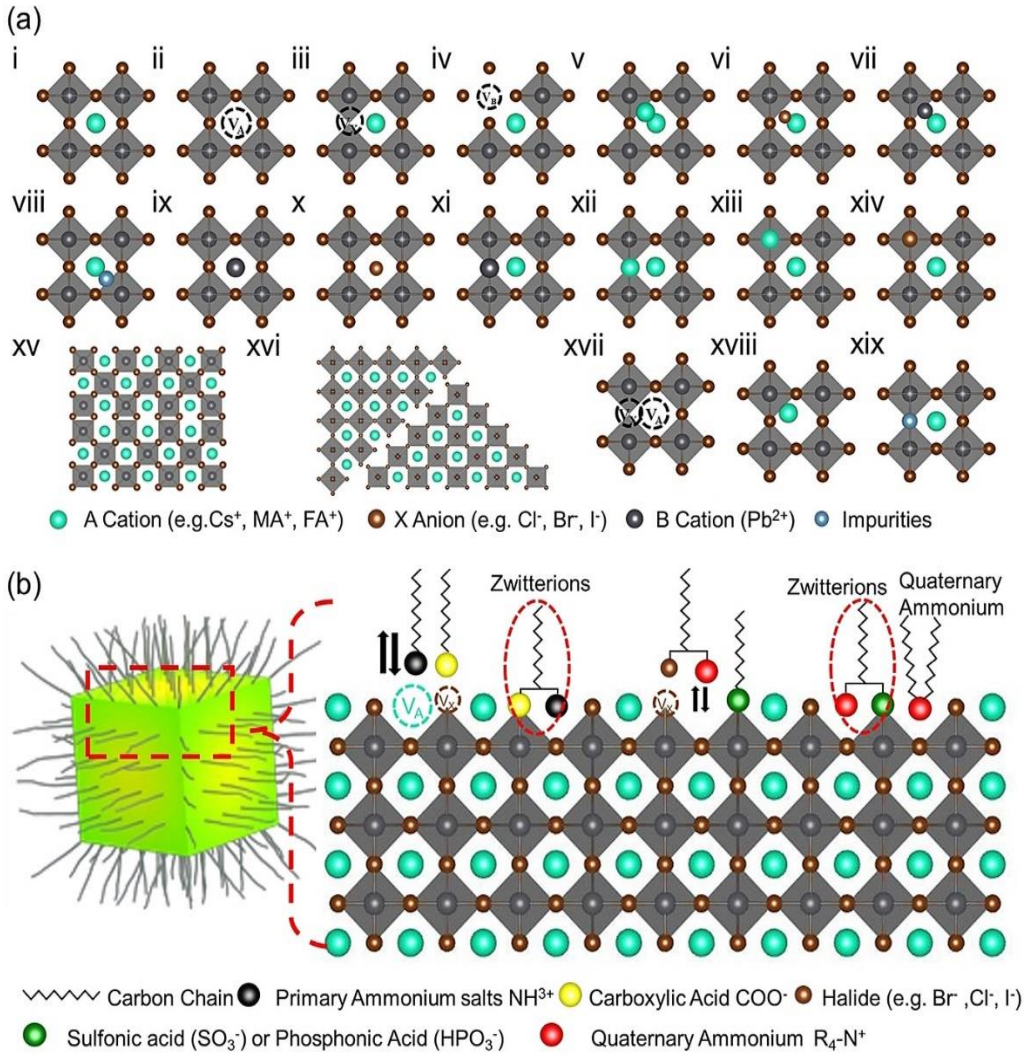

Figure 2:9: (a) Different types of defects in metal halide perovskites. (b) Schematic illustration of the perovskite nanocrystal surface capped by ligands and an enlarged view of the nanocrystal

surface with defects and different types of ligands such as alkylammonium ions, carboxylic acid, and zwitterions. Reproduced from [68], copyright 2021, Wiley-VCH GmbH.

In the form of colloidal NCs, these materials are terminated by long-chain alkyl ligands (**Figure 2:9**b) that contain ionic substituents like amine cation ($R\text{-}NH_3^+$) and carboxylate anion ($R\text{-}COO^-$) to achieve colloidal stability in nonpolar solvents. However, these ligands bind to the surface of NCs by weak electrostatic forces and only provide high coverage when present in excess in solution. In addition, the proton transfer between cationic amine and anionic carboxylate generates deprotonated NH_2 and protonated COOH groups that cause rapid desorption of ligands from the surface of NCs during the purification by washing, aging, and dilution. Hence, the main consequences of such weak binding interaction between NCs and ligands lead to the formation of surface defects and reduction in PLQY [69], [70]. Taken together, perovskite NCs and bulk thin films exhibit similar types of defects. In addition, NCs showed surface vacancies due to the desorption of surface ligands

2.6.1 Ball milling

The wet ball milling technique (**Figure 2:10**a-c) of bulk $APbBr_3$ (A=Cs, FA) was demonstrated with high yield and excellent optoelectronic properties of the same composition fabricated by the hot injection method. The method shown in **Figure 2:10**d, e uses two rotational movements: one of the milling balls, and the other is the supporting disk. The combined effort enabled the movement of the balls within the bowl, causing the grinding of the materials. **Figure 2:10**f-h photograph showed the colloids of $CsPbBr_3$ NCs after the ball milling and dilution in toluene [71].

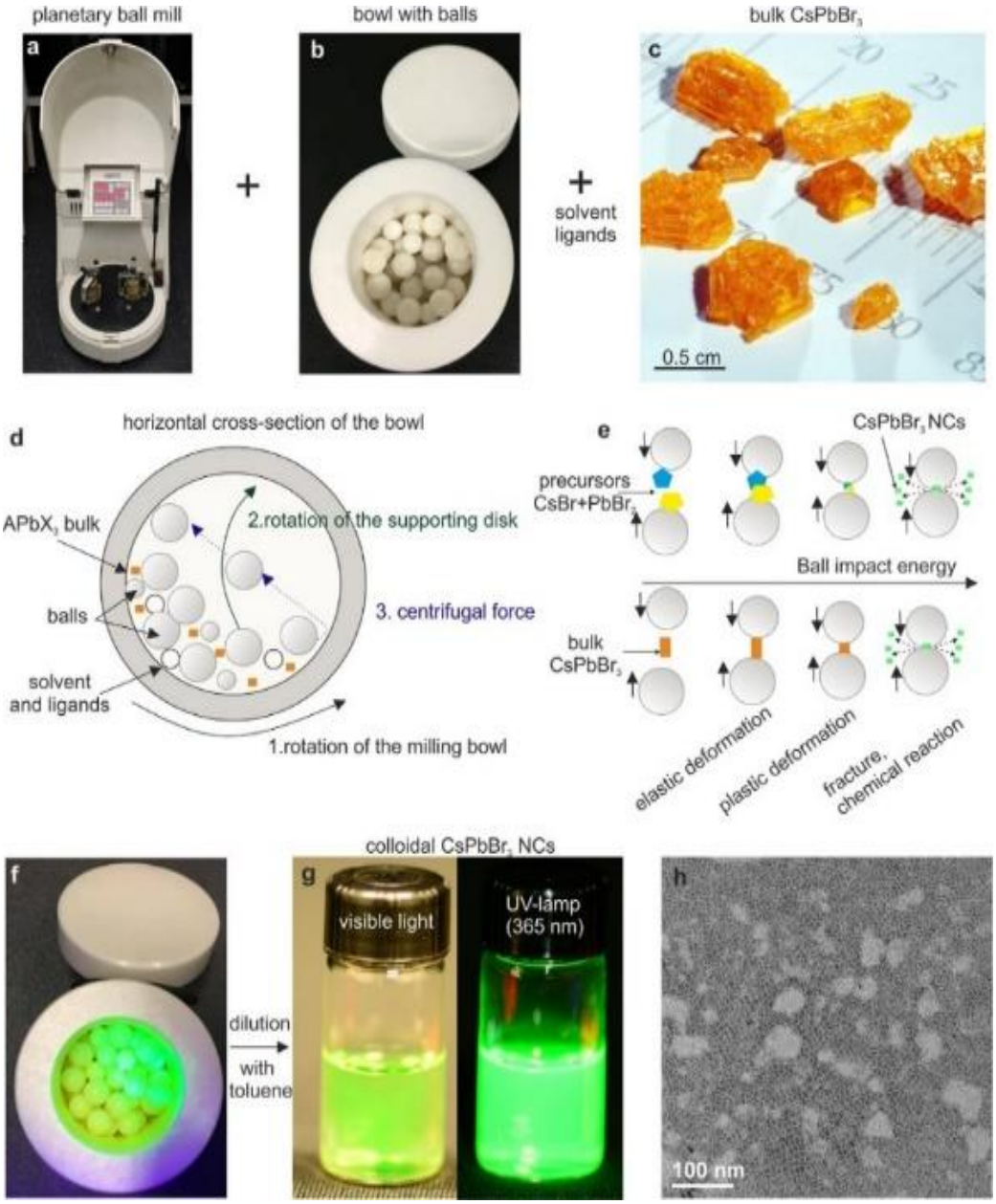

Figure 2:10: Photographs of the (a) planetary ball mill (b) zirconia bowl filled with zirconia balls (c) bulk $CsPbBr_3$ used as starting materials (d) working mechanism of the planetary ball mill (e) schematic of processes occurring during the mechanochemical production of PeNCs (f) just after the ball milling (g) NCs dispersion in toluene (h) TEM image of the resulting PeNCs. Reproduced from [71]**,** copyright 2018, American Chemical Society.

High-energy ball milling is a type of mechanical grinding of materials. This method can be used in wet (with solvents) and dry (without solvents) conditions. Laboratory-scale ball milling is a batch process, whereas large-scale ball milling can be operated in a continuous mode, hence offering a high production of required materials. The mechanism of ball-milling involves the friction of grinding medium, such as balls of the same sizes, and the ground material. Mechanical energy is provided to the system by the rotary movement of the bowl, as in the case of planetary ball mills. This technique has been popular since 1970 for the synthesis of oxide-based dispersions such as Al_2O_3, Y_2O_3, and ThO_2.

2.7 Strategies for defects passivation and stability of perovskite nanocrystals

One of the limitations of the commercialization of halide perovskite NCs is stability. To solve this issue, we must have a deep understanding of the origin of the degradation mechanism of NCs. Different methods such as compositional engineering, surface ligand modifications, and surface passivation methods have been proposed for defect passivation and to make the NCs more stable.

2.7.1 Compositional engineering

A-site doping

To date, cesium (Cs) is the only alkali metal that can substitute A-site cation in ABX_3 type perovskites due to its large ionic radii (1.67Å) [72], [73]. Mixing of Cs ions with other A-site cations (MA^+, FA^+) is considered a milestone to address the problem of structural instability, thermal and moisture sensitivity of halide perovskite devices [74]–[76]. HPM NCs can be characterized as minimizing the exciton dissociation and increasing the radiative recombination because of the quantum confinement effect [77]–[79]. However, their structural stability and

physicochemical-related issues may drop the efficiency of perovskite devices within a few operating hours [80], [81]. For instance, to address these issues, mixed cation $FA_{(1-x)}Cs_xPbBr_3$ and $MA_{1-x}Cs_xPbBr_3$ perovskite nanocrystals (NCs) have been prepared and tested with enhanced performance of LEDs [82], [83].

Moreover, rubidium (Rb) has been considered an emerging alkali metal that can be used as a functional dopant in HPM, which has a significant impact on the structural parameters of single or mixed cation perovskites [84]. Different nanostructures of $Rb_xCs_{1-x}PbBr_3$ namely nanocubes and nanoplates with tunable emission (450-500 nm) were reported to fabricate stable blue-emitting LEDs [85].

B-site doping

There is a growing body of literature that recognises the importance of B-site doping for $CsPbX_3$ nanocrystals. It has been regarded as the most effective technique that could not only tune their optical properties but also improve their stability and provide them with novel functionalities. Several studies have reported the importance of Mn^{2+} doping into the $CsPbX_3$ NCs. Manganese-doped highly crystalline Mn-CsPb $(Cl/Br)_3$ NCs were fabricated with two emission peaks, including the host emission peak at about 450 nm and the Mn^{2+} dopant emission at around 600 nm. By varying the amount of perovskite precursor amounts, the relative PL emission of dual-wavelength can be changed to a wide colour gamut, showing their potential application in light-emitting devices [45].

Yao et al. studied the effects of Mn doping into $CsPbCl_3$ and $CsPbCl_{3-x}Br_x$ perovskite NCs precipitated in glass through melt-quenching and thermal treatment for light emitting application. The amount of Mn^{2+} and subsequent thermal treatment affected the growth of perovskite NCs and band edge emission, enabling tunable PL ranging from UV-blue spectral

region [86]. Chen and co-workers also reported an Mn^{2+}-doped strategy to enhance the environmental stability and PL characteristics of QDs. About 60% of the initial PL brightness was preserved after exposure to ambient air for 120 days [87].

Until now, $CsPbBr_3$ QDs are incorporated with the number of metal ions. Most scientific investigations are focused on the effect of phase structure or optoelectronic properties depending on the doping techniques.

2.7.2 Surface ligand modifications

Figure 2:*11*a shows the formation of surface defects in perovskite NCs either by ageing or washing, and their passivation with ligand molecules or metal salts. Ligand detachment from perovskite NCs surface tends to form both A-site and X-site defects for charge neutralization.

Covalent bond classification (CBC) is an established theory to classify molecules by identifying the number and types of ligands. Jonathan De Roo's categorised the CBC system into L, X, and Z types, depending on the number of electrons (2, 1, 0 respectively) they donate when the neutral ligand binds to the surface of perovskite NCs. Due to the ionic nature of perovskite NCs surface, L-type ligands (anionic and cationic) have been mostly used for the passivation of A-site and X-site defects [88]. One of the earliest studies on defect passivation by surface ligand modification technique was mentioned by Pan and his research group. $CsPbBr_3$ perovskite NCs were protected by the use of didodecyldimethylammonium sulphide and this passivation leads to the formation of the surface enriched with sulphide [89]. However, the research does not take into account the mechanism behind the successful passivation of perovskite NCs. In early 2016, a comprehensive study was published about the chemistry of perovskite NCs and their highly dynamic nature of ligand binding. This research work also proved that the presence of excess amines improves the stability of perovskite NCs and PLQY. Following these early

studies, a considerable amount of literature has been published on the passivation and stability of perovskite NCs by modification of surface ligands **Figure 2:*11***b [90]–[93].

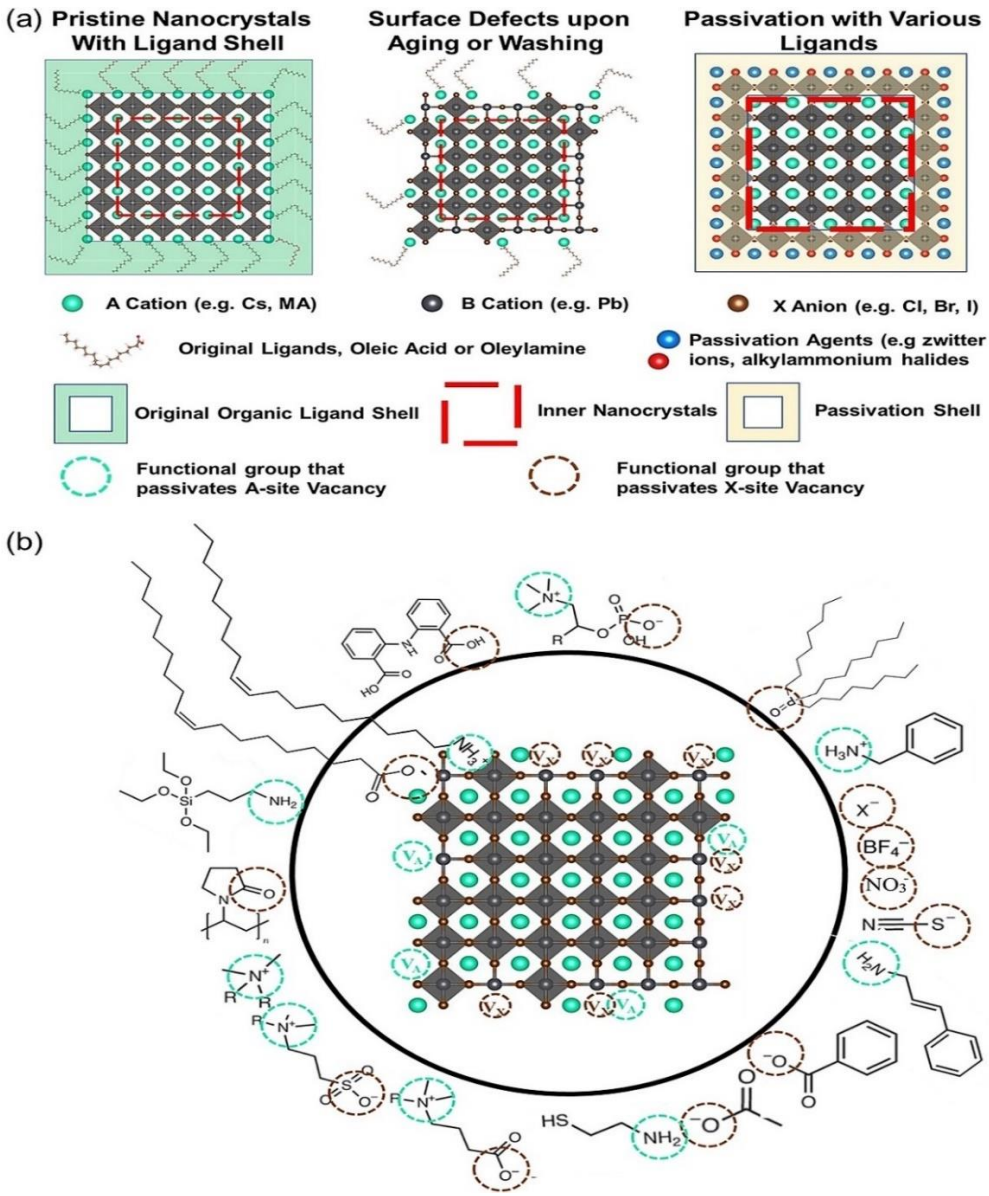

Figure 2:11: Surface chemistry and defect passivation of halide perovskite nanocrystals. (a) Schematic of the formation of surface defects on pristine NCs surface with well-capped ligands. (b) Types of ligands used to passivate NCs. Reproduced from [68], copyright 2021, Wiley-VCH GmbH.

The selection of surface ligand is generally based on the simultaneous refilling of the A-site and halide defects with an ammonium cation and the same halide respectively. This is due to the healing of the perovskite NCs surface requiring restoration of the damaged sites by filling the halide vacancies and forming a complete ligand shell. Alkylammonium halides have been a good selection for completing this criterion towards effective passivation and improved stability of perovskite NCs [94]–[96].

Another type of ligand family recognised by the growing body of literature is zwitterionic ligands, in which two functional groups with positive and negative charges simultaneously bind to the A-site and X-site, respectively. Hence, this ligand family binds to the perovskite NCs surface more strongly due to the chelating effect, and the perovskite NCs show long-term stability and PLQY [89], [97]–[99].

2.7.3 Coating strategies

The dynamic nature and low crystal lattice energy of perovskite NCs lead to reduced stability in nearly all polar solvents and hence disintegrate under such conditions. This problem was difficult to mitigate until a strategy of full encapsulation of perovskite NCs with inert shell material.

So far, extensive research has been reported about SiO_2 coating methods in traditional nanocrystals, such as lanthanide-doped nanocrystals and magnetic nanocomposites. SiO_2 is an inorganic oxide with chemical stability and optical transparency in the whole visible spectrum. The coating of perovskite NCs surface with SiO_2 has been reported to not change the optical properties but, make them stable against organic solvents. The silica coating method for $CsPbX_3$ QDs is a typical process using Stöberor or reverse emulsion method [100].

Fei et al. performed a series of experiments to prepare monodisperse $CsPbBr_3@SiO_2$ NCs by one pot route in non-polar solvents as shown in **Figure 2:*12*.** The precursor solution of $PbBr_2$, oleic acid, and oleylamine is prepared at 120°C. The Cs-oleic acid solution is rapidly injected into the precursor solution at 170°C. Then, the flask was cooled down by an ice-water bath, and $CsPbBr_3$ NCs were obtained. Trioctylphosphine oxide (TOPO) was added to avoid large SiO2 matrices and act as a surface ligand. Finally, tetraethoxysilane (TEOS) was added to the system to coat $CsPbBr_3$ NCs by forming a SiO_2 shell after exposing them to ambient air at room temperature [101].

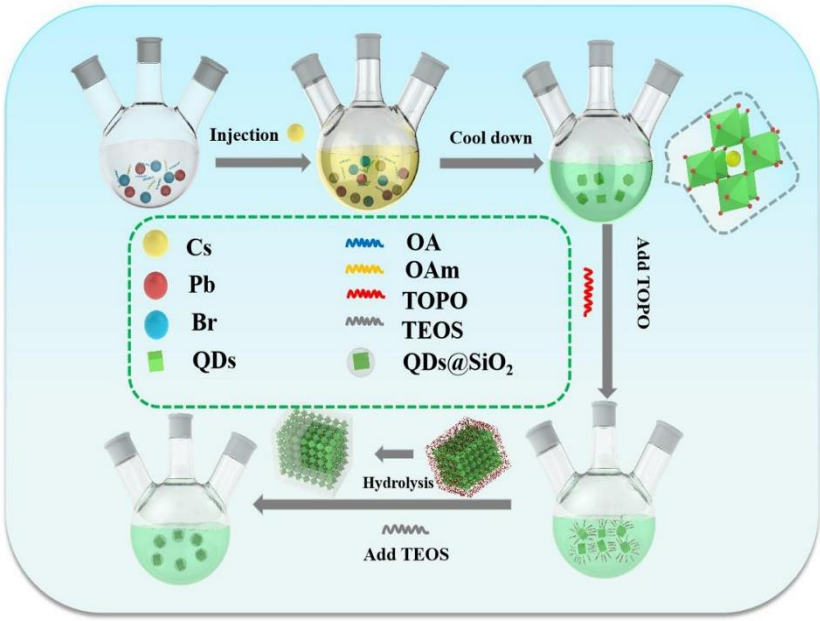

Figure 2:12: Schematic illustration of the synthesis of SiO_2-coated $CsPbBr_3$ NCs by one-pot technique. Reproduced from [101]**,** copyright 2020, Elsevier.

In addition to the silica coating technique, some reports mentioned that anchoring $CsPbBr_3$ NCs onto a template can effectively improve their stability. For instance, the proposed structure consists of $CsPbX_3$/ZnS heterostructure. The presence of ZnS showed chemical stability in which the $CsPbX_3$ NCs remained long-term stable in ambient air. Furthermore, presynthesized

porous materials were also used as a feasible strategy for the stability of $CsPbX_3$ NCs. These porous materials include CaF_2 hierarchical nanospheres and metal-organic frameworks (MOFs) with tunable pore size regarded as a great potential for encapsulation of perovskite NCs [102] [103]. Alkali metal salts including KX (X=Cl, Br or I) and other inorganic oxides (e.g. AlO_x) have been reported to preserve the optoelectronic properties as well as enhanced stability towards the air, high energy light irradiation, and thermal conditions [100]. In general, therefore, it seems that coating methods are promising alternative routes to make perovskite NCs more stable.

2.8 Applications of MHP nanocrystals

Metal halide perovskite nanocrystals have emerged as a major area of research for a wide range of scientific applications such as laser, field effect transistors (FFT), solar cells, LEDs, and photodetectors. Perovskite NCs have been studied by many researchers due to their excellent optoelectronic properties, for example, tunable bandgaps, narrow emission, high PLQY, and high defect tolerance. The promising advancement and recently reported achievements in the area of solar cells, light-emitting diodes, and photodetectors are briefly summarized in the following sections.

2.8.1 Solar cells

Halide perovskite solar cells have long been studied by many researchers with rapid progress in power conversion efficiency to reach over 25% in the photovoltaic performance race. Since the development of halide perovskite-based solar cells in 2012, considerable research work on material optimization, structure design, process engineering, and device physics have been done to make them strong candidates for next-generation solar energy harvester. The low cost

of the materials and process combining with high efficiency are the key factors of this device over commercial silicon or other organic or inorganic solar cells [104].

3D halide perovskite materials have exceptional electrical and optical properties, which have enabled their prevalent use as an active layer in optoelectronic, and in particular in photovoltaic devices. These materials have some of the most appealing properties including high absorption coefficient, direct photogeneration of free carriers, efficient charge transfer, and high mobilities diffusion length. In a typical solar cell design, the perovskite layer is sandwiched between an ETL such as mesoporous TiO2, and an organic HTL such as spiro-OMeTAD (2,2′,7,7′-tetrakis(N, N-di-p-methoxyphenylamine)-9,9′-spirobifluorene) in either n-i-p or p-i-n device architecture. Upon sunlight light exposure, the photogenerated charges are transported through the perovskite layer and then extracted at the interface with the electron transporting layer and hole transporting layer [22].

2.8.2 Light emitting diodes

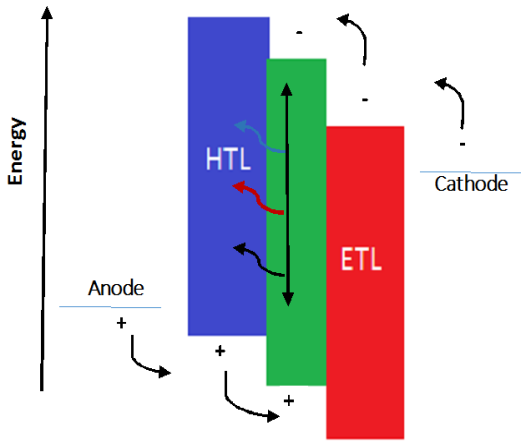

Figure 2:13: Perovskite LEDs structure and work mechanism. The perovskite emission layer is sandwiched between HTL and ETL. Reproduced from [8], copyright 2019, Elsevier.

In a typical device structure of perovskite LEDs, the perovskite active layer is placed between the p-type hole transporting layer and the n-type electron transporting layer as shown in **Figure 2:*13***. For light emission, charge carriers are injected into the perovskite thin layer where they are radiatively recombined. Perovskite LEDs can be classified as p-i-n or n-i-p structures based on the bottom interlayer on the substrate. In the p-i-n structure, the most common hydrophilic layers i.e., PEDOT: PSS or NiOx are always used to deposit and grow high-quality perovskite films. For the n-i-p structure, ZnO is commonly used as ETL because of high electron mobility and reduced electron injection hindrance between ZnO and the perovskite interface.

2.8.3 Photodetectors (PDs)

There has been renowned interest in photodetectors because of their ability to translate optical signals into electrical signals, which are important for industrial and scientific applications such as biomedical sensing, imaging, military affairs, and optical communication. The key aspects for particular photodetectors are photoresponse speed, detection ability to lower brightness, and detection band in which photodetectors can effectively detect light. Furthermore, to evaluate the performance of photodetectors the key parameters are the response time or speed, spectral responsivity, noise current, external quantum efficiency (EQE), specific detectivity (D*), and linear dynamic range (LDR) [105].

In recent years, the HPM has received considerable attention due to its high absorption coefficient, long carrier diffusion length, high dielectric constant, and low trap density. Also, the low-cost solution-processed synthesis techniques benefit commercialization, which makes them more competitive compared with the commonly used inorganic semiconductors such as Si and GaN [106].

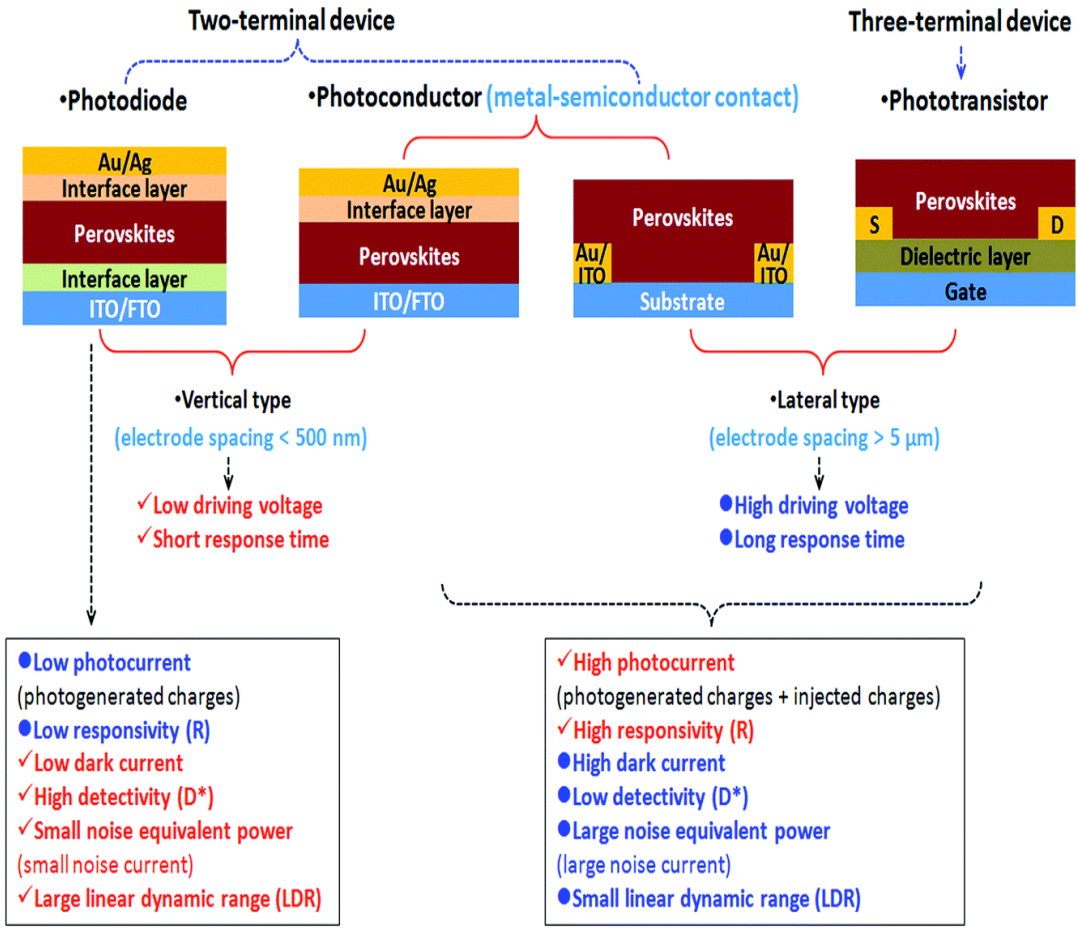

Figure 2:14: Classification of photodetectors. Reproduced from [107], copyright 2017, The Royal Society of Chemistry.

The photodetectors can be classified into three types: photodiodes, photoconductors, and phototransistors as shown in **Figure 2:*14*** [107]. The photodetectors can also be categorised as vertical and lateral regarding the special layout. Photodiodes and phototransistors, only show vertical and lateral types. Photodetectors may also divide into spectrally broadband and narrowband depending on the spectral response window. Broadband photodetectors can detect a broad spectrum of light for example, X-rays, UV light, and visible light, however, narrowband can sense a limited range of wavelengths such as blue, green, and red. Perovskite nanocrystals have a narrow spectrum, so suitable for narrowband photodetectors.

2.9 Advances in doping with alkali metals in halide perovskite materials

2.9.1 Overview

This section was published as a review paper "A review on advances in doping with alkali metals in halide perovskite materials" in SN Applied Sciences (2021). In this review, extensive literature was compared for the halide perovskite materials (HPM) and their doping strategies with alkali metal ions to enhance their optoelectronic efficiency without affecting their structure and inherent properties. In addition, future recommendation and conclusion about stability of HPM and other functional applications was provided.

Abstract

Recent progress in doping of halide perovskite materials (HPM) by using targeted elements has provided a dimension beyond structural and compositional modification, for achieving desired properties and resulting device performance. Herein doping of alkali metal ions (Li^+, Na^+, K^+, Rb^+, and Cs^+) in three-dimensional HPM is reviewed to lay a particular focus on advances in synthesis, doping-induced changes in optical and electrical properties, and their optoelectronic applications. The introduction of alkali metals in HPM shows an effective route for improved morphology, suppressed ion migration, reduction in non-radiative recombination, passivation of bulk and interface defects, and increased thermal stability. In the end, we provide our perspective that the effect of alkali metal incorporation on the efficiency and stability of HPM should be further investigated via in-situ characterization methods and doped HPM should be considered for more functional applications.

Keywords: Halide perovskites; Doping; Alkali metals; Morphology; Defects; Stability

Graphical Abstract:

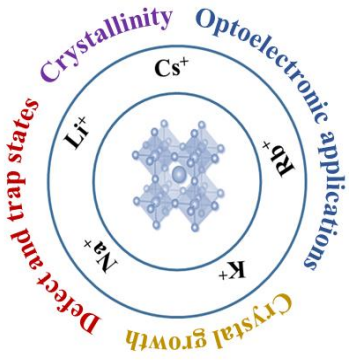

Introduction

Recent research on doping halide perovskites with alkali metal ions such as Li^+, Na^+, K^+, Rb^+, and Cs^+ has been acknowledged for polycrystalline and nanocrystalline thin films to maximize structural and optoelectronic properties i.e. to maximize luminance, facilitates charge injection, enhanced moisture resistance, and energy band alignment [108]–[110].

In this comprehensive review, we discussed advances in the doping of alkali metals for 3D ABX_3 type HPM, which are divided into two sections based on their polycrystalline and nanocrystalline nature. In detail, this review summarizes the impact of alkali metal ions on charge carrier dynamics, crystallinity, bulk and interface defects, and their ability to influence optoelectronic device properties of HPM. Furthermore, a brief outlook on unresolved issues is also reviewed.

2.9.2 Influence of cesium ions doping in HPM

To date, cesium (Cs) is the only alkali metal that can substitute A-site cation in ABX_3 type perovskites due to its large ionic radii (1.67Å) [72], [73]. Mixing of Cs ions with other A-site cations (MA^+, FA^+) is considered a milestone to address the problem of structural instability, and thermal and moisture sensitivity of halide perovskite devices [74]–[76]. Among all HPM

light harvesters, methylammonium lead triiodide ($MAPbI_3$) and formamidinium lead triiodide ($FAPbI_3$) have been considered champion compounds in recent years due to their exceptional absorption coefficient, low exciton binding energy, and excellent photovoltaic properties. However, $MAPbI_3$ shows a disturbing phase transition (tetragonal-cubic) at about 56°C, while the operating temperature of solar cells is approximately 85°C. Also, the bandgap of $MAPbI_3$ is 1.57eV, which hinders the absorption of solar light above 800nm and ultimately reduces the efficiency of PSCs. Although thermally stable $FAPbI_3$ with an appropriate bandgap of 1.48eV shows potential in the presence of sunlight, however, its photoactive α-phase (black phase) transformation into undesired nonphotoactive δ-phase (yellow phase) at room temperature is a big issue [73], [111], [112]. Therefore, optimization of a photovoltaic device efficiency is challenging while using a single cation and it has been suggested to modify the perovskites by mixing Cs-MA, Cs-FA or Cs-FA-MA cations [113], [114].

The incorporation of Cs ions into the $FAPbI_3$ perovskite system improves the phase stability, particularly its transformation from black to yellow phase [115], [116]. A report was published for the stabilization of α phase of $FAPbI_3$, where a computational study was performed to check the influence of FA^+ cation substitution with monovalent cation MA^+, Cs^+, and Rb^+. A series of simulations were performed for relative stabilization of α with respect to δ phase as a function of the chemical nature of the dopant, doping amount, and temperature. It was suggested that α perovskite phase of $FAPbI_3$ can be best stabilized at ambient temperature by 42-50% of mixed Cs/Rb doping and MA^+ can be avoided as it is directed to make the α phase less stable. Furthermore, the substitution of these alkali ions into the target system blue shifts the onset of optical spectra by 0.1-0.2eV with respect to pristine $FAPbI_3$. This study paves the way toward the replacement of organic cations with Cs and Rb ions which are efficient in

stabilizing its photoactive phase [110]. In a recent study, two-step spin coating for sequential doping of Cs and GA (guanidinium) cations was adopted to demonstrate the control on crystallization kinetics of $FAPbI_3$ perovskite thin film with an average grain size of ≈300nm for solar cell application. The addition of Cs cations in the first step induces the formation of δ-$CsPbI_3$ which provides an alternative phase transition pathway for perovskite α-phase. However, slightly larger crystalline grains of about 600nm with several pinholes are formed due to nonuniform nucleation by sparse δ-$CsPbI_3$ crystals. This problem is solved in the second step where doping of GA cations eliminates the pinholes and further enhanced grain boundaries of ≈1μm, hence solar cell device efficiencies above 23% were recorded [117]. Another study was reported about the addition of cesium chloride (CsCl) in mixed cation formulation of $FA_{0.80}Cs_{0.20}PbI_3$ results in a high-quality photoactive layer, large grain size (≈ 1μm), longer carrier lifetime (108.4ns), with perovskite solar cell devices showed PCE of 19.85% [118].

It is now well established from a variety of studies [119]–[123] that the doping of Cs ions into $MAPbX_3$ perovskites optimizes the optical and electrical parameters of the materials while retaining their fundamental properties. Guangcheng and Rui claimed that doping of Cs into the $MAPbI_{3-x}Cl_x$ perovskite films enhances the grain morphology, lifts the valence and conduction band edges, passivates the trap states, and hence promotes the flow of charge carriers [124].

Most importantly, the HPM among which the mixed cation (FAMA) perovskites showed many outstanding properties such as improved carrier diffusion length, and broad absorption spectrum giving rise to the solar power conversion efficiency of over 22% [125], [126]. According to recent studies, partial replacement of FA with smaller size cations (MA^+, Cs^+, and Rb^+) can be the most suitable strategy to work with photoelectric characteristics of FAMA mixed cation perovskites.

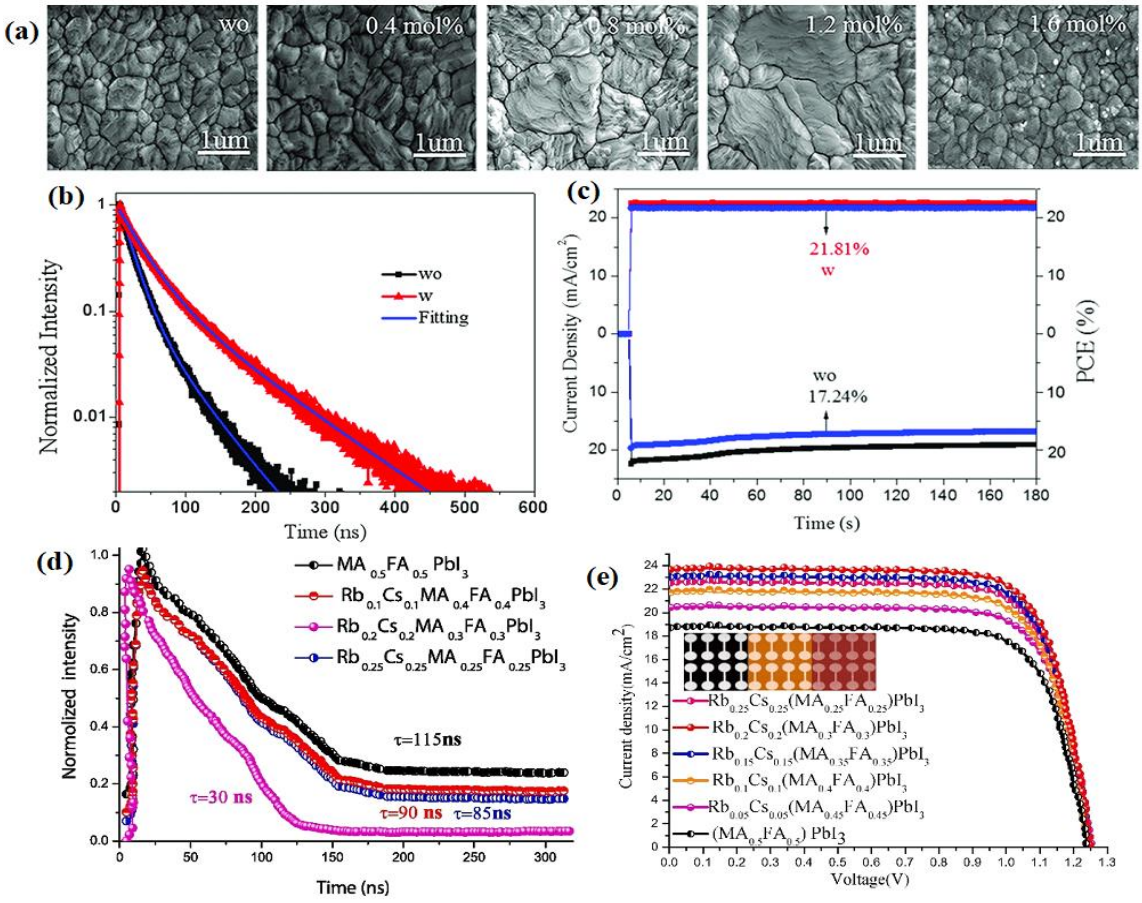

Figure 2:15: (a) SEM images of perovskite films deposited on FTO substrates with 0, 0.4, 0.8, 1.2, and 1.6 mol% CsAc alloying (left-right). (b) Time-resolved PL of perovskite films wo/w CsAc alloying. (c) Stable output curves of current densities and efficiencies of the best-performing PSCs wo/w CsAc alloying. Adapted with permission from ref. [127], copyright 2019, WILEY-VCH. (d) Time-resolved PL (e) and photovoltaic performance of perovskite thin films doped with different proportions of Rb^+ and Cs^+ ions. Adapted with permission from ref.[128], copyright 2020, Elsevier

Table 2.2: Summary of alkali metal ions doped perovskite solar cell performance.

Perovskite active layer	Doped alkali metal	V_{OC} [V]	J_{sc} [mA/cm2]	FF [%]	PCE [%]	Ref.
$CsMAFAPbI_{3-x}Br_x$	Rb	1.18	22.80	81.00	21.80	[129]
$MAFAPbI_{3-x}Br_x$	Rb	1.125	23.24	71.90	18.80	[130]
$(Cs,FA,MA)Pb(I_{0.85}Br_{0.15})_3$	K	1.17	23.20	79.00	21.50	[131]
$FA_{0.83}MA_{0.17}Pb(I_{0.83}Br_{0.17})_3$	K	1.15	23.50	75.00	20.40	[132]
$MA_{0.17}FA_{0.83}Pb(I_{0.83}Br_{0.17})_3$	Rb	1.16	22.80	78.00	21.00	[133]
$CsPbI_2Br$	Rb	1.24	14.02	69.00	12.00	[134]
$CsPbI_2Br$	Rb	1.32	16.25	80.03	17.16	[135]
$FA_{0.83}MA_{0.17}Pb(I_{0.83}Br_{0.17})_3$	Rb	1.14	19.97	72.00	16.51	[136]
	Cs	1.16	20.56	74.00	17.75	
	Na	1.10	21.16	78.00	18.16	
$MAPbI_3$	K	1.10	20.88	78.00	17.81	[137]
$FA_{0.85}MA_{0.15}Pb(I_{0.85}Br_{0.15})_3$	K	1.16	22.99	76.00	20.32	[138]
$Cs_{0.05}FA_{0.79}MA_{0.16}Pb(I_{0.6}Br_{0.4})_3$	K	1.26	19.19	76.00	18.38	[139]
$CH_3NH_3PbI_3$	K	0.92	19.07	68.00	12.07	[140]
$MAPbI_{3-x}Cl_x$	Cs	0.99	21.10	79.30	16.60	[124]
$FAPbI_3$	Cs+MDA*	1.16	26.17	80.10	24.40	[141]
$FA_{0.85}MA_{0.15}PbI_3$	Cs	1.16	24.92	78.64	21.95	[127]
$MA_{0.5}FA_{0.5}PbI_3$	Cs+Rb	1.25	23.70	77.00	22.81	[128]

*methylenediammonium

Shihao et al. treated mixed cation $FA_{0.85}MA_{0.15}PbI_3$ with cesium acetate (CsAc) and doped perovskite films exhibited a large grain size of about 1.39 µm (**Figure 2:*15***a), longer carrier lifetime of 61.5 ns is benefited from the reduction in trap assisted recombination (**Figure 2:*15***b). The maximum PCE of 21.95% and 97% retention in initial PCE values after aging for 55 days was recorded after alloying with Cs^+ and Ac^- (**Figure 2:*15***c, **Table 2.2**) [127]. After that, Bowen claimed the highest reported PCE (22.81%) of PSCs based on four components Rb_xCs_x ($MA_{(1-2x)/2}$ $FA_{(1-2x)/2}$) PbI_3. The reason behind enhanced efficiency is the controlled

doping of Rb^+ and Cs^+ into the precursor solution which facilitates the transformation of δ phase into α phase, improves the photovoltaic performance (**Figure 2:*15***e, **Table 2.2**), and reduced PL lifetimes from 115ns to 90 and 30ns for 10 and 20% doping concentration (**Figure 2:*15***d) [128]. The most recent research studies available on alkali doped HPM for photovoltaic applications are summarized in **Table 2.2**.

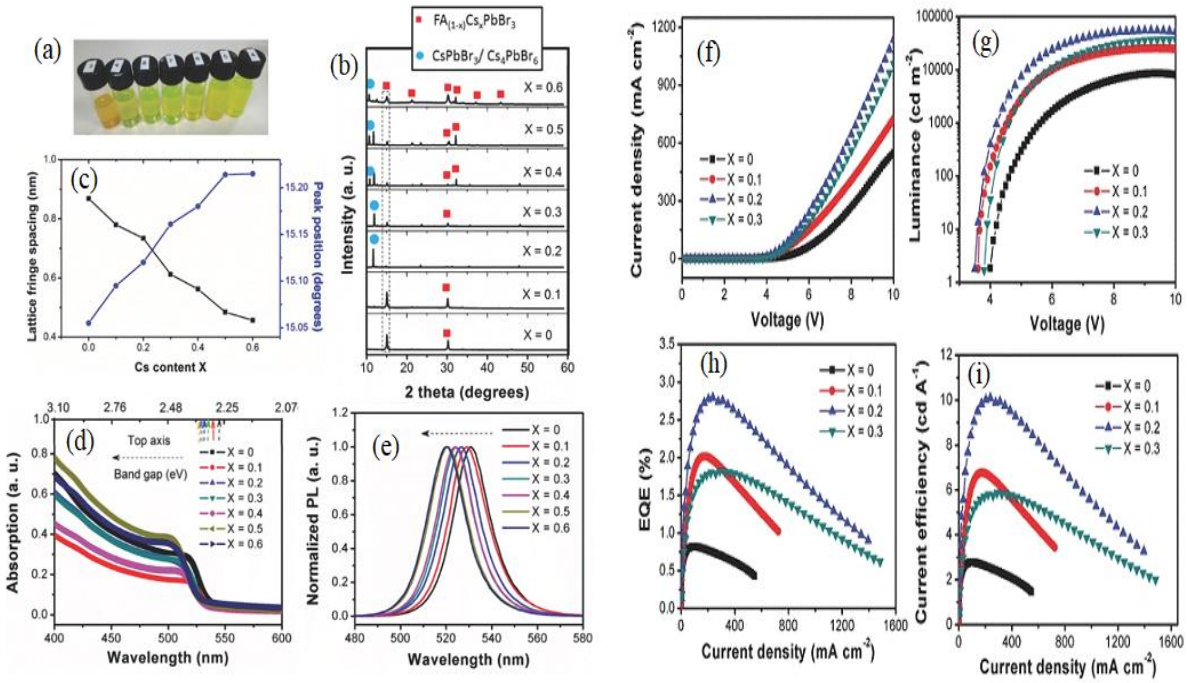

Figure 2:16 (a) Photographs of different perovskite NCs in solution. (b) XRD patterns of $FA_{(1-x)}Cs_xPbBr_3$ (x = 0–0.6). (c) Lattice fringe and peak position (≈15°) as a function of Cs content, x, in $FA_{(1-x)}CsxPbBr_3$. (d) Absorption spectra and (e) PL spectra of $FA_{(1-x)}CsxPbBr_3$ (x = 0–0.6). (f) J–V (g) luminance–voltage, (h) EQE–current density, and (i) current efficiency–current density characteristics of perovskite LEDs, based on $FA_{(1-x)}Cs_xPbBr_3$ (x = 0. 0.1, 0.2, and 0.3). Adapted with permission from ref. [82] , copyright 2017, WILEY-VCH

Nanocrystalline HPM can be characterized as minimizing the exciton dissociation and increasing the radiative recombination because of the quantum confinement effect [77]–[79]. However, their structural stability and physicochemical-related issues may drop the efficiency of perovskite devices within a few operating hours [80], [81]. To address these issues, mixed cation (Cs^+/FA^+) based $FA_{(1-x)}Cs_xPbBr_3$ perovskites nanocrystals (NCs) have been prepared to study the influence of Cs doping on the performance of LEDs. This study also offers some important insights into the different chemical composition ranges (**Figure 2:*16***a) with variable ratios of FA/Cs (x=0-0.6), crystal formation, and tuning of the optical bandgap. X-ray diffraction (XRD) analysis (**Figure 2:*16***b) of all composition ranges of these NCs showed standard perovskites crystal phase. The peak shift from 15.01° to 15.39° was displayed, which shows the shrinkage of d-spacing due to smaller size Cs insertion into the crystal lattice (**Figure 2:*16***c). To further confirm the effect of Cs doping, high-resolution transmission electron microscopy (TEM) is conducted and observe the reduction in lattice spacing and confirm the presence of smaller-size Cs cations. All the perovskite NCs crystallize with the cubic shape and a negligible effect was observed on their sizes after Cs doping. As the content of Cs increases, a blue shift in the absorption band from 525nm to 503nm (**Figure 2:*16***d**)**, corresponds to a shift in bandgap towards high energy levels from 2.27 to 2.33 eV. Moreover, the PL peak (**Figure 2:*16***e) was finely tuned from 531nm to 519nm, with varying ratios of Cs cation doping. Finally, **Figure 2:*16***f-i and **Table 2.3** show the overview of current density to voltage (J-V) characteristics of LEDs based on $FA_{(1-x)}Cs_xPbBr_3$. The best efficiency is achieved when x=0.2 with a maximum luminance of 55005 cdm^{-2}, a current efficiency of 10.09 cd A^{-1}, and an EQE of 2.80% [82].

The approach used in this study was also reported by Bin Xu et al., to support the stance of commercialization of perovskite LEDs [83]. The ligand-assisted reprecipitation (LARP) technique was used to prepare colloidal $MA_{1-x}Cs_xPbBr_3$ NCs with varying amounts (x=0-0.4) of Cs doping in the mixed cation. The precursor solution was prepared by dissolving MABr, CsBr, $PbBr_2$, oleic acid, and oleylamine in dimethylformamide (DMF), and a controlled amount of this solution was added in an anti-solvent to form a green colloidal solution of perovskite NCs.

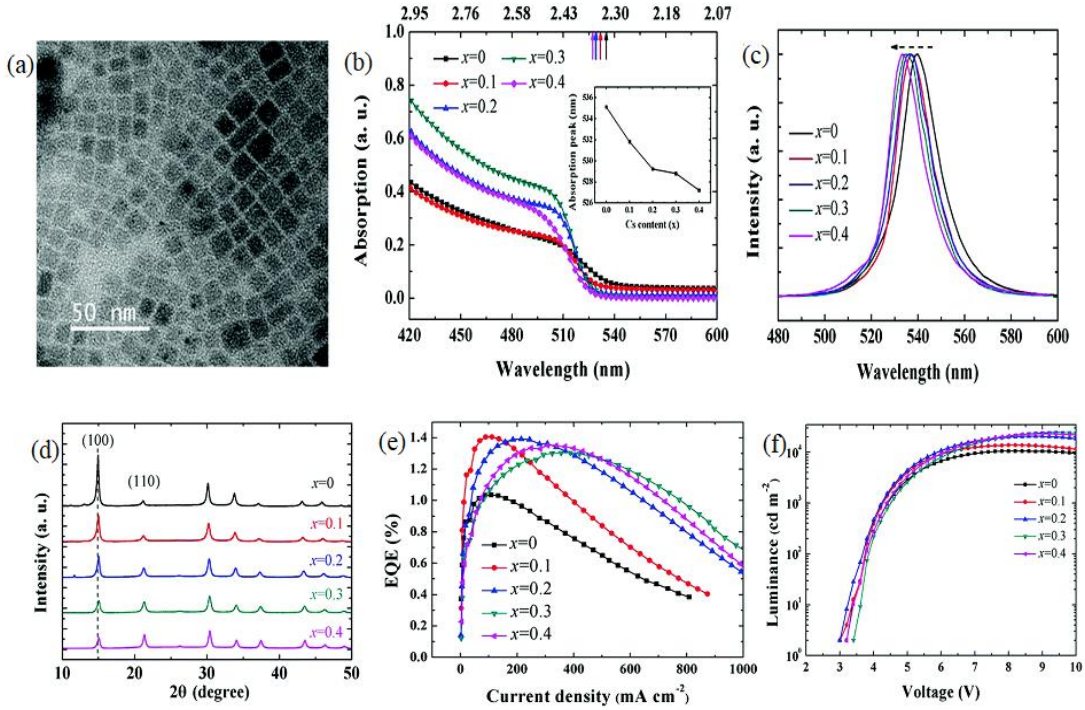

Figure 2:17: (a) TEM image of the $MA_{0.7}Cs_{0.3}PbBr_3$ NCs. (b) The absorption spectra, (c) PL spectra, (d) XRD patterns, (e) EQE vs. current density and (f) luminance vs. voltage, of $MA_{1-x}CsxPbBr_3$ (x = 0 to 0.4). Adapted with permission from ref. [83] , copyright 2017, The Royal Society of Chemistry

The as-synthesized perovskite NCs were single-crystalline of size between 8nm to 12nm (**Figure 2:*17*a).** To study the effect of Cs doping amount on the optical properties of mixed cation perovskite NCs, UV-Vis absorption, and photoluminescence (PL) spectra were recorded (**Figure 2:*17*b-c**). With the different amounts of Cs doping, the absorption band was blue shifted from 515nm to 505nm and PL spectra also changed from 539nm to 533nm. The crystalline structure of all Cs doped samples was exhibited from XRD patterns (**Figure 2:*17*d)** and the increase in (110) peak intensity shows the preferred crystal growth after the addition of dopant. The synthesized $MACsPbBr_3$ NCs were single crystalline with the sizes changing from 8nm to 12nm and had a cubic shape with no significant change observed after the addition of Cs ions into the samples. The J-V characteristics of optimized Cs-doped perovskite LEDs showed an excellent value of luminance of 24500 cdm^{-2} and an EQE of 1.3% (**Figure 2:*17*e-f**).

2.9.3 Role of incorporating rubidium ions in HPM

Rubidium (Rb) has been considered an emerging alkali metal that can be used as a functional dopant in HPM, which has a significant impact on the structural parameters of single or mixed cation perovskites [84].

The debate on whether Rb metal cations occupy the main A-site position in a perovskite crystal lattice or not is still controversial. However, few studies showed the presence of Rb^+ ions at the A-site of the perovskite crystal lattice. Saliba et al. [129] first embedded the Rb^+ into the mixed A-site cation (CsMAFA) formulations to achieve stabilized PCE of 21.6%. This study opens the avenue to study the influence of rubidium ions for multi-cation perovskites on solar cells, LEDs, and photo-detection applications. Daniel et al. [133] worked on the doping of rubidium iodide **(**RbI**)** for state-of-the-art triple cation composition $Cs_5(MA_{0.17}\,FA_{0.83})_{95}Pb(I_{0.83}\,Br_{0.17})_3$

synthesized in the recently published study [142]. The addition of Rb^{+} ions to the mixed A-cation perovskite showed an improved PCE of about 21% mainly due to high open-circuit voltage (1.16V) and fill factor (78%). Furthermore, different concentration of RbI (0.5-2%) for all in-organic perovskite ($CsPbI_2Br$) was analyzed in the construction of high-efficiency, low-cost, and improved air stability of hybrid PSCs [134]. Compared with un-doped $CsPbI_2Br$ perovskite films, excellent crystallinity, improved surface morphology, and enhanced absorbance were shown after the incorporation of RbI, as had been reported in previously published studies [136], [143].

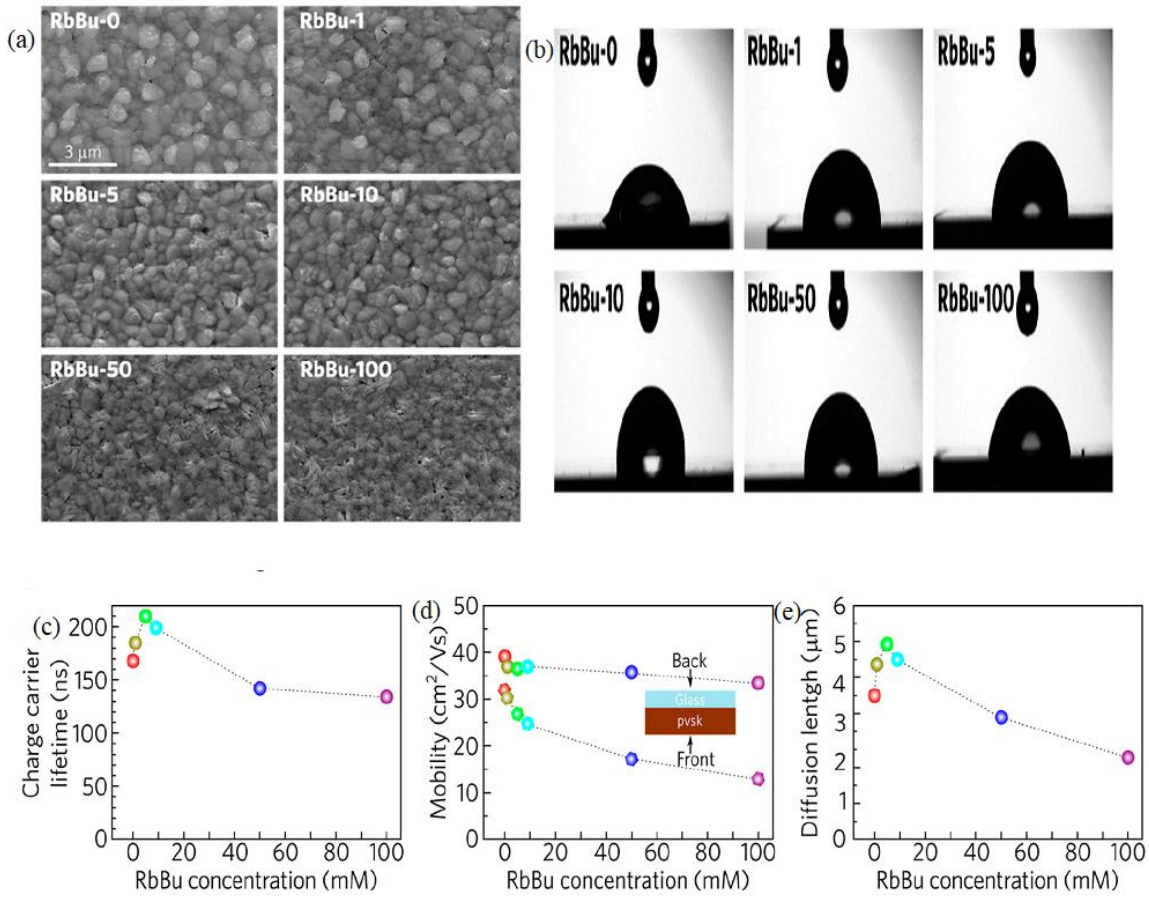

Figure 2:18: (a) SEM images, (b) contact angle images and (c) charge-carrier lifetimes, (d) electron−hole sum mobilities from optical-pump terahertz-probe (OPTP) measurements, (e) charge-carrier diffusion lengths considering front face excitation as a function of the RbBu concentration. Adapted with permission from ref. [144], copyright 2020, American Chemical Society

Recently, post-passivation of multi-cation perovskite $Cs_{0.10}FA_{0.90}Pb\ (I_{0.83}Br_{0.17})_3$ by rubidium butyrate (RbBu) was reported to explain the role of Rb^+ and butyrate anion without affecting the perovskite crystallinity and surface morphology. After annealing of spin coated $Cs_{0.10}FA_{0.90}Pb(I_{0.83}Br_{0.17})_3$ perovskite thin film, different concentrations (1, 5, 10, 50, and 100mM) of RbBu sprinkled on it to study the charge carriers lifetime, diffusion length, resistance against moisture, and photovoltaic performance. There is no obvious change in surface morphology from RbBu=0-10mM and grain sizes between 0.4-1.2µm were observed as shown in **Figure 2:*18***a. After that, rod-like crystals were noticed for a higher concentration of RbBu (50-100mM) due to the presence of δ-$RbPb(Br_xI_{1-x})_3$**.** To understand the effect of butyrate on the hydrophobicity of multi-cation perovskite, the maximum contact angle for RbBu-10 was recorded (**Figure 2:*18***b**)**. As a general trend, the additives increase the charge carrier lifetime (τ_S), and RbBu (5mM) showed a maximum lifetime of τ_S= 210ns while drop-in charge-carrier mobility from µ=31.9 cm^2/Vs to from µ=12.9 cm^2/Vs exhibiting the role of different RbBu molar concentrations (**Figure 2:*18***c,d). Diffusion length (L_D) (**Figure 2:*18***e**)** measurements of the passivated films enhanced up to 5µm for RbBu=5mM and charge carrier diffusion length decreases to 2µm for higher or non-passivated perovskite films [144].

Another interesting aspect of rubidium ions has been studied to successfully solve the crystals phase instability and high-temperature thermal instability problems of $FAPbI_3$ perovskite for

high-performance photodetection. A large amount of Rb^+ ions (up to 30%) was added to reduce the pinholes and increase the crystallinity and absorption intensity of $FAPbI_3$ thin films. As a result, the photodiode based on optimized $Rb_{0.3}FA_{0.7}PbI_3$ perovskite film exhibited high responsivity of 0.43 AW^{-1}, an ultrafast response speed of about 300ns, and detectivity of more than 10^{12} Jones [145].

Rubidium doping has been widely studied for tuning of absorption range, low PLQY, and thermal instability issues of all-inorganic halide perovskites ($CsPbX_3$) nano geometries. Taking into account the importance of Rb^+ ions, Amgar et al. embedded the certain content of Rb ions into $CsPbX_3$ (X=Cl or Br) nanoparticles to tune the absorption range in the near-ultraviolet and visible range (325-500nm). Size distribution analysis of all samples presented a declining trend with an increase of Rb ions for $CsPbX_3$ (X=Cl or Br) [146]. Another study to improve the emission of manganese (Mn) doped Mn: $CsPbCl_3$ NCs was conducted, where increased emission, highest PLQY (up to 63.18%), and thermal stability with the addition of Rb^+ ions were exhibited. The average size of Mn: $CsPbCl_3$ NCs without Rb doping was 11.37nm which decreases to 7.7nm after doping [147].

Similarly, different nanostructures of $Rb_xCs_{1-x}PbBr_3$ (**Figure 2:*19***a) namely nanocubes and nanoplates with tunable emission (450-500nm) were reported to fabricate blue-emitting LEDs (**Figure 2:*19***b). The as prepared nanoplates were of varying thicknesses and smaller in size due to the presence of Rb ions. The addition of Rb ions into the pure bromine phase could provide a path to increase the bandgap without introducing phase segregation at high voltage as it tends to distort the PbX_6 octahedra and reduces the overall orbital overlap. As a result, high PLQY (>60%), improved luminance, and EQE of 0.11% to 0.87% for deep-blue and sky-blue (**Figure 2:*19***c-e) LEDs were displayed [85].

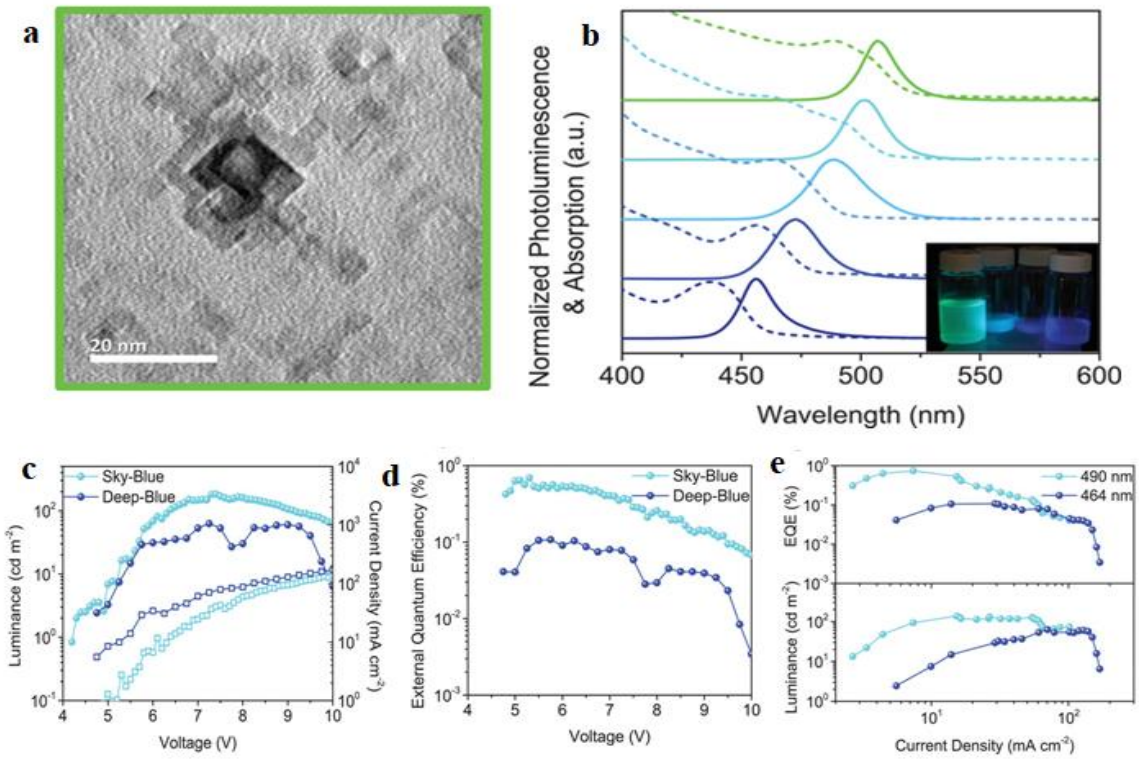

Figure 2:19 (a) TEM images of synthesized $RbxCs_{1-x}PbBr_3$ nanocubes (b) Photoluminescence (solid line) and absorption (dashed line) spectra of the synthesized solution. Inset is a picture of various solutions, illuminated by a UV-LED source (λ = 374 nm) displaying the tunable emission. (c) Current density (J) is displayed by squares and luminance (L) is displayed by circles. (d) External quantum efficiency as a function of applied bias. (e) Devices that exhibited the largest luminance at their peak EQEs. Adapted with permission from ref. [85],copyright 2019, WILEY-VCH

Fanyaun et al. studied the interplay of Rb^+ ions to realize the severe challenges of PL and EL in multi-cation blue-emitting perovskite quantum dots (QDs). It was noted that perovskite QDs exhibited cube-shaped and smaller size (5.17nm vs 6.38nm) structures since Rb ions were incorporated into them. The addition of Rb^+ realized to enlarge the bandgap due to octahedral

distortion and strong quantum confinement resulted in outstanding PLQY of 64.5% and 49.8% for greenish-blue $(Rb_{0.33}Cs_{0.67})_{0.42}FA_{0.58}$ $PbBr_3$ and deep-blue $(Rb_{0.33}Cs_{0.67})_{0.42}FA_{0.58}$ $PbCl_{1.25}Br_{1.75}$ perovskite QDs [148].

2.9.4 Incorporating other alkali metal ions (K^+, Na^+, and Li^+) for enhanced performance of HPM

After studying the beneficial aspects of rubidium, scientists were prompted to explore the other smaller alkali metal ions such as K^+, Na^+, and Li^+. Previously published studies about polycrystalline perovskite thin films have been extensively reported on their high trap state density, enlarged grain boundaries, instability to heat, UV (ultraviolet), and humidity [149]–[151].

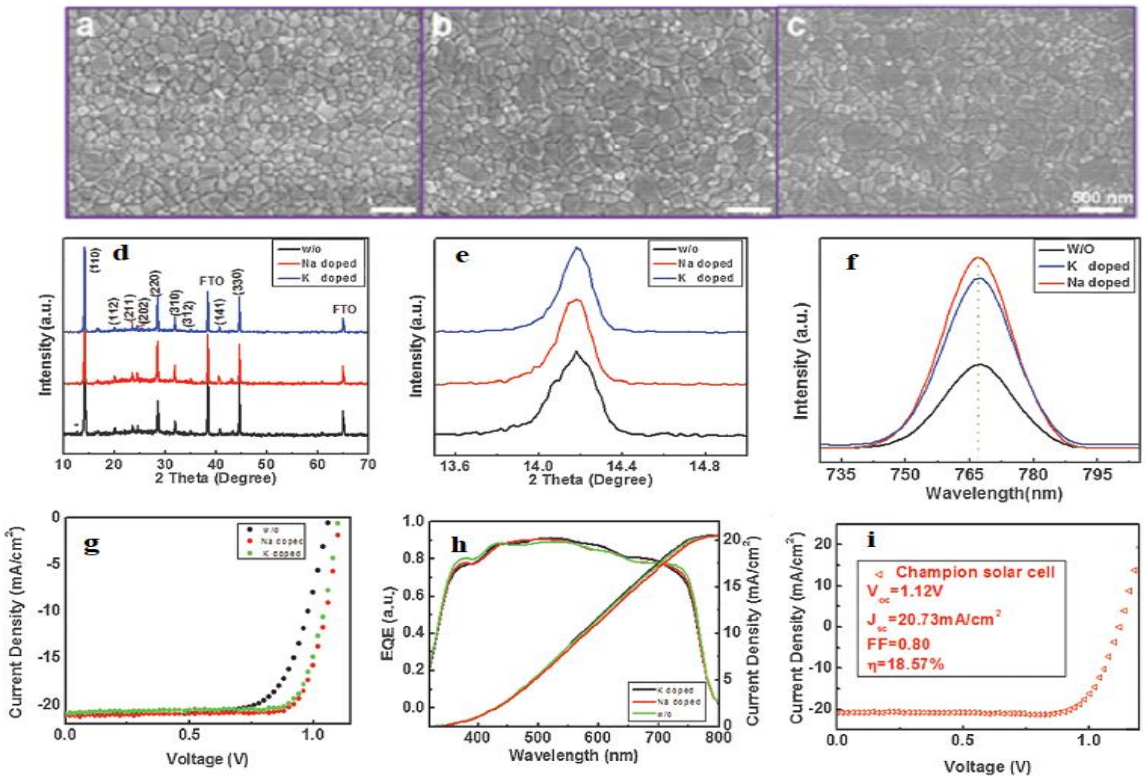

Figure 2:20: SEM images of (a) without, or with (b) NaI (c) KI doping (d) The X-ray diffraction patterns (e) the enlarged comparison of (110) diffraction peak (f) the steady-state

photoluminescence (PL) (g) the current density–voltage characteristics and (h) external quantum efficiency (EQE) spectra with Na^+, K^+ doped and the control sample without doping (i) The J–V curve of champion PSCs with 1.0 mol% Na^+ doping measured at the AM 1.5G solar spectra of 100mWcm^{-2} at a reverse scan. Adapted with permission from ref. [137], copyright 2017, WILEY-VCH.

Wangen et al. investigated the role of alkali metal ions (Na^+, K^+) to make the $MAPbI_3$ polycrystalline thin films with fewer trap states, reduced grain boundaries, and increased built-in potential leading to enhanced PCE. It was observed from morphological analysis **(Figure 2:20**a-c), the addition of Na^+ and K^+ ions help in high coverage and increases the grain size from ≈140 nm to ≈220nm and ≈230nm, respectively.

XRD analysis depicts **(Figure 2*:20*d-e)** the typical tetragonal $MAPbI_3$ phase of all samples and an enlarged (110) peak with a significantly narrow width showed that large grain sizes were obtained after the addition of Na^+ and K^+ ions. To check the trap states of the perovskite absorber layer, steady-state PL spectra were recorded **(Figure 2*:20*f)**. An obvious increase in PL intensity was detected, that assigned to the reduced trap centres due to the coverage of grain boundaries by alkali metal ions. The J-V curves **(Figure 2*:20*g-i)** showed that both alkali Na^+ and K^+ have a positive effect on the overall performance of perovskite photovoltaic devices.

Besides studying the influence of potassium on polycrystalline HPM, a considerable amount of literature has also been published on nanocrystalline HPM. It has been well reported as the passivating agent to form a potassium halide layer to overcome halide segregation in mixed-halide perovskite thin films. Moreover, modification of grain boundaries and suppression of ions migration are the potential benefits of using potassium in HPM [131].

Table 2.3: Summary of alkali metal-doped ions perovskite light-emitting diode

Perovskite emitting layer	Doped alkali metal	EL [nm]	Luminance [cd/m^2]	EQE %	CE [cd/A]	[Ref]
$MAPbBr_3$ (Polycrystalline)	Rb	527	7694	-	9.54	[152]
$FAPbBr_3$ (Polycrystalline)	Rb	532	66 353	7.17	24.22	[153]
$CsFAPbBr_3$ (QDs)					8.50	
$CsFAPbCl_{1.25}Br_{1.75}$		502	750	3.60	0.45	
	Rb	466	39	0.61		[148]
		490	183	0.69	-	
$CsPbBr_3$ [NCs]	Rb	464	63	0.11		[85]
$CsPbBr_3$ [NCs]	K	522	5759	5.60	-	[154]
$CsPbI_{3-x}Br_x$ [NCs]	K	637	2671	3.55	-	[155]
$CsPb(Br/Cl)_3$[NCs]	K	477	86.95	1.96		[156]
$FAPbBr_3$ [NCs]	Cs	525	55 005	2.80	10.09	[82]
$MAPbBr_3$[NCs]	Cs	523	24500	1.30	4.10	[83]

Halide segregation is a major problem in mixed HPM which results in poor electro-luminance (EL) stability in LEDs. To overcome this problem, potassium bromide surface coated all inorganic $CsPbI_{3-x}Br_x$ NCs emitting at 640nm were synthesized via the hot-injection method. The resulting potassium passivated high-quality NCs showed above 90% PLQY and good dispersion stability for weeks. As a result, pure red-emitting LEDs at 637nm exhibited a highly stable brightness of 2671 cdm^{-2} and EQE of 3.55% [155].

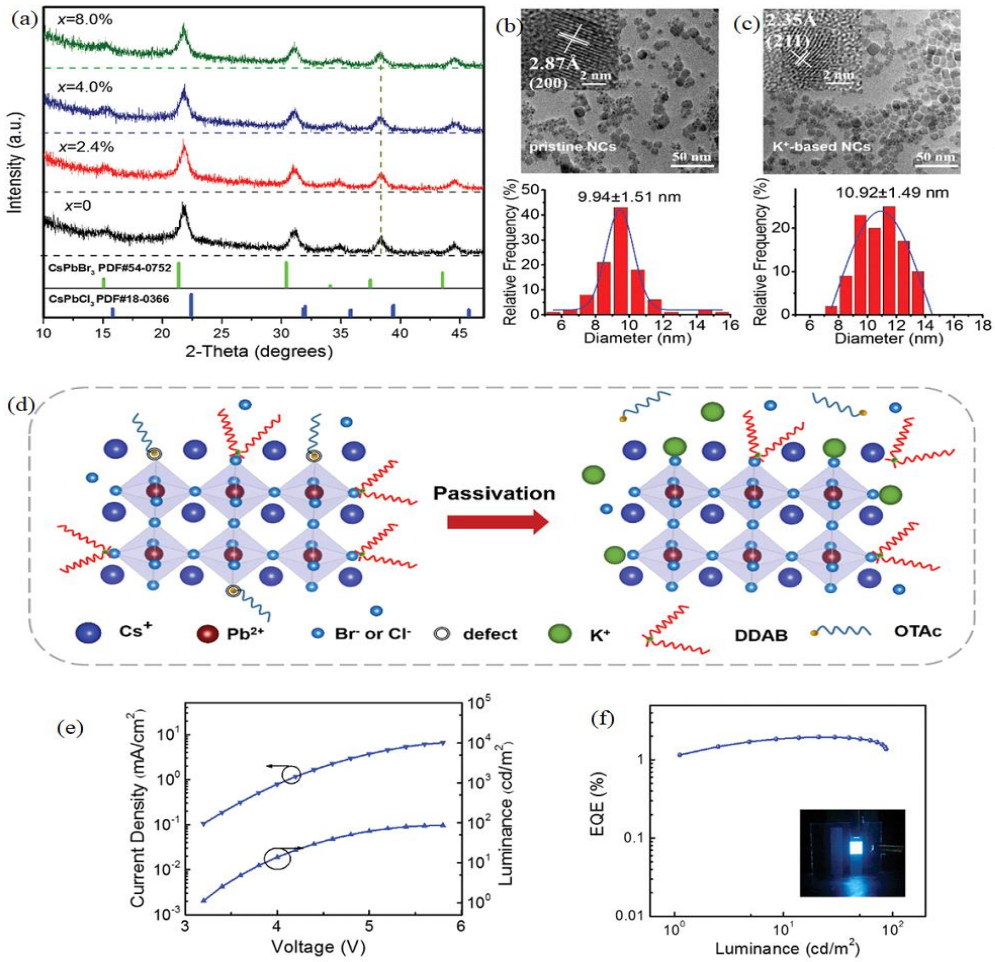

Figure 2:21: (a) XRD patterns of perovskite films with different x values and standard XRD patterns of $CsPbBr_3$ and $CsPbCl_3$. (b and c) TEM images of pristine and K^+ based (4.0% in terms of nominal K^+ ratio) NCs and size distribution analysis; the insets show the corresponding high-resolution TEM images. (d) Schematic illustration of potassium passivation. (e) Current density–voltage–luminance curves and (f) EQE-luminance curve for LED device based on x = 4.0%. Adapted with permission from ref [156], copyright 2020, WILEY-VCH

Several reports [157]–[160] have shown that blue perovskite LEDs still lag behind the red and green ones due to difficulties in synthesizing stable materials, maintaining high quantum efficiency, and halide segregation to get required emission parameters.

Table 2.4: Radiative lifetime analysis for the alkali-doped halide perovskite materials

Perovskite	Doped alkali element	Morphology of perovskite film	Radiative lifetime (ns)	Ref
$CsPbI_{3-x}Br_x$	K	Nanocrystalline	8.73	[155]
$CsPbCl_3$	K	Nanocrystalline	2.10	[161]
$CsPbBr_3$	K	Nanocrystalline	2.21	[154]
$FA_{0.85}MA_{0.15}Pb_{(I0.85Br0.15)3}$	K	Polycrystalline	32.7	[138]
$CsPb(Br/Cl)_3$	K	Nanocrystalline	4.57	[156]
$FAPbBr_3$	Rb	Polycrystalline	2.77	[153]
$CsPbBr_3$		Nanocrystalline	4.7	
$CsFAPbBr_3$	Rb		3.2	[148]
$CsFAPbCl_{3-x}Br_x$			3.5	
$CsPbBr_3$	Rb	Nanocrystalline	5.47	[85]
$MAFAPbBr_3$	Rb	Polycrystalline	4.68	[130]
$FAPbBr_3$	Cs	Nanocrystalline	4.80	[82]

The small amount of impurity ion doping has been considered an effective strategy to improve the optical properties of nanocrystalline HPM. Several studies have been published on doping of a variety of ions including lanthanides [162] and manganese [163] with great success. However, the introduction of new emissions due to additional ions causes the impurity in blue light. Smaller size alkali metal ions have the advantage to enhance the efficiency of blue-emitting devices without disturbing the original emission spectra. Given the low performance of $CsPbCl_3$ QDs, doping of potassium ions was introduced for controlling the emission properties of blue-violet light, and a blue shift in absorption edge was observed. Only a small

amount of potassium ions enhanced the PLQY of perovskite QDs at 408nm from 3.2 to 10.3% [161].

To further study the role of potassium incorporation into the $CsPb(Br/Cl)_3$ NCs, Fei et al. demonstrated the use of K^+ ions as metal-ligand to improve the nonradiative recombination and PLQY. It is clear from the XRD peaks (**Figure 2:21**a) that all samples showed the characteristic peaks of typical cubic crystal planes of $CsPb(Br/Cl)_3$, with no additional diffraction peak confirming the presence of K^+ ions as capping agent outside the crystal surface. The transmission electron microscopy (TEM) images (**Figure 2:21**b-c) exhibit the lattice plane of (200) and (211), which further confirms that the addition of K^+ ions does not affect the crystal structure. The NCs exhibit a slight increase in size with the addition of K^+ as shown in size distribution histograms (**Figure 2:21**b-c), where the average size for the untreated and K^+ treated is 9.94nm and 10.92nm respectively. It was demonstrated that alkali metal doping methods can accelerate the speed of reaction, leading to an increase in the NCs size.

Moreover, a schematic presentation (Figure 2**:21**d) of K^+ ions bonding with halides verified the reduced number of insulating ligands around the NCs. In terms of device performance (**Figure 2:21**e-f,

Table 2.3), the champion blue perovskite LED with 4.0% of K^+ ions showed the highest EQE of 1.96% and luminance of 86.95 cd m^{-2} [156].

In contrast to this study, Minh et al. demonstrated that potassium doping of NCs can enhance the coverage of capping ligands around $CsPbBr_3$ nanocrystal confirmed by N-H stretching at 3356 cm^{-1}. The reason for increased stretching is due to better oleylamine coverage which could be ascribed to the formation of the bromide-rich surface due to potassium ions. Furthermore,

Fourier transforms infrared (FTIR) peaks of 2.5% potassium doped sample showed nearly double intensity as compared to the sample without doping. Also, reduction in trap states and reduced surface energy of NCs were believed due to the more insulating ligands attached to the NCs surface [154].

2.9.5 Conclusion and outlook

In this review, we summarized comprehensive progress on doping of alkali metal ions (Li^+, Na^+, K^+, Rb^+, Cs^+) in terms of their ability to markedly influence the electrical, optical, and doping-induced charge carrier dynamics in halide perovskite materials. Alkali metals have been successfully doped in polycrystalline halide perovskites, giving rise to structural stability, reduced defect states, enlarged grain boundaries, and improved film morphology. Moreover, alkali metal doped NCs have shown reduced crystal native defects, improved thermal and moisture stability, prolonged charge carrier lifetime, and high PLQY.

Looking forward, to fully exploring the potential benefits of alkali metals in perovskites, considerably more research work will need to be done to determine the true position of alkali metals ions, the influence of doping on crystal orientation, and the principle behind the improved optoelectronic properties**.** Also, there is a wide research gap in co-doping the high-band gap perovskite to enhance stability and cover a wide luminance range. Thus, we expect that advanced characterization techniques such as in-situ transmission electron microscopy should be implemented to study the influence of the incorporation of alkali metal ions. At present, alkali metal-doped perovskites are mostly reported for solar cells and LED construction. Keeping in mind the unique properties of alkali metals in perovskites, doped perovskites should consider in other applications such as photodetectors, X-ray detectors, and single-photon sources.

2.10 Recent Developments in Smart Textiles Based on Perovskite Materials

2.10.1 Overview

This part is available as a review paper "A Review of Recent Developments in Smart Textiles Based on Perovskite Materials" in Textiles (2022). This study highlights the importance of using metal halide perovskites into the textile-based substrates. Also, future directions on integrating perovskites for flexible substrates were stated.

Abstract

Metal halide perovskites (MHPs) are thought to be among the most promising materials for smart electronic textiles because of their unique optical and electrical characteristics. Recently, wearable perovskite devices have been developed that combine the excellent properties of perovskite with those of textiles, such as flexibility, lightweight, and facile processability. In this review, advancements in wearable perovskite devices (e.g., solar cells, photodetectors, and light-emitting diodes) concerning their device architectures, working mechanisms, and fabrication techniques have been discussed. This study also highlights the technical benefits of integrating MHPs into wearable devices. Moreover, the application challenges faced by wearable perovskite optoelectronic devices-from single devices to roll-to-roll manufacturing, stability, and storage, and biosafety-are briefly discussed. Finally, future perspectives on using perovskites for other wearable optoelectronic devices are stated.

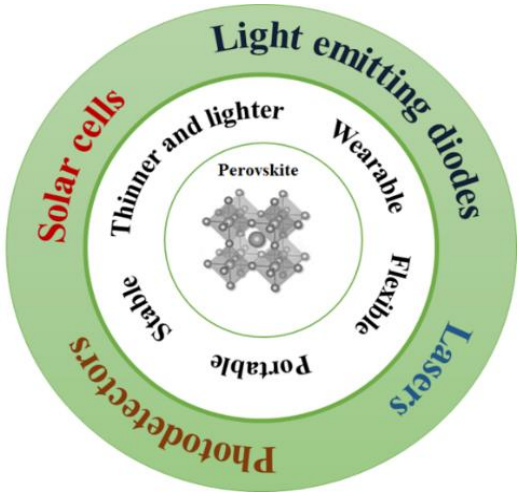

2.10.2 Introduction

Wearable and flexible optoelectronics have been the subject of many research studies due to promising applications in various emerging fields including health care systems, flexible displays, sensors, and human-activity monitoring. The dominant features of wearable optoelectronic devices are flexibility, lightweight, and large-area processability at low-temperature flexible substrates [164], [165].

Metal halide perovskites (MHP) have received considerable attention in textile-based flexible optoelectronic devices due to their high optical absorption coefficient, efficient charge carrier mobility, high photoluminescence quantum yield (PLQY), and low-cost solution fabrication techniques. MHP have been considered important materials by a growing body of research community due to their application in solar cells, light-emitting diodes (LEDs), photodetectors (PDs), lasers, and nonlinear optics [166].

In 2009, after Kojima and co-workers demonstrated the first perovskite device, MHP have been a question of great interest in a wide range of optoelectronic devices [167]. Kumar et al. reported the first flexible solar cells with a power conversion efficiency (PCE) of 2.6% [168].

Recent advances in flexible perovskite devices and an understanding of MHP have facilitated to boost in the PCE of solar cells by more than 20% [169]. Similarly, the first flexible LEDs were fabricated by Bade et al. in 2016. In this study, printed metal halide perovskite LEDs were reported where carbon nanotubes (CNT) and silver nanowires were used as anode and cathode respectively. A composite film made of $MAPbBr_3$, and polyethylene oxide was used as an emissive layer in LEDs. The devices on CNT/polymer were able to handle a radius curvature of 5mm and had an external quantum efficiency (EQE) of 0.14% [170]. To improve the efficiency of flexible LEDs, the perovskite emissive layer has been constantly improved and EQE has been greater than 20% [171]. Moreover, the first MHP-based broadband photodetector was reported on a flexible ITO-coated substrate. The flexible perovskite photodetector was sensitive to a broadband wavelength from the ultraviolet to the entire visible with measured photo-responsivity of $3.49AW^{-1}$, and $0.0367AW^{-1}$ at 365nm and 780nm wavelength respectively [172].

As solution-processable MHP offer opportunities for the fabrication of wearable, light-weight, portable, and bendable optoelectronic devices, perovskite-based wearable devices have become the focus of a wide range of electronic devices [173], [174]. Textile-based flexible perovskite devices have been developed by different methods such as vapour deposition [175], ink-jet printing [176], [177], and other roll-to-roll printing methods [178].

Recently, considerable literature has grown up around the theme of wearable optoelectronics and their applications in intelligent devices such as flexible solar panels, and intelligent sensors. For textile-based wearable optoelectronics, mechanical flexibility is an important parameter. However, conventional perovskite-based optoelectronic devices are fabricated on rigid and brittle substrates, which hinders their use in wearable electronics. One of the greatest challenges

is the weight and special layout requirements for wearable optoelectronics. The optoelectronics devices synthesized on rigid substrates are not the proper selection for smart wearables. So far, flexible optoelectronic devices are fabricated on substrates such as polyethylene terephthalate (PET) or polyester, poly (ethylene 2,6-naphthalate) (PEN), and polyimide (PI).

Indium tin oxide (ITO) is the most widely used electrode material due to its excellent optical transparency and low electrical resistance, whereas rigidness limits its use in flexible devices [179], [180]. Although many plastic-based flexible and bendable substrates such as PET have been reported to replace the rigid electrode [181]–[183], the researcher has concerns about their ability to be wearable, breathable, and conformable [184]. In addition, electron transport layers (ETL) and hole transport layers (HTL) are also important components of textile-based flexible perovskite devices. Their optical transparency and high charge conductivity are the main factors to evaluate the performance of wearable perovskite optoelectronic devices [185].

The purpose of this paper is to review recent research and development into textile-based flexible perovskite devices. The specific objectives of this study are to explore the device architectures, working mechanisms, fabrication techniques, and recent advances in fibre and fabric-based perovskite optoelectronic devices**.** This study seeks to do a comprehensive comparison of available data which will help to address the research gaps in textile-based perovskite devices. Moreover, the challenges of wearable perovskite devices are proposed, and future directions are mentioned.

2.10.3 Perovskite Device structures and working mechanism.

Solar cells

The device configuration is a key aspect of analysing the overall efficiency of perovskite solar cells. Flexible PSCs have a similar configuration to rigid devices. PSCs are mostly categorized

as regular (n-i-p) and inverted (p-i-n) architectures depending on which carrier transport layer (ETL/HTL) is encountered by the solar light first [186]–[190]. These two architectures can be further classified into mesoscopic and planar. A mesoporous layer is integrated into the mesoscopic structure while all the planar layers are used in the planar structure. Perovskite solar cells without electron and hole transport layers are also reported by the researcher. In brief, six types of PSCs have been studied by many researchers: n-i-p structure (planar), p-i-n structure (planar), n-i-p structure (mesoscopic), p-i-n structure (mesoscopic) (**Figure 2:*22***a-d), ETL, and HTL free structures. In a typical device structure, perovskites act as a photoactive layer and absorb the light to generate the free charges. Electrons and holes are transferred by ETL and HTL to the cathode or anode to avoid the chances of charge recombination [185], [191], [192].

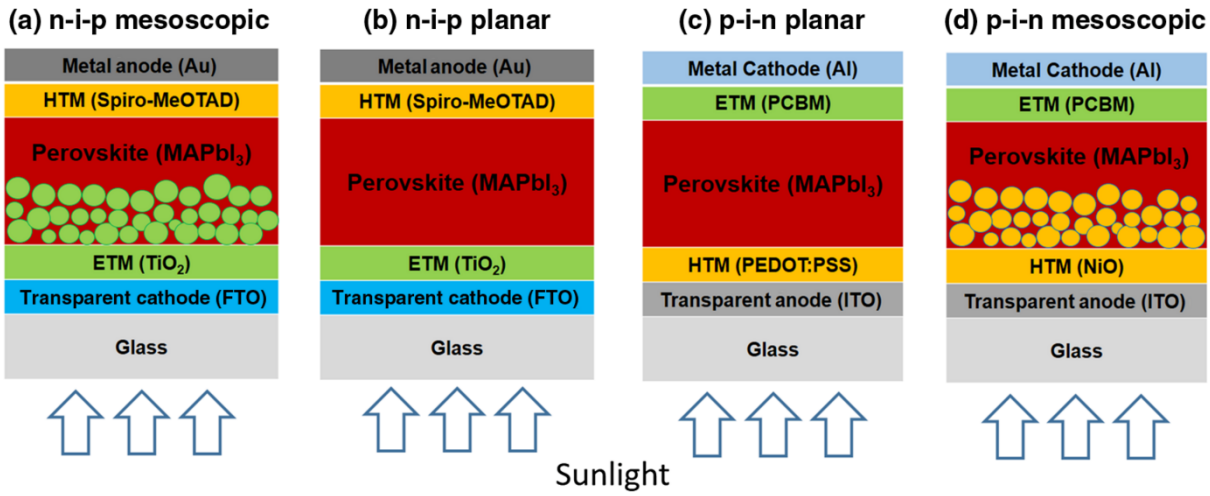

Figure 2:22: Schematic diagram showing the four typical layered structures of perovskite solar cells. (a) n-i-p mesoscopic (b) n-i-p planar (c) p-i-n planar (d) p-i-n mesoscopic. Reproduced from ref. [192], copy right 2018, Springer nature.

Light-emitting diodes (LEDs)

Typical perovskite LEDs adopt one of the two configurations: conventional and inverted, which mostly refers to n-i-p or p-i-n structures respectively. For the conventional layout, LEDs are generally comprised of a glass substrate covered with a transparent conductive electrode such as ITO, to work as a cathode. This electrode injects an electron into the ETL and then into the perovskite emissive layer (EML). Similarly, the holes are injected from HTL to the perovskite layer for radiative recombination with electrons. For an inverted layout, the electrons and holes are injected in the opposite direction, where ITO worked as an anode to inject holes into the HTL and then into the perovskite emitter. At the same time, electrons are injected from the cathode to ETL to enter the EML where radiative recombination occurs [193].

Ideally, the device structure is designed in a way that electrons and holes injected from electrodes recombine radiatively in perovskite EML, giving rise to the emission of photons [194], [195]. For the fabrication of textile-based perovskite LEDs, flexible substrates and the choice of electrodes are the key factors. These are important components that define the mechanical behavior, surface roughness, breathability, and wearability of textile-based perovskite LEDs [170].

Photodetectors

MHP have emerged as the most efficient and low-cost energy materials for diverse optoelectronic and photonic device applications. Recently, many exciting results on perovskite-based light detector devices have been reported. Different device configurations of perovskite photodetectors have developed and demonstrated a significant increase in photodetection efficiency. MHP-based photodetectors are generally divided into, photodiodes, photoconductors, and phototransistors. Photodiodes also known as vertical-structure photodetectors, consist of photoactive material sandwiched between two electrodes. The

vertical configuration of photodetectors is structured from planar heteronode PSCs, hence this layout can be roughly divided into regular (n-i-p) and inverted (p-i-n) categories [165], [196]. The lateral-structure photodetectors comprise photoconductors and phototransistors, which can detect light and signal amplification. Photoconductors have the simplest device structure, which consists of photoactive material and two ohmic metal contacts to form a metal-semiconductor-metal configuration. Due to the considerable distance between two electrodes, photogenerated charge carriers will take a long time to reach electrodes, hence slow response time and high-driving voltage [197].

For textile-based flexible photodetectors, flexible substrates, flexible electrodes, and functional layers are the main elements. So far, a variety of flexible substrates including carbon cloth, fibre, paper, PET, PI, and polydimethylsiloxane (PDMS) have been reported in perovskite flexible photodetectors [193].

2.10.4 Manufacturing Techniques

Due to the chemical nature of MHP, perovskite thin films can be synthesized by using a precursor solution. The processability of perovskite solutions can be made possible by the lab-scale spin coating method, which has provided the most efficient PSC devices with PCE of over 25% being the present best-reported result [198]. At the commercial scale, solution processing is also compatible with roll-to-roll (R2R) manufacturing [199], [200]. R2R production is the ultimate solution to fabricating large-area modules in terms of low-cost and high output. Printing/coating techniques that are compatible with R2R manufacturing include ink-jet printing, slot-die coating, blade coating, and spray coating [186].

Spin coating

Spin coating (**Figure 2:23**a) is a convenient and widely used solution-based method to fabricate uniform and pinhole-free perovskite thin films. By using this method, the compact thin films can be directly deposited on a variety of substrates (glass, quartz, plastic, and silicon) from a precursor solution made of metal halides and organic halides. In addition to spinning speed and time, a post-annealing treatment at low temperature (T< 25°C) is essential to increase the phase purity and crystallinity of perovskites [201], [202]. The spin coating can be categorized into one-step and two-step methods for the fabrication of perovskite thin films with thicknesses range 10nm to 100nm. Generally, the one-step spinning coating involves anti-solvents. Chlorobenzene and toluene are mostly widely used anti-solvents during the spin-coating of MHP in N, N-Dimethylformamide (DMF), and a mixed solvent of dimethylsulfoxide (DMSO), and γ-butyrolactone (GBL) [203]. The precise control of anti-solvent to time is the main weakness of the one-step method spinning method for the production of large-size thin films. On the other hand, the two-step spinning method was found efficient because of better morphology and interface control. However, the incomplete conversion of Pb-based salts into perovskite is a serious issue related to the two-step spinning method, limiting its large-scale production with good repeatability. For both methods, the waste of perovskite-based precursor materials determines that spinning coating is a lab-scale method to fabricate wearable and flexible perovskite-based smart optoelectronics devices in small areas. Another reason to use spinning coating at the lab scale is that with the large size area pinholes and nonuniform thickness are more probable to appear on surface morphology, which leads to the loss of final device performance [186], [204].

Thermal evaporation

Thermal evaporation (**Figure 2:23**b) is another lab-scale method to form smooth and uniform perovskite thin films. This method converts perovskite precursor materials into the vapor phase

by heating the process inside the vacuum chamber. The vapour particles produced move towards the substrates where it settled, and therefore, a uniform perovskite thin film is deposited. This method can be used to make flexible perovskite optoelectronic devices as it does not work at high temperatures during the deposition process. However, the production cost for the set-up of the vacuum process makes this method complex for the large-scale production of flexible perovskite-based devices [204], [205].

There are two main types of this method: single-source and dual-source evaporation. Single-source evaporation uses one precursor material (organic or inorganic) from one source, and the rest of the precursors would be used via other production techniques such as spin-coating or blade coating. For dual-source evaporation, both inorganic and organic precursor materials are evaporated at the same time [206]. Era et al. first reported the dual-source evaporation of lead iodide (PbI_2) and organic ammonium iodide for the synthesis of layered perovskite thin films [207]. Recently, for the first time, all vacuum-processed PSCs using an inverted architecture with PCE of 19.4% for small areas ($0.054cm^2$) and 18.1% for a large areas ($1cm^2$) were reported [208]. Similarly, all vacuum-processed perovskite thin films were also fabricated for yellow perovskite LEDs. By co-evaporation of CsI and $PbBr_2$, highly smooth and uniform perovskite thin films with a small grain size of ~31.8nm were achieved and demonstrated the EQE of ~3.7% and luminance of ~16,200cd/m^2 [209]. Using the vacuum deposition technique, dual-phase $CsPbBr_3$- $CsPb_2Br_5$ perovskite thin films were synthesized for high-performance rigid and flexible PDs. The device has a responsivity and detectivity of $0.375AW^{-1}$ and 10^{11} jones respectively [210]. Therefore, the use of the thermal evaporation technique highlights the great potential to produce the highly uniform perovskite thin film in the production of optoelectronic devices.

Roll-to-roll manufacturing

Ink-jet printing

Printing methods are mostly recommended for patterned device fabrication, including contact and non-contact printing technique. The mainly used non-contact printing method is ink-jet printing (**Figure 2:23**e). This method uses the array of fine nozzles in a controlled manner to release fine droplets of the precursor solution to generate high-resolution patterns and arrays on different substrates. Several factors such as printing speed, droplet volume, trajectory, the temperature of the substrate, and environmental conditions influence the final film characteristics. Ink-jet printing has major advantages including low-precursor waste, mask less, and the ability to fabricate large-size modules with direct writing technology. The major disadvantage of the ink-jet printing method is that perovskite films are discontinuous with increasing defects due to rapid ink crystallization during the printing process. Also, the unavoidable waste of ink-jet materials during the deposition process is another problem for the handling of lead-based precursor materials. Many researchers have used this method to fabricate rigid and flexible perovskite optoelectronic devices. Recently, flexible perovskite ($CH_3NH_3PbI_3$) solar cells were produced based on all ink-jet printing including bottom electrode (PEN/Ag), top electrode (Ag nanowires), hole transport layer (PEDOT: PSS), etc. The results of module areas 120 cm^2, 150 cm^2, and 180 cm^2 with PCE of 16.78%, 12.56%, and 10.68%, were reported [177].

In another fully ink-jet printing method, flexible and efficient PDs were achieved under ambient conditions. The fully printed perovskite (cesium-doped cation) PDs showed excellent mechanical and electrical stability for 700hr without any encapsulation. PDs exhibit a high detectivity value of $7.7* 10^{12}$ jones, I_{light}/I_{dark} ratio of $1.83*10^4$, and a photoresponsivity value

of 1.62AW^{-1} [211]. It can thus be suggested that ink-jet printing can freely print any design pattern with high speed and strong adaptability on various substrates.

Slot-die coating

To scale up perovskite optoelectronic devices, the fabrication of a perovskite active layer through a scalable printing method is considered the next move toward industrial bulk production and high output.

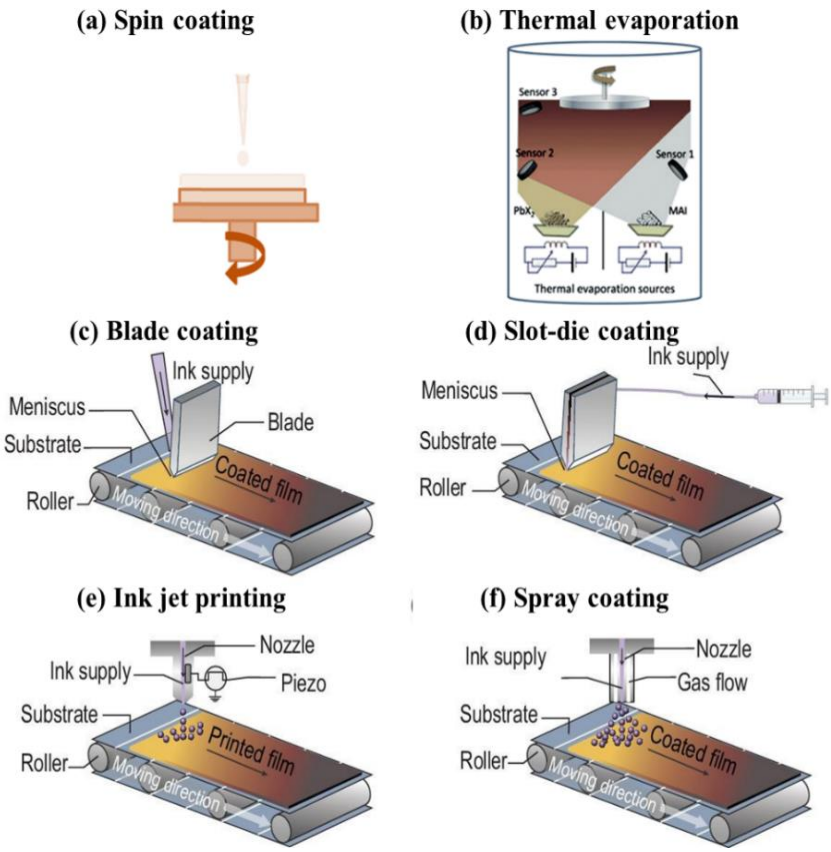

Figure 2:23: Deposition technique for halide perovskite thin films at laboratory scale and large scale. (a) Spin coating (b) Thermal evaporation (c) Blade coating (d) Slot-die coating (e) Inkjet printing (f) Spray coating. Reproduced from ref. [215], copy right 2021, Oxford university press.

Figure 2:24d) includes a moving substrate, slot-die head, and a pumping system for the deposition of perovskite thin films. By carefully adjusting the flow rate, substrate speed, and width of the printing head, highly crystalline perovskite films can be formed. [212]–[214].

Recently, a homemade slot-die coating setup has been reported to prepare fully covered ZnO ETLs which exhibited good reproducibility and ambient stability for PSCs. With the controlled deposition parameters, a champion device (FTO/ZnO/$Cs_{0.17}FA_{0.83}Pb$ $(I_{0.83}Br_{0.17})_3$/spiro-OMeTAD/carbon) showed PCE of 10.8% [216]. Another group of researchers formed slot-die printed tin oxide thin films for hysteresis-free flexible PSCs. The small-size flexible FPSCs exhibited a high efficiency of 17.18% and the large-size flexible module obtained a PCE of over 15% [216].

Spray coating

Spray coating (**Figure 2:23**f) is a technique to get high-quality thin films over large area substrates [217]. In this method, the spray coater tip divides the solution into a fine mist which is then directed toward the substrate assisted by an inert gas jet. During the film formation, the spray head passes over the substrate at a fixed height to get the required film thickness. Film morphology closely relies on head speed, droplet volume, solution concentration, substrate temperature, etc. [218]. This method requires a high temperature (100°C to 120°C) to evaporate the precursor solution which hinders its use on polymer substrates. To date, many researchers developed low-temperature spray coating processes to fabricate a variety of perovskite thin films that help to make a range of flexible perovskite optoelectronic devices [205].

Blade coating

The blade coating technique (**Figure 2:23**c) has been used for the synthesis of thin films in photovoltaic and optoelectronic devices due to its simplicity, reduced cost, and high deposition

rate. The first attempt to replace spin-coating for the fabrication of perovskite thin films was the blade coating technique. During blade coating, a sharp blade is placed in front of the perovskite solution at a suitable position above the target substrate. The linear movement of the blade across the substrate leaves the wet perovskite film [214]. The morphology of the final film is highly dependent on the substrate temperature, so the evaporation rate is mandatory to control to get good quality film [217].

The $CH_3NH_3PbI_3$ perovskite thin films with large-size grains and domains at ambient conditions were fabricated for solar cells via the blade coating method [219]. The film's fabrication process could be optimized by controlling blade speed, the distance between blade and substrate, solution concentration, and in situ thermal treatment temperature.

2.10.5 Textile-based perovskite optoelectronic applications

Wearable Solar cells

Textile-based flexible perovskite solar cells have long been a question of great interest because of their unique properties such as high flexibility, wearability, and ability to conform in any shape. Compared with conventional rigid solar cells, wearable perovskite solar cells can be easily deployed on curved or irregular surfaces of vehicles or tents. The wearability of PSC mainly depends on the flexibility of substrates which not only define the final efficiency but also the mechanical and environmental stability. Furthermore, charge transport layers (HTL/ETL) must have better stability against chemicals, oxygen, and water vapours to avoid corrosion and degradation [186], [220], [221].

The low-temperature synthesis of charge transport layers and high-quality perovskite films are necessary to get high-efficiency wearable perovskite solar cells. As mesoporous structure (i.e. TiO_2 as ETL) always demands high-temperature arrangements (≈500°C) which are not suitable

for flexible substrates, there are only a few scientific reports about the application of this architecture in this field [222]–[224]. Therefore the advancement in textile-based flexible perovskite solar cells is mostly reported in regular (n-i-p) or inverted (p-i-n) structures [225]–[227].

The first flexible perovskite solar cell was structured using ZnO nanorods as a mesoscopic scaffold layer and an ETL which allow the fabrication of low-temperature solution-based perovskite $CH_3NH_3PbI_3$ solar cells. The PCE of 8.90% and 2.62% were recorded for rigid fluorine tin oxide (FTO) and flexible PET/ITO substrates respectively [168]. Sisi et al. reported another effective strategy for the fabrication of textile-based PSC by synthesizing obelisk-like ZnO arrays on stainless-steel fabric by a mild solution process. The perovskite $CH_3NH_3PbI_3$ thin layer was formed by the dip-coating process and the resulting solar cells showed PCE of 3.3% with only 7% variation after bending for 200 cycles [228].

A novel stainless-steel fibre-shaped PSC with high flexibility and low cost was developed by continuously winding carbon nanotubes on a fibre substrate. Photoactive perovskite $CH_3NH_3PbI_3$ was sandwiched in between them via the solution process technique and fibre-shaped PSC showed PCE of 3.3%. The fibre-shaped PSC can be woven into smart textiles for large-scale applications [229].

A recent study to develop novel fibre-based solar cell textile (**Figure 2:24**a) that works at -40°C to 160°C was reported by Limin and his co-workers. Briefly, a family of inorganic perovskite solar cell fibres and textiles were made by multiple-sintering techniques to fully cover the curved surface of fibre substrate with uniform large-size perovskite crystals. Firstly, $CsPbBr_3$ quantum dots (QDs) were fabricated by a room-temperature ligand-assisted method.

Aligned TiO_2 nanotubes were successfully grown on Ti-wire and dipped into inorganic perovskite QDs to form a uniform layer on the fibre substrate.

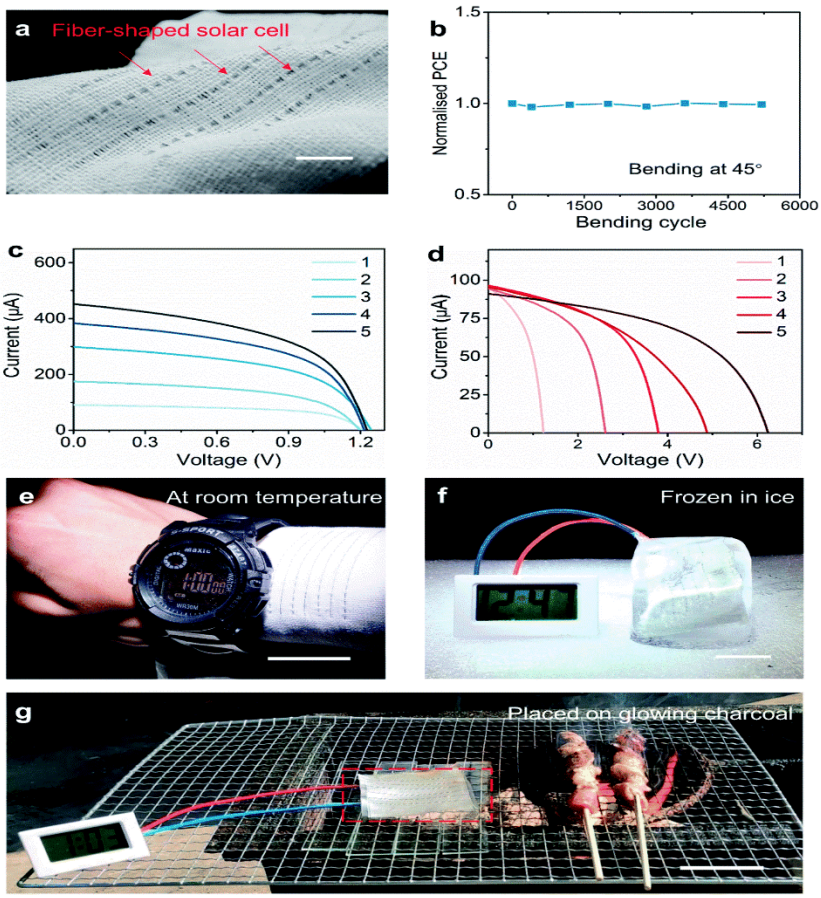

Figure 2:24: Application and performance of perovskite solar cell textile. (a) Photograph of perovskite solar cell (scale bar = 1cm). (b) Power conversion efficiency with a bending angle of 45° of solar cell textile (c-d) I-V curves of fibre-shaped perovskite solar cells connected in parallel and in series, respectively (e) Textile perovskite solar cell powering an electronic watch at room temperature (scale bar = 2cm) (f) A textile perovskite solar cell frozen in ice powering an electronic clock (g) Testing of textile perovskite solar cells placed at charcoal powering an

electronic clock (scale bar = 4cm). Reproduced from ref. [164], copyright 2020, Royal society of chemistry.

This modified fibre-shaped PSC was woven into textiles for further applications. The solar cell textile maintained about 90% of its original PCE after bending at 45° for 500 cycles as shown in **Figure 2:24**b**.** The fibre-shaped devices connected in parallel showed short-circuit current (I_{sc}) increased linearly with device number whereas open-circuit voltage (V_{oc}) remained unchanged (**Figure 2:24**c). For the five devices connected in series, and I_{sc} value of 0.09 mA and V_{oc} value of 6.22 has been achieved (**Figure 2:24**d). After that, a solar cell textile was used to power an electronic watch worn by human skin **Figure 2:24**e). In addition, it could also work under harsh working conditions such as being frozen in ice and when it was placed on glowing charcoal (**Figure 2:24**f-g) [164]. The most recent research studies available on textile-based perovskite photovoltaic applications are summarized in **Table 2.5**.

Jung et al. performed a series of experiments on fully solution-processed perovskite ($CH_3NH_3PbI_3$) solar cells fabricated on PU-coated polyester fabric. A thin layer of PU was coated as a planarization layer that effectively improved the wettability, processability, and surface morphology of the textile surface. The textile-based flexible PSC was successfully fabricated and PCE of 5.72% was achieved by using solution-processed anode, HTL, and ETL materials [230]. In another textile-based PSC report, low-temperature tin oxide (SnO_2) ETL, perovskite ($CH_3NH_3PbI_3$), and a novel encapsulation layer were realized. An ITO/PEN flexible substrate was chosen to fabricate the most efficient, and textile-based PSC with improved wash capability and ambient stability. The PCE of 15% of this unique textile-based PSC was recorded with potential future in wearable device applications [231].

To realize a wearable power source, highly flexible, lightweight, and efficient PSC based on PEN/ITO substrates with PCE of 12.2 % were reported. In addition, bending stability was recorded for solar devices with three effective bending radii of 400mm, 10mm, and 4mm for the human neck, wrist, and finger, respectively. In the case of a human finger, the PCE significantly drops to 50% of the initial value after 1000 cycles. It was noted that the origin of degradation was due to the fracture in the ITO layer on the PEN substrate [232].

Table 2.5: Summary of the textile-based perovskite solar cells performance [a]

Textile substrate	Perovskite photoactive layer	Fabrication method	VOC [V]	Jsc [mA/cm2]	FF [%]	PCE [%]	Ref.
Polyester fabric	$CH_3NH_3PbI_3$	Bar-coating	0.88	12.44	49	5.72	[230]
Stainless-steel fabric	$CH_3NH_3PbI_3$	Dip-coating	0.55	3.72	-	3.80	[228]
Stainless-steel fibre	$CH_3NH_3PbI_3$	Dip-coating	0.66	10.20	48	3.30	[229]
PAN/PU fabric	$CH_3NH_3PbI_3$	Spin coating	0.80	8.86	57	4.06	[233]
TiO2 modified Ti-fibre	$CsPbBr_3$	Dip-coating	1.19	6.48	70	5.37	[164]
Acrylic elastomer	$CH_3NH_3PbI_3$	Spin coating	1.06	17.05	65	14.80	[231]
Carbon fabric	$CsMAFAPbI_{3-x}Br_x$	Spin coating	1.12	20.42	67	15.29	[234]
PEN	$CH_3NH_3PbI_{3-x}Cl_x$	Spin coating	0.96	19.06	59	12.20	[232]
Carbon fibre	$CH_3NH_3PbI_{3-x}Cl_x$	Dip-coating	0.61	8.75	56	3.03	[235]
Polyester fabric	$(FAPbI_3)_{0.85}(MAPbBr_3)_{0.15}$	Spin coating	1.09	22.41	72	17.68	[235]

a Abbreviations: Ti= Titanium; PAN/PU =Poly(acrylonitrile)/ Polyurethane ; TiO_2 = Titanium dioxide

Photodetectors for wearable optoelectronics

Textile-based photodetectors (PDs) are a major area of interest within the field of video imaging, bioinspired sensing, optical communication, and biomedical imaging. In recent years, wearable PDs fabricated on a variety of flexible substrates because of their possible applications in touch screens, wearable electronic devices, and pressure-induced sensing [236]. Several key factors define the final efficiency of wearable PDs such as the morphology of substrates, and retention of initial performance values after repeated bending, stretching or folding capability. Therefore, the main components of wearable PDs such as substrates, charge transport layers, and electrodes should be stable enough to resist environmental and mechanical hazards. In addition, MHP can be easily synthesized by low-temperature solution process techniques, which is helpful to make wearable PDs [237]–[239].

Dong et al. reported highly flexible fibrous yarn bundles and their knitted structure as a template to fabricate $MAPbI_3$-based PDs (**Figure 2:*25***e). They fabricated quasi-spring-like network-based wearable PDs consisting of silver (Ag) electrode/perovskite ($MAPbI_3$)/ yarn bundles and their photoelectric properties were examined. In **Figure 2:25**a, I-V curves depicted a linear behaviour with an increase in voltage, which confirms the ohmic contact between perovskite and Ag electrodes. After illumination, the current gradually increased with an increase in the power from $10mWcm^{-2}$ to $80mWcm^{-2,}$ and the time-dependent photocurrent was also recorded under the same power conditions (**Figure 2:*25***b). During repeated ON/OFF cycles, good stability, and repeatable light-sensing behavior were observed. Also, the PDs showed fast photo-response speed (t_{rise} ~ 4ms, t_{decay} ~ 10ms) and high detectivity ($2.2* 10^{11}$ jones) at $10mW/cm^2$ (**Figure 2:*25***c-d) [240].

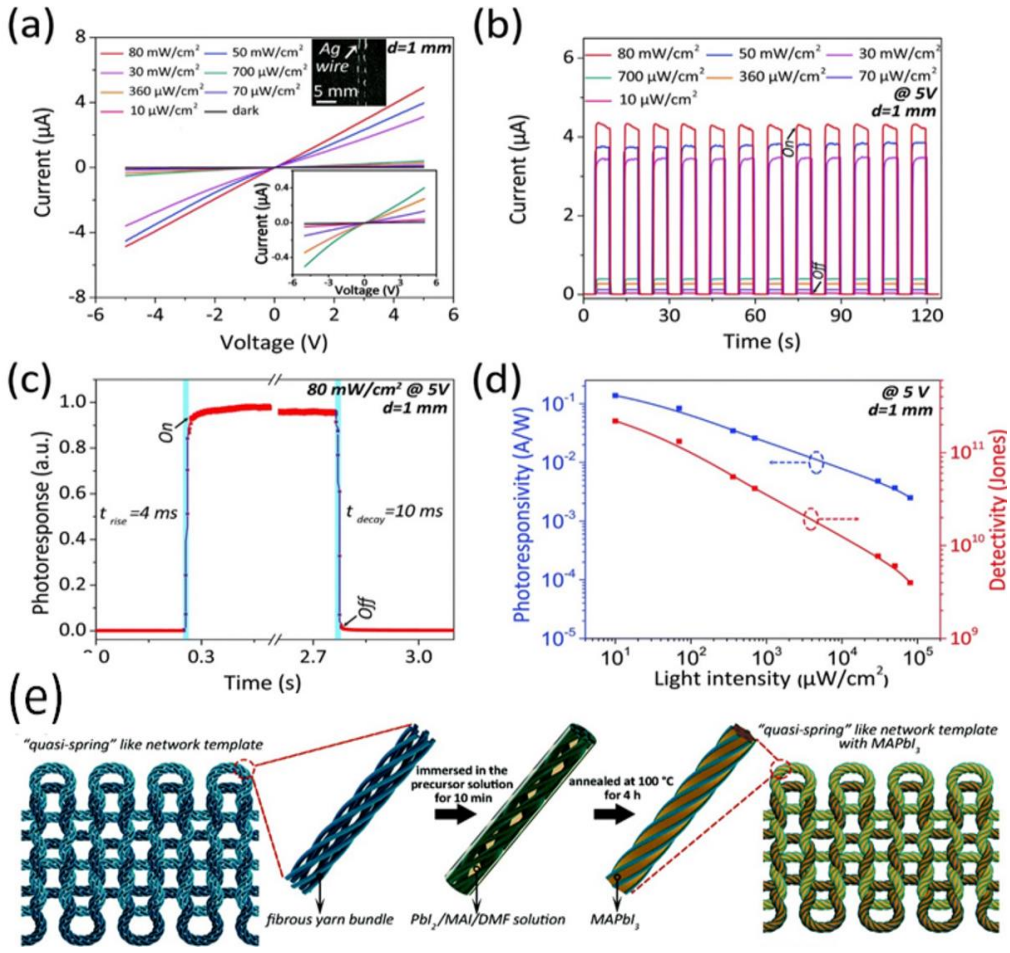

Figure 2:25: Photoelectric characteristics of perovskite photodetectors. (a) I-V curves in dark and light exposure with different power densities of the photodetectors. (b) Time-dependant (I-t) curves under light illumination with different power densities at a bias voltage of 5V. (c) Photo-response with light switch On and Off at a fixed light power density of 80mW/cm^2 and a bias voltage of 5V. (d) Photoresponsivity and detectivity are the functions of light intensity. (e) Illustration of the fabrication process of quasi-spring-like network structured photodetectors. Reproduced from ref. [240], copyright 2019, Royal society of chemistry.

Poly (vinylidene fluoride) (PVDF) based flexible and self-powered PDs were fabricated that use a mixed-cation perovskite $(FAPbI_3)_{1-x}(MAPbBr_3)_x$ as the photoactive material. These wearable PDs have some advantages of being lightweight, low cost, and the ability to reshape

in any form for the human body without any physical restriction. The synthesized PDs showed good performance with a fast response speed (t_{rise}=82ms, t_{decay}=64ms), high detectivity (7.21* 10^{10} jones at zero bias) under 254 UV illumination, and excellent mechanical stability at some bending angles [241]. In another study, PVDF was reported as a flexible substrate to integrate $CsPbBr_3$ nanosheets into ZnO nanowires and graphene. The resultant PN junction due to ZnO and $CsPbBr_3$ can facilitate the enhanced transportation of photogenerated charge carriers that leads to a high I_{light}/I_{dark} ratio of ~ 10^3. The flexible thin-film PDs can be easily attached to human skin for wearable applications [242].

Polymer/perovskite composite nanofibers were prepared by electrospinning technique to demonstrate their potential stretchable and wearable PDs. The poly(vinylpyrrolidone)/ $MAPBI_3$ nanofibrous membranes showed an ability to endure 15% strain and started to break at 20% strain. At 15% strain, the detectivity and photoresponsivity of the wearable PDs at λ= 550nm were 51.2mWA^{-1} and 2.23*10^{11} jones, respectively [243].

Fibre and fabric-based perovskite Light-emitting diodes

Alongside the development of PSCs, the perovskite LEDs (PeLEDs) have exciting potential to be the first next-generation LEDs based on their excellent electric-optical properties. Since the first demonstration of PeLEDs incorporating 3D perovskite in 2014, intense efforts have been dedicated to developing high-performance PeLEDs [244], [245]. As it has shown good performance on rigid substrates, the next important direction for PeLEDs is its integration with textile-based optoelectronics for wearable applications. Wearable LEDs can meet the requirement of lightweight and portable electronic devices. For the wearable LEDs, tremendous efforts have been reported for preparing different components of PeLEDs such as flexible electrodes and HTL/ETL.

A recent study by Shan and Wei involved a hybrid strategy to fabricate wearable and tunable perovskite quantum dots-based light-emitting/ detecting bifunctional fibres. In this method, a transparent PET fibre coated with PEDOT: PSS was used as a working electrode for the synthesis of flexible electroluminescent (EL) fibres as presented in **Figure 2:*26***a-b. In **Figure 2:*26***c-d, the current density-luminance-voltage curves of the green EL fibres (FWHM=19nm) showed a luminance of ~100cd/m^2 at 7V and current efficiency of 1.67 cd/A. Red EL fibres (**Figure 2:*26***e) were also prepared with the same composition and exhibited the chromaticity coordinates of (0.65, and 0.27). The bending test of EL perovskite fibres was also performed along a round shape of radius about 4.5mm (**Figure 2:*26***f) [246].

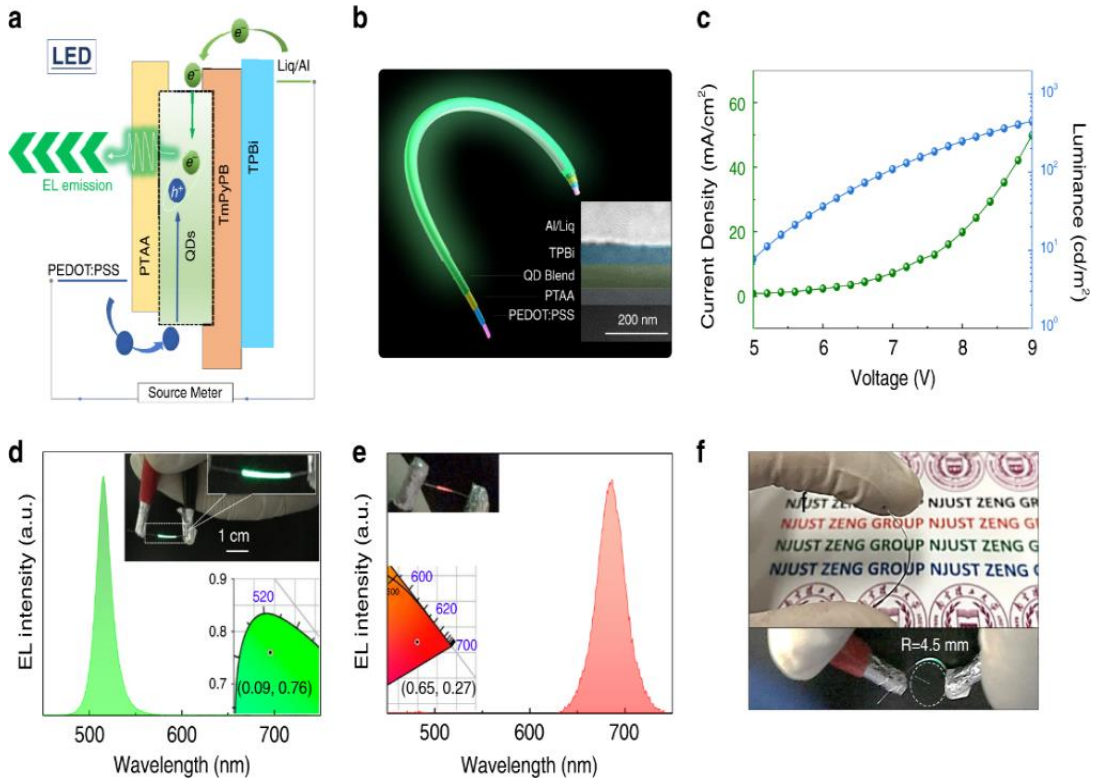

Figure 2:26: Device structure and electric behavior of light-emitting perovskite fibre. (a) Illustration of the working mechanism of light-emitting perovskite fibres. (b) Schematic of the perovskite fibre. Inset, cross-sectional SEM image of fibre. (c) Luminance and current-density

curves of perovskite fibres. (d-e) Electroluminescent spectra of green and red perovskite fibre. Insert, a photograph of the red and green perovskite fibre. (e) Photographs of the bend perovskite fibre and its electroluminescent behavior under bending position. Reproduced from ref. [246] , copyright 2020, Springer nature.

Jiang et al. demonstrated stretchable touch-responsive PeLEDs by using highly conductive and transparent polyurethane (PU) /Ag nanowires composite electrodes as shown in **Figure 2:*27***a. Also, a stretchable perovskite active layer was synthesized by mixing poly(vinylpyrrolidone), and poly(ethylene oxide) with $CsPbBr_3$. When the pressure was applied to the PU/Ag, a connection between the electrode and perovskite layer allowed electrons and holes to recombine when voltage was applied. As the pressure was released, PU/Ag electrodes disconnected from the emissive layer and returned to their original position. The device exhibited a luminance of 380.5cd/m^2 at 7.5V with good touch responsivity after 315 cycles (**Figure 2:*27***b-c). In addition, the fabricated device showed certain stretchability before 40 stretching cycles (**Figure 2:*27***d). **Figure 2:*27***e-g presented the flexibility of touch-responsive PeLEDs to emit instantaneous light when bent around different mechanical objects [247].

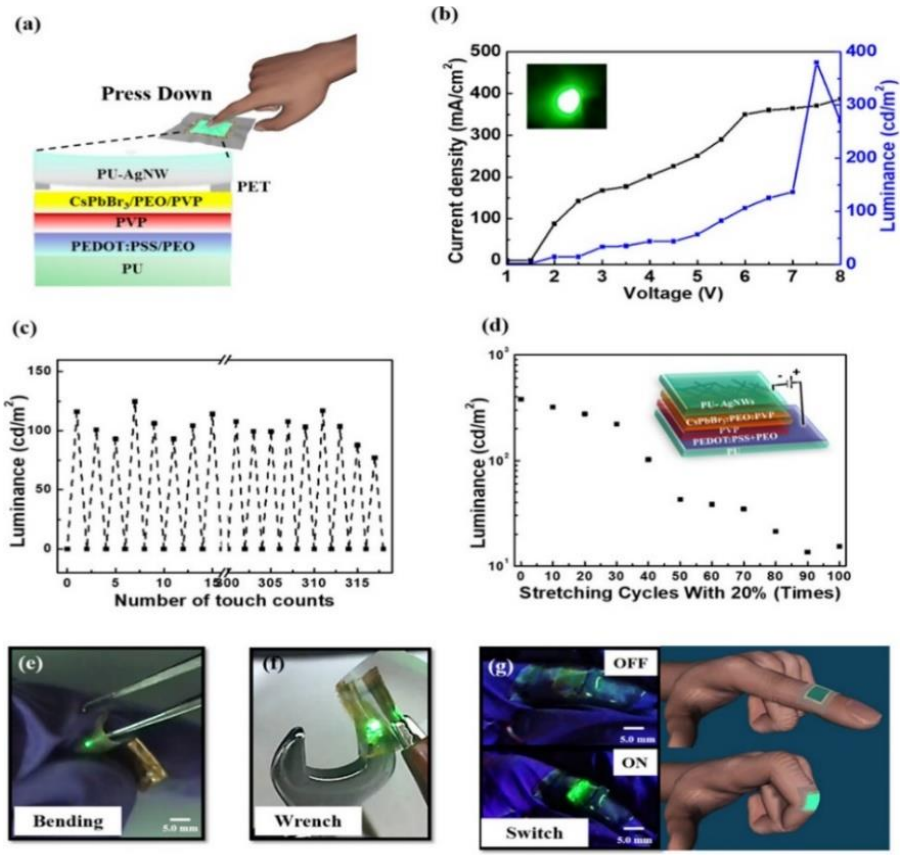

Figure 2:27: Photograph of stretchable perovskite light-emitting diodes. (a) Current density-voltage and luminance-voltage characteristics of perovskite light-emitting diodes with stretchable electrodes. (b) A durability test before and after pressure was applied on flexible electrodes under a voltage of 3V. (d) Change in luminance characteristics after repetitive stretching cycles at strains of 20%. (e-f) Bending behavior of stretchable perovskite light-emitting diodes, touched by wrench and finger at the voltage of 7V. Reproduced from ref [247], copyright 2020, American chemical society.

A significant discussion and the influence of solvent traps in ITO/PEN substrates on the efficiency of flexible PeLEDs was presented by Kim et al. In device fabrication, cleaning, and ultraviolet-ozone treatment are considered important for uniform perovskite deposition. However, the trapped solvents can easily generate radicals and adsorb on the ITO surface. This leads to the effect of the sheet resistance and fermi level. The complete removal of solvents

helps to enhance the luminance from 87.2 cd/m^2 to 329.6cd/m^2 at 4V [248]. Some researchers also highlight the importance of mono-layered graphene for flexible photonic applications. This unique material can be used as an anode of flexible LEDs due to high light transparency and theoretical resistance (>6.4k Ω /sq) [249].

To solve the intrinsic instability and crystal friability of MHP, a facile approach through liquid-to-liquid encapsulation ink-jet printing was presented. Perovskite inks were directly ink-jet printed into the liquid PDMS to in situ synthesize the single-crystal embedded PDMS structures. The space-confined effect of liquid PDMS is the key to producing single-crystal arrays in PDMS, which can effectively control the crystallization process and help to form the single-crystalline perovskite structures. This technique can lead to the scalable formation of air-stable single-crystalline perovskite structures for wearable light-emitting devices [250].

2.10.6 Challenges and future perspectives

Research on halide perovskite materials has promoted the opportunity to produce cheap, highly flexible, and a solution to self-power devices for next-generation wearable optoelectronics. However, the efficiency of textiles-based perovskite devices is not very encouraging, there are many challenges to overcome before commercial applications. For instance, the preparation of charge transport layers at low temperatures is still under development. In addition, there are limits to fabricating perovskite thin films and other functional layers with roll-to-roll manufacturing at a large scale. The challenges are the short processing time for MHP which require a wide processing window and degradation by humidity and temperature variation. These things can be controlled by making a composite of perovskite with humidity and temperature-tolerant materials and by developing a temperature-invariant process.

More broadly, research is also needed to make textile-based perovskite devices more stable including environmental and mechanical stability. Environmental instability is mostly due to oxygen, humidity, and temperature. Some techniques have been developed such as device encapsulation, optimization of perovskite photoactive layer, and charge transport layers. Some researchers reported new materials that are resistant to light oxidation and moisture for MHP like SiO_2, surface hydrophobic modifiers, choline chloride, and L-α-phosphatidylcholine and sputtered inorganic barrier layers [251], [252]. The simple device architecture is also used to enhance the device's environmental stability. The mechanical stability of wearable optoelectronics can be improved by optimizing the perovskite layer itself, selecting flexible electrodes, and self-healing materials.

The hazard potential of wearable perovskite devices is essential to consider for practical use. A large number of toxic precursor materials are used for the preparation of perovskite devices; hence, non-toxic materials are highly needed. In the large-scale fabrication of perovskite devices, a more green and non-toxic solvent should be considered. Moreover, the leakage of lead (Pb) from lead-based perovskite tends to produce toxic elements that can cause serious damage to human and aquatic life. A high level of lead can be serious and life-threatening for lead-based wearable perovskite devices. Some efforts to reduce or eliminate the use of lead for wearable optoelectronics have been reported [253][254].

In general, therefore, it seems that multidisciplinary collaboration is required to improve the performance, ambient stability, and biosafety to produce fibre and textile-based perovskite devices at a large-scale. In the future, further experimental investigations will enable wearable perovskite devices to come into daily life. Driven by the advancement of perovskites in textile-based solar cells, photodetectors, and light-emitting diodes, further research could also be

conducted to explore the effectiveness of perovskites for other wearable devices such as X-ray detectors, etc.

Chapter 3 Tuning the Optical Properties of Perovskite Nanocrystals

3.1 Overview

This work was published as "Tuning the Optical Properties of $MAPbBr_3$ Perovskite Nanocrystals via Alkali Metal Ions Doping" in Advanced Materials proceedings (2022). This work describes the use of Cs and Rb cations into $MAPbBr_3$ PeNCs to optimize their morphology, crystal structure, and optical properties**.**

Abstract

Halide perovskite nanocrystals (PeNCs) have emerged as a class of excellent semiconductors in the past few years for their high-performance optoelectronic applications. These materials have received considerable attention due to efficient charge carrier mobility, high photoluminescence quantum yields (PLQYs), and near theoretical efficiencies for green emitters. However, methylammonium (MA) cation-based perovskites exhibit their inherent instability such as high sensitivity to light, heat, oxygen, and moisture which influence their performance in practical applications. Their low production cost and ease of synthesis make them suitable candidates for upcoming technologies. In this research, we study the mixed cation of Cs and Rb into $MAPbBr_3$ PeNCs to optimize their morphology, crystal structure, and optical properties. It is found that addition of rubidium cations can greatly enhance the photoluminescence intensity of the $MAPBBr_3$ PeNCs, whereas cesium cations can improve structural stability owing to the increased valance bond intensity. This work provides useful thoughts for the synthesis of high-performance optoelectronic devices based on mixed-cation PeNCs.

Keywords

Perovskite nanocrystals; Alkali metal ions; optical bandgap, structural stability.

Graphical abstract

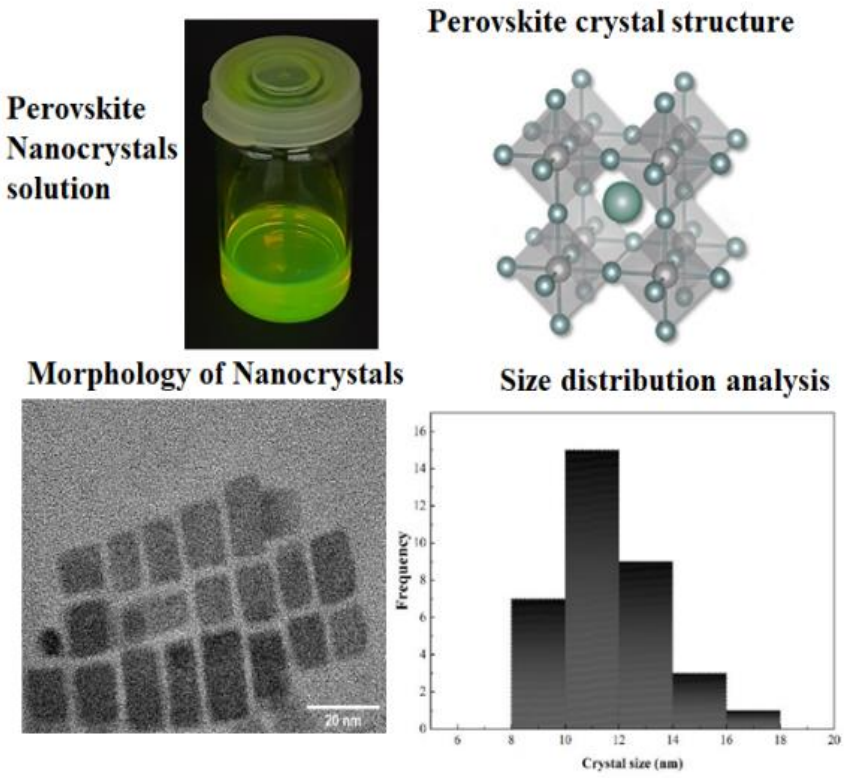

3.2 Introduction

In recent years, researchers have shown an increased interest in metal halide perovskite nanocrystals (NCs) for optoelectronic applications in various fields, including light-emitting and light-harvesting devices, photodetectors and lasers. The superior performance of perovskite nanocrystals (PeNCs) is mainly attributed to high photoluminescence quantum yields (PLQYs), and their tunable bandgaps through the precise mixing of halogens and particle size [1-3]. The

first PeNCs were synthesized by Schmidt in 2014, and since then, there has been a growing body of literature that recognises the importance of these materials [257].

The general structural formula of perovskites is ABX_3, where A is a methylammonium ($CH_3NH_3^+$; MA^+), formamidinium ($CH(NH_2)_2^+$; FA^+) or cesium (Cs^+) cation; B is a divalent cation (mostly Pb^{2+} (lead)); and X is a halide anion (Cl^-, Br^-, or I^-) [258]. Metal halide perovskites (MHPs), particularly the methylammonium lead halide ($CH_3NH_3PbX_3$; X = Cl^-, Br^-, I^-), which show superior optoelectronic properties from excellent efficiency of detection of photons to photovoltaic applications [259], [260]. However, the potential concern of MA-cation-based perovskites is their inherent instability such as high sensitivity to light, heat, oxygen, and moisture which reduces their future applications [82]. Thus far, several reports have shown that the stability of $MAPbBr_3$ NCs could be enhanced by replacing MA cations with other smaller-size cations or compositional engineering [261]. For example, Bing Xu et al. reported for the first time the fabrication of PeNCs by mixing the organic cation (MA) with inorganic cation (Cs) to use as an emission layer for perovskite light-emitting diodes (LEDs). The high-performance LEDs based on these PeNCs showed a maximum luminance of 24500 cd/m^2, a current efficiency of 4.1 cd/A, and external quantum efficiency of 1.3% [83]. Another study was reported about the incorporation of rubidium (Rb^+) ions into $MAPbBr_3$–based LEDs. The addition of Rb ions partially replaced the MA cations and showed excellent electroluminescent behaviour with a current efficiency of 9.45 cd/A and a luminance of 7694 cd/m^2. A 19-fold increase in current efficiency and a 10-fold increase in luminance were demonstrated in Rb cations doped LEDs compared to pristine $MAPbBr_3$-based perovskite devices [152]. In this work, we study the incorporation of Cs and Rb cations into $MAPbBr_3$ PeNCs to optimize their morphology, crystal structure, and optical properties. The RbBr and

CsBr are used as a substitute to partially replace the MA cations. Band-gap engineering of mixed-cation PeNCs has been demonstrated during the fabrication process, by replacing the MA cations with alkali metal ions (Cs and Rb), with different concentrations.

3.3 Experimental

3.3.1 Materials

Lead bromide ($PbBr_2$) (99.9%), cesium bromide (CsBr) (99.9%), rubidium bromide (RbBr) (99.6%), oleic acid (90%), oleylamine (70%), dimethylformamide (DMF) (99.8%), hexane (95%), and toluene (99.8%) were purchased from Sigma-Aldrich. Methylammonium bromide (MABr) (98%) was purchased from Ossila Ltd.

3.3.2 Material synthesis

The $MAPbBr_3$ PeNCs were fabricated by ligand-assisted re-precipitation (LARP) technique. Briefly, 0.122mmol of $PbBr_2$ and 0.098mmol of MABr were dissolved in 5ml of DMF. In a separate glass vial, 500µl oleic acid and 50µl oleylamine were mixed and injected into the precursor solution. After that, 500µl precursor solution was dropped into vigorously stirred 10ml toluene at room temperature to initiate the crystallization of nanocrystals, which was observed by strong greenish-yellow PL emission. For the $MA_{0.7}Cs_{0.3}PbBr_3$ synthesis, 0.098 mmol of MABr was replaced by 0.068 mmol of MABr and 0.029 mmol of CsBr. The crude solution was centrifuged at 4000rpm for 10 min to remove bulk and unreacted materials, and the resultant precipitate was re-dispersed in 1ml of hexane. After another centrifugation at 4000rpm for 5 min to remove precipitates, a bright green solution was obtained for further characterization.

For the rubidium-based composition ($MA_{0.6}Rb_{0.4}PbBr_3$), 0.098 mmol of MABr was replaced by 0.059 mmol of MABr and 0.039 mmol of RbBr.

3.3.3 Characterizations

Transmission electron microscopy images were captured on a JEOL-JEM TEM machine operating at an accelerating voltage of 200 kV. X-ray diffraction data were collected by using PANalytical XpertPro diffractometer with Cu Kα radiation over the 2θ range from 10° to 60°. The ultraviolet-visible (UV-Vis) spectrum was measured with the LAMBDA 35 PerkinElmer spectrometer. Photoluminescence (PL) spectra were recorded at room temperature by using a fluorescence spectrometer (FLS920, Edinburgh Instruments).

3.4 Results and discussion

To study the effect of Rb and Cs cations on the structure and optical properties of $MAPbBr_3$, the LARP method was used to form highly crystalline and monodisperse PeNCs. This method is a simple and versatile technique to fabricate NCs at room temperature via a solvent-mixing approach by introducing ligands on the surface.

We found that the optimal substituent content of Cs and Rb cations to achieve excellent PL for $MA_{1-x}Cs_xPbBr_3$ and $MA_{1-x}Rb_xPbBr_3$ is x=0.3 and x=0.4 relative to MA cations respectively [83], [152]. The as-synthesized $MAPbBr_3$ PeNCs are predominantly single crystalline with sizes varying from 9nm to 15nm as shown in **Figure 3:1**a. All the PeNCs have a cubic shape with no substantial change in shape after doping Cs or Rb ions into the pristine samples as

displayed in **Figure 3:1**b, c. The TEM histograms as presented in **Figure 3:1**d-f reveal a small degree of size reduction for the alkali metal ions (Cs and Rb) doped PeNCs.

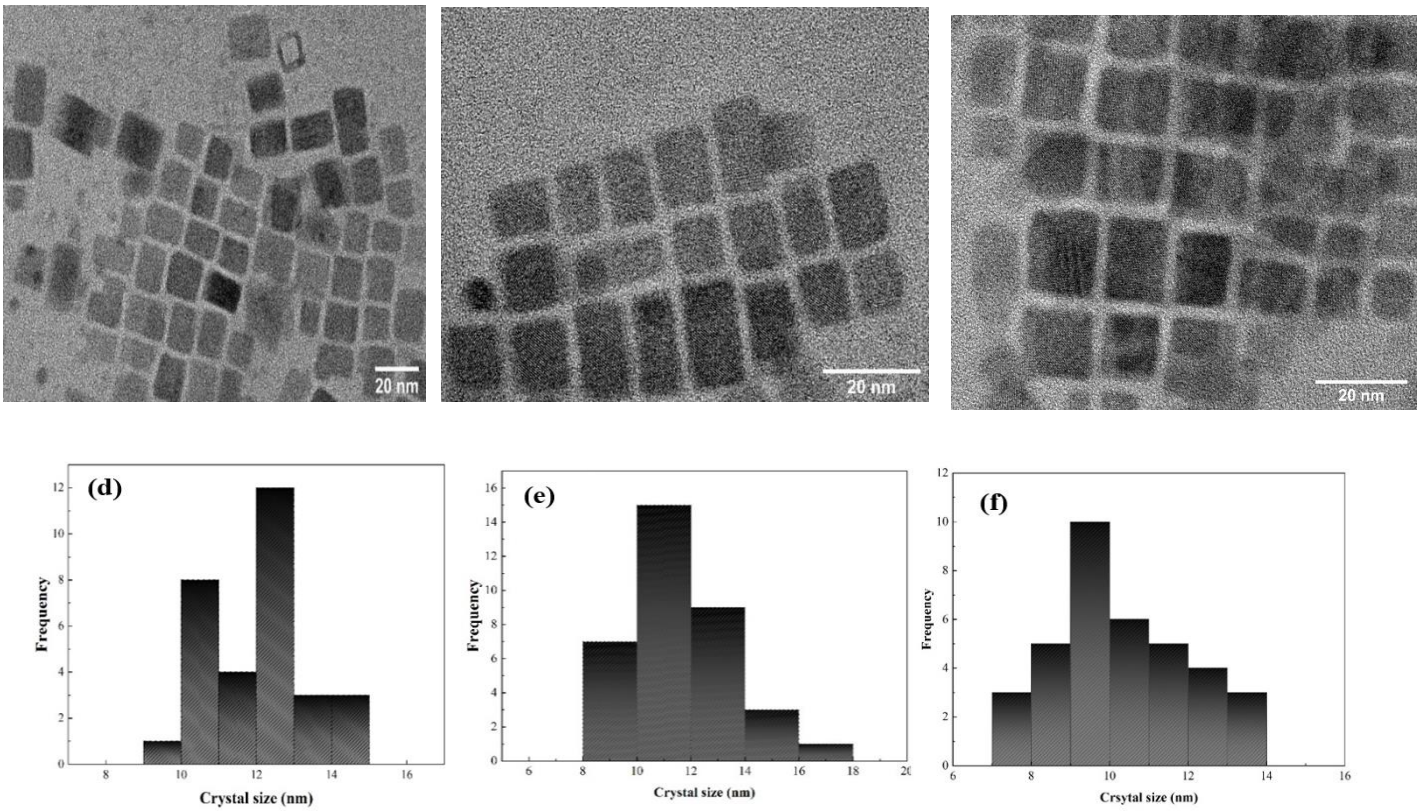

Figure 3:1: (a) TEM image of the $MAPbBr_3$ PeNCs (b-c) Morphology of $MAPbBr_3$ PeNCs with mixed-cations Cs/Rb (d) Histogram of as-prepared $MAPbBr_3$ PeNCs (e) Histogram of $MA_{1-x}Cs_xPbBr_3$ when x=0.3 for Cs cations (f) Histogram of $MA_{1-x}Rb_xPbBr_3$ PeNCs when x=o.4 for Rb ions.

To study the changes in the optical band gap of alkali metal ions (Cs and Rb) doped PeNCs, we performed UV-Vis absorption spectroscopy measurements. As demonstrated in **Figure 3:2**a, the absorption spectra were blue shifted from 535nm to 527nm upon Cs cations addition into the $MAPbBr_3$ NCs. This absorption band was further blue shifted to 521nm after Rb cations insertion into the pristine PeNCs.

The band gap of such materials is the minimum required energy that outermost electrons get rid of the valence band. The valence bond strength depends on the lattice constant as the smaller the atomic spacing, the greater the force between neighbouring atoms. The optical band gap of these undoped and doped samples was calculated by the following Tauc's formula which is `given by $\alpha h\nu = A(h\nu - Eg)^n$ where hν is photon energy, α is the absorption constant, A is the proportionality constant, and Eg is the value of band gap. The value of n=1/2, 3/2, 2, and 3 is used for direct, direct-forbidden, indirect, and indirect-forbidden bandgaps, respectively [156]. As depicted in **Figure 3:2**b, the decrease in lattice constant due to the insertion of smaller size cations (Cs and Rb), shows the potential in the increased value of the band gap from 2.23eV to 2.40eV.

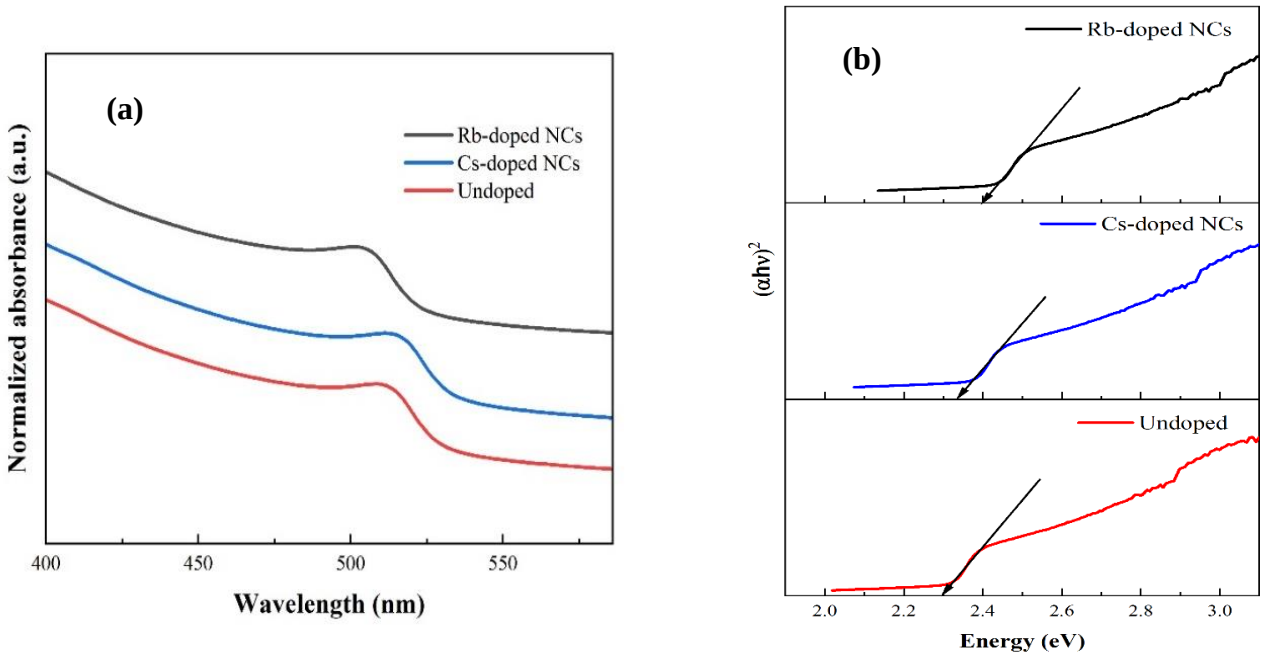

Figure 3:2: a) The absorption spectra of $MAPbBr_3$ and alkali metal ions (Cs and Rb) substituted PeNCs. (b) Optical band gap energy calculation (Tauc's plot) of the untreated and treated PeNCs.

In addition, Figure 3**:*3***a presents the dependence of PL characteristics of $MAPbBr_3$ PeNCs on substituebt content of Cs and Rb cations **.** As we can see from the PL spectra, with alkali metal ions incorporation, the intensity of each PL spectrum was increased. Furthermore, compared with $MAPbBr_3$ PeNCs, the peak position of Cs and Rb cations treated samples, PL spectra was blue shifted from 532nm to 526nm, showing that alkali metal ions can slightly change the luminance spectra. The presence of stokes shift may be because when a system absorbs photons with high energy and is directed to the excited state, followed by the rapid relaxation to the ground state. The system would come to the original condition with the loss of energy due to vibrational and relaxation dissipation which causes the redshift of the emission spectrum compared with the absorption spectrum [262].

To confirm the composition and crystallization of the NCs, the x-ray diffraction (XRD) measurements were recorded with Cs and Rb ions treated $MAPbBr_3$ perovskite NCs. The as-prepared NCs showed highly crystalline behavior, as depicted by the XRD patterns in

Figure 3:*3*b. It can be noticed that the intensity of the (100) peak decreases and the intensity of the (110) peak gradually increases because of Cs ions presence into the crystal lattice. Interestingly, we also observe that the Rb-dope PeNCs did not show any significant changes in the XRD spectra because of their small size.

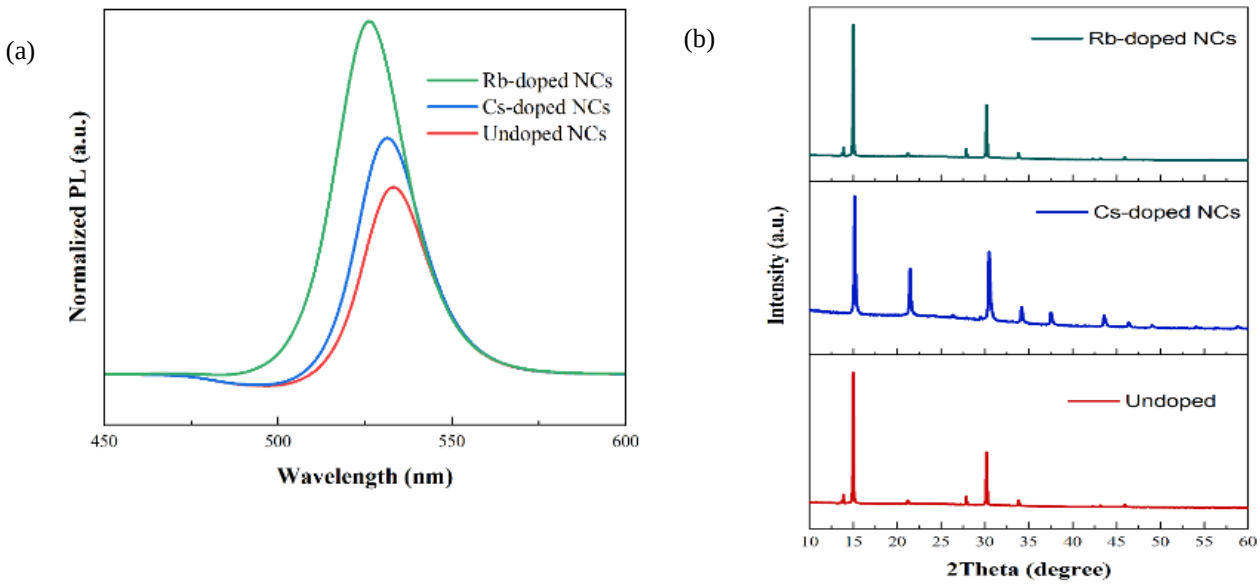

Figure 3:3: (a) PL spectra as a function of alkali metal cations content in $MAPbBr_3$ PeNCs. (b) X-ray-diffraction patterns of alkali metal cations treated $MAPbBr_3$ PeNCs.

3.5 Conclusion

In this study, we have synthesized Cs and Rb cations based $MAPbBr_3$ perovskite NCs via the LARP method. The alkali metal ions partially replace the MA cations and affects the crystal lattice of $MAPbBr_3$, hence tuning the optical properties of $MAPbBr_3$ PeNCs in turn. The results of this study have shown that there are no significant changes in the morphology of PeNCs, whereas alkali metal cations treated PeNCs show a reduction in size due to crystal lattice contraction. We found that PL intensity increases to a higher value with Rb cations than that with Cs due to the more tolerance of the PeNCs for higher amount of smaller-size alkali metal ions. These findings describe an advancement in understanding the chemistry and structural stability of perovskite NCs essential for various optoelectronic applications. Considerably more work will need to be done to determine the long-term effects of alkali metal ions treatments for halide PeNCs.

3.6 Preliminary data

Effects of Cesium cations treatment for Iodide-based perovskites ($Cs_xMA_{1-x}PbI_2Br$) nanocrystals.

Method

Colloidal $MAPbI_2Br$ nanocrystals were fabricated (**Table 3.1)** by modifying previously reported ligand-assisted re-precipitation (LARP) method [263]. Briefly, 0.1mmol of PbI_2, 0.080mmol of CH_3NH_3Br, 20µl of oleylamine, 200µl of oleic acid were dissolved in 2ml of acetonitrile. This mixed solution was stirred for 2hr to get a clear precursor solution. The precursor solution was dropped into vigorously stirred 10ml toluene at room temperature to initiate the crystallization of nanocrystals, which became cloudy. After centrifugation at 4000rpm for 15minutes, and after precipitates had been discarded, the bright red colloidal solution was obtained. To remove the residual solvent, nitrogen gas was bubbled through the solution. Solid nanocrystals can be obtained by eliminating the organic solvents.

Table 3.1: Different levels of reactants for Cesium doped MAI_2Br samples

Sample ID	Cesium content (x)	CsBr (mmol)	MABr (mmol)	PbI_2 (mmol)
C	0	0	0.080	0.1
CS1	0.1	0.008	0.072	0.1
CS2	0.2	0.016	0.064	0.1
CS3	0.3	0.024	0.056	0.1
CS4	0.4	0.032	0.048	0.1
CS5	0.5	0.040	0.039	0.1
CS6	0.6	0.048	0.032	0.1

Results

The main focus of our research work was to get efficient luminescence in the red region, where for display applications the emission peak should be at ≈630 nm.

Here, we exhibit the facile synthesis (**Figure 3:4**) and characterization of $MAPbI_3$, $MAPbI_2Br$, $Cs_xMA_{1-x}PbI_3$ nanocrystals labelled as C1, C2 and C3 respectively to optimize the sample for further doping with cesium ions.

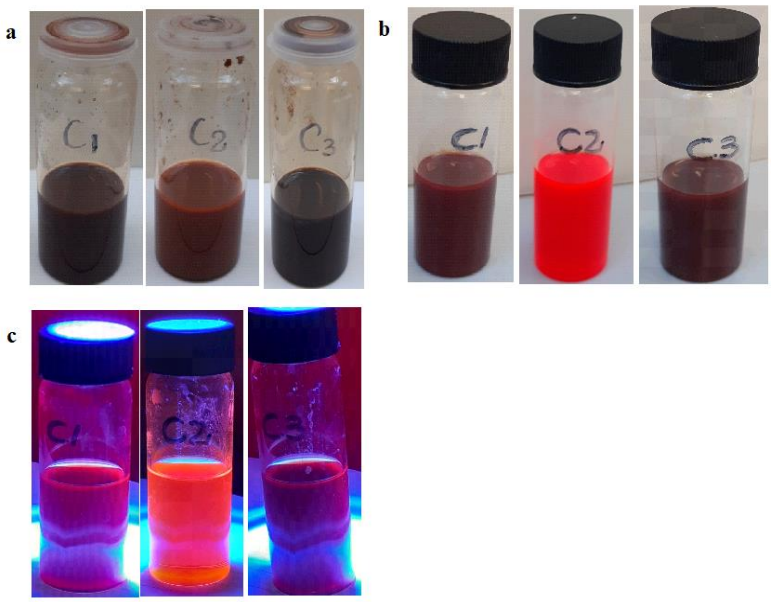

Figure 3:4: Photographs of the precipitates obtained in toluene solution. (a) Ligand assited repricipitation of $MAPbI_3$, $MAPbI_2Br$, $Cs0.3MA0.7PbI_3$ in toluene. (b) photographs of Dnanocrystals under ambient light. (c) photographs of nanocrystals under UV-irradation

In **Figure 3:5** the room temperature UV-VIS absorption spectra of $MAPbI_3$, $MAPbI_2Br$, and $CsMAPbI_3$ nanocrystals dispersed in toluene was recorded to compare the effect of cesium cation doping in $MAPbI_3$ with $MAPbI_2Br$. It is clearly seen that the absorption edge of $MAPbI_3$ nanocrystals at ≈765nm shifted to maximum ≈753nm when doped with cesium cations. First, we tried to tune the absorption edge of $MAPbI_3$ nanocrystals by doping woth cesium cations, but the largest blue shift which we get on UV-Vis absorption was only ≈10nm.

As a result, we tuned the halide composition with increasing amount of bromine. Among different mixed halides composition [55], we found that $MAPbI_2Br$ show PL of nanocrystal solution at the desired red region, at 630-640nm [264] . Therefore, we focus on this halide composition for the following experiments.

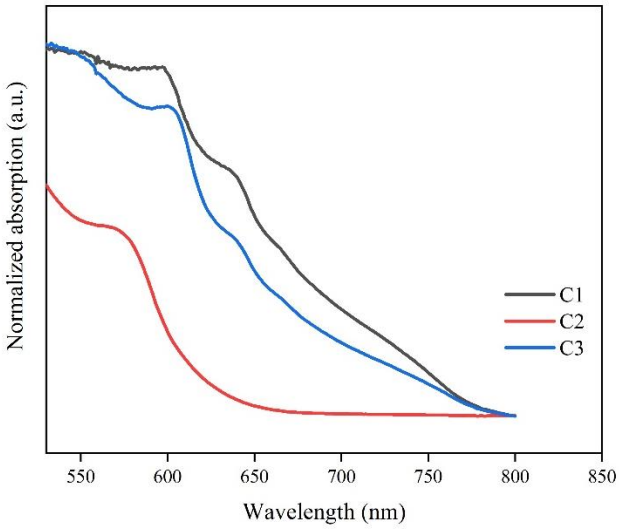

Figure 3:5: Absorption spectra of $MAPbI_3$ (C1), $MAPbI_2Br$ (C2), $Cs0.3MA0.7PbI_3$ (C3) nanocrystals.

To identify the effect of cesium doping on $Cs_xMA_{(1-x)}PbI_2Br$ nanocrystals, different precursor solution with cesium content (x=0-0.6) were prepared in acetonitrile followed by injecting these them into the toluene as shown in **Figure 3:*6***a. After swiftly injecting the perovskite nanostructures, bright red solution under ambient light and UV-irradiation was captured as shown in **Figure 3:*6***b.

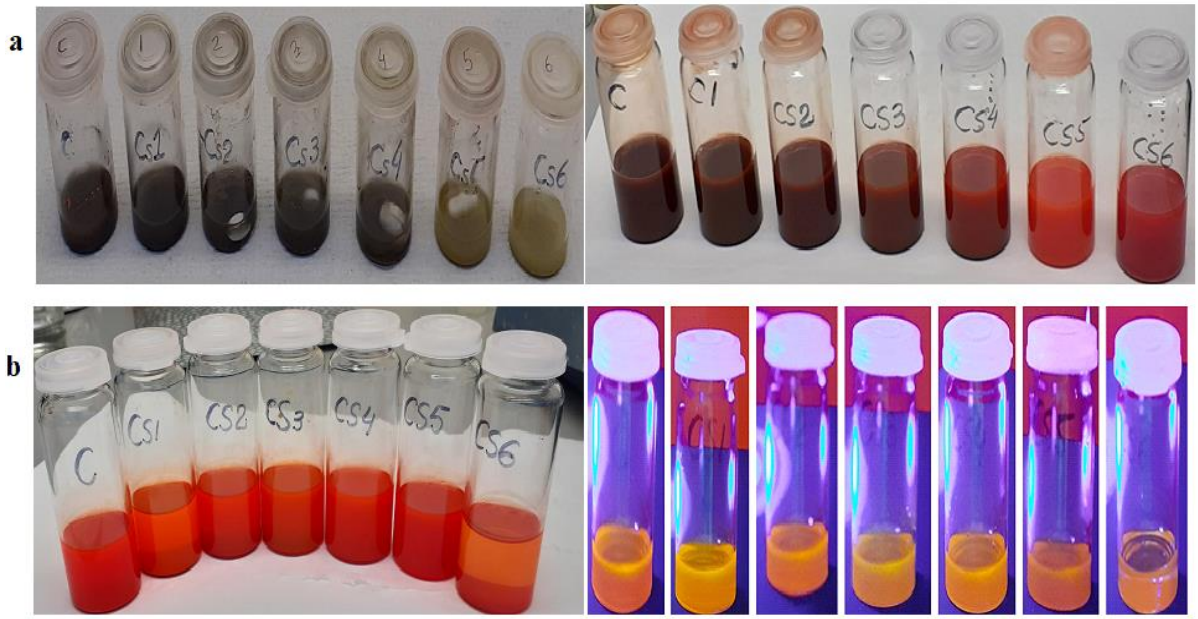

Figure 3:6: Photographs of precursor solution and precipitates in toluene solution. (a)Precursor solution in acetonitrile solvent and precipitation in toluene. (b) Photographs of cesium doped nanocrystals under ambient light and UV-irradiation.

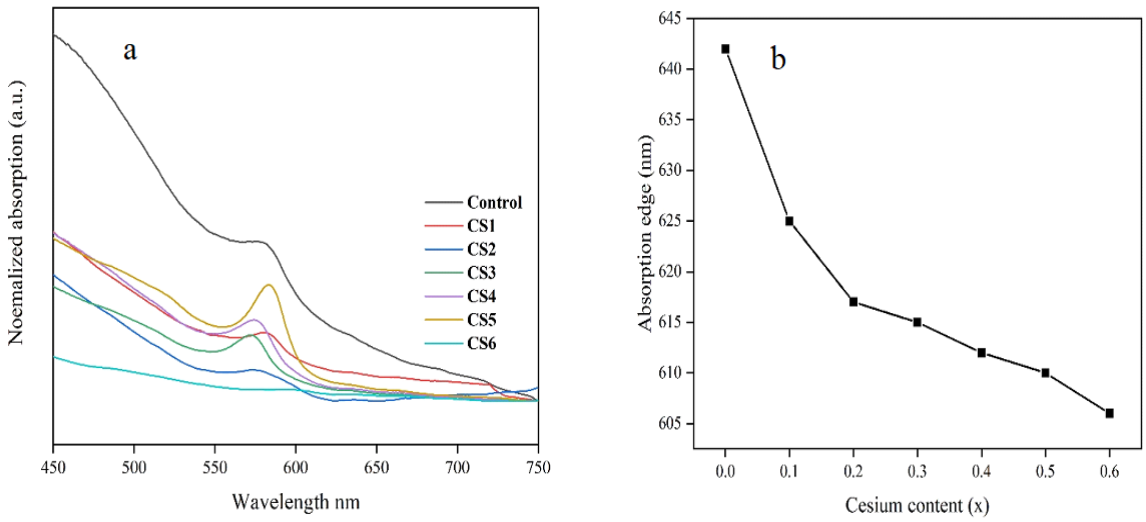

Figure 3:7: Absorption spectra of (a) $MAPbI_2Br$ and (b) $Cs_xMA_{1-x}PbI_2Br$ (x=0 to 0.6) nanocrystals

We performed UV-absorption (**Figure 3:*7***) and PL spectroscopy **(Figure 3:*8*)** experiments to study the effect of cesium content on optical properties of all these samples. Without adding cesium compound in the precursor solution (x=0), $MAPbI_2Br$ exhibits an absorbance edge at 642nm. As the amount of cesium increases, the absorption band is blue shifted to 606nm, when x=0.6. Therefore, corresponding band gap is of the doped perovskite nanocrystals is steadily shifted to higher energy direction. Hence, the use of mixed cation perovskites provides an excellent opportunity in the fine tuning of the optical bandgap and the emission wavelength of the $Cs_xMA_{1-x}PbI_2Br$.

In PL spectroscopy, it can be clrealy concluded that luminescence peaks can be effectively shifted in the range of 608 to 575 nm, with a varying amount of Cs cations into the perovskite nanocrystals.

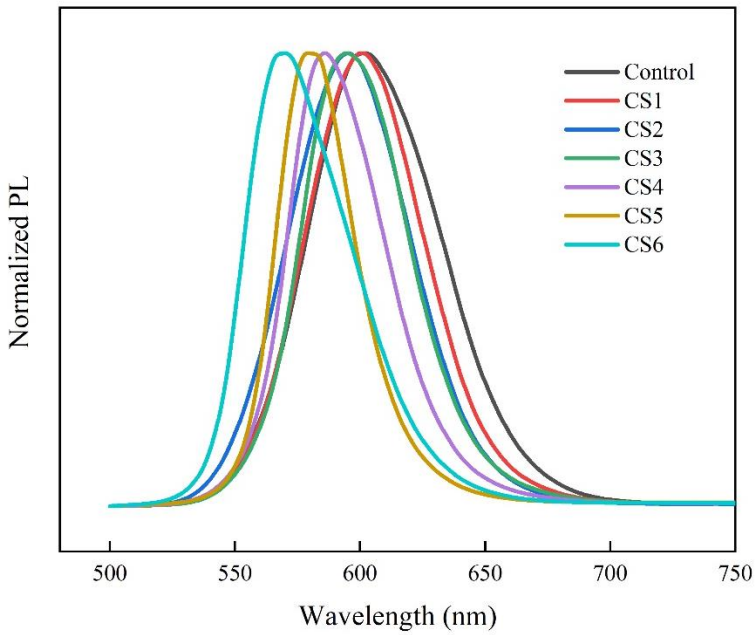

Figure 3:8: PL spectra of $MAPbI_2Br$ and $CsxMA_{1-x}PbI_2Br$ (x=0 to 0.6) nanocrystals

Figure 3:9 (a-g) show the transmission electron miscroscopy of the as formed colloidal nanocrystals of $MAPbI_2Br$ and doped with cesium ions synthesized with fixed amount of

oleylamine. Figure 3***:9***(a,b) exhibit the morphology and high magnification micrograph of as prepared $MAPbI_2Br$ nanocrystals, which are stable in the open air for few months. From HRTEM and corresponding Fourier transform (FFT) image, interplanar distances of 0.32nm were calculated, showing the (220) plane of $MAPbI_2Br$ nanocrystals. It was further confirmed by using XRD technique for these samples. As presented in Figure 3***:11***, the main diffraction peak intensity for these samples can be assigned to a tetragonal crystal structure (space group I4/mcm) $MAPbI_2Br$ [263]. After addition of cesium atom into the main crystal structure of $MAPbI_2Br$, a change in interplanar distances can be observed. In Figure 3**:*9***e, the interplanar distance was reduced to 0.24nm for cesium content (x=0.3) which is due to the presence of shorter cation in the crystal lattice.

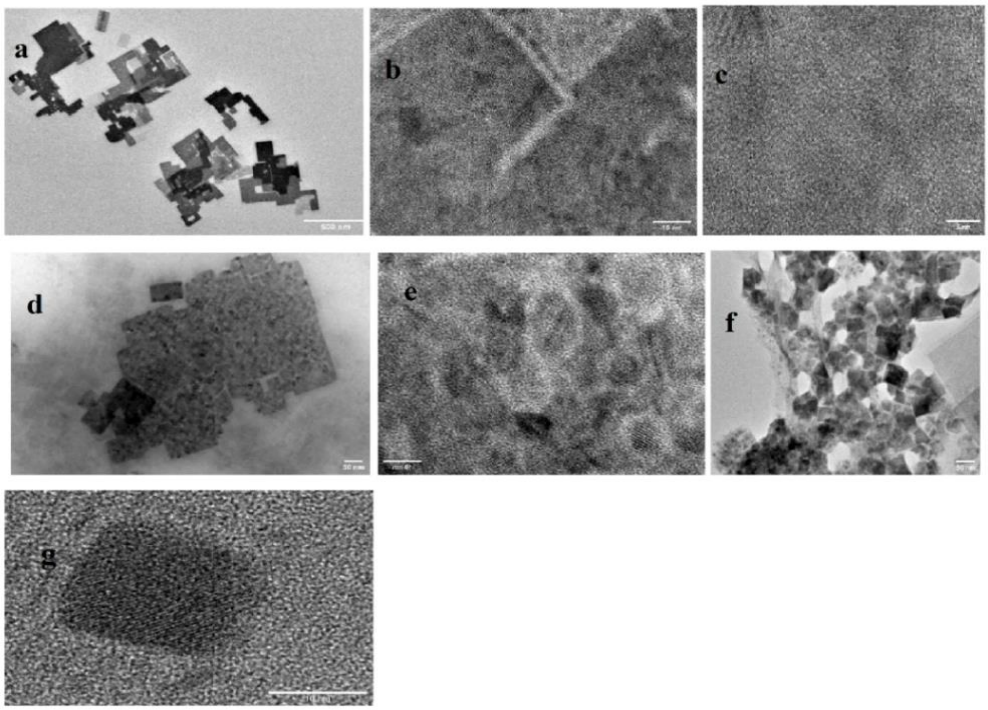

Figure 3:9: TEM micrograph of the $MAPbI_2Br$ nanocrystals. (a) $MAPbI_2Br$ (b)-(c) HRTEM micrograph of $Cs_{0.1}MA_{0.9}$ PbI2Br (d) $Cs_{0.2}MA_{0.8}$ PbI_2Br (e) HRTEM micrograph of $Cs_{0.2}MA_{0.8}PbI_2Br$ (f) $Cs_{0.3}MA_{0.7}PbI_2Br$ (g) HRTEM micrograph of $Cs_{0.3}MA_{0.7}$ PbI_2Br.

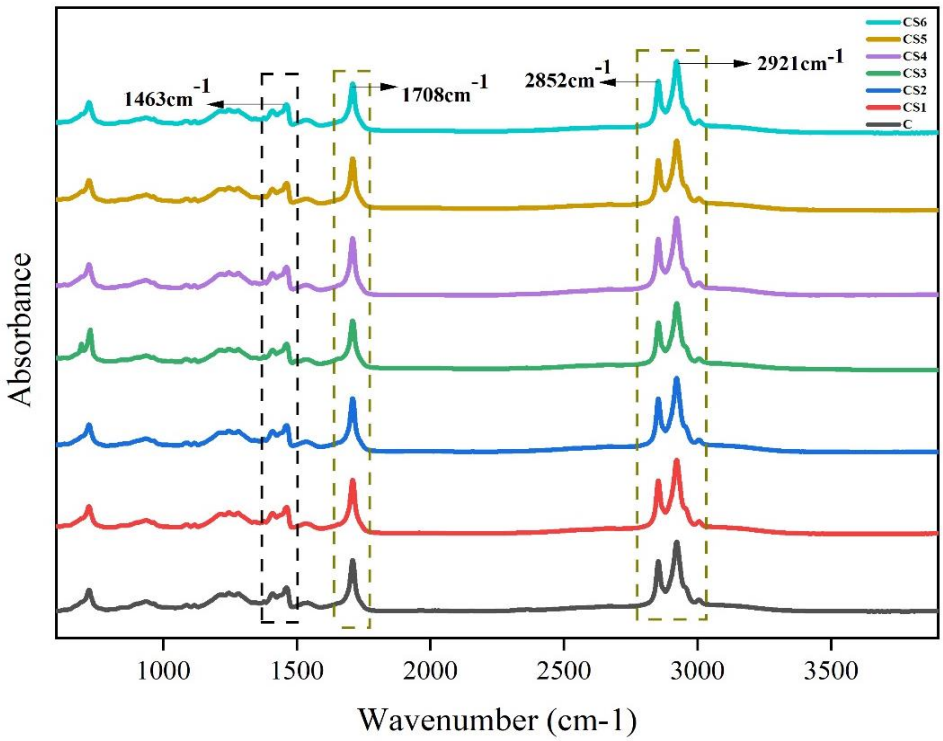

Figure 3:10: FTIR spectra of $MAPbI_2Br$ and $Cs_xMA_{1-x}PbI_2Br$ (x=0 to 0.6)

Here, Fourier transform infrared spectroscopy (FTIR) was used to study the all cesium (x=0-0.6) doped perovskite nanocrystals to analyse their surface properties. In **Figure 3:*10***, the sharp absorption peaks at 2852 and 2921cm^{-1} shows the CH_2 and CH_3 symmetric and asymmetric stretching vibrations, respectively, and C=O vibration band at 1708cm^{-1} can be ascribed as the presence of oleic acid on the surface of perovskite nanocrystals. The typical vibration band at 1463cm^{-1} can be attributed due to CH_2 bending for those species with hydrocarbon functional groups [148], [265].

In **Figure 3:*11***, X-ray powder diffraction patterns of as synthesized nanocrystals of $MAPbI_2Br$ and doped with cesium $Cs_xMA_{1-x}PbI_2Br$ was presented. The control sample without cesium doping shows diffraction peaks at 14.24°, 19.70°, 24.80°, 28.60°, 32.11°, 40.90°, 43.55° corresponding to the (110), (200), (202), (220), (114), (321), and (402) planes respectively,

indicate high crystallinity of a typical diffraction pattern indexed as $MAPbI_3$ tetragonal phase (space group I4/mcm). From XRD patterns, we therefore concluded that the addition of bromine in the structure of nanocrystals does not change the shape and the structure.

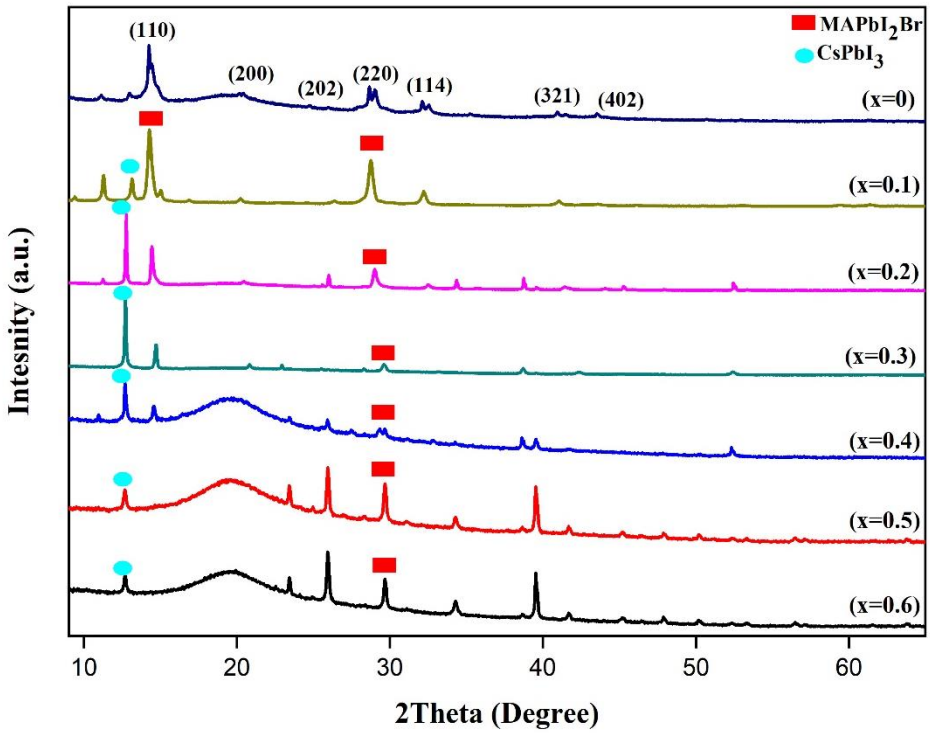

Figure 3:11: The X-ray diffraction (XRD) patterns obtained for the $MAPbI_2Br$ and $Cs_xMA_{1-x}PbI_2Br$ nanocrystals.

To identify the effect of cesium, a series of powder nanocrystal samples were checked for XRD patterns. All through the composition range x=0-0.6 the standard perovskite structure was observed. The diffraction pattern around 15° shifted towards high degrees shows the reduction of d-spacing due to incorporation of cesium into the structure. There is a linear relationship between cesium amount and d-spacing which follows Vegard's law [266].

Rubidium cation doping in MA-based perovskites ($MA_{1-x}Rb_xPbBr_3$)

Three-dimensional $CH_3NH_3PbBr_3$ nanocrystals were prepared by modified LARP technique. The precursor solution was prepared by dissolving lead bromide ($PbBr_2$), methyl ammonium bromide (CH_3NH_3Br), oleic acid, and oleylamine in DMF. After that, a specified amount of precursor solution was injected in toluene under vigorous stirring at room temperature, followed by centrifugation to get bright nanocrystals dispersion in hexane. For Rb/Ma mixed cation nanocrystals, rubidium bromide was added to precursor solution before injecting into the anti-solvent.

Results and discussion

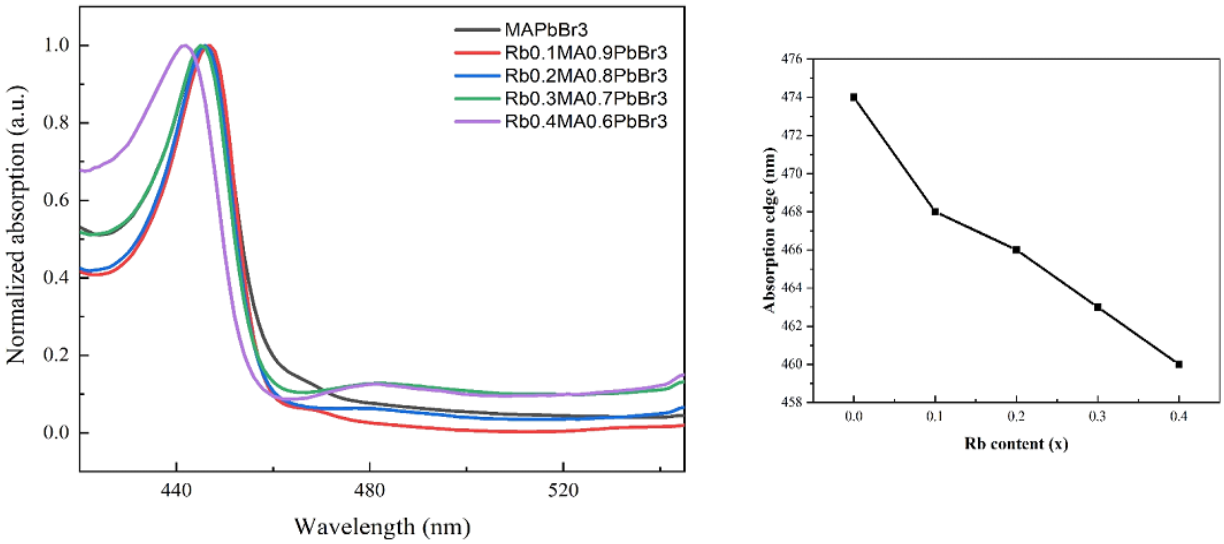

Figure 3:12: Absorption spectra of $MAPbBr_3$ and RbxMA1-x PbBr3 (x=0 to 0.4) nanocrystals

The optical properties of perovskites nanocrystals were measured by UV-Vis spectroscopy to study the effect on optical band gap upon incorporation of smaller size rubidium cation. As shown in **Figure 3:12** and **Figure 3:13** the absorption band was blue shifted from 475nm to 460nm after doping of rubidium atoms indicates the increase in bandgap.

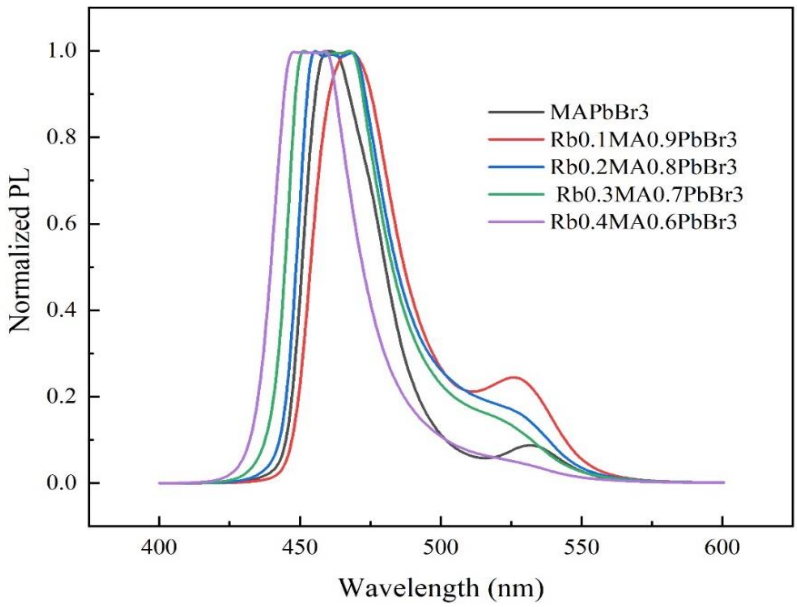

Figure 3:13: PL spectra of MAPbBr3 and RbxMA1-x $PbBr_3$ (x=0 to 0.4) nanocrystals

To study the effect of rubidium doping on crystallization of $MAPbBr_3$ nanocrystals, X-ray diffraction (XRD) was conducted on powder nanocrystals.

As concluded from XRD patterns, the as prepared nanocrystals present good crystallinity shown in **Figure 3:14**. It can be observed after addition of rubidium doping (100) peak of $MAPbBr_3$ at 14.91° shifted to higher angle 15.0° as the amount of rubidium increased, showing the lattice constant reduction upon incorporation of rubidium ions. The addition of smaller size rubidium ions can be attributed in the reduction of lattice constant. Perovskite structure shrinkage after addition of smaller cation was earlier reported when MA, and Cs was incorporated into $MAPbBr_3$ or FAPbBr3 nanocrystals or Rb was added to polycrystalline thin films [152], [153] [82], [83]. Therefore, Rb ions appears to partially replace MA to form a perovskite with a composition of RbxMA1-x PbBr3.

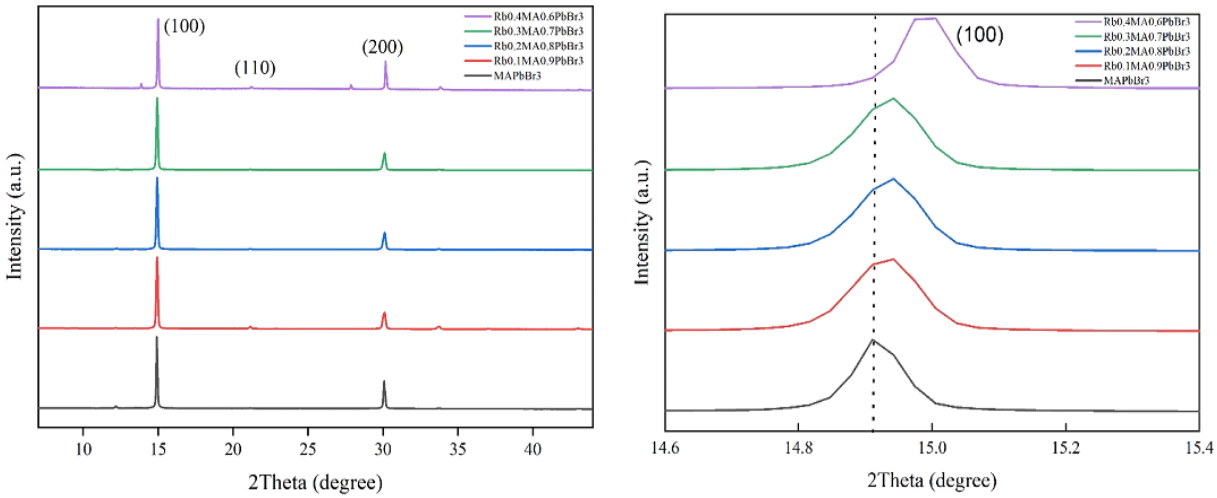

Figure 3:14: The X-ray diffraction (XRD) patterns obtained for the RbxMA1-xPbBr3 and MAPbBr3 nanocrystals.

Chapter 4 Fabrication of Potassium- and Rubidium-doped Formamidinium Lead Bromide Nanocrystals for Surface Defects Passivation and Improved Photoluminescence Stability

4.1 Overview

This work was published as "Fabrication of Potassium- and Rubidium-doped Formamidinium Lead Bromide Nanocrystals for Surface Defects Passivation and Improved Photoluminescence Stability" in ACS Applied Electronic Materials.

ABSTRACT

Metal halide perovskite nanocrystals (NCs) have emerged as a flourishing area of research, which has been witnessed by their potential applications in photovoltaics and optoelectronics. The fundamental science behind their unique photoluminescence characteristics has attracted a growing body of researchers. However, the low intrinsic stability and surface defects of the perovskite NCs have hampered their widespread applications. Therefore, numerous techniques such as doping and encapsulation (polymer matrices, silica coating, salt matrix, etc.) have been explored for the surface modification of NCs and to increase their efficiency and stability. In this study, we demonstrated the self-passivation method for the surface defects by introducing potassium (K) or rubidium (Rb) during the colloidal fabrication of NCs, leading to the much-improved crystallinity, photoluminescence, and improved radiative efficiency. In addition, K-

doped NCs showed long-term colloidal stability for more than 1 month which indicates the strong bonding between the NCs and smaller-size potassium cations (K^+). We observed the enhancement of radiative lifetime that can also be explained by the prevention of Frenkel defects when K^+ stays at the interstitial site of the nanocrystal structure. Furthermore, our current findings signify the importance of surface modification techniques using alkali metal ions to reduce the surface traps of perovskite nanocrystals (PeNCs). Comparable developments could be applied to polycrystalline thin films to reduce the interface trap densities. The findings of this study have several important implications for future light-emitting applications.

KEYWORDS: Halide perovskite nanocrystals; Surface defects; Colloidal stability; Alkali metal ions; Doping

4.2 Introduction

In the past few years, metal halide perovskite nanocrystals (MHP NCs) have received considerable attention owing to their high color purity, enhanced photoluminescence (PL) properties, and readily tunable band gaps from visible to the near-infrared region through halide exchange or size control [267]. Perovskite NCs have emerged as materials of choice because of predominantly ionic lattice and low-temperature synthesis, and hence are readily precipitated via low-cost solution processes [66]. So far, formamidinium lead bromide ($FAPbBr_3$) NCs have arrested outstanding photophysical properties such as stable and ultrapure green emission with tunable PL (525-535nm), small full-width at half-maxima (FWHM < 25 nm) and excellent stability in the air at high temperatures. In contrast, the most popular methylammonium lead bromide ($MAPbBr_3$) and cesium lead bromide ($CsPbBr_3$) have shown difficulties in achieving the desirable “525-535” PL defined by International Telecommunication Union (ITU) Recommendation BT 2020 (Rec. 2020) standard for next-generation displays. Therefore,

$FAPbBr_3$ NCs can ideally realize the critical window of the Rec. 2020 standard for ultrapure green emitters [268].

Metal halide perovskites (MHPs) crystallize in the cubic ABX_3-type perovskite structure, where A is a cation that can be organic (for example, methylammonium ($CH_3NH_3^+$/ MA^+), formamidinium ($CH(NH_2)_2^+$/FA^+)) or inorganic cesium (Cs^+), B is a divalent metal cation mostly lead (Pb^{2+}), and X is one or more halide anion (Cl^-, Br^-, I^-) [269]. In the form of colloidal NCs, these materials are terminated by long-chain alkyl ligands that contain ionic substituents like amine cation ($R\text{-}NH_3^+$) and carboxylate anion ($R\text{-}COO^-$) to achieve colloidal stability in nonpolar solvents. However, these ligands bind to the surface of NCs by weak electrostatic forces and only provide high coverage when present in excess in solution. In addition, the proton transfer between cationic amine and anionic carboxylate generates deprotonated NH_2 and protonated COOH groups that cause rapid desorption of ligands from the surface of NCs during the purification stage and storage in dispersion. The main consequences of such weak binding interaction between NCs and ligands decrease luminance efficiency and colloidal stability by incomplete surface passivation of NCs sites or defects [69], [70].

A high photoluminescence quantum yield (PLQY) and long-term structural stability of MHP NCs are fundamental requirements for commercial applications in television displays and related devices. However, surface defects of MHP NCs have accentuated the problem of charge-trapping and significantly increase the trap-assisted nonradiative carrier recombination pathways, reducing the performance of NCs for desired applications. To date, researchers have been able to explore various techniques to overcome the problem of long-term NCs stability including post-synthetic surface treatment [69], doping into NCs with metal and rare earth ions [270], [271], and reducing defects using surface-capping methods [272]. In particular, many

studies have established that the addition of alkali metal ions to perovskite NCs can significantly tailor the properties of the fascinating material. K addition was reported to increase the structural rigidity of mixed-halide $CsPbBr_{1.5}I_{1.5}$ NCs, which elevates thermal activation energy, hence enabling the NCs to retain high emission intensity at high temperature (>353 K) [273]. Another study reported an outstanding external quantum efficiency (EQE) of 21.8% and a lifetime T_{50} of 69 min by inserting K as a passivating agent between the emissive layer ($CsPbBrI_3$:Sr) and the hole transport layer [274]. A PL inhibition phenomenon was unveiled by a group of researchers, where PL was first increased by the addition of K into the $MAPbBr_3$ NCs and then inhibited with a further amount of K^+ [275]. Likewise, Rb doping into the perovskite NCs improves the crystallinity and reduces the defects/traps, thereby improving the thermal behavior of doped NCs. Manganese (Mn) doped $CsPbCl_3$ NCs with the addition of Rb^+ were studied by measuring optoelectronic properties. The experimental findings showed that Mn^{2+} cations emission for Mn-doped $CsPbCl_3$ NCs enhanced after doping of Rb^+ [147]. Furthermore, Rb was explored to study the dynamics of carriers in $CsPbBr_3$ single crystals for high-performance X-ray detection. This work has revealed that a small amount (0.037%) of Rb incorporation can increase the atomic interaction and orbital coupling between Br and Pb atoms, thereby leading to the enhancement of carrier transport and X-ray detection performance [276]. However, few researchers have been able to draw any systematic research on the treatment of organic-inorganic perovskite materials with alkali metal ions. Therefore, perovskite research studies would have been more useful if they focused on studying the effect of K^+ and Rb^+ on perovskite nanocrystals to understand these discrepancies.

The present research sets out to investigate the effects of introducing potassium cations (K^+) and rubidium cations (Rb^+) during the ligand-assisted reprecipitation (LARP) process for the

fabrication of formamidinium lead bromide ($FAPbBr_3$) nanocrystals. The introduced alkali metal cations (K^+/Rb^+) act as new passivating agents, which not only occupy the places of dangling organic ligands but also reduce the density of surface defects of PeNCs. This study, therefore, set out to suppress the nonradiative recombination of the $FAPbBr_3$ NCs, and, consequently, NCs with a high photoluminescence quantum yield (PLQY) are obtained. In addition, K^+/Rb^+ passivated $FAPbBr_3$ NCs showed long-term colloidal stability of more than 1 month that indicates the strong bond between the NCs and new metal ligands.

4.3 Experimental section

4.3.1 Materials

Chemicals including lead bromide ($PbBr_2$, ≥98%), formamidinium bromide (FABr, ≥98%), rubidium bromide (RbBr, 99.6%), potassium bromide (KBr, ≥99%), oleic acid (technical grade, 90%), oleylamine (technical grade, 70%), dimethylformamide (DMF, 99.8%), chloroform (≥99%), toluene (99.8%), hexane (≥95%), and acetonitrile (99.8%) were purchased from Sigma-Aldrich. All the chemicals were directly used as received without further purification.

4.3.2 Synthesis of $FAPbBr_3$ NCs

The $FAPbBr_3$ NCs were fabricated by the ligand-assisted reprecipitation (LARP) method as previously reported by Chen et al. with some modifications [277]. For the synthesis of unpassivated NCs, $PbBr_2$ (0.1 mmol, 0.0376 g) and FABr (0.1 mmol, 0.0124 g) were dissolved in 0.5 ml of DMF. Then, 250 µl oleic acid and 20 µl oleylamine were mixed and added to the solution. Next, 130 µl of this precursor solution was added dropwise into the vigorously stirred solution containing 8 ml chloroform at room temperature. Bright greenish-yellow emitting NCs were formed immediately while stirring for 30 s. For the purification of NCs, 3 ml acetonitrile was added to the as-prepared $FAPbBr_3$ NCs crude solution, and the dispersion was centrifuged

at 1200 rpm for 5 min to remove bulk and unreacted materials. The supernatant was discarded and the collected NCs precipitate was dispersed in 4 ml hexane. Finally, the solution was centrifuged at 5000 rpm for 3 min and, the bottom precipitate was discarded.

4.3.3 Fabrication of K^+/Rb^+ doped $FAPbBr_3$ NCs

For the synthesis of K^+ and Rb^+ passivated NCs, KBr, and RbBr powders were first dissolved in a mixed solution of DMSO: DMF (3:2 v/v ratio) to make a stock solution of 0.07 M and 0.05 M respectively. The resulting KBr and RbBr solutions were added separately into the formamidinium precursor solution using fixed volume of 30 µl. The remaining steps of K^+/Rb^+ doped $FAPbBr_3$ NCs are same as mentioned in the "Synthesis of $FAPbBr_3$ NCs" section.

4.3.4 Characterizations

The steady-state PL spectra of $FAPbBr_3$ NCs were recorded through a fluorescence spectrometer (FLS920, Edinburgh Instruments). The NCs dispersions in hexane were illuminated using 475 nm light at room temperature. The Ultraviolet–Visible (UV-Vis) absorbance spectrum of the samples was collected over a range of 400-650 nm using LAMBDA 35 PerkinElmer spectrometer.

The time-resolved PL spectroscopy was performed utilizing Horiba Triax 550 spectrometer and detected using a Hamamatsu R5509-72 NIR-PMT detector. A 405 nm vortran diode laser with a pulse width of 5 ns was used to excite the perovskite NCs. The TEM and HR-TEM images of the NCs were captured on a JEOL-JEM TEM machine operating at an accelerating voltage of 200 kV with a camera length of 40 cm. The samples for TEM were prepared by depositing 45 µl of solution in hexane onto carbon-coated copper grids and air-dried well. Fourier transform infrared spectroscopy (FTIR) spectroscopy was recorded by a Burker model FTIR with ATR accessory over the range of 4000-400 cm^{-1}. X-ray diffraction (XRD) profile

of as prepared NCs was measured by using PANalytical XpertPro diffractometer with an angular range of $5 < 2\theta < 70°$. Spectra were recorded by using monochromatic CuKα ($\lambda = 1.541$ Å) as a radiation source. X-ray Photoelectron Spectroscopy (XPS) of the NCs were collected on Thermo Scientific Nexsa XPS System using Al Kα X-rays as the excitation source.

4.4 Results and discussion

The $FAPbBr_3$ nanocrystals (NCs) were prepared by the ligand-assisted reprecipitation (LARP) method. A precursor solution containing a controlled amount of lead bromide ($PbBr_2$) and formamidinium bromide (FABr) in dimethylformamide (DMF) was prepared according to a previous report with some modifications [277]. Details of the fabrication procedure are mentioned in the Experimental section.

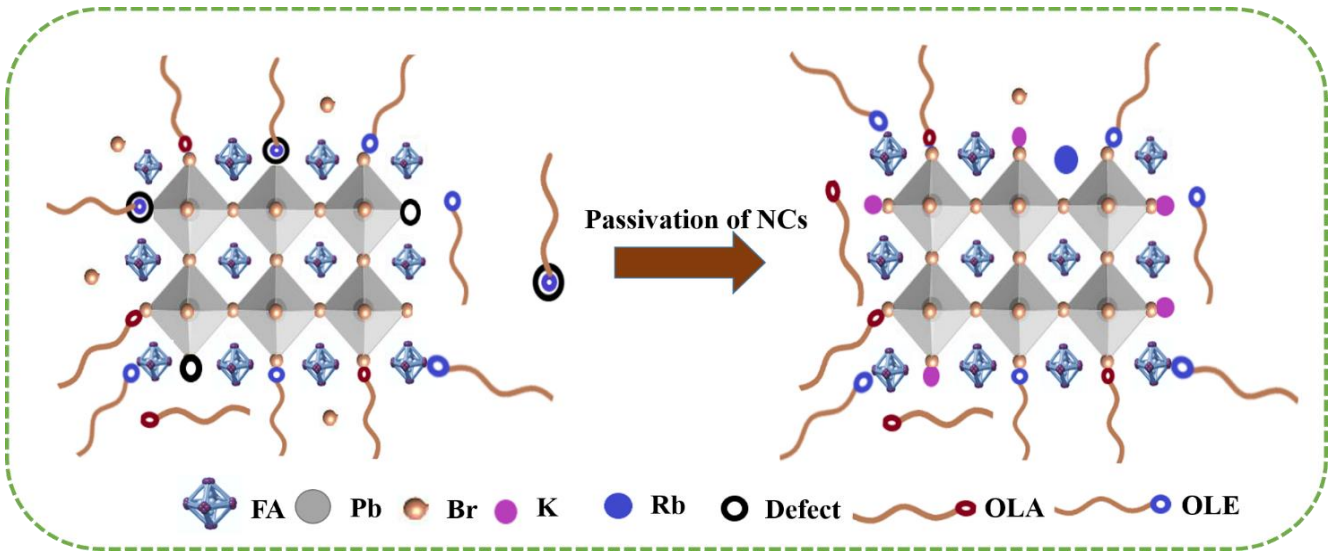

Figure 4:1. Schematic illustration of potassium and rubidium passivation.

To prepare perovskite nanocrystals (PeNCs) with K and Rb cations, a controlled amount of KBr and RbBr in DMF were added separately into the formamidinium precursor solution. The concentration of K-cations and Rb-cations to prepare PeNCs was controlled by a fixed molar

feed ratio of potassium or rubidium to lead source [K or Rb]/Pb. The added potassium ([K]/[Pb]) and rubidium ([Rb]/[Pb]) concentration was 5% and 3% respectively in the precursor solution. The PeNCs were precipitated by acetonitrile before centrifugation. After purification with hexane several times, the prepared PeNCs were dispersed in hexane for further characterization. To understand the doping behavior of these alkali metal ions, we show a schematic diagram of the treatment technique of K^+/Rb^+ in **Figure 4:1**.

4.4.1 Structural and optical characteristics

The optical properties of the synthesized PeNCs with and without alkali metal ions [K^+/Rb^+] was demonstrated by UV-visible absorption and PL measurement. In **Figure 4:2**a, the absorbance spectra and the PL spectra show a redshift with K-cations NCs compared to Rb-cations NCs which exhibit blueshift. Consequently, the band gap of PeNCs containing different concentrations of alkali metal ions determined by using a Tauc plot of UV-visible spectrum is 2.23 (Undoped), 2.21 (K-doped NCs), and 2.32 (Rb-doped NCs), respectively as can be seen from **Figure S1**.

A slight decrease in the optical band gap for potassium cations treated nanocrystals may be due to the formation of larger NCs caused by the decrease in the number of organic ligands as mentioned before [278]. For rubidium treated NCs, the widening of the optical band gap could be the result of orientational or electrostatic disorder as well as the fabrication of smaller NCs [152].

Table 4.1 allows key parameters comparison of the treated and untreated $FAPbBr_3$ perovskite NCs.

A slight decrease in the optical band gap for potassium cations treated nanocrystals may be due to the formation of larger NCs caused by the decrease in the number of organic ligands as

mentioned before [278]. For rubidium treated NCs, the widening of the optical band gap could be the result of orientational or electrostatic disorder as well as the fabrication of smaller NCs [152].

Table 4.1. Summary of characterization of all $FAPbBr_3$ perovskite NCs samples.

Sample	λ_{Abs} [nm]	λ_{PL} [nm]	Energy gap [eV]	FWHM [nm]	NCs size [nm]
Undoped	532	529	2.23	23	10.72
K-doped NCs	536	532	2.21	22	12.36
Rb-doped NCs	520	516	2.32	23	9.58

The morphology of the alkali metal ions substituted (K^+/Rb^+) NCs was characterized by transmission electron microscopy (TEM). TEM images showed the cubic shape of the NCs regardless of the K^+/Rb^+ cations as shown in **Figure 4:2**(b-d). We investigated that K^+ can bond with the halide ions in the solution of NCs to form an inorganic ligand outside the NCs surface. Therefore, the reduced amount of organic ligands could be a primary reason for to increased size of NCs [156], where the average size of pristine and K-doped NCs is 10.72 nm and 12.36 nm, respectively. After 3% Rb^+ cations, the average size of NCs decreases to 9.58 nm. Because of the smaller size of Rb^+ ions, the d-plane spacing between crystallographic planes is reduced, and the size of Rb^+ treated NCs decreases [147].

Accordingly, X-ray diffraction (XRD) measurements are performed to further explore the structure of PeNCs and to track the growth of perovskite and nonperovskite crystals after aging at laboratory ambient conditions. We stored the pristine perovskite samples at a constant room

temperature of 298 ± 1 K and relative humidity of 25±3% for 15 days. The main X-ray diffraction peaks for doped and undoped samples (

Figure 4:3a, b) located at 14.79, 21.20, 29.98, 33.52, 36.85, 42.84, 45.53° corresponding to the crystal planes (100), (110), (200), (210), (211), (220), and (300) respectively, confirm the cubic phase of $FAPBr_3$ with the PM-3m space group. These results are consistent with the cubic structure JCD 87-0158 and with those reported elsewhere [277], [279].

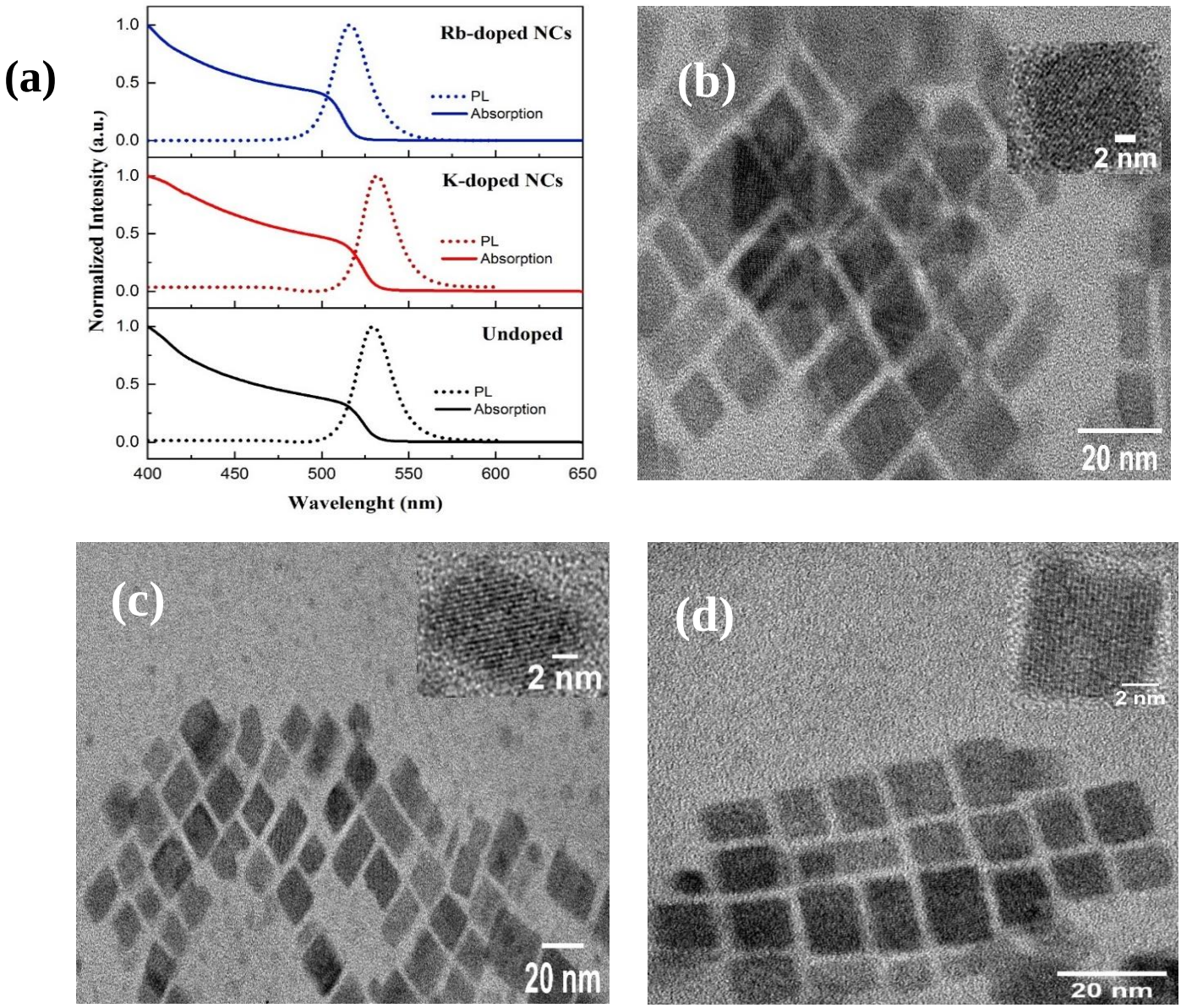

Figure 4:2. (a) UV–vis absorption and PL spectra. (b-d) TEM images of undoped $FAPbBr_3$ NCs, K-doped NCs, and Rb-doped NCs respectively. The inset shows the high-resolution TEM images of the corresponding samples.

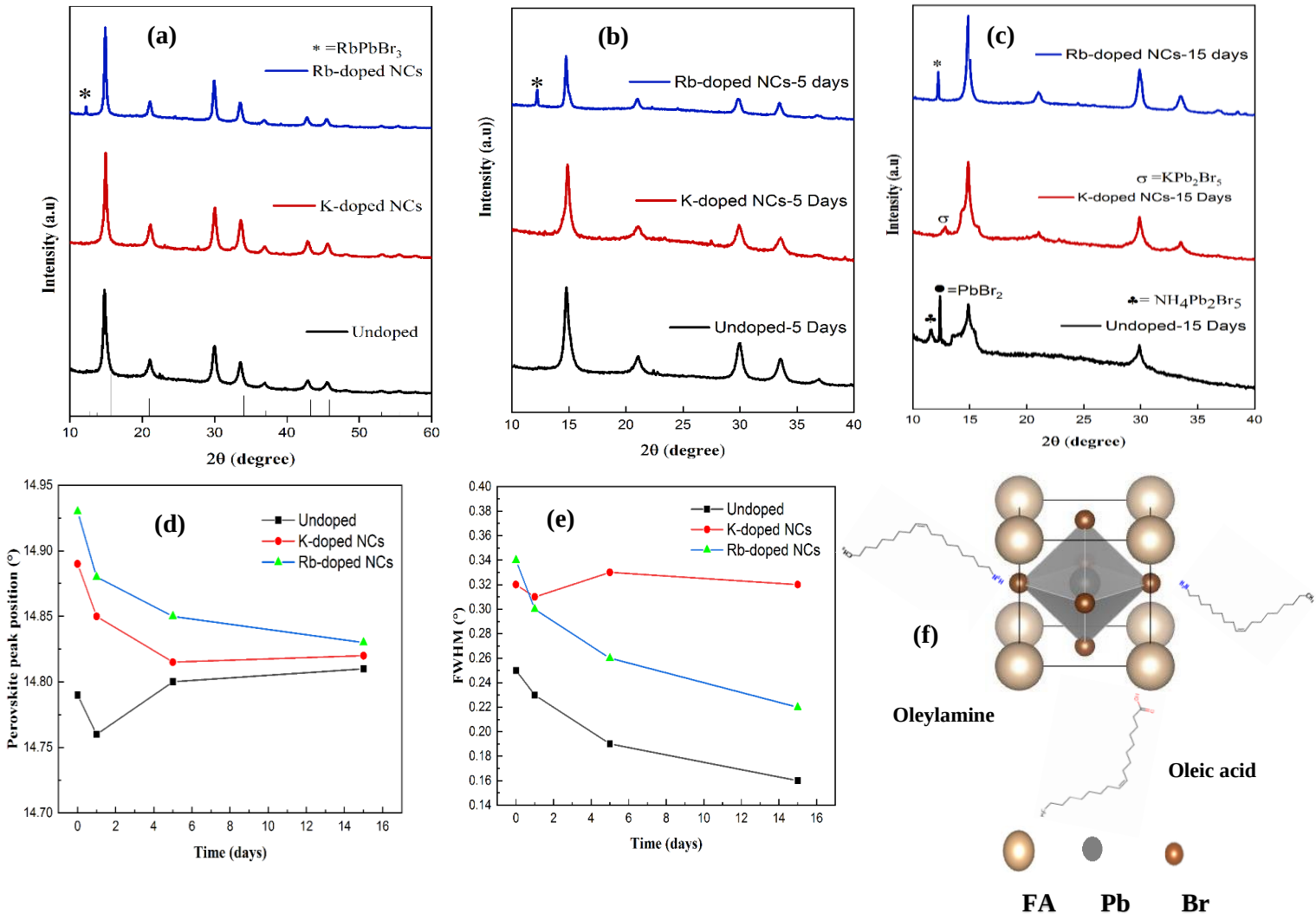

Figure 4:3. XRD pattern of (a) freshly prepared thin films on the glass substrate. (b-c) XRD patterns of all samples exposed to a humid environment for the stated times. The features are assigned as stated; we assign the feature marked * to be the non-perovskite phase of $RbPbBr_3$. (d) Peak position and (e) FWHM for the perovskite NCs over time. (f) Basic cubic crystal structure of $FAPbBr_3$ NCs at room temperature.

In

Figure 4:3c for the undoped NCs, we observed an intense $PbBr_2$ peak at 2θ=12.3° after storing samples at ambient conditions for 15 days. The humidity exposure for undoped samples also leads to the formation of new reflection with the peak at 2θ=11.6° that we assign to the undesired white-phase $NH_4Pb_2Br_5$ [280]. The NH_4^+ could form by the decomposition of FA^+ during the storage of samples. For the Rb-based perovskite samples (

Figure 4:3a-c), we found a different diffraction peak at 2θ=12.25° that we describe as nonperovskite phase of $RbPbBr_3$ [281]. We observe that there is a systematic increase in the intensity of the diffraction peak at 2θ= 12.25° with a storage time of up to several days. The X-ray patterns correspond to K-treated NCs exposed for 15 days and contain a weak reflection at 2θ = 12.86° that may depict the non-perovskite phase KPb_2Br_5 (

Figure 4:3c).

Figure 4:3d and e demonstrate the changes in the primary diffraction peak at 2θ ≈ 14.80° and the full width at half-maximum for the substituted and undoped samples at different exposure times at ambient conditions. We observe that for both K- and Rb-based NCs the peak position is shifted toward a higher angle relative to the undoped NCs, as smaller ions cause lattice contraction. This phenomenon is consistent with the recent studies on K and Rb cations for efficient perovskite devices [153], [156]. We note that we have not realized any significant change in peak position after humidity exposure, proposing that these effects are not affected by ambient conditions. We noted that FWHM for undoped and Rb-cations based NCs dropped significantly, which is in agreement with the previously mentioned report. By contrast, these parameters remain similar for K-doped NCs after ambient conditions exposure.

Figure 4:3f presents the typical cubic structure of $FAPbBr_3$ NCs.

We performed the Fourier transform infrared spectroscopy (FTIR) spectroscopy to investigate further how K^+ and Rb^+ influence the surface ligands of perovskite NCs. By comparing data with and without alkali metal ions doping (**Figure 4:4**), we notice that the peaks at 3270 and 1603 cm^{-1} attributed to N-H stretching and N-H bending are significantly reduced with K^+ and Rb^+ doping. These findings are consistent with that of Feng who also found similar results, which show a higher coverage of ligands on the surface of perovskite nanocrystals [156]. The strong peaks at 2700-3000, 1713 cm^{-1} correspond to C-H bending vibration, and C=O stretching of oleic acid. The reason for the reduction in ligands coverage could be attributed to K^+/Rb^+ which can make a bond with the halide ions in the solution of NCs to form an inorganic ligand capped outside the NCs surface.

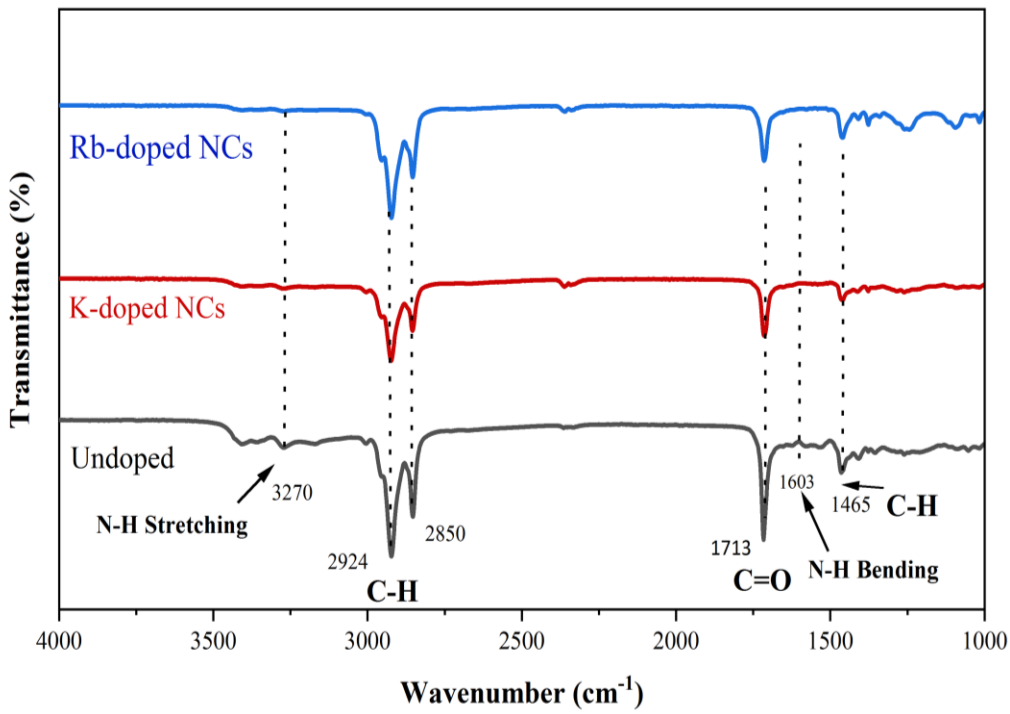

Figure 4:4. FTIR spectra of undoped, K-passivated, and Rb-passivated $FAPbBr_3$ NCs.

Furthermore, X-ray photoelectron spectroscopy (XPS) spectra were recorded to identify the chemical states of different elements of undoped, and alkali metal ions doped NCs. As shown

in **Figure 4:5**a, the XPS spectral peaks of Pb $4f_{7/2}$ and Pb $4f_{5/2}$, which were measured from Undoped NCs, were identified at 138.4 and 143.8 eV, respectively.

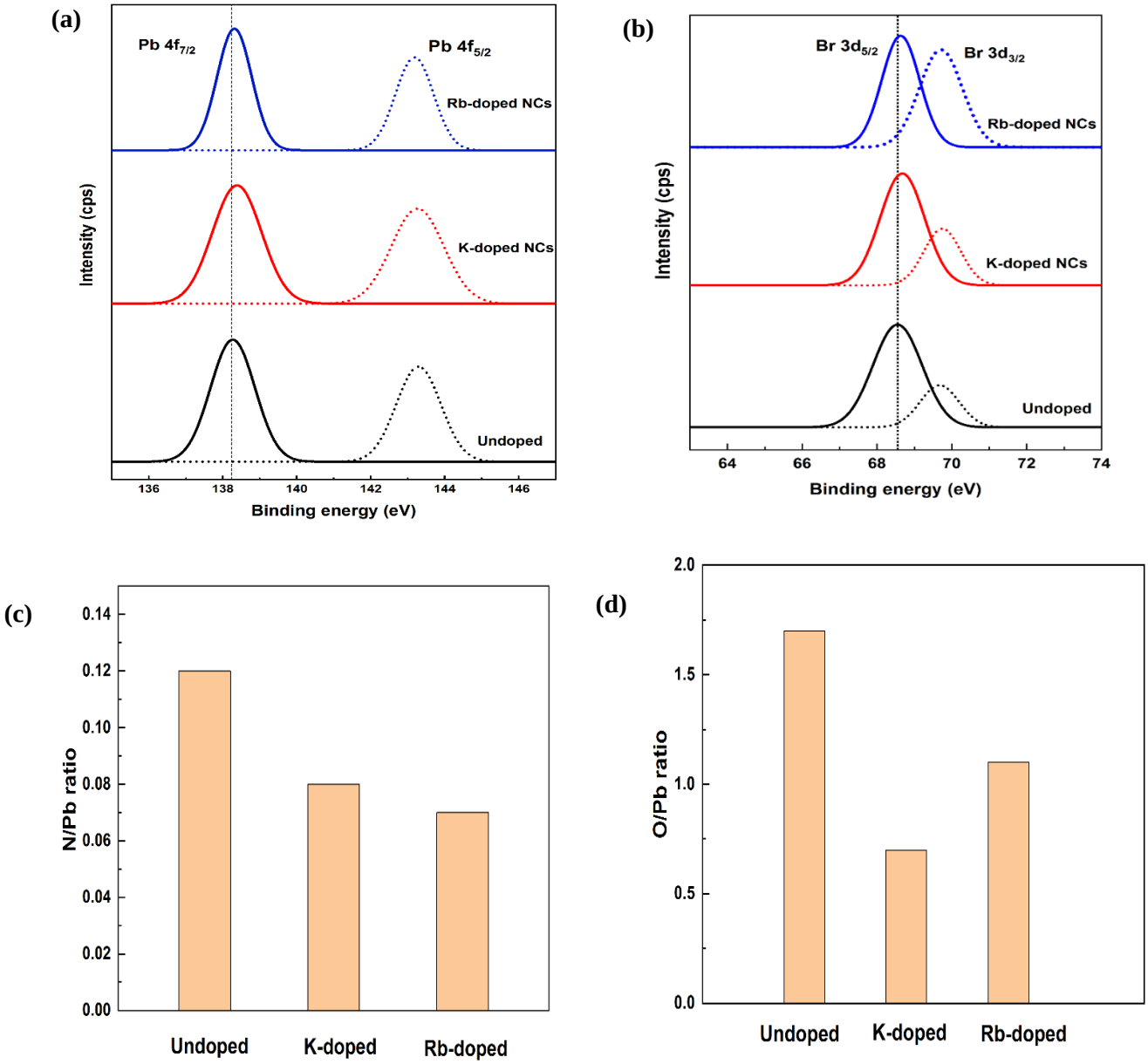

Figure 4:5. (a) Pb4f and Br3d XPS spectra and (c) N/Pb ratio (d) (O/Pb) ratio of all samples of $FAPbBr_3$ NCs.

Interestingly, these peaks were found to show a shift toward higher binding energy as the NCs were treated with K^+ and Rb^+ showing a different chemical environment of the Pb element. Similarly, the XPS spectral peaks of undoped samples for Br $3d_{5/2}$ and Br $3d_{3/2}$ (**Figure 4:5**b and **Figure S**2) were noticed at 68.7 and 69.7 eV, and the peaks also showed a higher binding energy shift with K- and Rb-doped samples. In addition, we calculate the O/Pb and N/Pb from the XPS data (**Figure 4:5**c, d) which shows that the O/Pb ratio drastically declined from 1.7 to 0.7 with the addition of alkali metal ions. As the O element only exists in the oleic acid, the amount of oleic acid severely decreases. The decrease in the N/Pb ratio from 0.11 to 0.07 indicates the reduced concentration of oleylamine outside the perovskite NCs.

4.4.2 Dynamics of photoexcited charge carriers

From the data in **Figure 4:6**, we study the time-resolved PL to understand the dynamics of excitons and the generation and transport of the photoexcited charge carriers in the NCs treated with K^+ and Rb^+. The PL decay curves are well-fitted with a biexponential function which can be expressed by the following equation [282]:

$$A = A_1 \exp\ (-t/\tau_1)\ +\ A_2 \exp(-t/\tau_2) \qquad (1)$$

Here, A_1 and A_2 are constants, t is time, τ_1 is ascribed to the trap-assisted recombination and τ_2 represents the radiative recombination.

In previous studies on the kinetics of excitons, the PL decay times were measured as a function of faster decay, related to trap-assisted recombination as an index of a shorter lifetime (τ_1), slower decay, related to radiative recombination as an indicator of a longer lifetime (τ_2), and

its fractional amplitude (A_i) [279]. The average recombination lifetime (τ_{ave}) was calculated from the fitted curve date according to the equation [282] :

$$\tau_{ave} = (A_1\tau_1{}^2 + A_2\tau_2{}^2)/(A_1\tau_1 + A_2\tau_2) \quad (2)$$

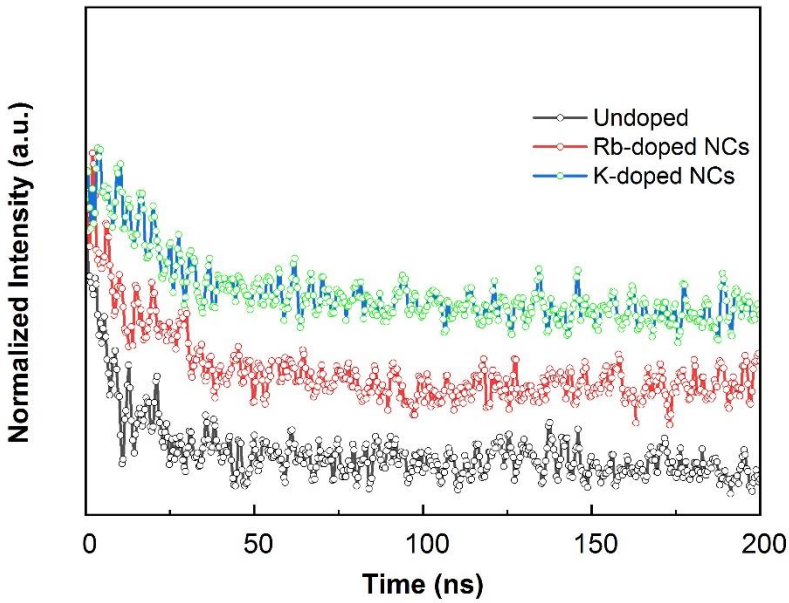

Figure 4:6. Time-resolved PL spectra for colloidal undoped, K-doped, and Rb-doped FAPbBr3 NCs

Table 4.2. PL lifetime of undoped, potassium, and rubidium passivated FAPbBr3 NCs.

Alkali metal ions treated samples	τ_1 (ns)	A_1 (%)	τ_2 (ns)	A_2 (%)	τ_{ave} (ns)
Undoped	20.15	46.43	55.62	50.46	45.60
K-doped NCs	21.15	50.2	70.62	55.46	62.55
Rb-doped NCs	10.87	45.10	45.32	30.06`	35.20

What is interesting about the data in **Table 4.2** is the τ_{ave} value increased from 45.6ns of Undoped $FAPbBr_3$ NCs to 62.5ns of K-doped samples. We find that the average lifetime

decreased to 35.2ns with Rb-doped $FAPbBr_3$ NCs. These results suggest that an adequate amount of K^+ can help to passivate the surface defects in the form of KBr which inhibit the halide phase segregation, contributing to stronger radiative recombination. The enhancement of radiative lifetime can also be explained by the prevention of Frenkel defects when K^+ stays at the interstitial site of the nanocrystal structure. In the case of Rb-passivated samples, reduced average PL lifetime may be due to the presence of PL-inactive nonperovskite $RbPbBr_3$ as reported in previous studies [281] [136].

4.4.3 Passivation mechanism of alkali metal ions for stable PeNCs

Theories in the literature regarding K^+/Rb^+ are extensive and focus particularly on the ions position inside the perovskite structure. Importantly, K^+ moves into the interstitial position of the PeNCs to increase the structural rigidity, which impedes the exciton-phonon interaction and increase the thermal activation energy, hence PeNCs continue to show high emission intensity at high temperature [273]. The K^+ has been reported as a highly effective passivator on the surface of lead halide PeNCs and binds with the halide ions to enhance the PL stability and suppress the halide ions segregation of the PeNCs [66], [155]. The definite location of both K^+/Rb^+ is still an open question for the researchers, however recent work suggests that neither K nor Rb is located within the perovskite lattice, yet there are also studies reported that these ions may occupy the interstitial sites on the PeNCs surface. Also, the perovskite films can consolidate a higher amount of K^+ than Rb^+ before undergoing large-scale phase segregation [283]. Rb^+ addition into the perovskite films can stabilize the crystal phase, reduce surface traps, and increase the withstand voltage and efficiency of devices. Electrical characterization of Rb^+ doped single crystal PeNCs revealed the enhanced atomic interaction and orbital

coupling between lead and halide ions, leading to the increased carrier transport for x-ray detection performance [147], [276].

4.4.4 Effects of K^+/Rb^+ on the colloidal stability of PeNCs

One of the main limitations of the PeNCs is their inadequate colloidal stability because of the high surface energy of small-size particles. Therefore, numerous passivating techniques have been widely explored to protect the PeNCs by using chemical ligands. Due to the liable chemistry of commonly used ligands including oleylamine and oleic acid, leading to the weak interaction between PeNCs surface. These ligands easily detached from the PeNCs surface upon dilution or long storage time, hence, structural damage or aggregation can occur. To test the effect of alkali metal ions on the stability of perovskite material, we recorded the PL of the $FAPbBr_3$ NCs dispersion in hexane with and without K^+/Rb^+ doping.

The results obtained from the $FAPbBr_3$ NCs without doping show that the PL intensity reduced dramatically (**Figure 4:7**a), while K^+ cations treated $FAPbBr_3$ NCs show insignificant change after 30 days of storage in ambient conditions (**Figure 4:7**b). This finding shows that strong bonding between the perovskite NCs and smaller size K^+. Due to the strong K^+ bonding, rapid desorption of ligands from the surface of NCs reduced during the purification and storage stage. However, there is a continuous decline in PL intensity after 30 days. We believe this happening could be due to the formation of KPb_2Br_5. Turning now to the experimental evidence from Rb^+-based $FAPbBr_3$ NCs, an abrupt change in PL intensity can be seen after 15 days of storage in air (**Figure 4:7**c). This phenomenon could be the reason for the formation of the non-perovskite phase of $RbPbBr_3$ as confirmed by XRD analysis. **Figure 4:7**d presents the comparison of undoped and K^+/Rb^+ treated $FAPbBr_3$ NCs. For pristine and Rb^+-treated $FAPbBr_3$ NCs, the colloidal solution becomes cloudy after 25 days of storage while K^+-based NCs retain their

stability even after 30 days of exposure in ambient air. Due to a much stronger ionic bond, K-based NCs show improved colloidal stability and reduced nonradiative recombination. For pristine and Rb-doped NCs, the NCs dispersions become cloudy, which might be related to the loss of highly dynamic surface ligands and the formation of nonperovskite phases.

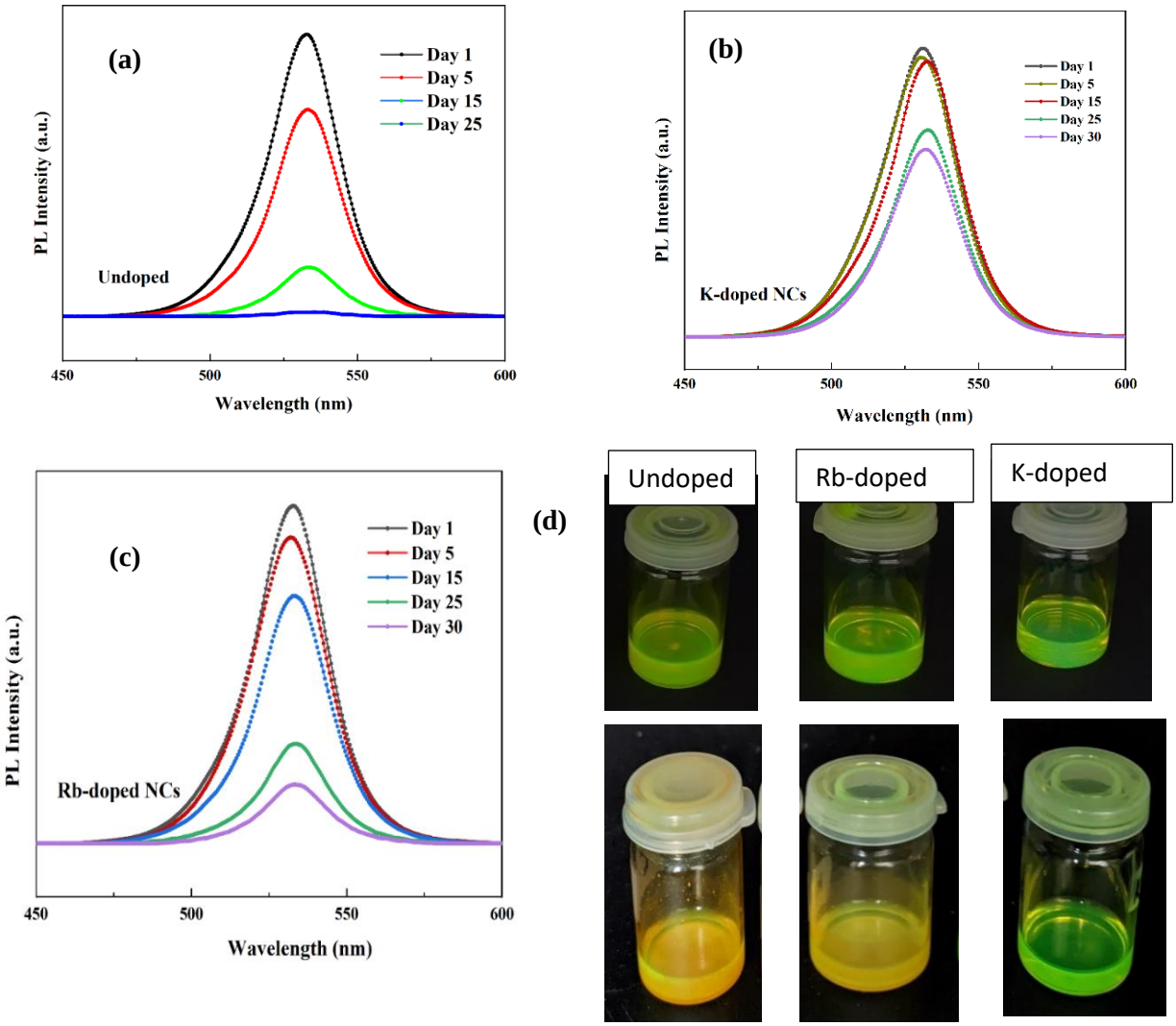

Figure 4:7. Stability test of the perovskite NCs. (a-c) Recorded PL spectra of the dispersion solution of undoped and doped FAPbBr3 NCs for 30 days. (d) Optical image of corresponding perovskite NCs dispersed in hexane under 365 nm UV excitation.

4.5 Comparison of effects of alkali metal ions on MA and FA-based nanocrystals

Table 4.3 shows the detailed comparison of alkali metal ions treated perovskite nanocrystals. It shows that both FA and MA-based nanocrystals shows similar behaviour when treated by the alkali metal ions. For example, Cs and Rb tend to reduce the crystal size after replacing MA or FA cations. Also, absorbance spectra and the PL spectra exhibit blueshift after treated with Rb or Cs cations. In addition, by adjusting the synthesis conditions and composition of the nanocrystals, a photoluminescence quantum yield (PLQY) exceeding 90% was achieved, as detailed in **Table 4.4**.

Table 4.3: Comparison of alkali metal ions treated perovskite nanocrystals.

Sample	**λ_{Abs} [nm]**	**λ_{PL} [nm]**	**Energy gap [eV]**	**NCs size [nm]**
Untreated $MAPbBr_3$ NCs	535	532	2.22	12.0
Untreated $FAPbBr_3$ NCs	532	529	2.23	10.72
Rb-doped $MAPbBr_3$ NCs	521	526	2.40	9.0
Cs-doped $MAPbBr_3$ NCs	527	528	2.30	11.0
Rb-doped $FAPbBr_3$ NCs	520	516	2.32	9.58
K-doped $FAPbBr_3$ NCs	536	532	2.21	12.36

Table 4.4: PLQY of $FAPbBr_3$ Nanocrystals treated with different additives.

Materials	Additives	Structure	PLQY (%)	Ref.
$FAPbBr_3$	Stearic acid, Octadecyl amine	QDs	88	[279]
$FAPbBr_3$	Excess FABr	NCs films	78	[277]
$FAPbBr_3$	CsPbBr3	Core/shell FAPbBr3/CsPbBr3 NCs	93	[282]
$FAPbBr_3$	3,3-diphenylpropylamine	NCs films	78	[284]
$FAPbBr_3$	Sulfobetaine-18 (SBE-18)	2D NCs	90.6	[268]
$FAPbBr_3$	Rb	Polycrystalline thin films	21.42	[153]
$CsPbBr_3$	K	NCs	84.2	[154]
$CsPb\ (Br/Cl)_3$	K	NCs	38.4	[156]
$(Cs,MAFA)Pb(I_{0.85}Br_{0.15})_3$	K	Polycrystalline thin films	66	[131]
$(Cs_{0.06}\ MA_{0.15}\ FA_{\ 0.79})\ Pb(I_{0.85}\ Br_{0.15})_3$	K	Polycrystalline thin films	52	[283]

4.6 Conclusion

The alkali metal ions substituted $FAPbBr_3$ perovskite NCs with green emission were synthesized by ligand-assisted reprecipitation method under room temperature to reduce the surface defects. This strategy of K^+/Rb^+ cations treatment was demonstrated to improve the PL emission intensity and colloidal stability of the perovskite NCs. The chemical bonding of K^+ with the halide ions in the solution of NCs to form an inorganic ligand capped outside the NCs surface can help to passivate the surface defects in the form of KBr which inhibit the halide phase segregation, contributing to stronger radiative recombination. Furthermore, the K^+ entered the interstitial position of the NCs structure, which increases the structural rigidity and limits the dissociation of perovskite NCs, representing remarkable stability for commercial use. The Rb^+ tends to form the non-perovskite phase of $RbPbBr_3$ with an average lifetime of 35.2ns

compared to 62.5ns of K^+ samples. To the best of our knowledge, the improved properties of $FAPbBr_3$ perovskite NCs by alkali metal ions are rarely reported in the literature. This research work paves the way to fabricate low-cost and highly stable PeNCs inks for optoelectronic devices.

Supplementary information

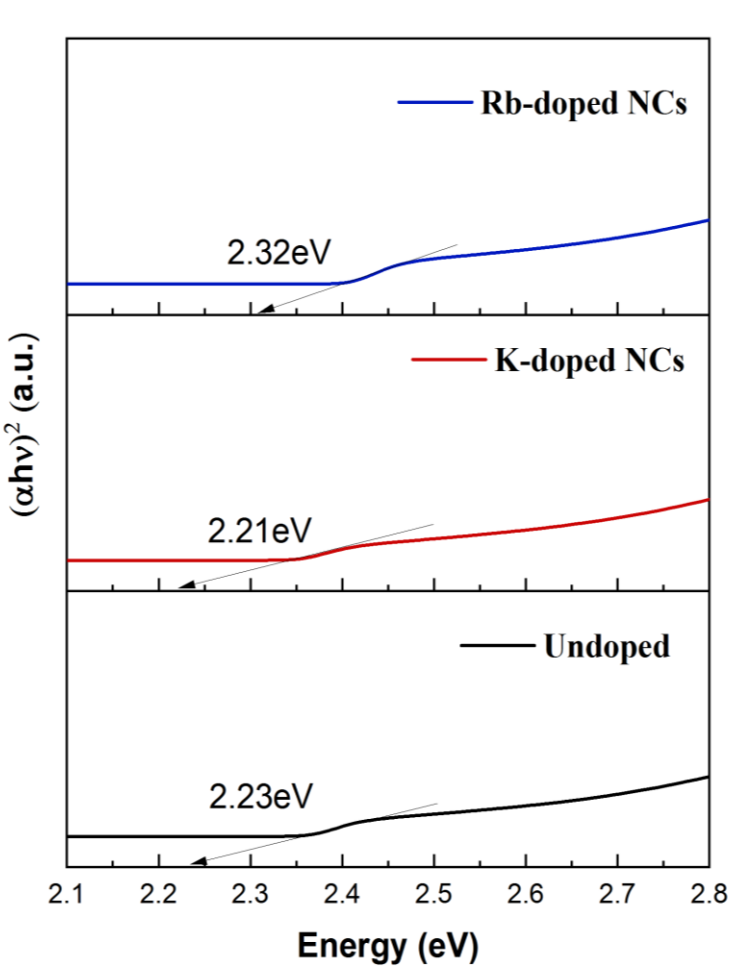

Figure S1. Band gap analysis of PeNCs using Tauc plots.

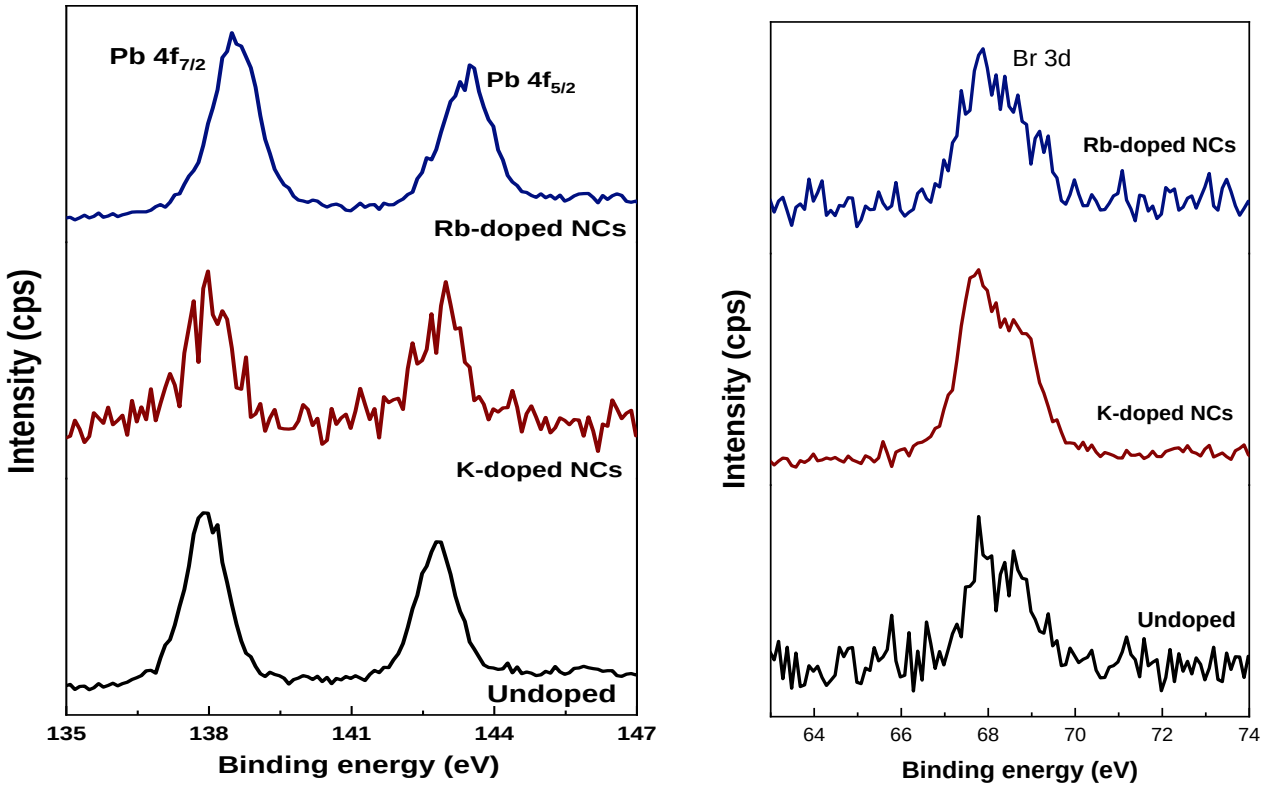

Figure S2. Experimental spectra of Pb 4f and Br 3d

4.7 Preliminary data

In this report, we provide discussion on doping of alkali metal ions (Na^+, K^+, $Rb^{+)}$ for formamidinium lead bromide ($FAPbBr_3$) nanocrystals (NCs) (**Figure 4:11**). For alkali metal ions (Na^+, K^+, Rb^+) passivated samples, 30µl of different concentrations (0.068M, 0.063M, 0.057M in DMF) of each alkali metals were added into the $PbBr_2$ and FABr precursor solution.

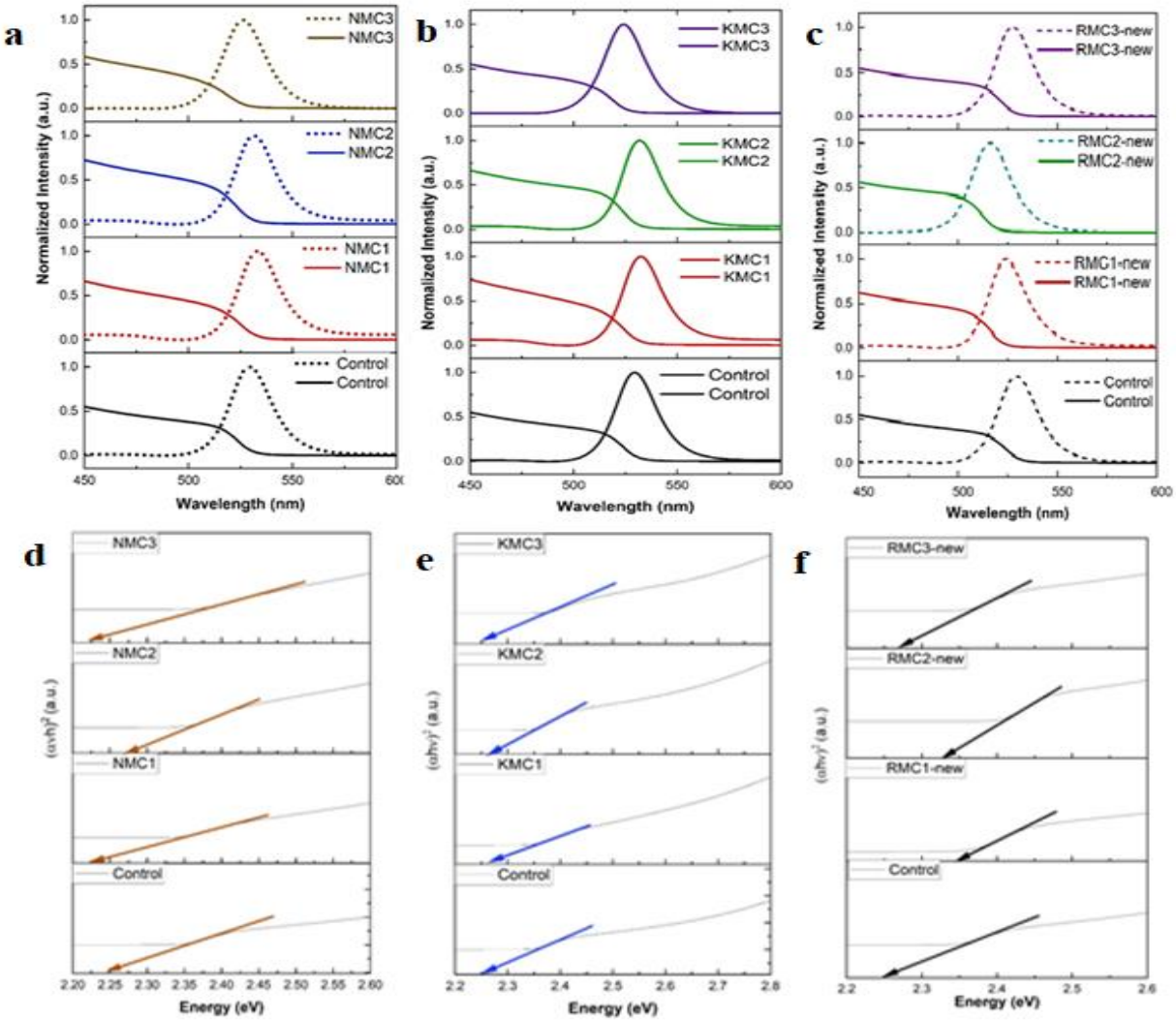

Figure 4:8: PL and UV–vis absorption spectra of $FAPbBr_3$ NCs solutions. (a) Sodium ion (b) potassium ion and (c) rubidium ion passivated NCs. Tauc plot showing the band gap calculation for (d) Na^+ (e) K^+ (f) Rb^+ treated NCs.

We performed UV-absorption and PL spectroscopy to study the effect of alkali metal ions (Na^+, K^+, Rb^+) treatment on optical properties of NCs (**Figure 4:8**a-c). As shown in **Figure 4:*8***d-f, optical band gap of $FAPbBr_3$ NCs containing different amount of Na^+, K^+, and Rb^+ ions were calculated by using Tauc plot of UV-visible spectrum. For Na^+ ion passivated

sample, band gap is 2.24, 2.22, 2.26 and 2.22 for untreated and treated samples of three concentrations (C1, C2 and C3) respectively. The change in bandgap is negligible, which is good agreement of the previous research that A-site cation does not affect the energetic band position of HPM.

Table 4.5: PL and absorption values of $FAPbBr_3$ NCs for different concentrations of Na, K, and Rb ions

Sample ID	**PL [nm]**	**Absorption [nm]**	**Eg [eV]**	**FWHM [nm]**
Control	529	532	2.24	23
NMC1	533	535	2.22	23
NMC2	531	532	2.26	22
NMC3	526	527	2.22	24
KMC1	532	534	2.25	23
KMC2	531	535	2.26	22
KMC3	524	528	2.24	24
RMC1	523	524	2.34	22
RMC2	516	520	2.32	23
RMC3	527	530	2.26	23

Figure 4:8(a-c) shows the UV-absorption and PL spectra of $FAPbBr_3$ NCs solutions with different amount of Na^+, K^+ and Rb^+ ions, in which PL spectra tune from 532nm-535nm when initial two concentration (C1, C2) of Na^+ was used and decrease to 524nm for higher concentration. For rubidium ions passivated samples, PL spectra was blue shifted from 532nm-527nm from untreated (control) to treated samples of three different concentration.

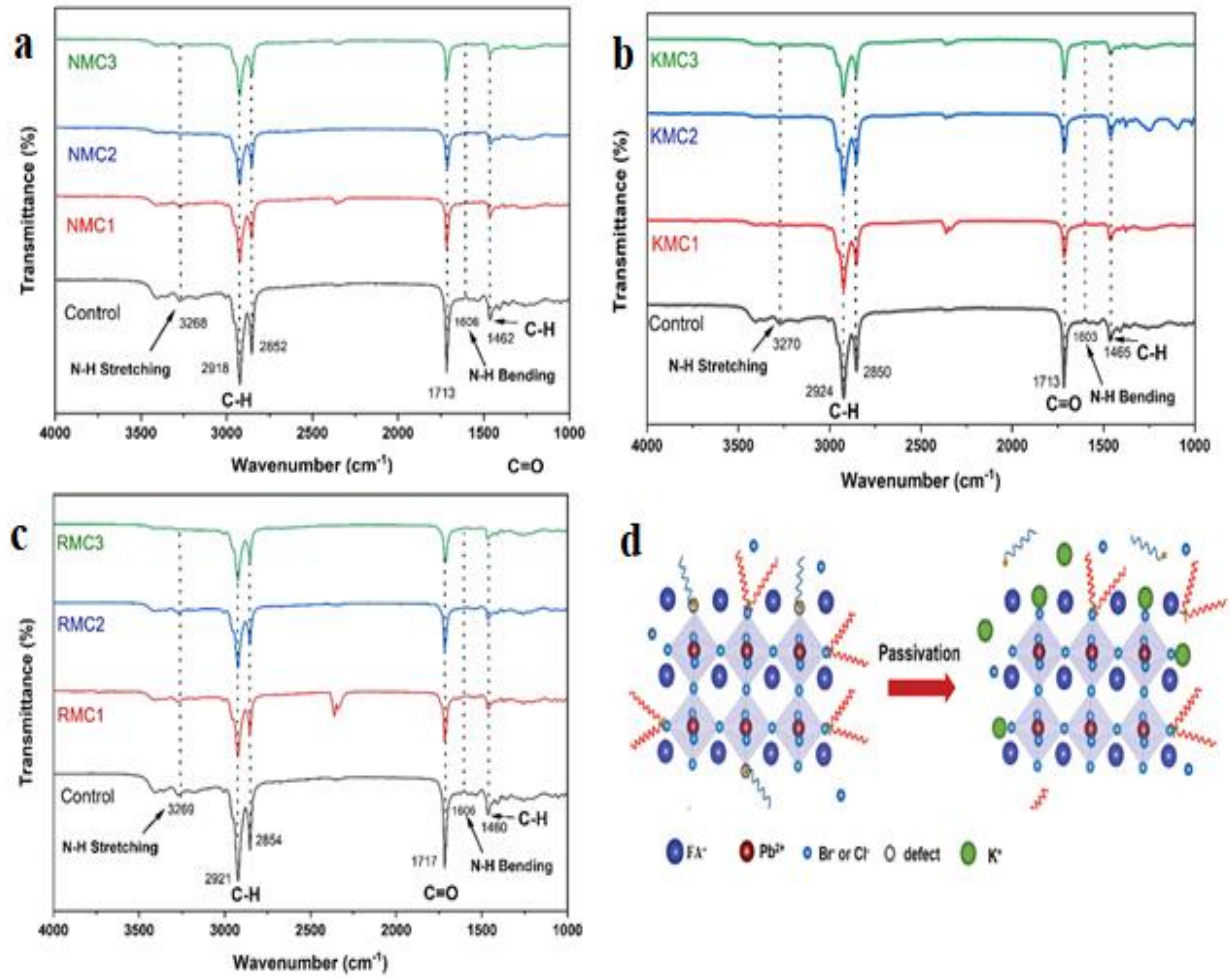

Figure 4:9: Fourier-transform infrared spectroscopy *(*FTIR*) of $FAPbBr_3$* NCs. (a) Sodium ion (b) potassium ion and (c) rubidium ion passivated NCs. (d) Schematic illustration of potassium passivation. Adapted with permission from ref [156],copyright © 2020, WILEY-VCH

Fourier-transform infrared spectroscopy (FTIR) was performed to determine the evolution of

long chain organic ligands after treatment with Na^+, K^+ and Rb^+ ions. As shown in **Figure 4:9**a-c, the strong peaks at 2700-3000, 1465, 1713 cm^{-1} can be ascribed as C-H bending vibration and C=O stretching of oleylamine and oleic acid respectively. After treatment of Na^+, K^+ and Rb^+ ions, the typical intensity of long chain organic ligands is reduced, demonstrating the reduction of organic ligands in the $FAPbBr_3$ NCs. Based on the above discussion, it is proved that Na^+, K^+ and Rb^+ ions can bond with halide ions to form metal ligands attached on the surface of $FAPbBr_3$ NCs, as schematically shown in **Figure 4:9**d.

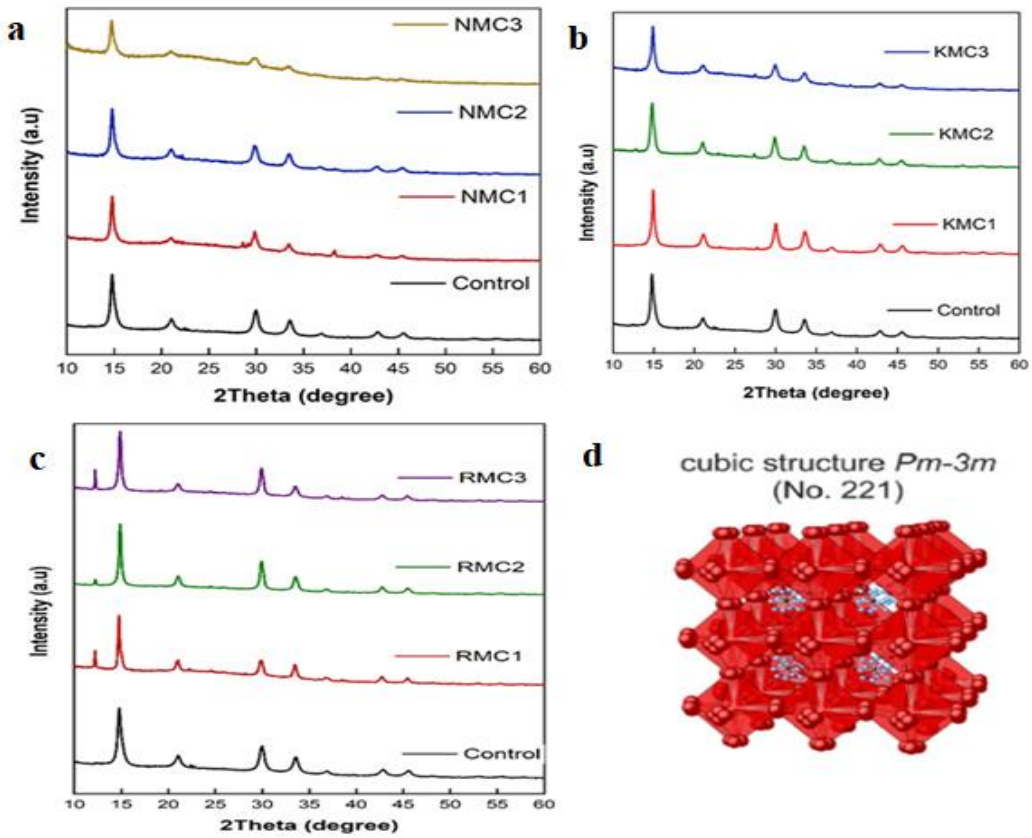

Figure 4:10: The X-ray diffraction (XRD) patterns obtained for the FAPbBr3 nanocrystals (a) Sodium ions (b) potassium ions and (c) rubidium ions passivated $FAPbBr_3$ NCs. (d) Crystal structure of $FAPbBr_3$

X-ray diffraction (XRD) is performed to analyse the effects of Na^+, K^+, and Rb^+ ions on the structural parameters of the resulting $FAPbBr_3$ NCs. All the treated samples show diffraction peaks around 2θ= 14.97°, 21.06°, 30.07°, 33.52°, 42.81°, and 45.57°, corresponding to the (110), (200), (210), (211), and (220) crystal planes of the cubic $FAPbBr_3$ NCs with the Pm-3m space group (**Figure 4:10**), as mentioned in previous studies [285], [286]. No diffraction peak shift can be observed in the alkali metal ions treated samples, signifying that small size ions remain outside the $FAPbBr_3$ NCs rather than being doped into the perovskite lattice. This phenomenon is proved with the recently published studies for perovskite solar cells [137].

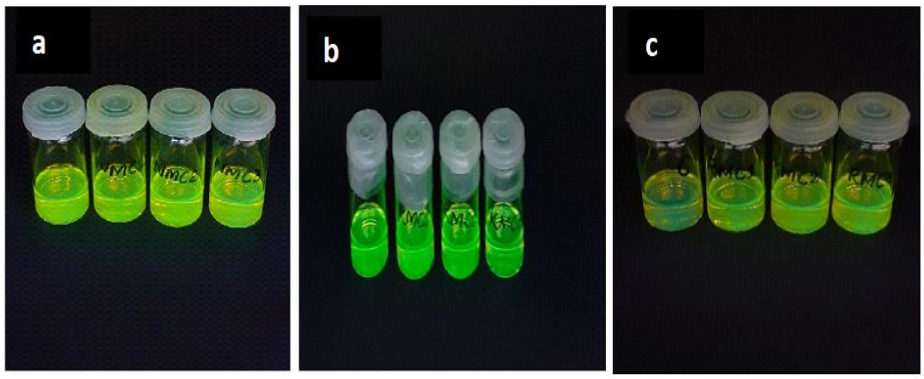

Figure 4:11: Digital photographs of FAPbBr3 NCs under room light.

Dopants vs dopant concentration to study steady PL to be added to support conclusion that K is best as dopant.

The **Figure 4:12** illustrates the enhanced stability of $FAPbBr_3$ nanocrystals treated with potassium ions compared to those treated with rubidium or sodium ions. We opted to treat the perovskite nanocrystals with potassium and rubidium to facilitate a comparative analysis. However, samples treated with sodium ions exhibited rapid degradation of the $FAPbBr_3$ nanocrystals.

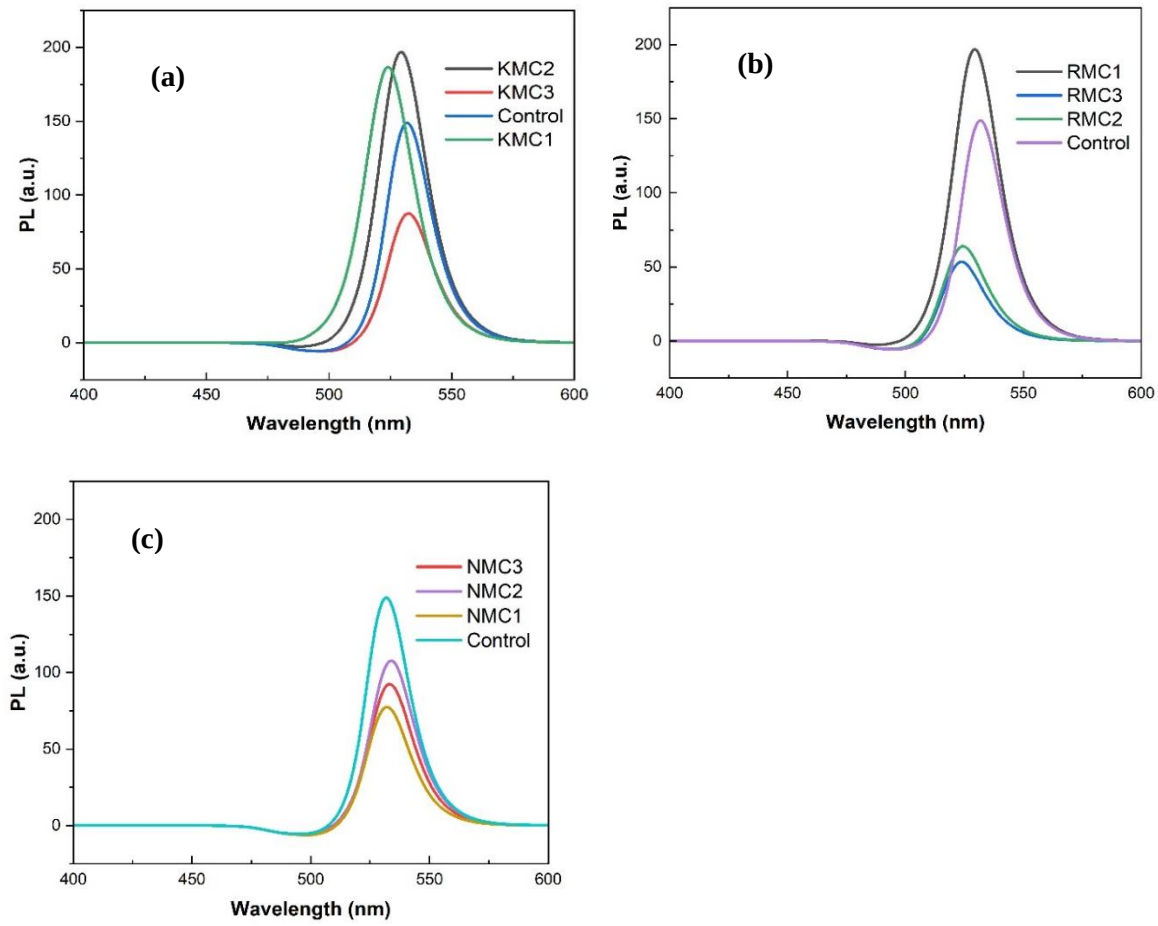

Figure 4:12: PL spectra of $FAPbBr_3$ NCs solutions. (a) potassium ion (b) rubidium ion (c) Sodium ion and passivated NCs.

Chapter 5 $FAPbBr_3$ perovskite nanocrystals embedded in poly (L–lactic acid) nanofibrous membranes for enhanced air and water stability.

5.1 Overview

This chapter was published as the article "$FAPbBr_3$ Perovskite Nanocrystals Embedded in Poly (L–lactic acid) Nanofibrous Membranes for Enhanced Air and Water Stability in *Membranes (2023)*. In this work, I prepared the poly (L-lactic acid) (PLLA) nanofibrous membrane embedded with $FAPbBr_3$ perovskite nanocrystals by electrospinning the perovskite and PLLA precursor solution. It was observed that resultant membranes were stable and remained in water for longer period.

Abstract

Formamidinium lead bromide ($FAPbBr_3$) nanocrystals have emerged as powerful platforms for optoelectronic applications due to their pure greener photoluminescence (PL). However, their low colloidal stability under storage and operation reduces the potential use of $FAPbBr_3$ perovskite nanocrystals (PeNCs) in various applications. In this study, we prepared the poly (L-lactic acid) (PLLA) nanofibrous membrane embedded with $FAPbBr_3$ perovskite nanocrystals by electrospinning the perovskite and PLLA precursor solution. This is a simple and low-cost technique for the direct confinement of nano-sized functional materials in continuous polymer nanofibres. PLLA as a polymer matrix provided a high surface framework to fully encapsulate the perovskite NCs. In addition, it is found that $FAPbBr_3$ PeNCs crystallize

spontaneously inside the PLLA nanofibre. The resultant PLLA-$FAPbBr_3$ nanofibrous membranes were stable and remained in the water for about 45 days while maintaining their PL peak intensity at 50% of the original value. The results of this research support the idea of new possibilities to produce air stable $FAPbBr_3$ PeNCs by forming a composite with PLLA polymer. I believe this study is a new milestone in the development of highly stable metal halide perovskite-based nanofibres, which allow potential use in stretchable photodetectors, mechanical energy harvesting applications, LEDs, and high-performance solar cells.

Keywords: metal halide perovskite, polymers, perovskite nanocrystals, air stability, nanofibres

5.2 Introduction

Organic-inorganic hybrid perovskites have been a major area of interest within the field of efficient light-emitting sources [287]. Most recently, formamidinium lead bromide ($FAPbBr_3$) NCs have received considerable attention due to their ultrapure green photoluminescence (PL) (530-535 nm) and higher thermal stability in comparison to more popular methylammonium lead bromide ($MAPbBr_3$) [288]. These NCs are capped with long-chain ligands that enhanced their stability in nonpolar or moderately polar organic solvents. However, perovskite nanocrystals (PeNCs) have poor stability against aqueous media, polar solvents, and long-term exposure to a moist environment [289]. Thus far, PeNCs stability was achieved mainly by alloyed perovskite nanostructures [290], core/shell-like structures [291], [292], and encapsulation into polymer matrices [293], [294]. Among them, the polymer matrix is the widely used approach to synthesizing highly stable PeNCs. For instance, Cai et al. reported a new technique to synthesize polymer-assisted Cs-based perovskite nanocrystalline film. The polymer, poly(2-ethyl-2-oxazoline) (PEOXA), which coordinates with the metal cations in the perovskite, improves the phase stability of PeNCs and reduces the fabrication temperature. In

addition, a pure red perovskite light emitting diodes (LEDs) with maximum luminance of 338 cd/m^2 and external quantum efficiency (EQE) of 6.55% were produced [295]. In another major study, Hou et al. reported the use of bolck copolymers that worked as nanoreactors during perovskite crystallization and passivates the NCs surface defects, hence improving its photostability in strong polar solvents [296].

Polymer nanofibres (PNFs) are one-dimensional long filaments with diameters in the range of tens to hundreds of nanometres. They offer unique properties of high porosity, bending elasticity, and high encapsulation capacity. Among several techniques to produce PNFs, electrospinning is the most cost-effective and efficient way to process a wide range of polymers [297]. Furthermore, the processing conditions of electrospinning offer advantages to encapsulate functional nanoparticles in the long fibres without the post-treatments [298]. To date, numerous studies have attempted to produce perovskite-polymer hybrid NFs by employing electrospinning approach. Wang and co-workers used the emulsion electrospinning technique to prepare ultra-stable perovskite-polymer nanofibres [299]. In another extensive study by Tsai and colleagues, the one-step core/shell electrospinning method was used to prepare perovskite-based NFs. The uniform perovskite-polymer nanofibres showed the hydrophobic properties of shell polymer and were endowed with high resistance to water for 48 h [300].

Electrospinning is a simple technique to produce highly uniform nanofibres from a variety of polymers including poly(methyl methacrylate (PMMA), poly(vinylidene fluoride) (PVDF), poly(vinylpyrrolidone) (PVP), polyacrylonitrile (PAN), and polystyrene (PS). The excellent mechanical properties of some polymers such as flexibility and easy preparation of PVDF-perovskite-based nanofibres show significant advantages over rigid polymers (for example,

PMMA, PS, etc.) [301], [302]. Also, environmental issues related to different polymers in electrospinning have not been completely understood. Taken together, the current research studies highlight the importance of the use of biodegradable biopolymers, as well as green solvents.

Polylactic acid (PLA) is the most commonly used bioplastic. Lactic acid, the precursor of PLA, can be derived from various raw materials including corn, starch, and sugarcane, which is then polymerized to PLA. Among different kinds of PLA, poly (L–lactic acid) (PLLA) has been an object of many studies due to its biocompatibility, biodegradability, and eco-friendly nature [303]. It has proven to be a good alternative to petro-chemical based polymers for numerous purposes. In contrast to other biodegradable and bio-based polymers, PLLA shows better processing parameters and can be processed by injection molding, extrusion techniques, ultrasonication, and fibre spinning. There are relatively few PLLA-based studies in the area of perovskites to make them stable at ambient conditions with low-cost processing methods. Yanyan et al. reported the first in situ synthesis of highly stable biopolymer phosphors with $CH_3NH_3PbBr_3$ as NCs and PLLA as the matrix. The fabricated perovskite-polymer composite films showed uniform morphology with outstanding emission characteristics of PeNCs and high transmittance of PLLA matrices [304]. In another study, an ultra-flexible and transparent conductive substrate was fabricated from PLA with silver nanowires to advance green electronics [305]. The research to date, however, has not fully explored the potential of PLLA in the emerging field of perovskites.

The present research explores, for the first time, the use of PLLA nanofibres to encapsulate $FAPbBr_3$ NCs. We mentioned in-situ room temperature fabrication of $FAPbBr_3$ NCs-PLLA nanofibres with $FAPbBr_3$ NCs as an emitter and PLLA as the matrix. $FAPbBr_3$ NCs-PLLA

nanofibres can be easily produced by the electrospinning technique, which is low-cost, versatile, and allows the control of NFs composition. The as-produced composite film shows a homogeneous morphology combining the excellent properties of both materials. The outstanding properties of PLLA help to make highly stable and efficient electrospun nanofibrous films with excellent stability in ambient environments retaining >50% of PL emission intensity. Overall, this study established a straightforward and low-cost method to prepare the composite film of $FAPbBr_3$ NCs-PLLA for strong stability in air and water.

5.3 Experimental

5.3.1 Materials:

Poly (L-lactic acid) (PLLA) (MW = 1.43×10^6) was supplied by PURAC biochem, Holland. Chemicals including lead bromide ($PbBr_2$, ≥98%), formamidinium bromide (FABr, ≥98%), oleic acid (technical grade, 90%), oleylamine (technical grade, 70%), dimethylformamide (DMF, 99.8%), and dichloromethane (DCM, 99.99%) were purchased from Sigma-Aldrich.

5.3.2 Fabrication of nanocrystals embedded PLLA electrospun NFs:

The $FAPbBr_3$ perovskite NCs incorporated in PLLA NFs were prepared by electrospinning technique as previously mentioned by Qasim et al. with some modifications [303]. PLLA (1.8%) was dissolved in 5 ml of dichloromethane in a closed glass vial by stirring and heating at 50 °C until the solution becomes clear and PLLA was completely dissolved. In parallel, $PbBr_2$ (0.0376 g) and FABr (0.0124 g) were dissolved in 0.5 ml of DMF. Then, 200 µl oleic acid and 15 µl oleylamine were mixed and poured into the perovskite solution. Next, this perovskite precursor solution was added dropwise into vigorously stirred PLLA solution at room temperature (25 °C) for 24 h. Then, the mixture was filled into a plastic syringe using a metal needle (19G) and was loaded into a syringe pump. The distance between the syringe tip

and the collector was fixed at 30 cm and a high voltage of about 23 kV was applied to charge the precursor solution. The electrospinning solution was released towards the moving roller (200 rpm) to collect NFs. The collected NFs were allowed to dry overnight.

5.3.3 Synthesis of $FAPbBr_3$ perovskite NCs:

We followed the ligand-assisted reprecipitation (LARP) method for the synthesis of $FAPbBr_3$ perovskite NCs according to the literature with reasonable changes [277]. $PbBr_2$ (0.1 mmol) and FABr (0.1 mmol) were dissolved in 0.5 ml DMF to prepare the precursor solution. Then, 250 µl oleic acid and 15 µl oleylamine were mixed separately in a vial and added to the solution. After that, 130 µl of this freshly prepared precursor solution was dropped into the 10ml of chloroform under constant stirring and observed the immediate formation of a green solution. Purification of PeNCs was completed by introducing a small amount of acetonitrile followed by centrifugation at 1200 rpm for 10 min. The collected PeNCs precipitate was further dispersed in 4 ml hexane for characterization.

5.3.4 Characterization:

The morphology of $FAPbBr_3$ NCs and $FAPbBr_3$ NCs-PLLA nanofibres was examined by using TEM (JEOL-JEM, accelerating voltage 200 kV) and SEM (FEI Inspect F) respectively. The chemical composition of samples was determined by EDS (attached to FEI Inspect F) at a voltage of 10 kV. The confocal microscope was used to record the fluorescence images with a 488 nm laser as the excitation light source. X-ray diffraction analysis of as-prepared NFs and $FAPbBr_3$ NCs was performed by PANalytical diffractometer with an angular range of $5 < 2\theta < 70°$.

The UV-Vis absorption and PL spectra were recorded using Perkin Elmer Lambda 35 UV-vis spectrophotometer and Perkin Elmer LS55 spectrofluorometer, respectively. Fourier transform

infrared (FTIR) spectra were recorded using a Burker model FTIR with a range of 4000-400 cm^{-1}. The composition of as-prepared samples was confirmed by X-ray photoelectron spectroscopy (Thermo Scientific Nexsa XPS system) with an excitation source of AL Kα x-rays.

5.4 Results and discussion

PLLA was used as a matrix for $FAPbBbr_3$ NCs due to its outstanding resistance against water and ambient conditions. As schematically shown in **Figure 5:*1***, we followed the electrospinning technique for the in-situ ambient fabrication of $FAPbBbr_3$ NCs-PLLA nanofibres. A precursor solution of $PbBr_2$, FABr, and PLLA in DMF/DCM was used for electrospinning.

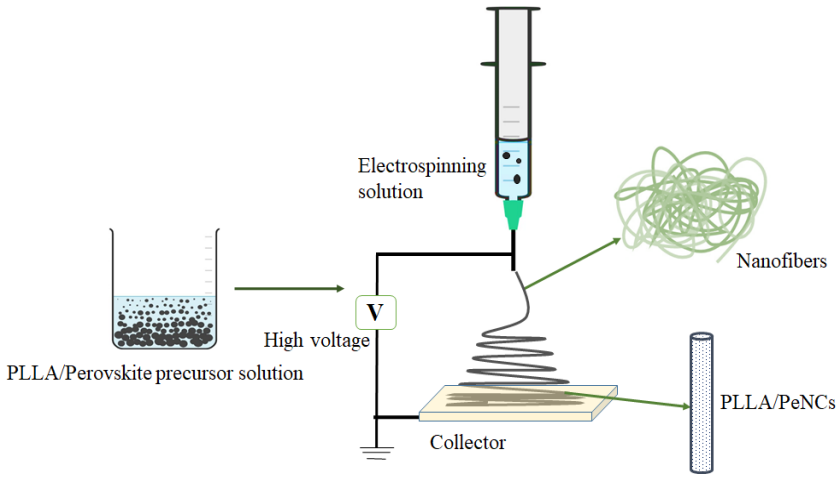

Figure 5:1: Schematic of electrospinning set-up for the fabrication of perovskite NCs-PLLA nanofibres.

A liquid is electrified to generate a jet that was directed toward the grounded collector, and the solvent evaporated simultaneously during the electrospinning. The high electric potential between two electrodes able to overcome the surface tension inside the electrospinning solution allows the facile synthesis of continuous fibres. When the concentration of the electrospinning solution reached the critical saturation level, crystallization of the $FAPbBbr_3$ NCs took place within the PLLA polymer.

5.4.1 Morphology of $FAPbBbr_3$ NCs-PLLA nanofibres

Figure 5:2(a-b) presents the scanning electron microscopy (SEM) images of PLLA NFs, which show the individual and highly uniform nanofibre structure. The morphological characterization of the composite film of $FAPbBr_3$ NCs-PLLA nanofibres reveals the smooth nanofibre structure with the $FAPbBr_3$ NCs embedded homogeneously in the PLLA polymer matrix as shown in

Figure 5:2(c).

The average diameter of as synthesized nanofibres is 1.45 µm and is not influenced by the incorporation of $FAPbBr_3$ NCs. Many recent studies have shown that well-distributed NCs inside the polymer matrices do not affect the diameter of the nanofibres [306], [307].

Respective high-resolution SEM images (

Figure 5:2(d)) of $FAPbBr_3$ NCs-PLLA nanofibres show that the fabricated PeNCs are well dispersed inside the PLLA matrix, and have a different shape, from cubic to spherical, depending on the amount of precursor solution concentration. Respective confocal fluorescence images exhibit strong PL emission (

Figure 5:2(e-f)).

Scanning electron microscopy coupled with energy dispersive spectroscopy (EDS) was used for the analysis of $FAPbBr_3$ NCs–PLLA nanofibres to observe the elemental composition. The results, as shown in Figure S1, indicate that both Pb and Br are present in the composite films. Therefore, above mentioned discussions demonstrate that the $FAPbBr_3$ NCs are

homogeneously distributed in the PLLA matrix network through the in-situ ambient fabrication technique.

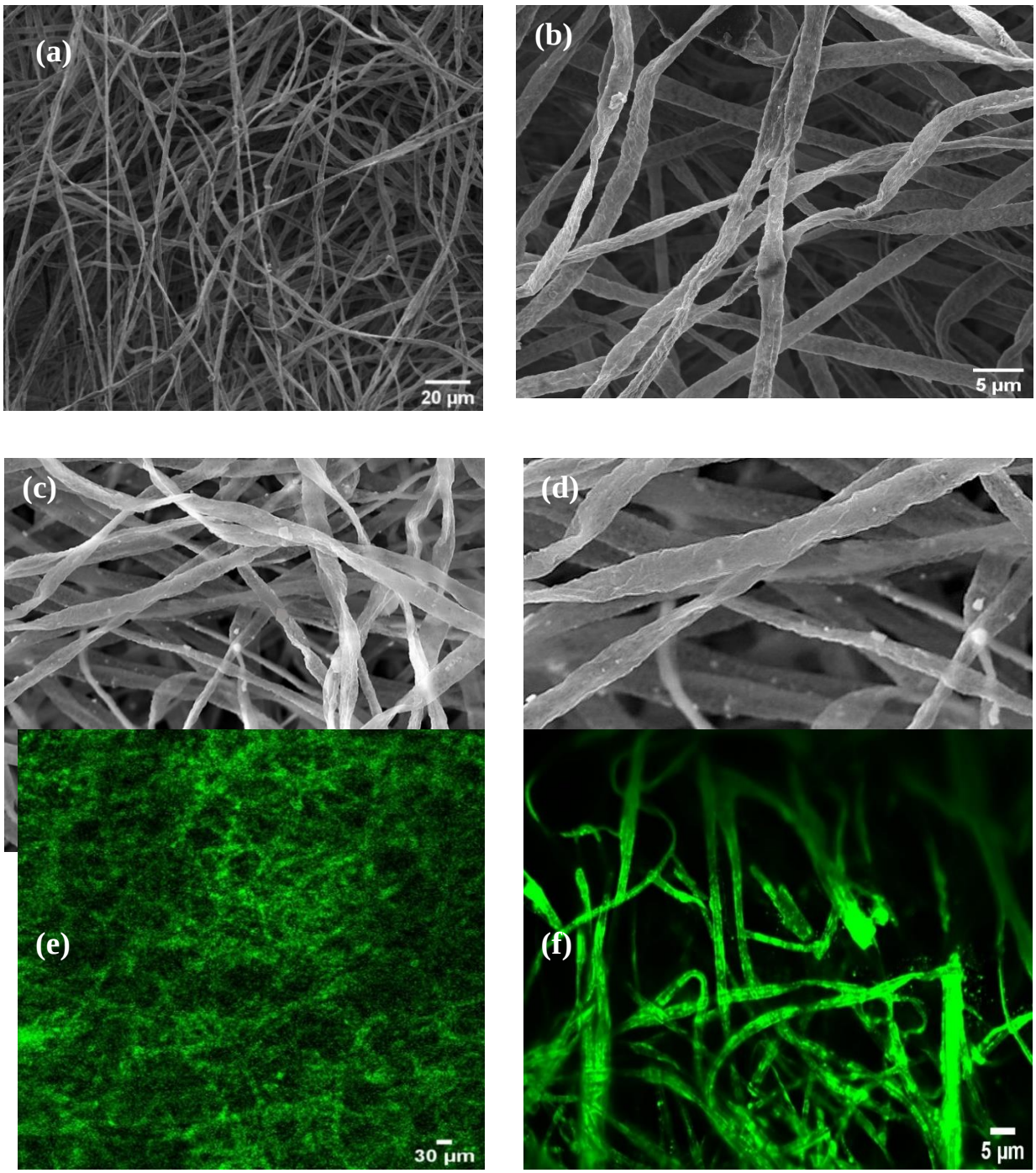

Figure 5:2: SEM images of the electrospun perovskite-polymer membranes. (a)-(b) Morphology of pristine PLLA nanofibres with different magnifications. (c)-(d) SEM image $FAPbBr_3$ NCs@PLLA nanofibres (e)-(f) Confocal fluorescence microphotographs of perovskite-polymer membranes with a 488 nm laser as the light source.

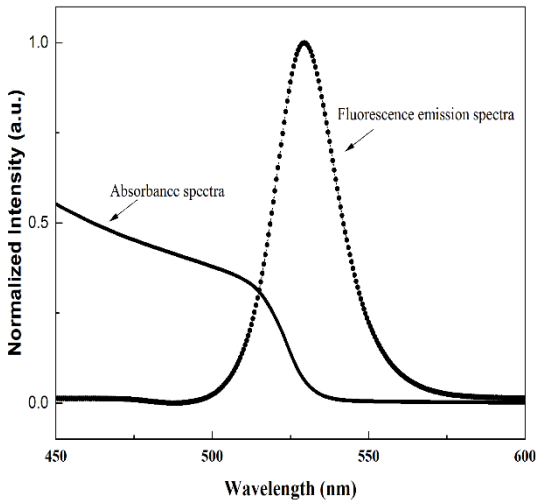

(**a**)

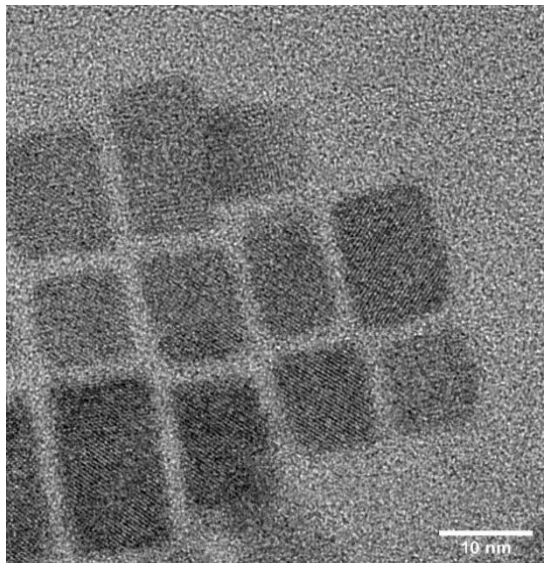

(**b**)

Figure 5:3:(a) UV-VIS absorption and PL spectra of $FAPbBr_3$ NCs. (b) TEM images of $FAPbBr_3$ NCs.

$FAPbBr_3$ NCs are synthesized with $FABr/PbBr_2$ using the LARP technique and purified according to the previously mentioned report by Chen et al. with rational changes [277]. In this method, oleic acid (OA) and oleylamine (OLA) are used as surface ligands, where OA plays a key role to prevent the PeNCs from segregation and improving the colloidal stability PeNCs. We investigated the optical properties of pristine $FAPbBr_3$ NCs via UV absorption and photoluminescence (PL) measurements. In **Figure 5:*3***(a), the PL spectrum displays a pure-

green emission at 530 nm. The PL emission spectra, with FWHM ≈ 22 nm are from pure $FAPbBr_3$ NCs dispersion in hexane. From the normalized UV-vis spectra, it demonstrated a strong light absorption edge at 512 nm.

Figure 5:*3*(b) shows the TEM images of the as-obtained $FAPbBr_3$ NCs. The PeNCs crystallize which a cubic shape, monodispersed, with an average size of 10-12 nm. The PeNCs follow the typical perovskite structure ABX_3 as shown in **Figure 5:*4***(b).

5.4.2 The crystallinity of $FAPbBbr_3$ NCs-PLLA nanofibrous membranes

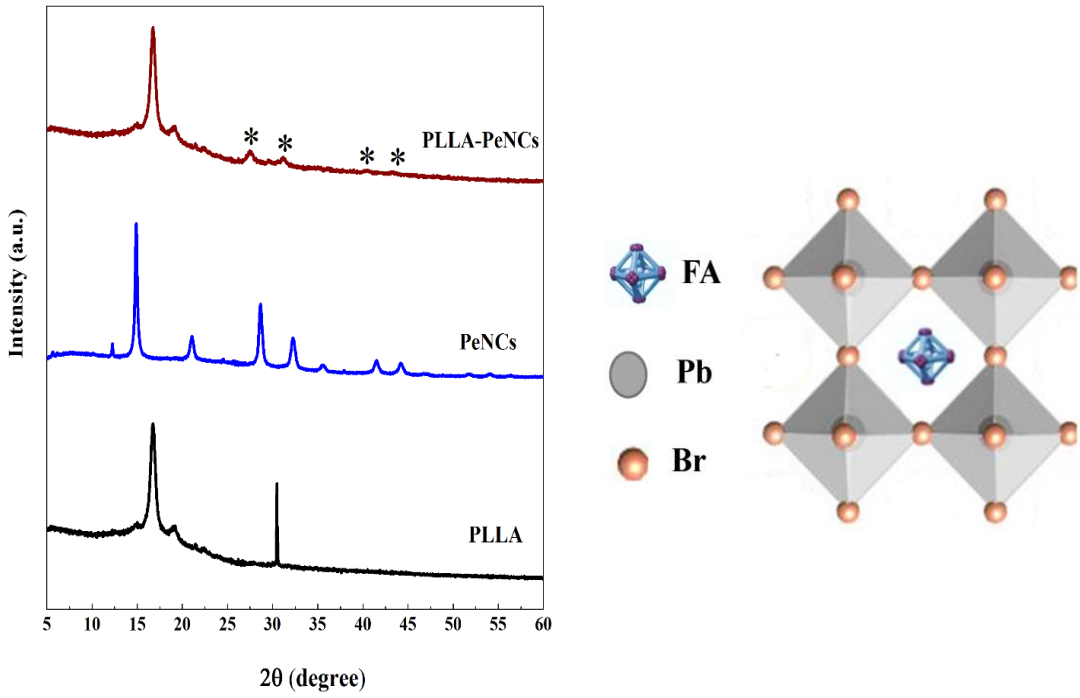

(**a**) (**b**)

Figure 5:4: (a) X-ray diffraction pattern of pure $FAPbBr_3$ NCs, PLLA, and PeNCs-PLLA nanofibres; * indicates the peaks belonging to $FAPbBr_3$. (b) The cubic crystal structure of $FAPbBr_3$ NCs at room temperature.

The crystallinity of $FAPbBr_3$ NCs was further analysed by X-ray diffraction (XRD) patterns. XRD pattern of PLLA nanofibres, $FAPbBr_3$ NCs, and $FAPbBr_3$ NCs-PLLA nanofibres are displayed in **Figure 5:*4***(a). Diffraction peaks located at $2\theta = 14.8°$, 16.8°, and 19.07° refer to PLLA nanofibres. The diffractogram of $FAPbBr_3$ NCs (Figure S2) consists of major peaks at $2\theta = 14.80°$, 21.1°, 29.96°, 33.50°, 37.93, 42.81°, and 45.52° corresponding to the crystal planes of (100), (110), (200), (210), (211), (220), and (300), respectively. These diffraction peaks correspond to the cubic phase of PeNCs with the Pm–3m space group as reported in the literature [308], [284]. In XRD patterns of $FAPbBr_3$ NCs–PLLA nanofibres, the peaks of perovskite appear at 29.96°, 33.50°, 42.81°, and 45.52° which correspond to the (200), (210), (220), and (300) planes of $FAPbBr_3$ NCs. Nevertheless, the diffraction peak intensity is very low due to the low concentration of FAPbBr3 NCs in the PLLA matrix, as well as the coverage effect of the PLLA matrix [304]. These peaks show slight shift towards lower angle as slightly larger NCs are formed compared to pristine ones. These findings show that high-quality $FAPbBr_3$ NCs have been successfully fabricated inside the PLLA matrix. These findings show that high-quality $FAPbBr_3$ NCs have been successfully fabricated inside the PLLA matrix.

5.4.3 Surface chemistry of the $FAPbBr_3$ NCs-PLLA nanofibres

Fourier transform infrared spectroscopy (FTIR) has been widely used to study the chemical changes and quantitative analysis of polymers and, also to investigate the functional groups of the attached molecules. In **Figure 5:*5***, FTIR spectra of PLLA nanofibres, $FAPbBr_3$ NCs, and $FAPbBr_3$ NCs-PLLA nanofibres are demonstrated. The spectrum shows bands at 2944 and 3000 cm^{-1} for PLLA, 2850 and 2924 cm^{-1} for PeNCs, and 2850 cm^{-1} for $FAPbBr_3$ NCs-PLLA nanofibres. These bands belong to the C-H stretch from CH_3. The presence of these stretching confirms the encapsulation of $FAPbBr_3$ NCs into the polymer matrix. Compared to PeNCs

bands at 3270 cm^{-1} for N-H stretching, there is negligible vibration for $FAPbBr_3$ NCs-PLLA. This is due to the lower amount of PeNCs and coverage effects of the PLLA polymer matrix as confirmed by the X-ray diffraction patterns of these samples. In addition, the bands at 1745 cm^{-1} for PLLA and $FAPbBr_3$ NCs-PLLA correspond to the C=O extending of the ester. For $FAPbBr_3$ NCs, the C=O stretch can be ascribed to the presence of oleic acid at the surface of perovskite NCs.

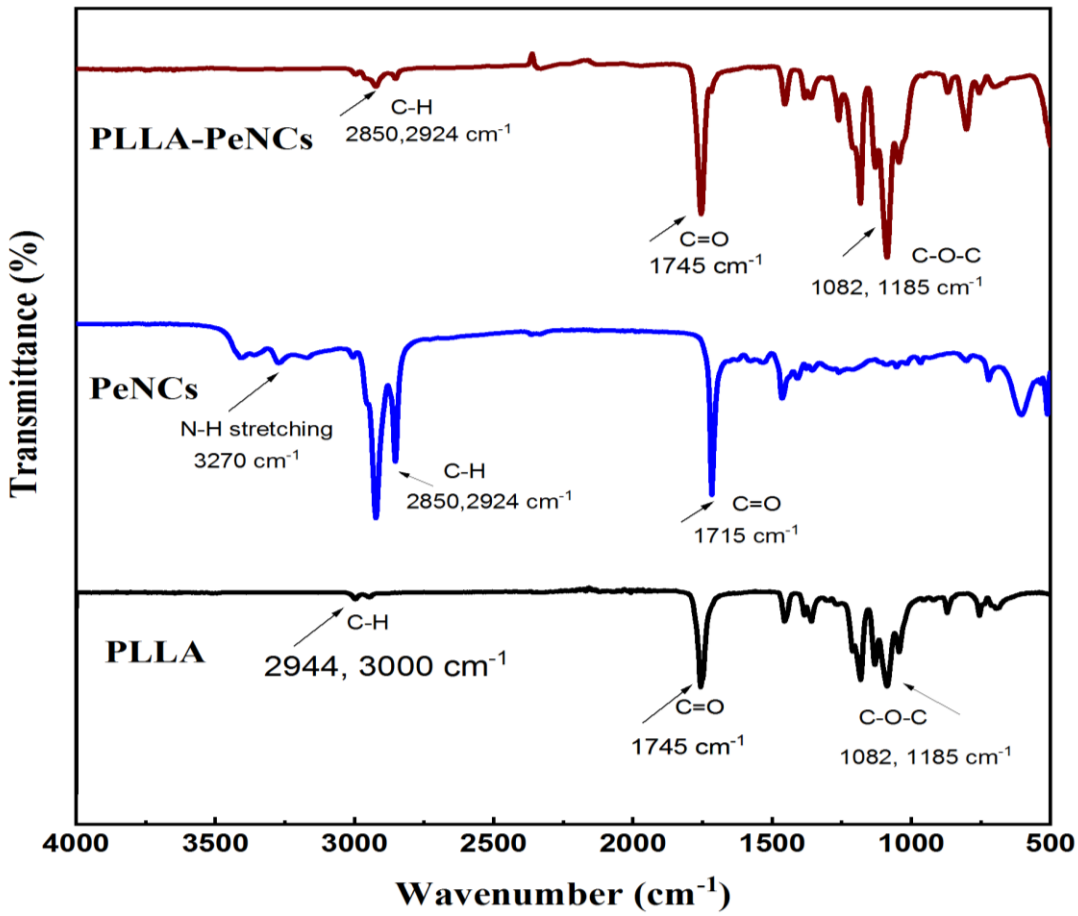

Figure 5:5: FTIR spectra of PLLA nanofibres, pure $FAPbBr_3$ NCs, and perovskite nanocrystals encapsulated by PLLA nanofibres.

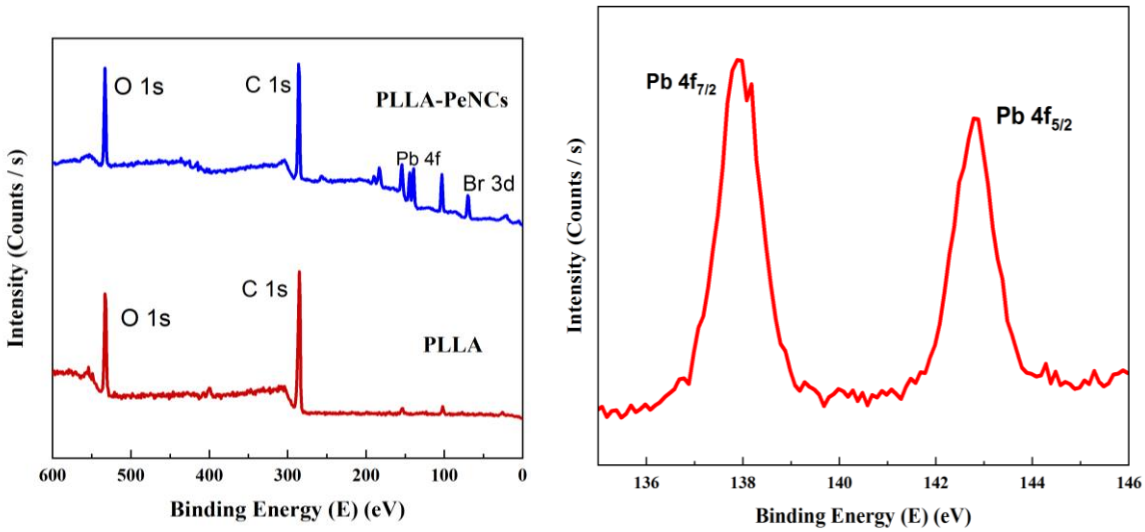

(**a**) (**b**)

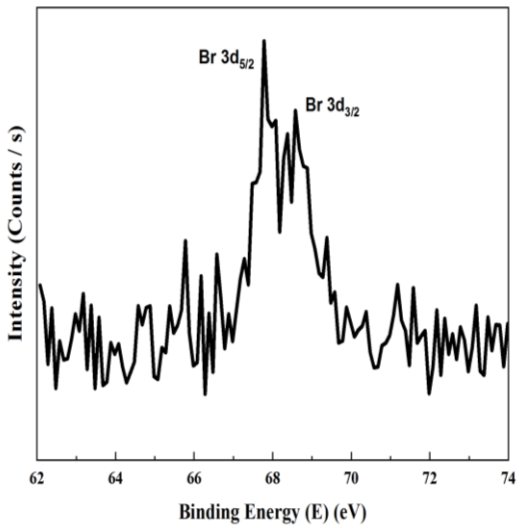

(**c**)

Figure 5:6: XPS analysis of (a) PLLA and PeNCs- PLLA nanofibres. (b-c) Pb 4f and Br 3d XPS spectra of composite nanofibres

X-ray photoelectron spectroscopy (XPS) is extensively employed to measure the binding energy and composition of constituents. As shown by the XPS spectra, it further confirms the

presence of Pb and Br in the PLLA matrix, suggesting the formation of $FAPbBr_3$ NCs inside the PLLA matrix. As can be seen in **Figure 5:*6***(a), elements of O (≈ 531 eV), C (≈ 284eV), Pb (≈ 143 and 138), and Br (≈ 69) were observed on the surface of $FAPbBr_3$ NCs-PLLA nanofibres. However, there is no obvious peak of elements of N (≈ 401 eV) present on the composite film, because of the lower concentration of PeNCs as confirmed by the XRD analysis. Regarding the Pb 4f and Br 3d spectra, the intrinsic peaks show the presence of encapsulated NCs inside the PLLA matrix (**Figure 5:*6***(b-c)). In addition, the measured binding energies of different elements (Pb 4f, Br 3d) were very similar to those of $FAPbBr_3$ NCs fabricated by other techniques.

5.4.4 Air and water stability of composite membranes

PeNCs can be embedded in a variety of polymers to fabricate nanocomposites that show an array of advantageous properties. The polymer matrix provides stability and flexibility while the PeNCs maintain their size, morphology, and composition-dependent characteristics. Polymers offer unique attributes, such as the ability to interact with the perovskites, low diffusion rates of moisture and oxygen, passivation of NCs surface defects, and decreased agglomeration of PeNCs in the solid state. The use of polymers provides strong chemical interaction with PeNCs, hence reducing the chances of moisture-induced degradation. Also, the morphology and shape of polymer-encapsulated NCs do not change and PL intensity decreases considerably slower [309].

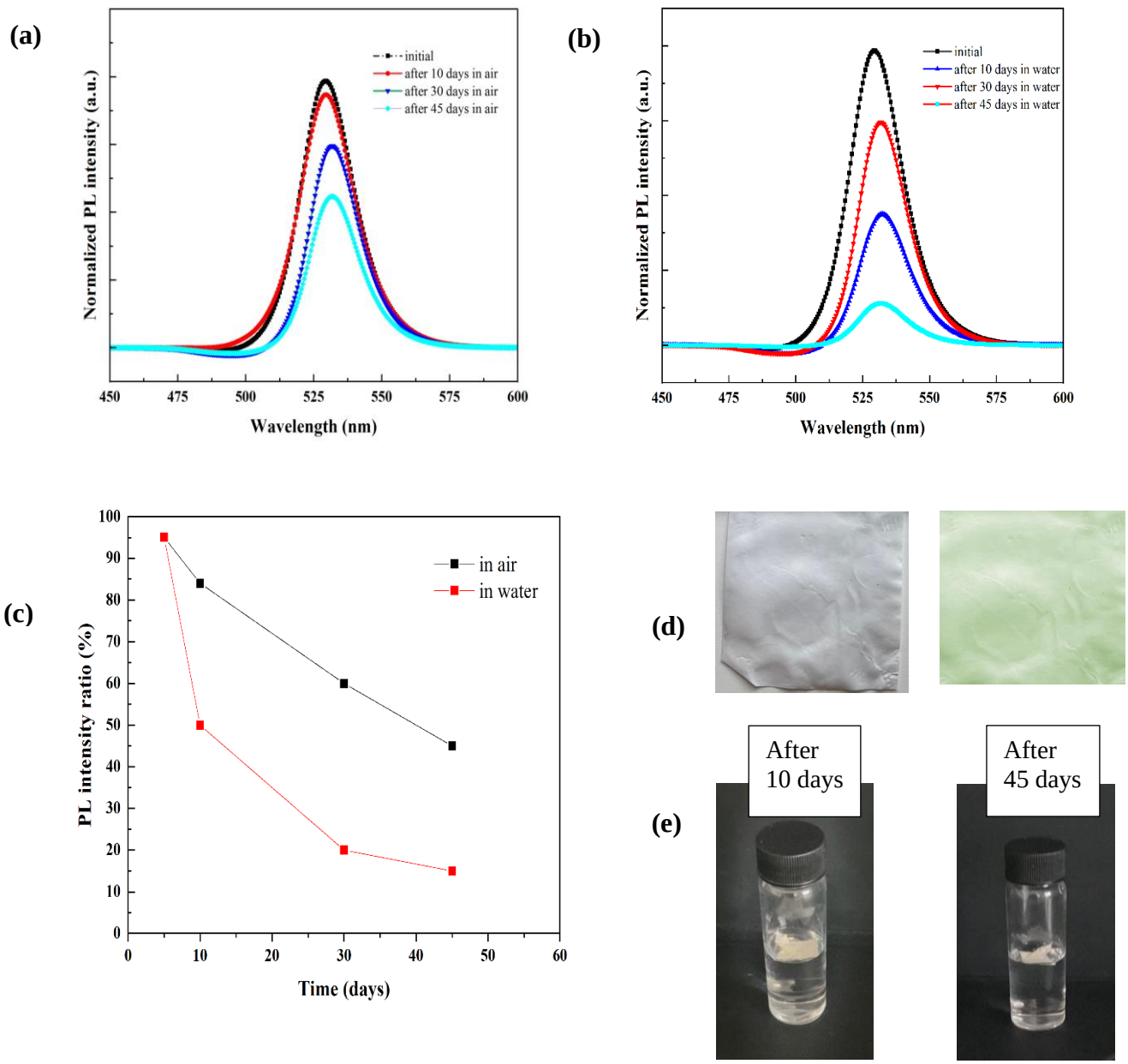

Figure 5:7: PL intensity variation spectra of $FAPbBr_3$ NCs-PLLA nanofibres with storage time (a) in air and (b) in water. (c) Summary of PL intensity ratio for the composite films as a function of storage time in air and water. (d) Photograps of PLLA nanofibres and $FAPbBr_3$ NCs-PLLA nanofibres. (e) Photographs of $FAPbBr_3$ NCs-PLLA nanofibres after immersion in water after 10 and 45 days.

Table 5:5.1: Comparison of the FAPbBr3 perovskite NCs incorporated in poly (L–lactic acid) nanofibers with some other materials.

Materials	Polymer used for encapsulation	Fabrication technique	Structure	PL intensity and stability parameters	Ref.
$MAPbBr_3$ NCs	PM NFs MA, PVDF	Electrospinning	Core-shell NFs	10 days in the air ≈ 93%	[299]
$CsPbBr_3$ NCs	PVP , PAN	Electrospinning	NFs	96 hr exposure in the air ≈73%	[306]
$CsPbX_3$ (X = Cl, Br, and I) QDs	PVP	Electrospinning	NFs	4 days in water for green emitters	[307]
$CsPbI_3$ QDs	PVDF	Electrospinning	NFs	3 days in water ≈ 80%	[302]
$CsPbX_3$ (X = Cl, Br, and I) NCs	PAN	Electrospinning	Core-shell NFs	48 hr in water ≈ 50%	[300]
$CsPbBr_3$ NCs	PVDF-PS	Electrospinning	NFs	70 days in water ≈ 90%	[310]
$CsPbX_3$ (X = Cl, Br, and I) QDs	PS, PMMA, poly(styrene-butadiene-styrene) (SBS)	Electrospinning	NFs	3 months in water ≈ 80%	[311]
$FAPbX_3$ (X = Cl, Br, and I) QDs	PS, PMMA	Microfluidic electrospinning	NFs	Consistent PL after 5 days immersion in water	[312]
$CsCu_2I_3$, $Cs_3Cu_2I_5$	PS	Electrospinning	NFs	Consistent PL after 20 days immersion in water	[313]
$FAPbBr_3$ NCs	PLLA	Electrospinning	NFs	45 days in the air ≈ 50%, 10 days in water ≈ 70%	

This section of the study was concerned with the stability of $FAPbBr_3$ NCs-PLLA nanofibrous films in water and air. The PL peak position and intensity were slightly changed after 10 days of storage in air (**Figure 5:7**a), which showed that composite films are extremely stable in air.

After 45 days of storage in ambient conditions, the PL peak intensity was still about 50% of its original value. Moreover, after 10 days of direct contact with water (**Figure 5:*7***b), the PL intensity still retained 70% of the original value. Also, there is a negligible shift in the PL peak of the $FAPbBr_3$ NCs-PLLA nanofibrous films after storage in air and water. The change in PL intensity value as a function of storage time in air and water was summarized in **Figure 5:*7***c. In **Figure 5:*7***d, e, the photographs of PLLA nanofibres, $FAPbBr_3$ NCs-PLLA nanofibrous films, and their water immersion is displayed.

A comparison of the most recent research studies available on the $FAPbBr_3$ PeNCs embedded into the polymers using the electrospinning method for water and air stability is summarized in **Table 5:5.1**. The encapsulation of PeNCs inside the PLLA nanofibres substantially enhances the stability against air and even under full immersion in water.

5.5 Conclusion

In summary, the first stable $FAPbBr_3$ NCs-PLLA electrospun composite films were prepared via ambient or room temperature conditions and tested for air and water stability. We established that this technique is simple, low cost, and robust to fabricate $FAPbBr_3$ NCs that are homogenously distributed into the PLLA polymer nanofibres. These PeNCs are effectively protected and exhibited similar stabilities against air and water stress as those mentioned in the previous studies. Moreover, more than 70% PL intensity is still maintained after 45 days of storage. The findings reported here shed new light on the use of biopolymers for optoelectronic applications including lasers, waveguides, and flexible energy harvesters. Also, the flexible nature of nanofibres films may open the door for the production of flexible and bendable optoelectronics. However, PeNCs-based composite films with tunable emissions in the visible

spectrum remain to be explored. Hence, this research will stimulate further study in the area of high-performance luminescence applications.

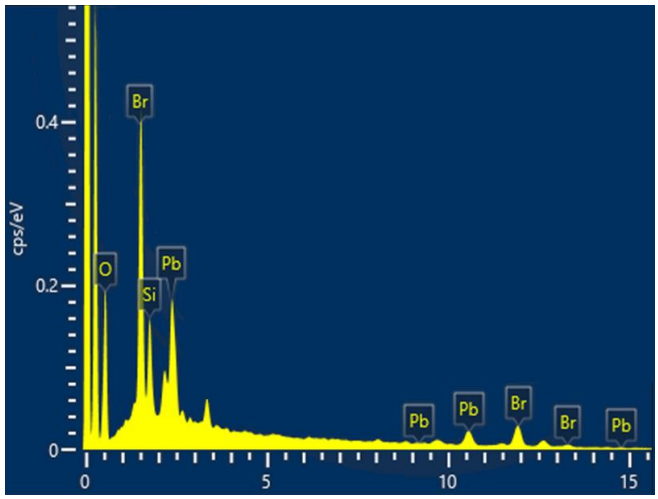

Figure S1: EDX analysis of $FAPbBr_3$ NCs-PLLA nanofibres

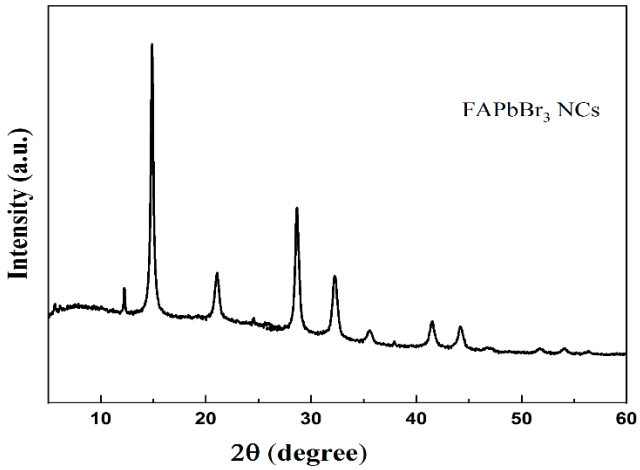

Figure S2: XRD pattern of $FAPbBr_3$ NCs

5.6 Preliminary Data

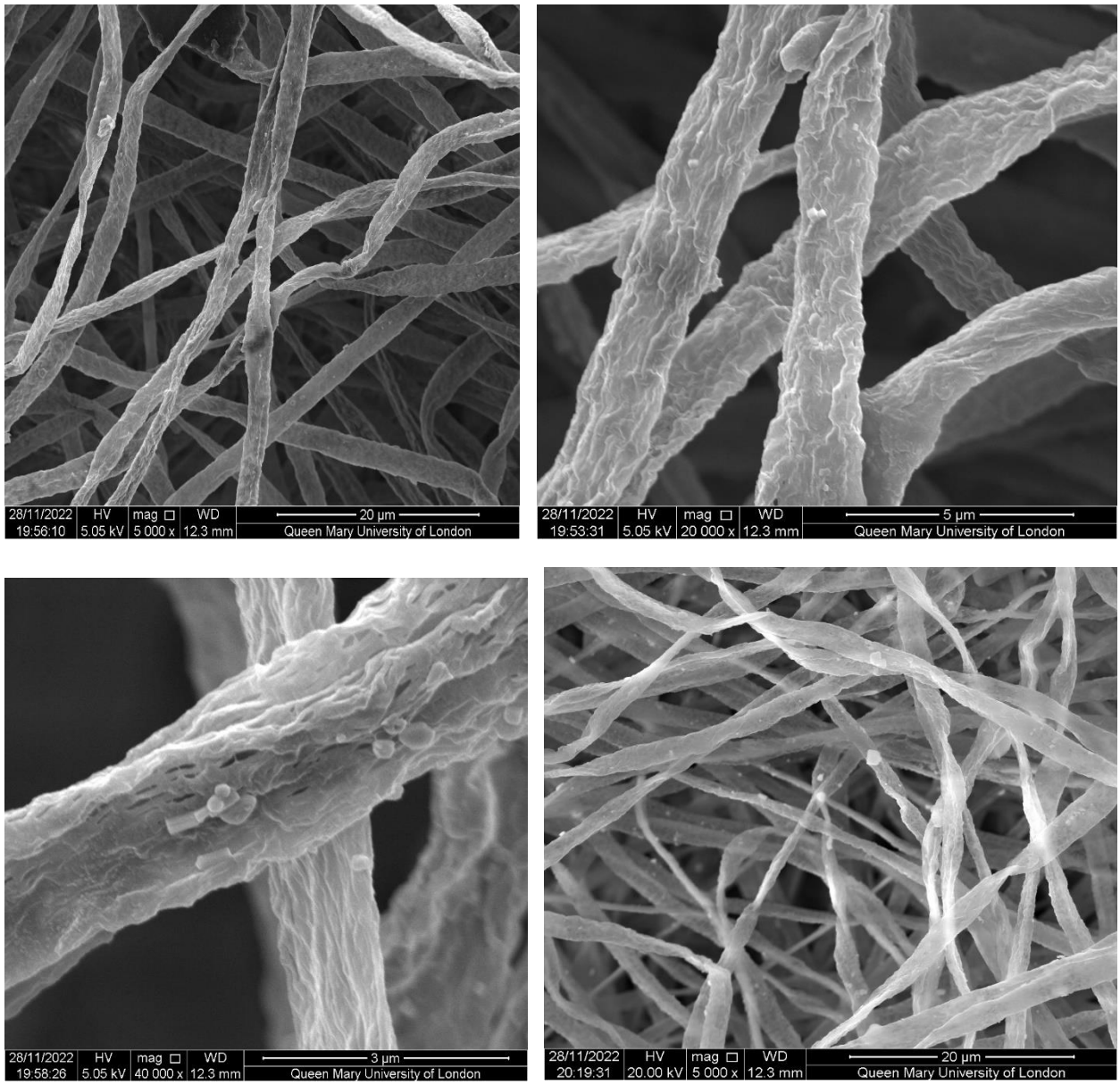

Figure 5:8: Trials images of Electrospun membranes.

Chapter 6 Hybrid organic-inorganic perovskite nanocrystals for flexible photoelectric applications

Abstract

Hybrid organic-inorganic perovskite nanostructures, such as formamidinium lead bromide ($FAPbBr_3$) nanocrystals (NCs) have been the subject of many applications including light-emitting devices, sensitive light detection, and piezoelectric energy harvesting [173], [314]. Flexible photoelectric devices based on halide perovskite NCs with excellent light-sensing performance and mechanical flexibility have been fabricated to achieve wearable/portable electronics [240], [315]**.** In this study, the ligand-assisted re-precipitation (LARP) method for the synthesis of $FAPbBr_3$ NCs and knitted polyester fabric was used as a flexible substrate. This nano-scale imaging using confocal laser scanning provides a fundamental understanding of the optical properties of the directly formed NCs in highly flexible knitted structures. Scanning electron microscopy was also performed to confirm the morphology of polyester-PeNCs. In addition, the highly flexible knitted polyester substrate coated with $FAPbBr_3$ NCs showed the diffraction peaks at $2\theta = 14.80°$, 29.96°, and 33.50° confirming the crystalline behavior of samples.

Keywords: Flexible substrates; Perovskite nanocrystals; Metal halide perovskites.

6.1 Introuction

Smart wearable electronics have received considerable attention because of stretchability and bendability for different body movements. Hybrid organic-inorganic perovskites have shown

great potential in wearable electronics due to the low-cost fabrication and advantage of extraordinary optoelectronic properties. Many research studies have been focused on optimizing the efficiency and high-performance of flexible perovskite-based photodetectors by using $MAPbI_3$ crystals coated on fibrous yarn bundles to form shape-adjustable devices [240]. For wearable electronic devices, mechanical flexibility and stress endurance are two important areas of merit. With this aim, we fabricated a fibrous flexible perovskite material by using a capillary effect of a PeNCs solution in hexane.

6.1.1 Experimental

6.1.2 Materials and Method

We report a ligand-assisted re-precipitation (LARP) method for the synthesis of $FAPbBr_3$ NCs by using FABr (0.1mm) and $PbBr_2$ (0.1mm), oleic acid, and oleylamine at ambient conditions. Then flexible substrate (knitted polyester fabric) was immersed in the NCs solution in hexane for 10 min, and the aforementioned specimen underwent further annealing at 80 °C for 30 min to completely evaporate the solvent. This is a simple and unique technique for the direct confinement of nano-sized functional materials inside continuous fibrous structures.

6.1.3 Characterizations

Local emission centres of embedded perovskite NCs in the flexible fibrous structures were successfully determined by confocal laser scanning microscopy. The FTIR spectra of $FAPbBr_3$ embedded in flexible fibers were recorded to reveal the basic functional groups. Scanning electron microscopy was used to record the morphology of as-prepared samples. The ultraviolet-visible (UV-Vis) spectrum was measured with the LAMBDA 35 PerkinElmer spectrometer.

6.2 Results and discussion

Figure 6:1a shows the schematic of PeNCs synthesis using the LARP method. **Figure 6:1**b shows the TEM images of the as-synthesized $FAPbBr_3$ PeNCs. The PeNCs crystallize which a cubic shape, monodispersed, with an average size of 10-12 nm. The PeNCs follow the typical perovskite structure ABX_3. We examined the optical properties of pristine polyester-PeNCs via UV absorption measurements as shown in **Figure 6:1c**. From the normalized UV-vis spectra, it demonstrated a strong light absorption edge at 514 nm.

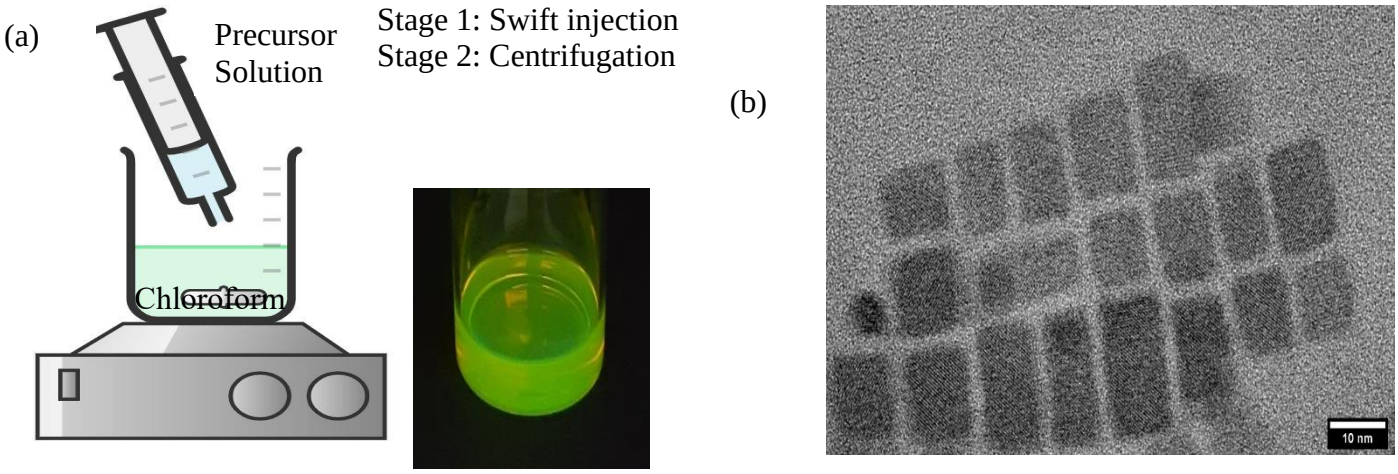

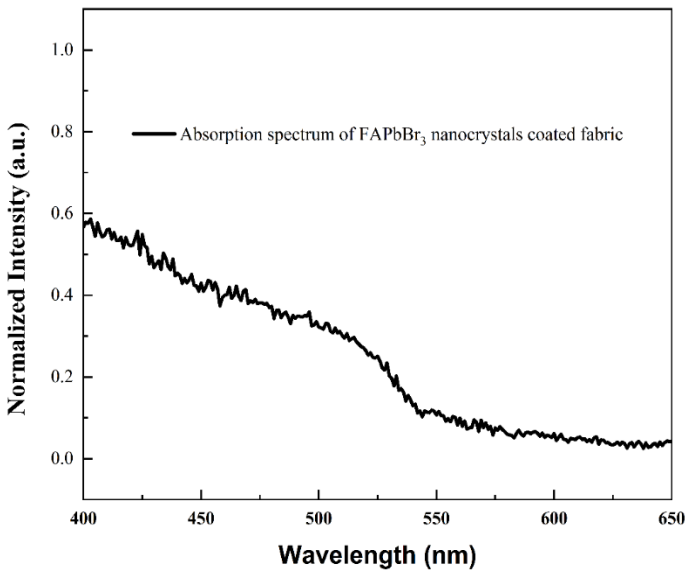

(c)

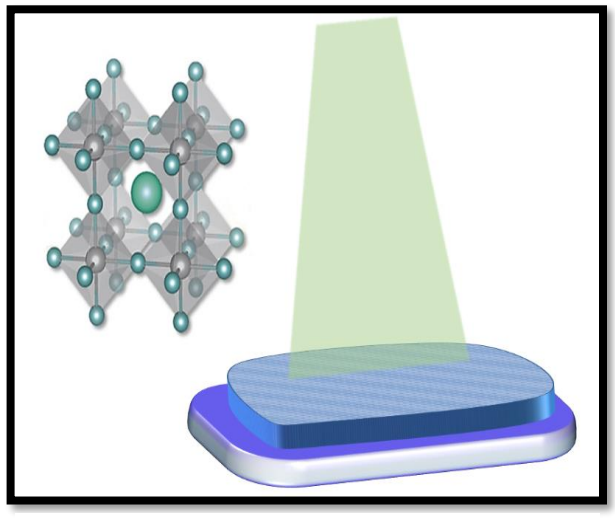

(d)

Figure 6:1. (a) Schematic diagram of synthesis of FAPbBr3 NCs. (b-c) UV-VIS absorption of polyester-PeNCs and TEM of $FAPbBr_3$ NCs, respectively (d) Schematic diagram of the photoelectric device using a FAPbBr3 NCs.

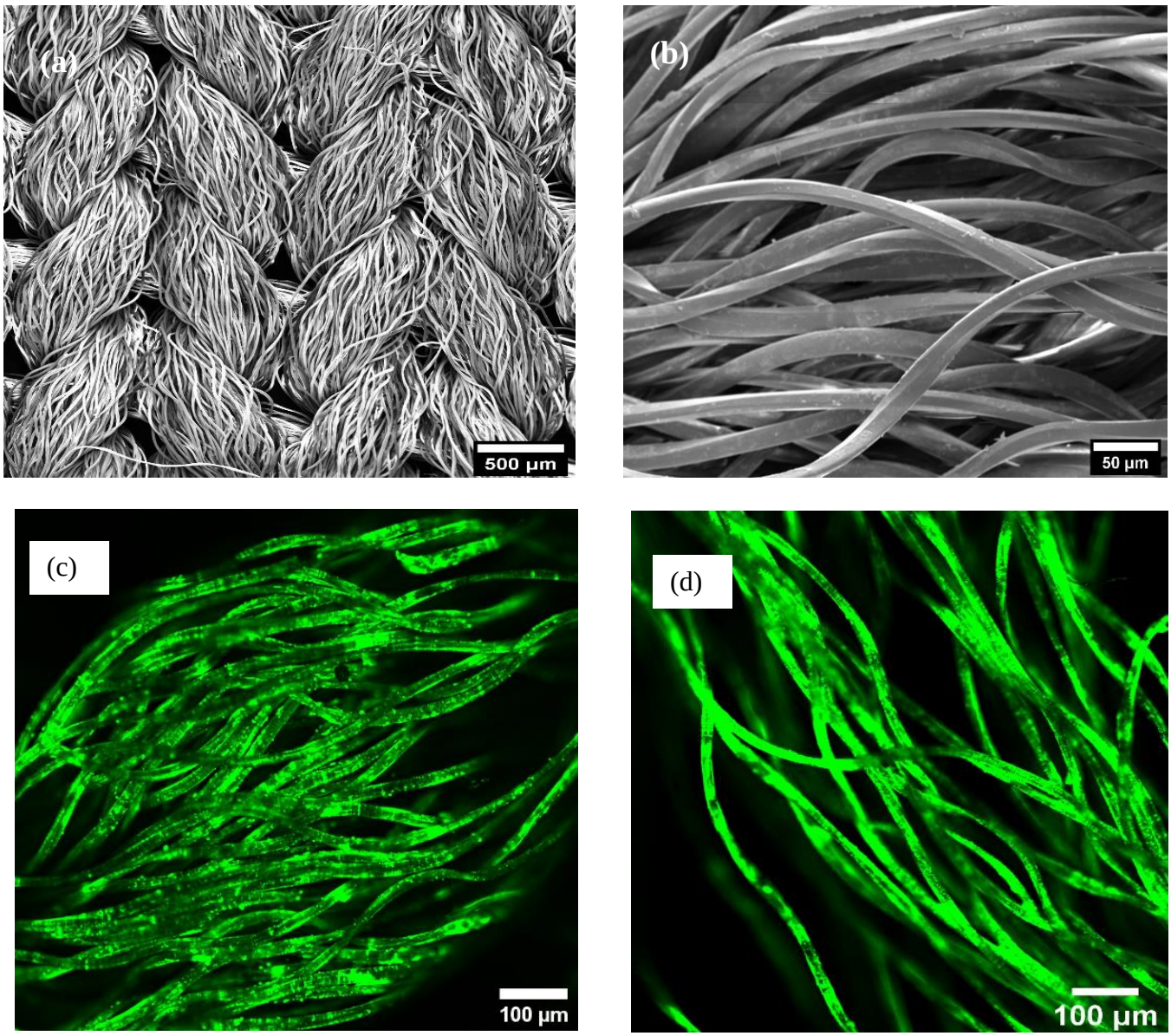

Figure 6:2. (a) SEM images of the polyester knitted structure. (b) SEM image of polyester-PeNCs sample. (c-d) Confocal fluorescence microphotographs of polyester-PeNCs with a 488 nm laser as the light source

Figure 6:1d depicts the schematic of perovskite-based photoelectric device.

Figure 6:2a presents the scanning electron microscopy (SEM) images of the polyester knitted structure, which show the flexible and spiral-like yarn structure. The structural characterization of the polyester knitted substrate coated with PeNCs reveals the smooth structure with the $FAPbBr_3$ NCs coated homogeneously on the surface of a flexible substrate as shown in **Figure 6:2b.**

Respective confocal fluorescence images exhibit strong PL emission **Figure 6:2**c, d.

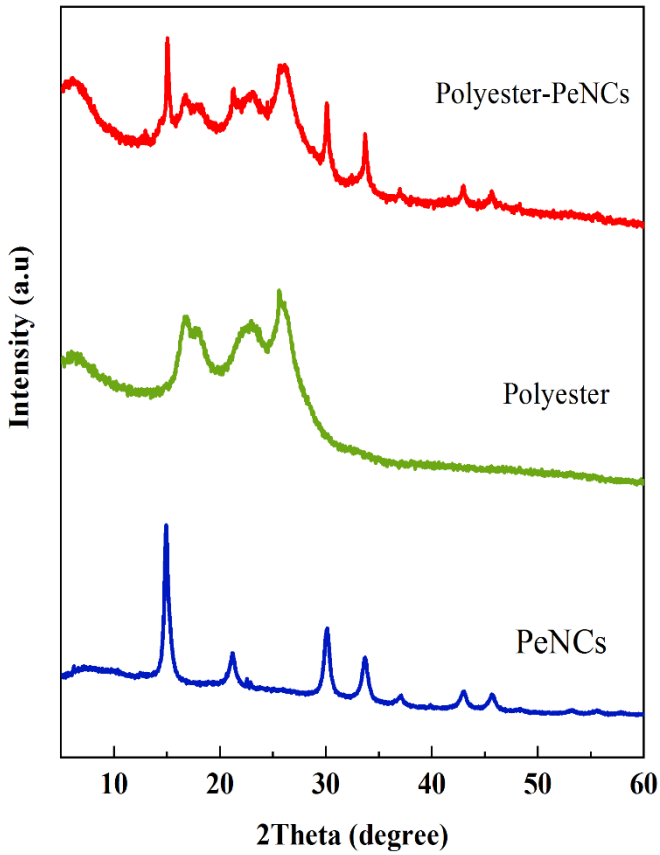

Figure 6:3. X-ray diffraction pattern of pure $FAPbBr_3$ NCs, polyester, and polyester-PeNCs samples.

In **Figure 6:*3***, X-ray diffraction (XRD) was recorded on samples of PeNCs, which were deposited by spin coating of the NC solution on the glass. The clean polyester knitted fabric was also provided to record the XRD peaks. For polyester-PeNCs, it was immersed in the NCs solution in hexane for 10 min, and the aforementioned specimen underwent further annealing at 80 °C for 30 min to completely evaporate the solvent.

Diffraction peaks located at 2θ = 17.9°, 22.8°, and 25.6° refer to the polyester knitted substrate. The diffractogram of PeNCs consists of major peaks at 2θ = 14.80°, 21.1°, 29.96°, 33.50°, 37.93, 42.81°, and 45.52° corresponding to the crystal planes of (100), (110), (200), (210), (211), (220), and (300), respectively. These diffraction peaks correspond to the cubic phase of PeNCs with the Pm–3m space group as reported in the literature [308], [284]. In XRD patterns of Polyester-PeNCs, the peaks of perovskite appear at 14.80°, 29.96°, 33.50°, 42.81°, and 45.52° which correspond to the (100), (200), (210), (220), and (300) planes of PeNCs. Nevertheless, the diffraction peak intensity is very low due to the low concentration of PeNCs on the surface of the polyester substrate [304]. These findings show that high-quality PeNCs have been successfully coated on the surface of the polyester substrate.

X-ray photoelectron spectroscopy (XPS) has been used to record the binding energy and composition of different elements. As shown by the XPS spectra, it further confirms the presence of Pb and Br in the polyester-PeNCs samples, suggesting the presence of $FAPbBr_3$ PeNCs on the surface of the flexible substrate. As can be seen in **Figure 6:4**a, elements of O (≈ 531 eV), C (≈ 284eV), Pb (≈ 143 and 138), and Br (≈ 69) were observed on the surface of polyester-PeNCs. However, there is slight vibration to show the peak of elements of N (≈ 401

eV) present on the polyester substrate, because of the small amount of PeNCs as confirmed by the XRD analysis. Regarding the Pb 4f spectra (**Figure 6:4**b), the intrinsic peaks show the presence of coated NCs on the surface of the used substrate.

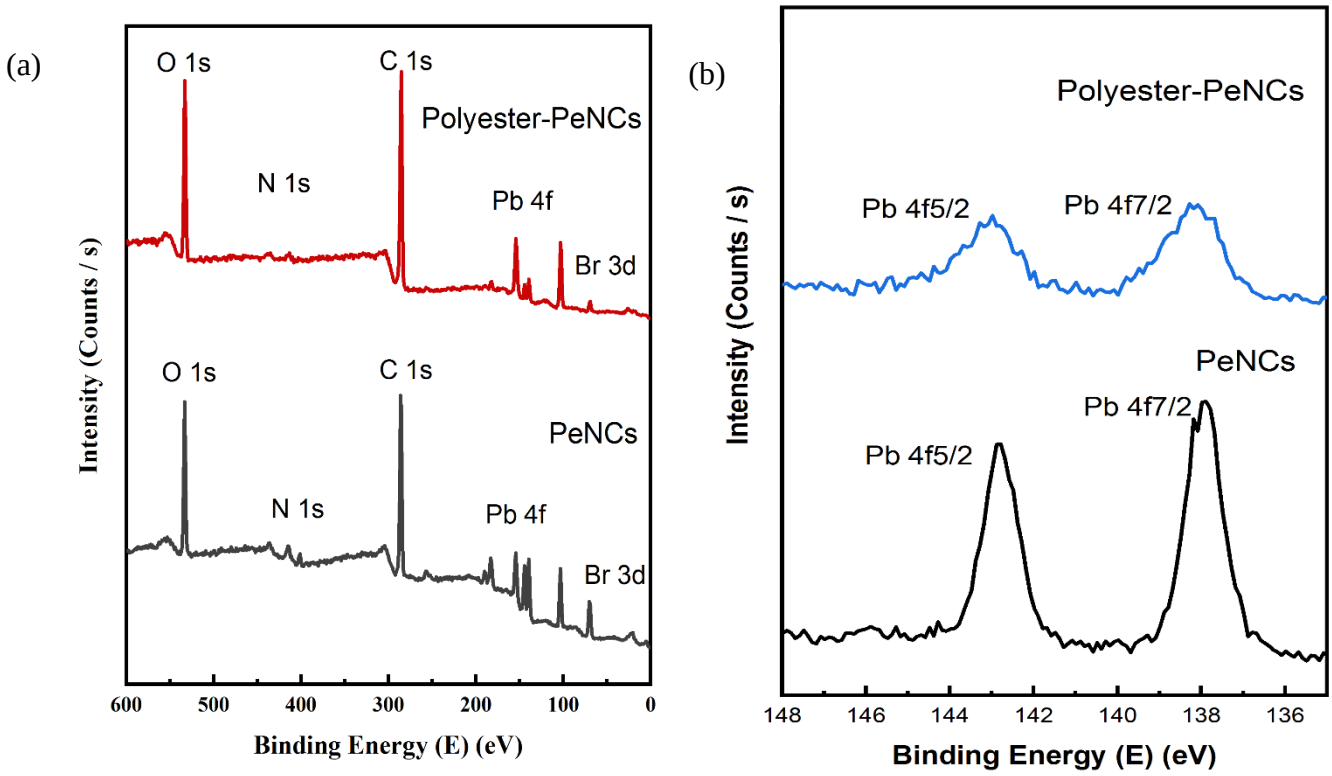

Figure 6:4. (a) XPS analysis of (a) PeNCs and polyester-PeNCs. (b) Pb 4f spectra of composite flexible structure

In **Figure 6:5**, FTIR spectra of PeNCs and polyester coated PeNCs are demonstrated.

The spectrum shows band 1716 for polyester, 2850 and 2924 cm^{-1} for PeNCs, and 2854 and 2926 cm^{-1} for polyester-PeNCs.

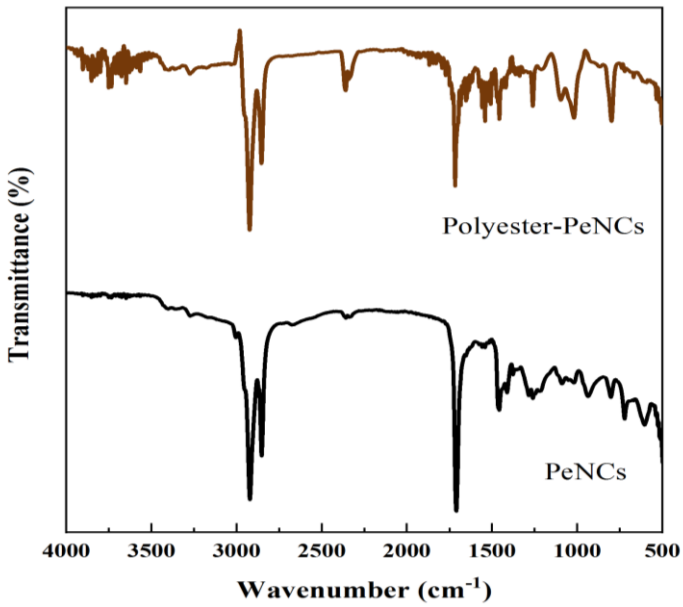

Figure 6:5. FTIR spectra of PeNCs and polyester coated PeNCs.

Device characterization

A prototype photodetector device (Figure 6***:6***a) was developed by using gold wire (electrode) stitched into polyester-PeNCs and electric characteristics were examined. This device consists of Au (gold wire electrode)/ $FAPbBr_3$ NCs (light absorption layer) / knitted polyester fabric (spiral like yarn structures) with distance between two electrodes is 2mm.

The I-V curves (Figure 6***:6***b) in dark depicts a typical linear current-voltage behaviour with increasing bias, which demonstrates that an ohmic contact is formed between the PeNCs and the Au electrode. The outcome of this test shows that perovskite structures formed good coordination, which provides good routes for charge carriers. In addition, in the dark the device exhibits a very small current on the order of nanoamperes. To fully unlock the full potential of this device, several experiments including I-V curves upon light illumination with different power densities, time-dependent photocurrent response, response speed of device with light

switched ON and OFF, and photoresponsivity and detectivity as a function of light power density can be explored.

(a)

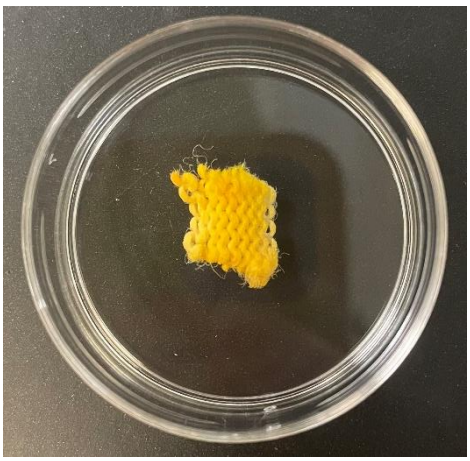

(b)

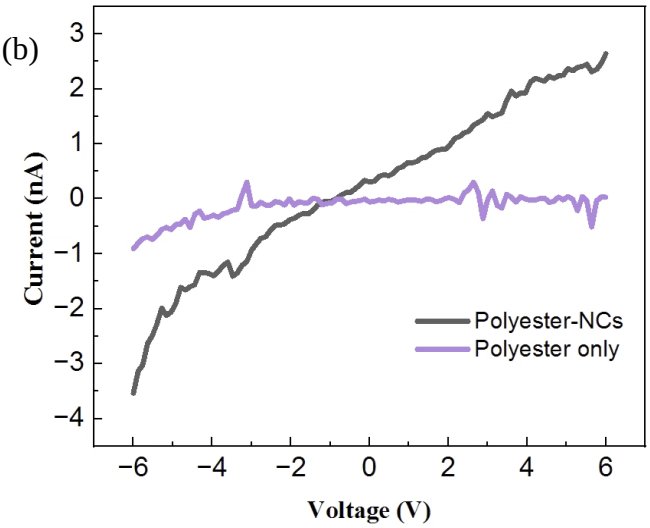

Figure 6:6: (a) Photograph of the device (b) I-V characteristics in dark.

6.3 Conclusion

In conclusion, we synthesized perovskite nanocrystals based polyester knitted structures. When the substrate is soaked in the NCs solution, the PeNCs are confined on the surface of the knitted yarn bundles. Accordingly, fibrous perovskite materials with controllable shapes and dimensions are obtained by simple fabrication techniques.

Chapter 7 Conclusions and Future work

Metal halide perovskites (MHP) have received considerable attention in optoelectronic devices due to their high optical absorption coefficient, efficient charge carrier mobility, high photoluminescence quantum yield (PLQY), and low-cost solution fabrication techniques. MHP has been considered important materials by a growing body of research community due to their application in solar cells, light-emitting diodes (LEDs), photodetectors (PDs), lasers, and nonlinear optics [166].

This research study summarizes the impact of alkali metal ions on charge carrier dynamics, crystallinity, bulk and interface defects, and their ability to influence optoelectronic device properties of HPM. In addition, advancements in wearable perovskite devices (e.g., solar cells, photodetectors, and light-emitting diodes) concerning their device architectures, working mechanisms, and fabrication techniques have been discussed. This study also highlights the technical benefits of integrating MHPs into wearable devices. Moreover, the application challenges faced by wearable perovskite optoelectronic devices-from single devices to roll-to-roll manufacturing, stability, storage, and biosafety-are briefly discussed.

First of all, a focused study was conducted for the fabrication of Cs and Rb cations passivated $MAPbBr_3$ perovskite NCs via the LARP method. The alkali metal ions doping replaces the MA cations and affects the crystal lattice of $MAPbBr_3$, hence tuning the optical properties of $MAPbBr_3$ PeNCs in turn. The results of this study have shown that there are no significant changes in the morphology of PeNCs, whereas alkali metal ions doped PeNCs show a reduction in size due to crystal lattice contraction. We found that PL intensity increases to a higher value

with Rb cations doping than that with Cs due to the more tolerance of the PeNCs for higher doping of smaller-size alkali metal ions. These findings describe an advancement in understanding the chemistry and structural stability of perovskite NCs essential for various optoelectronic applications. Considerably more work will need to be done to determine the long-term effects of alkali metal ions treatments for halide PeNCs.

Afterwards, the alkali metal ions doped $FAPbBr_3$ perovskite NCs with green emission were synthesized by ligand-assisted reprecipitation method under room temperature to reduce the surface defects. This strategy of K^+/Rb^+ was demonstrated to improve the PL emission intensity and colloidal stability of the perovskite NCs. The chemical bonding of K^+ with the halide ions in the solution of NCs to form an inorganic ligand capped outside the NCs surface can help to passivate the surface defects in the form of KBr which inhibit the halide phase segregation, contributing to stronger radiative recombination. Furthermore, the K^+ entered the interstitial position of the NCs structure, which increases the structural rigidity and limits the dissociation of perovskite NCs, representing remarkable stability for commercial use. The Rb^+ cations tend to form the non-perovskite phase of $RbPbBr_3$ with an average lifetime of 35.2ns compared to 62.5ns of K^+ samples.

In another study, the first stable $FAPbBr_3$ NCs-PLLA electrospun composite films were prepared via ambient or room temperature conditions and tested for air and water stability. We established that this technique is simple, low cost, and robust to fabricate $FAPbBr_3$ NCs that are homogenously distributed into the PLLA polymer nanofibres. These PeNCs are effectively protected and exhibited similar stabilities against air and water stress as those mentioned in the previous studies. Moreover, more than 70% PL intensity is still maintained after 45 days of storage.

Moreover, another small-scale study for the synthesis of perovskite nanocrystals-based polyester knitted structures. When the substrate is soaked in the NCs solution, the PeNCs are confined on the surface of the knitted yarn bundles. Accordingly, fibrous perovskite materials with controllable shapes and dimensions are obtained by simple fabrication techniques.

In conclusion, different strategies have been reported for the passivation of PeNCs surface defects and extensively study their surface chemistry.

Future work

In the recent Consumer Electronic Show 2023, many companies exhibited their boldest and most innovative ideas for advanced display or lighting technologies, providing an opportunity for the future development of perovskite-based devices. For instance, Samsun and LG companies showed a series of large-scale, flexible, and self-lighting display devices. Macroblock company presented the use of LEDs for head-up displays in modern cars, which shows high brightness characteristics in outdoor environments. Carmaker of Audi revealed the car headlight for the interactive human experience by smart lighting and imaging. Meeting consumer demands and recent developments of advanced electronics, perovskite nanocrystals have great potential in wide colour gamut backlighting and high-resolution full-colour display.

However, considering the use of perovskite nanocrystals on large-scale, three main obstacles still exist to restrict their practical application. First is the batch manufacturing methods. Though the fabrication of PeNCs is simple to industrialize, and they show great compatibility with different methods including spin-coating, and roll-to-roll techniques, all reports are still conducted in labs. Taking PeLEDs as an example, the cost is estimated as 2533 lm per $, which is much higher than those of other technologies. Second is the structural and emission stability. Currently, the lifetime of the perovskite-based device varies from less than an hour to hundreds,

which is far behind the commercial goals. Third is environmental protection. It is expected for electronic devices generate metal or non-biodegradable pollutants to the natural environment, and heavy metal-based devices are strictly limited by many countries. All perovskite-based NCs contain elements of the lead family, which increase the risks of bringing danger to the human nervous, cardiovascular, skeleton, reproductive, and immune systems. The development of lead-free PeNCs and their devices are necessary, which also need to be focused.

Looking forward, to fully exploring the potential benefits of doping with various metal ions in perovskites, considerably more research work will need to be done for unexplored transition and inner transition metals. One of the open and important questions is to find the exact location of alkali metal ions, the influence of doping on crystal orientation, and the principle behind the improved optoelectronic properties**.** Considerably more work will need to be done to determine the long-term effects of doped metal ions for halide PeNCs. Moreover, recent studies have shown that surface defects that appeared by the detachment of ligands can severely reduce the PLQY. Therefore, it shows that the nature of surface traps is not fully explored. The type and nature of surface traps created by the detachment of ligands need to be assessed.

For metal halide perovskite NCs, photoluminescence intermittency known as “blinking” is another important phenomenon that requires further understanding. This restricts the application of these materials in quantum optical devices. Several studies have been reported to explain how blinking occurs. These include the effects of photocurrent and Auger recombination or the effects of nonradiative recombination centres that could be metastable. However, further research work is needed to understand how these defects could be activated or deactivated, and whether light could play a role.

In addition, multidisciplinary collaboration is required to improve the performance, ambient stability, and biosafety to produce flexible and wearable perovskite devices at a large-scale. In the future, further experimental investigations will enable wearable perovskite devices to come into daily life. Driven by the advancement of perovskites in textile-based solar cells, photodetectors, and light-emitting diodes, further research could also be conducted to explore the effectiveness of perovskites for other wearable devices such as X-ray detectors, etc.

References

[1] W. G. Brooks, “Optoelectronics: Emerging Technology Focused on Light-detecting Devices,” 2020. [Online]. Available: https://blog.ttelectronics.com/optoelectronics.

[2] H. Fujiwara, *Hybrid Perovskite Solar Cells Characteristics and Operation*. John Wiley & Sons, 2022.

[3] Solar Energy Technologies Office, “Perovskite Solar Cells,” 2019. [Online]. Available: https://www.energy.gov/eere/solar/perovskite-solar-cells.

[4] S. Thomas and A. Thankappan, *Perovskite photovoltaics: Basic to advanced concepts and implementation*. 2018.

[5] Oxford PV, “Oxford PV hits new world record for solar cell,” 2020. [Online]. Available: https://www.oxfordpv.com/news/oxford-pv-hits-new-world-record-solar-cell.

[6] L. Zhang *et al.*, “High-performance quasi-2D perovskite light-emitting diodes: from materials to devices,” *Light: Science and Applications*. 2021, doi: 10.1038/s41377-021-00501-0.

[7] A. Dey *et al.*, “State of the Art and Prospects for Halide Perovskite Nanocrystals,” *ACS Nano*, vol. 15, no. 7, pp. 10775–10981, 2021, doi: 10.1021/acsnano.0c08903.

[8] Y. Zou, Z. Yuan, S. Bai, F. Gao, and B. Sun, “Recent progress toward perovskite light-emitting diodes with enhanced spectral and operational stability,” *Mater. Today Nano*, vol. 5, p. 100028, 2019, doi: 10.1016/j.mtnano.2019.100028.

[9] K. Wang *et al.*, “Metal Cations in Efficient Perovskite Solar Cells: Progress and Perspective,” *Adv. Mater.*, 2019, doi: 10.1002/adma.201902037.

[10] F. Rahimi, A. K. Jafari, C. A. Hsu, C. S. Ferekides, and A. M. Hoff, “Selective sensing in perovskite-based Image Sensors,” *Org. Electron.*, vol. 75, 2019, doi: 10.1016/j.orgel.2019.105397.

[11] S. Shyamal and N. Pradhan, “Halide Perovskite Nanocrystal Photocatalysts for

CO2Reduction: Successes and Challenges," *J. Phys. Chem. Lett.*, vol. 11, no. 16, 2020, doi: 10.1021/acs.jpclett.0c00191.

[12] V. Nguyen, H. Katsuki, F. Sasaki, and H. Yanagi, "Single-crystal perovskite CH3NH3PbBr3 prepared by cast capping method for light-emitting diodes," vol. 10, pp. 2–5, 2018.

[13] Z. K. Tan *et al.*, "Bright light-emitting diodes based on organometal halide perovskite," *Nat. Nanotechnol.*, vol. 9, no. 9, pp. 687–692, 2014, doi: 10.1038/nnano.2014.149.

[14] Y. Shen *et al.*, "High-Efficiency Perovskite Light-Emitting Diodes with Synergetic Outcoupling Enhancement," *Adv. Mater.*, 2019, doi: 10.1002/adma.201901517.

[15] P. N. Rudd and J. Huang, "Metal Ions in Halide Perovskite Materials and Devices," *Trends Chem.*, vol. 1, no. 4, pp. 394–409, 2019, doi: 10.1016/j.trechm.2019.04.010.

[16] Y. Fu, H. Zhu, J. Chen, M. P. Hautzinger, X. Y. Zhu, and S. Jin, "Metal halide perovskite nanostructures for optoelectronic applications and the study of physical properties," *Nat. Rev. Mater.*, vol. 4, no. 3, pp. 169–188, 2019, doi: 10.1038/s41578-019-0080-9.

[17] C. H. Lu, G. V. Biesold-Mcgee, Y. Liu, Z. Kang, and Z. Lin, "Doping and ion substitution in colloidal metal halide perovskite nanocrystals," *Chem. Soc. Rev.*, vol. 49, no. 14, pp. 4953–5007, 2020, doi: 10.1039/c9cs00790c.

[18] Q. Zhang, Y. Yin, and Y. Yin, "All-Inorganic Metal Halide Perovskite Nanocrystals: Opportunities and Challenges," *ACS Cent. Sci.*, vol. 4, pp. 668–679, 2018, doi: 10.1021/acscentsci.8b00201.

[19] M. Liu *et al.*, "Manganese Doping Promotes the Synthesis of Bismuth-based Perovskite Nanocrystals While Tuning Their Band Structures," *Small*, 2021, doi: 10.1002/smll.202100101.

[20] M. Liu *et al.*, "B-Site Co-Alloying with Germanium Improves the Efficiency and Stability of All-Inorganic Tin-Based Perovskite Nanocrystal Solar Cells," *Angew.*

Chemie, 2020, doi: 10.1002/ange.202008724.

[21] Q. Wali, F. J. Iftikhar, M. E. Khan, A. Ullah, Y. Iqbal, and R. Jose, "Advances in stability of perovskite solar cells," *Org. Electron.*, vol. 78, no. December 2019, p. 105590, 2020, doi: 10.1016/j.orgel.2019.105590.

[22] G. Grancini and M. K. Nazeeruddin, "Dimensional tailoring of hybrid perovskites for photovoltaics," *Nature Reviews Materials*. 2019, doi: 10.1038/s41578-018-0065-0.

[23] C. C. Vidyasagar, B. M. Muñoz Flores, and V. M. Jiménez Pérez, "Recent Advances in Synthesis and Properties of Hybrid Halide Perovskites for Photovoltaics," *Nano-Micro Letters*. 2018, doi: 10.1007/s40820-018-0221-5.

[24] D. Zhou, T. Zhou, Y. Tian, X. Zhu, and Y. Tu, "Perovskite-Based Solar Cells: Materials, Methods, and Future Perspectives," *Journal of Nanomaterials*. 2018, doi: 10.1155/2018/8148072.

[25] T. Dai *et al.*, "Strategies for high-performance large-area perovskite solar cells toward commercialization," *Crystals*, 2021, doi: 10.3390/cryst11030295.

[26] Y. Zhou, J. Chen, O. M. Bakr, and H. T. Sun, "Metal-Doped Lead Halide Perovskites: Synthesis, Properties, and Optoelectronic Applications," *Chemistry of Materials*. 2018, doi: 10.1021/acs.chemmater.8b02989.

[27] A. L. Abdelhady *et al.*, "Heterovalent Dopant Incorporation for Bandgap and Type Engineering of Perovskite Crystals," *J. Phys. Chem. Lett.*, 2016, doi: 10.1021/acs.jpclett.5b02681.

[28] T. S. Sherkar *et al.*, "Recombination in Perovskite Solar Cells: Significance of Grain Boundaries, Interface Traps, and Defect Ions," *ACS Energy Lett.*, 2017, doi: 10.1021/acsenergylett.7b00236.

[29] P. Zhao, B. J. Kim, and H. S. Jung, "Passivation in perovskite solar cells: A review," *Materials Today Energy*. 2018, doi: 10.1016/j.mtener.2018.01.004.

[30] F. Wang, S. Bai, W. Tress, A. Hagfeldt, and F. Gao, “Defects engineering for high-performance perovskite solar cells,” *npj Flexible Electronics*. 2018, doi: 10.1038/s41528-018-0035-z.

[31] S. Das Adhikari, S. K. Dutta, A. Dutta, A. K. Guria, and N. Pradhan, “Chemically Tailoring the Dopant Emission in Manganese-Doped CsPbCl3 Perovskite Nanocrystals,” *Angew. Chemie - Int. Ed.*, 2017, doi: 10.1002/anie.201703863.

[32] W. J. Mir, M. Jagadeeswararao, S. Das, and A. Nag, “Colloidal Mn-doped cesium lead halide perovskite nanoplatelets,” *ACS Energy Lett.*, 2017, doi: 10.1021/acsenergylett.6b00741.

[33] F. Meinardi *et al.*, “Doped Halide Perovskite Nanocrystals for Reabsorption-Free Luminescent Solar Concentrators,” *ACS Energy Lett.*, 2017, doi: 10.1021/acsenergylett.7b00701.

[34] X. Zhang, L. Li, Z. Sun, and J. Luo, “Rational chemical doping of metal halide perovskites,” *Chem. Soc. Rev.*, vol. 48, no. 2, pp. 517–539, 2019, doi: 10.1039/c8cs00563j.

[35] Z. Yang *et al.*, “Anchored Ligands Facilitate Efficient B-Site doping in metal halide perovskites,” *J. Am. Chem. Soc.*, 2020, doi: 10.1021/jacs.9b02565.

[36] Y. Cai *et al.*, “Tuning the A-site cation and X-site anion composition of CH3NH3PbI3 perovskite material for efficient planar perovskite solar cells,” *Electrochim. Acta*, 2019, doi: 10.1016/j.electacta.2018.10.034.

[37] B. Luo *et al.*, “B-Site doped lead halide perovskites: Synthesis, band engineering, photophysics, and light emission applications,” *Journal of Materials Chemistry C*. 2019, doi: 10.1039/c8tc05741a.

[38] A. Swarnkar, W. J. Mir, and A. Nag, “Can B-Site Doping or Alloying Improve Thermal- and Phase-Stability of All-Inorganic CsPbX3 (X = Cl, Br, I) Perovskites?,” *ACS Energy*

Lett., 2018, doi: 10.1021/acsenergylett.7b01197.

[39] L. Xu, S. Yuan, H. Zeng, and J. Song, "A comprehensive review of doping in perovskite nanocrystals/quantum dots: evolution of structure, electronics, optics, and light-emitting diodes," *Mater. Today Nano*, vol. 6, 2019, doi: 10.1016/j.mtnano.2019.100036.

[40] J. Kim, A. Ho-Baillie, and S. Huang, "Review of Novel Passivation Techniques for Efficient and Stable Perovskite Solar Cells," *Solar RRL*. 2019, doi: 10.1002/solr.201800302.

[41] C. J. Bartel *et al.*, "New tolerance factor to predict the stability of perovskite oxides and halides," *arXiv*, pp. 1–10, 2018.

[42] T. Sato, S. Takagi, S. Deledda, B. C. Hauback, and S. I. Orimo, "Extending the applicability of the Goldschmidt tolerance factor to arbitrary ionic compounds," *Sci. Rep.*, vol. 6, no. April, pp. 1–10, 2016, doi: 10.1038/srep23592.

[43] T. T. Ava, A. Al Mamun, S. Marsillac, and G. Namkoong, "A review: Thermal stability of methylammonium lead halide based perovskite solar cells," *Applied Sciences (Switzerland)*, vol. 9, no. 1. 2019, doi: 10.3390/app9010188.

[44] T. J. Whitcher *et al.*, "Dual phases of crystalline and electronic structures in the nanocrystalline perovskite CsPbBr3," *NPG Asia Mater.*, vol. 11, no. 1, 2019, doi: 10.1038/s41427-019-0170-6.

[45] P. Wang *et al.*, "Synthesis and characterization of mn-doped cspb(Cl/Br)3 perovskite nanocrystals with controllable dual-color emission," *RSC Adv.*, vol. 8, no. 4, 2018, doi: 10.1039/c7ra13306e.

[46] R. X. Yang, J. M. Skelton, E. L. Da Silva, J. M. Frost, and A. Walsh, "Spontaneous octahedral tilting in the cubic inorganic cesium halide perovskites CsSnX3 and CsPbX3 (X = F, Cl, Br, I)," *J. Phys. Chem. Lett.*, vol. 8, no. 19, 2017, doi: 10.1021/acs.jpclett.7b02423.

[47] T. Chen *et al.*, “Entropy-driven structural transition and kinetic trapping in formamidinium lead iodide perovskite,” *Sci. Adv.*, vol. 2, no. 10, 2016, doi: 10.1126/sciadv.1601650.

[48] H. Ying *et al.*, “Surfactant-assisted doctor-blading-printed FAPbBr3 films for efficient semitransparent perovskite solar cells,” *Front. Optoelectron.*, vol. 13, no. 3, 2020, doi: 10.1007/s12200-020-1031-1.

[49] S. A. Michael Grätzel, Samrana Kazim, Ed., *Perovskite Solar Cells: Materials, Processes, and Devices.* 2022.

[50] C. Li, X. Lu, W. Ding, L. Feng, Y. Gao, and Z. Guo, “Formability of ABX 3 (X = F, Cl, Br, I) halide perovskites,” *Acta Crystallogr. Sect. B Struct. Sci.*, 2008, doi: 10.1107/S0108768108032734.

[51] G. Kieslich, S. Sun, and A. K. Cheetham, “An extended Tolerance Factor approach for organic-inorganic perovskites,” *Chem. Sci.*, 2015, doi: 10.1039/c5sc00961h.

[52] Y. Fu *et al.*, “Incorporating Large A Cations into Lead Iodide Perovskite Cages: Relaxed Goldschmidt Tolerance Factor and Impact on Exciton-Phonon Interaction,” *ACS Cent. Sci.*, 2019, doi: 10.1021/acscentsci.9b00367.

[53] Q. Chen *et al.*, “Under the spotlight: The organic-inorganic hybrid halide perovskite for optoelectronic applications,” *Nano Today*. 2015, doi: 10.1016/j.nantod.2015.04.009.

[54] S. N. Van-Huy Nguyen, Dai-Viet Vo, Ed., *Nanostructured Photocatalysts From Fundamental to Practical Applications*. Elsevier Science, 2021.

[55] F. Zhang *et al.*, “Brightly luminescent and color-tunable colloidal CH3NH3PbX3 (X = Br, I, Cl) quantum dots: Potential alternatives for display technology,” *ACS Nano*, vol. 9, no. 4, pp. 4533–4542, 2015, doi: 10.1021/acsnano.5b01154.

[56] G. C. Papavassiliou, G. Pagona, N. Karousis, G. A. Mousdis, I. Koutselas, and A. Vassilakopoulou, “Nanocrystalline/microcrystalline materials based on lead-halide

units," *J. Mater. Chem.*, 2012, doi: 10.1039/c2jm15783g.

[57] M. Leng *et al.*, "Lead-Free, Blue Emitting Bismuth Halide Perovskite Quantum Dots," *Angew. Chemie - Int. Ed.*, 2016, doi: 10.1002/anie.201608160.

[58] L. Zhang *et al.*, "Ultra-bright and highly efficient inorganic based perovskite light-emitting diodes," *Nat. Commun.*, 2017, doi: 10.1038/ncomms15640.

[59] A. Kostopoulou, M. Sygletou, K. Brintakis, A. Lappas, and E. Stratakis, "Low-temperature benchtop-synthesis of all-inorganic perovskite nanowires," *Nanoscale*, 2017, doi: 10.1039/c7nr06404g.

[60] H. Ma, M. Imran, Z. Dang, and Z. Hu, "Growth of Metal Halide Perovskite, from Nanocrystal to Micron-Scale Crystal: A Review," *Crystals*, 2018, doi: 10.3390/cryst8050182.

[61] L. Protesescu *et al.*, "Nanocrystals of Cesium Lead Halide Perovskites (CsPbX3, X = Cl, Br, and I): Novel Optoelectronic Materials Showing Bright Emission with Wide Color Gamut," *Nano Lett.*, vol. 15, no. 6, pp. 3692–3696, 2015, doi: 10.1021/nl5048779.

[62] Y. Tong *et al.*, "Highly Luminescent Cesium Lead Halide Perovskite Nanocrystals with Tunable Composition and Thickness by Ultrasonication," *Angew. Chemie - Int. Ed.*, 2016, doi: 10.1002/anie.201605909.

[63] H. Huang *et al.*, "Top-Down Fabrication of Stable Methylammonium Lead Halide Perovskite Nanocrystals by Employing a Mixture of Ligands as Coordinating Solvents," *Angew. Chemie*, 2017, doi: 10.1002/ange.201705595.

[64] D. Chen *et al.*, "Mn-Doped CsPbCl3 perovskite nanocrystals: Solvothermal synthesis, dual-color luminescence and improved stability," *J. Mater. Chem. C*, 2018, doi: 10.1039/c8tc03139h.

[65] M. Chen *et al.*, "Solvothermal Synthesis of High-Quality All-Inorganic Cesium Lead Halide Perovskite Nanocrystals: From Nanocube to Ultrathin Nanowire," *Adv. Funct.*

Mater., 2017, doi: 10.1002/adfm.201701121.

[66] X. Zheng, Y. Hou, H. T. Sun, O. F. Mohammed, E. H. Sargent, and O. M. Bakr, "Reducing Defects in Halide Perovskite Nanocrystals for Light-Emitting Applications," *J. Phys. Chem. Lett.*, vol. 10, no. 10, pp. 2629–2640, 2019, doi: 10.1021/acs.jpclett.9b00689.

[67] S. Seth, T. Ahmed, A. De, and A. Samanta, "Tackling the Defects, Stability, and Photoluminescence of CsPbX3 Perovskite Nanocrystals," *ACS Energy Letters*. 2019, doi: 10.1021/acsenergylett.9b00849.

[68] J. Ye, M. M. Byranvand, C. O. Martínez, R. L. Z. Hoye, M. Saliba, and L. Polavarapu, "Defect Passivation in Lead-Halide Perovskite Nanocrystals and Thin Films: Toward Efficient LEDs and Solar Cells," *Angew. Chemie*, 2021, doi: 10.1002/ange.202102360.

[69] T. Chiba *et al.*, "Surface Crystal Growth of Perovskite Nanocrystals via Postsynthetic Lead(II) Bromide Treatment to Increase the Colloidal Stability and Efficiency of Light-Emitting Devices," *ACS Appl. Mater. Interfaces*, vol. 12, no. 40, pp. 45574–45581, 2020, doi: 10.1021/acsami.0c13212.

[70] G. Almeida, I. Infante, and L. Manna, "Resurfacing halide perovskite nanocrystals," *Science (80-.).*, vol. 364, no. 6443, pp. 833–834, 2019, doi: 10.1126/science.aax5825.

[71] L. Protesescu, S. Yakunin, O. Nazarenko, D. N. Dirin, and M. V. Kovalenko, "Low-Cost Synthesis of Highly Luminescent Colloidal Lead Halide Perovskite Nanocrystals by Wet Ball Milling," *ACS Appl. Nano Mater.*, 2018, doi: 10.1021/acsanm.8b00038.

[72] S. F. Hoefler, G. Trimmel, and T. Rath, "Progress on lead-free metal halide perovskites for photovoltaic applications: a review," *Monatshefte fur Chemie*. 2017, doi: 10.1007/s00706-017-1933-9.

[73] C. Zhang *et al.*, "Effects of A site doping on the crystallization of perovskite films," *J. Mater. Chem. A*, 2020, doi: 10.1039/d0ta08656h.

[74] S. Kim, T. Eom, Y. S. Ha, K. H. Hong, and H. Kim, “Thermodynamics of Multicomponent Perovskites: A Guide to Highly Efficient and Stable Solar Cell Materials,” *Chem. Mater.*, 2020, doi: 10.1021/acs.chemmater.0c00893.

[75] N. T. P. Hartono *et al.*, “The effect of structural dimensionality on carrier mobility in lead-halide perovskites,” *J. Mater. Chem. A*, 2019, doi: 10.1039/c9ta05241k.

[76] G. E. Eperon *et al.*, “The Role of Dimethylammonium in Bandgap Modulation for Stable Halide Perovskites,” *ACS Energy Lett.*, 2020, doi: 10.1021/acsenergylett.0c00872.

[77] R. J. Stewart, C. Grieco, A. V. Larsen, J. J. Maier, and J. B. Asbury, “Approaching Bulk Carrier Dynamics in Organo-Halide Perovskite Nanocrystalline Films by Surface Passivation,” *J. Phys. Chem. Lett.*, 2016, doi: 10.1021/acs.jpclett.6b00366.

[78] L. Polavarapu, B. Nickel, J. Feldmann, and A. S. Urban, “Advances in Quantum-Confined Perovskite Nanocrystals for Optoelectronics,” *Adv. Energy Mater.*, 2017, doi: 10.1002/aenm.201700267.

[79] G. Li, “Bulk-and nanocrystalline-halide perovskite light-emitting diodes,” in *Advanced Nanomaterials for Solar Cells and Light Emitting Diodes*, 2019.

[80] B. Sharma *et al.*, “Additive engineering of 4, 4′-Bis (N-carbazolyl)-1, 1′-biphenyl (CBP) molecules for defects passivation and moisture stability of hybrid perovskite layer,” *Sol. Energy*, 2020, doi: 10.1016/j.solener.2020.10.035.

[81] S. Yang, Y. Wang, P. Liu, Y. B. Cheng, H. J. Zhao, and H. G. Yang, “Functionalization of perovskite thin films with moisture-tolerant molecules,” *Nat. Energy*, 2016, doi: 10.1038/NENERGY.2015.16.

[82] X. Zhang *et al.*, “Hybrid Perovskite Light-Emitting Diodes Based on Perovskite Nanocrystals with Organic–Inorganic Mixed Cations,” *Adv. Mater.*, 2017, doi: 10.1002/adma.201606405.

[83] B. Xu *et al.*, “Bright and efficient light-emitting diodes based on MA/Cs double cation

perovskite nanocrystals," *J. Mater. Chem. C*, vol. 5, no. 25, pp. 6123–6128, 2017, doi: 10.1039/c7tc01300k.

[84] Y. Zong *et al.*, "Homogenous Alloys of Formamidinium Lead Triiodide and Cesium Tin Triiodide for Efficient Ideal-Bandgap Perovskite Solar Cells," *Angew. Chemie - Int. Ed.*, 2017, doi: 10.1002/anie.201705965.

[85] P. Todorović *et al.*, "Spectrally Tunable and Stable Electroluminescence Enabled by Rubidium Doping of CsPbBr3 Nanocrystals," *Adv. Opt. Mater.*, 2019, doi: 10.1002/adom.201901440.

[86] Y. Zhou *et al.*, "Enhanced luminescence of Mn doped CsPbCl3 and CsPb(Cl/Br)3 perovskite nanocrystals stabilized in glasses," *J. Alloys Compd.*, vol. 827, 2020, doi: 10.1016/j.jallcom.2020.154349.

[87] S. Zou *et al.*, "Stabilizing Cesium Lead Halide Perovskite Lattice through Mn(II) Substitution for Air-Stable Light-Emitting Diodes," *J. Am. Chem. Soc.*, vol. 139, no. 33, 2017, doi: 10.1021/jacs.7b04000.

[88] Y. Zhou, Ye and Wang, *Perovskite Quantum Dots: Synthesis, Properties and Applications*. Springer Nature, 2020.

[89] J. Pan *et al.*, "Halogen Vacancies Enable Ligand-Assisted Self-Assembly of Perovskite Quantum Dots into Nanowires," *Angew. Chemie - Int. Ed.*, vol. 58, no. 45, 2019, doi: 10.1002/anie.201909109.

[90] J. H. Park *et al.*, "Surface Ligand Engineering for Efficient Perovskite Nanocrystal-Based Light-Emitting Diodes," *ACS Appl. Mater. Interfaces*, vol. 11, no. 8, 2019, doi: 10.1021/acsami.8b20808.

[91] W. Zheng *et al.*, "Stabilizing perovskite nanocrystals by controlling protective surface ligands density," *Nano Res.*, vol. 12, no. 6, 2019, doi: 10.1007/s12274-019-2407-7.

[92] D. Yang, X. Li, and H. Zeng, "Surface Chemistry of All Inorganic Halide Perovskite

Nanocrystals: Passivation Mechanism and Stability," *Advanced Materials Interfaces*, vol. 5, no. 8. 2018, doi: 10.1002/admi.201701662.

[93] A. Pan *et al.*, "Insight into the Ligand-Mediated Synthesis of Colloidal CsPbBr3 Perovskite Nanocrystals: The Role of Organic Acid, Base, and Cesium Precursors," *ACS Nano*, vol. 10, no. 8, 2016, doi: 10.1021/acsnano.6b03863.

[94] O. Vybornyi, S. Yakunin, and M. V. Kovalenko, "Polar-solvent-free colloidal synthesis of highly luminescent alkylammonium lead halide perovskite nanocrystals," *Nanoscale*, vol. 8, no. 12, 2016, doi: 10.1039/c5nr06890h.

[95] M. Imran *et al.*, "Benzoyl Halides as Alternative Precursors for the Colloidal Synthesis of Lead-Based Halide Perovskite Nanocrystals," *J. Am. Chem. Soc.*, vol. 140, no. 7, 2018, doi: 10.1021/jacs.7b13477.

[96] Y. Shynkarenko *et al.*, "Direct synthesis of quaternary alkylammonium-capped perovskite nanocrystals for efficient blue and green light-emitting diodes," *ACS Energy Lett.*, vol. 4, no. 11, 2019, doi: 10.1021/acsenergylett.9b01915.

[97] T. A. Cohen *et al.*, "Modular Zwitterion-Functionalized Poly(isopropyl methacrylate) Polymers for Hosting Luminescent Lead Halide Perovskite Nanocrystals," *Chem. Mater.*, vol. 33, no. 10, 2021, doi: 10.1021/acs.chemmater.1c00902.

[98] F. Montanarella *et al.*, "Highly Concentrated, Zwitterionic Ligand-Capped Mn2+:CsPb(BrxCl1- x)3Nanocrystals as Bright Scintillators for Fast Neutron Imaging," *ACS Energy Lett.*, vol. 6, no. 12, 2021, doi: 10.1021/acsenergylett.1c01923.

[99] F. Krieg *et al.*, "Colloidal CsPbX3 (X = Cl, Br, I) Nanocrystals 2.0: Zwitterionic Capping Ligands for Improved Durability and Stability," *ACS Energy Lett.*, vol. 3, no. 3, 2018, doi: 10.1021/acsenergylett.8b00035.

[100] W. Zheng *et al., Perovskite Quantum Dots*, vol. 9, no. 1. 2020.

[101] F. Gao *et al.*, "Highly stable and luminescent silica-coated perovskite quantum dots at

nanoscale-particle level via nonpolar solvent synthesis," *Chem. Eng. J.*, vol. 407, 2021, doi: 10.1016/j.cej.2020.128001.

[102] L. Y. Wu *et al.*, "Encapsulating Perovskite Quantum Dots in Iron-Based Metal–Organic Frameworks (MOFs) for Efficient Photocatalytic CO2 Reduction," *Angew. Chemie - Int. Ed.*, vol. 58, no. 28, 2019, doi: 10.1002/anie.201904537.

[103] Y. Wei *et al.*, "Highly Luminescent Lead Halide Perovskite Quantum Dots in Hierarchical CaF2 Matrices with Enhanced Stability as Phosphors for White Light-Emitting Diodes," *Adv. Opt. Mater.*, vol. 6, no. 11, 2018, doi: 10.1002/adom.201701343.

[104] H. Tang, S. He, and C. Peng, "A Short Progress Report on High-Efficiency Perovskite Solar Cells," *Nanoscale Research Letters*, vol. 12. 2017, doi: 10.1186/s11671-017-2187-5.

[105] C. Li *et al.*, "Ultrafast and broadband photodetectors based on a perovskite/organic bulk heterojunction for large-dynamic-range imaging," *Light Sci. Appl.*, 2020, doi: 10.1038/s41377-020-0264-5.

[106] S. Wang, A. A. Yousefi Amin, L. Wu, M. Cao, Q. Zhang, and T. Ameri, "Perovskite Nanocrystals: Synthesis, Stability, and Optoelectronic Applications," *Small Struct.*, vol. 2, no. 3, p. 2000124, 2021, doi: 10.1002/sstr.202000124.

[107] H. Wang and D. H. Kim, "Perovskite-based photodetectors: Materials and devices," *Chemical Society Reviews*. 2017, doi: 10.1039/c6cs00896h.

[108] J. Jiang *et al.*, "The Doping of Alkali Metal for Halide Perovskites," *ES Mater. Manuf.*, pp. 25–33, 2019, doi: 10.30919/esmm5f705.

[109] T. Liu *et al.*, "High-Performance Formamidinium-Based Perovskite Solar Cells via Microstructure-Mediated δ-to-α Phase Transformation," *Chem. Mater.*, 2017, doi: 10.1021/acs.chemmater.7b00523.

[110] O. A. Syzgantseva, M. Saliba, M. Grätzel, and U. Rothlisberger, "Stabilization of the

Perovskite Phase of Formamidinium Lead Triiodide by Methylammonium, Cs, and/or Rb Doping," *J. Phys. Chem. Lett.*, vol. 8, no. 6, pp. 1191–1196, 2017, doi: 10.1021/acs.jpclett.6b03014.

[111] R. T. Ginting, E. S. Jung, M. K. Jeon, W. Y. Jin, M. Song, and J. W. Kang, "Low-temperature operation of perovskite solar cells: With efficiency improvement and hysteresis-less," *Nano Energy*, 2016, doi: 10.1016/j.nanoen.2016.08.016.

[112] F. F. Targhi, Y. S. Jalili, and F. Kanjouri, "MAPbI3 and FAPbI3 perovskites as solar cells: Case study on structural, electrical and optical properties," *Results Phys.*, 2018, doi: 10.1016/j.rinp.2018.07.007.

[113] J. W. Lee, D. H. Kim, H. S. Kim, S. W. Seo, S. M. Cho, and N. G. Park, "Formamidinium and cesium hybridization for photo- and moisture-stable perovskite solar cell," *Adv. Energy Mater.*, 2015, doi: 10.1002/aenm.201501310.

[114] Z. Li, M. Yang, J. S. Park, S. H. Wei, J. J. Berry, and K. Zhu, "Stabilizing Perovskite Structures by Tuning Tolerance Factor: Formation of Formamidinium and Cesium Lead Iodide Solid-State Alloys," *Chem. Mater.*, 2016, doi: 10.1021/acs.chemmater.5b04107.

[115] M. Saliba *et al.*, "Cesium-containing triple cation perovskite solar cells: Improved stability, reproducibility and high efficiency," *Energy Environ. Sci.*, 2016, doi: 10.1039/c5ee03874j.

[116] L. Xie *et al.*, "Revealing the compositional effect on the intrinsic long-term stability of perovskite solar cells," *J. Mater. Chem. A*, 2020, doi: 10.1039/d0ta01668c.

[117] M. Qin *et al.*, "Precise Control of Perovskite Crystallization Kinetics via Sequential A-Site Doping," *Adv. Mater.*, 2020, doi: 10.1002/adma.202004630.

[118] D. Prochowicz *et al.*, "Engineering of Perovskite Materials Based on Formamidinium and Cesium Hybridization for High-Efficiency Solar Cells," *Chem. Mater.*, 2019, doi: 10.1021/acs.chemmater.8b04871.

[119] G. Murugadoss, R. Thangamuthu, S. Vijayaraghavan, H. Kanda, and S. Ito, “Caesium −Methyl Ammonium Mixed-Cation Lead Iodide Perovskite Crystals: Analysis and Application for Perovskite Solar Cells,” *Electrochim. Acta*, 2017, doi: 10.1016/j.electacta.2017.10.092.

[120] Y. Fan, H. Qin, W. Ye, M. Liu, F. Huang, and D. Zhong, “Improving the stability of methylammonium lead iodide perovskite solar cells by cesium doping,” *Thin Solid Films*, 2018, doi: 10.1016/j.tsf.2018.10.001.

[121] F. Ye, W. Yang, D. Luo, R. Zhu, and Q. Gong, “Applications of cesium in the perovskite solar cells,” *J. Semicond.*, 2017, doi: 10.1088/1674-4926/38/1/011003.

[122] H. Choi *et al.*, “Cesium-doped methylammonium lead iodide perovskite light absorber for hybrid solar cells,” *Nano Energy*, 2014, doi: 10.1016/j.nanoen.2014.04.017.

[123] A. Amat *et al.*, “Cation-induced band-gap tuning in organohalide perovskites: Interplay of spin-orbit coupling and octahedra tilting,” *Nano Lett.*, 2014, doi: 10.1021/nl5012992.

[124] G. Wu *et al.*, “Synergistic Benefits of Cesium-Doped Aqueous Precursor in Air-Processed Inverted Perovskite Solar Cells,” *Sol. RRL*, 2020, doi: 10.1002/solr.201900406.

[125] Q. Jiang *et al.*, “Surface passivation of perovskite film for efficient solar cells,” *Nat. Photonics*, 2019, doi: 10.1038/s41566-019-0398-2.

[126] Y. Zhang, S. G. Kim, D. Lee, H. Shin, and N. G. Park, “Bifacial stamping for high efficiency perovskite solar cells,” *Energy Environ. Sci.*, 2019, doi: 10.1039/c8ee02730g.

[127] S. Yuan *et al.*, “Simultaneous Cesium and Acetate Coalloying Improves Efficiency and Stability of FA0.85MA0.15PbI3 Perovskite Solar Cell with an Efficiency of 21.95%,” *Sol. RRL*, 2019, doi: 10.1002/solr.201900220.

[128] B. Gao and J. Meng, “RbCs(MAFA)PbI3 perovskite solar cell with 22.81% efficiency using the precise ions cascade regulation,” *Appl. Surf. Sci.*, 2020, doi:

10.1016/j.apsusc.2020.147240.

[129] M. Saliba *et al.*, “Incorporation of rubidium cations into perovskite solar cells improves photovoltaic performance,” *Science (80-.).*, 2016, doi: 10.1126/science.aah5557.

[130] T. Duong *et al.*, “Structural engineering using rubidium iodide as a dopant under excess lead iodide conditions for high efficiency and stable perovskites,” *Nano Energy*, 2016, doi: 10.1016/j.nanoen.2016.10.027.

[131] M. Abdi-Jalebi *et al.*, “Maximizing and stabilizing luminescence from halide perovskites with potassium passivation,” *Nature*, 2018, doi: 10.1038/nature25989.

[132] L. Kuai *et al.*, “Passivating Crystal Boundaries with Potassium-Rich Phase in Organic Halide Perovskite,” *Sol. RRL*, 2019, doi: 10.1002/solr.201900053.

[133] D. Prochowicz *et al.*, “Influence of A-site cations on the open-circuit voltage of efficient perovskite solar cells: A case of rubidium and guanidinium additives,” *J. Mater. Chem. A*, 2019, doi: 10.1039/c9ta00272c.

[134] Y. Guo *et al.*, “Efficient and Hole-Transporting-Layer-Free CsPbI 2 Br Planar Heterojunction Perovskite Solar Cells through Rubidium Passivation,” *ChemSusChem*, 2019, doi: 10.1002/cssc.201802690.

[135] J. V. Patil, S. S. Mali, and C. K. Hong, “A-Site Rubidium Cation-Incorporated CsPbI2Br All-Inorganic Perovskite Solar Cells Exceeding 17% Efficiency,” *Sol. RRL*, 2020, doi: 10.1002/solr.202000164.

[136] Y. Hu, M. F. Aygüler, M. L. Petrus, T. Bein, and P. Docampo, “Impact of Rubidium and Cesium Cations on the Moisture Stability of Multiple-Cation Mixed-Halide Perovskites,” *ACS Energy Lett.*, vol. 2, no. 10, pp. 2212–2218, 2017, doi: 10.1021/acsenergylett.7b00731.

[137] W. Zhao, Z. Yao, F. Yu, D. Yang, and S. F. Liu, “Alkali Metal Doping for Improved CH3NH3PbI3 Perovskite Solar Cells,” *Adv. Sci.*, 2018, doi: 10.1002/advs.201700131.

[138] Z. Tang *et al.*, “Hysteresis-free perovskite solar cells made of potassium-doped organometal halide perovskite,” *Sci. Rep.*, 2017, doi: 10.1038/s41598-017-12436-x.

[139] L. Wang *et al.*, “Potassium-Induced Phase Stability Enables Stable and Efficient Wide-Bandgap Perovskite Solar Cells,” *Sol. RRL*, 2020, doi: 10.1002/solr.202000098.

[140] M. F. Vildanova, A. B. Nikolskaia, S. S. Kozlov, O. K. Karyagina, and O. I. Shevaleevskiy, “Potassium Doping Effect on the Photovoltaic Performance of Perovskite Solar Cells,” *Tech. Phys. Lett.*, vol. 46, no. 3, pp. 231–234, 2020, doi: 10.1134/S1063785020030153.

[141] G. Kim, H. Min, K. S. Lee, D. Y. Lee, S. M. Yoon, and S. Il Seok, “Impact of strain relaxation on performance of a-formamidinium lead iodide perovskite solar cells,” *Science (80-.).*, 2020, doi: 10.1126/science.abc4417.

[142] M. M. Tavakoli, R. Tavakoli, D. Prochowicz, P. Yadav, and M. Saliba, “Surface modification of a hole transporting layer for an efficient perovskite solar cell with an enhanced fill factor and stability,” *Mol. Syst. Des. Eng.*, 2018, doi: 10.1039/c8me00036k.

[143] Y. Hu *et al.*, “Perovskite Solar Cells: Understanding the Role of Cesium and Rubidium Additives in Perovskite Solar Cells: Trap States, Charge Transport, and Recombination (Adv. Energy Mater. 16/2018),” *Adv. Energy Mater.*, 2018, doi: 10.1002/aenm.201870073.

[144] J. C. Germino *et al.*, “Postpassivation of Multication Perovskite with Rubidium Butyrate,” *ACS Photonics*, 2020, doi: 10.1021/acsphotonics.0c00878.

[145] F. Yao *et al.*, “High-Rubidium-Formamidinium-Ratio Perovskites for High-Performance Photodetection with Enhanced Stability,” *ACS Appl. Mater. Interfaces*, 2019, doi: 10.1021/acsami.9b12799.

[146] D. Amgar, T. Binyamin, V. Uvarov, and L. Etgar, “Near ultra-violet to mid-visible band

gap tuning of mixed cation Rb: XCs1- xPbX3 (X = Cl or Br) perovskite nanoparticles," *Nanoscale*, 2018, doi: 10.1039/c7nr09607k.

[147] J. Yang *et al.*, "Enhancing Mn Emission of CsPbCl3 Perovskite Nanocrystals via Incorporation of Rubidium Ions," *Mater. Res. Bull.*, vol. 133, p. 111080, 2021, doi: 10.1016/j.materresbull.2020.111080.

[148] F. Meng *et al.*, "Incorporation of rubidium cations into blue perovskite quantum dot light-emitting diodes: Via FABr-modified multi-cation hot-injection method," *Nanoscale*, vol. 11, no. 3, pp. 1295–1303, 2019, doi: 10.1039/c8nr07907b.

[149] M. A. Haque *et al.*, "Giant Humidity Effect on Hybrid Halide Perovskite Microstripes: Reversibility and Sensing Mechanism," *ACS Appl. Mater. Interfaces*, 2019, doi: 10.1021/acsami.9b07751.

[150] Q. Wang *et al.*, "Scaling behavior of moisture-induced grain degradation in polycrystalline hybrid perovskite thin films," *Energy Environ. Sci.*, 2017, doi: 10.1039/c6ee02941h.

[151] B. Jeong *et al.*, "Humidity controlled crystallization of thin CH3NH3PbI3 films for high performance perovskite solar cell," *Phys. Status Solidi - Rapid Res. Lett.*, 2016, doi: 10.1002/pssr.201600004.

[152] A. Kanwat, E. Moyen, S. Cho, and J. Jang, "Rubidium as an Alternative Cation for Efficient Perovskite Light-Emitting Diodes," *ACS Appl. Mater. Interfaces*, vol. 10, no. 19, pp. 16852–16860, 2018, doi: 10.1021/acsami.8b01292.

[153] Y. Shi *et al.*, "Rubidium Doping for Enhanced Performance of Highly Efficient Formamidinium-Based Perovskite Light-Emitting Diodes," *ACS Appl. Mater. Interfaces*, vol. 10, no. 11, pp. 9849–9857, 2018, doi: 10.1021/acsami.8b00079.

[154] M. T. Hoang *et al.*, "Potassium Doping to Enhance Green Photoemission of Light-Emitting Diodes Based on CsPbBr3 Perovskite Nanocrystals," *Adv. Opt. Mater.*, 2020,

doi: 10.1002/adom.202000742.

[155] J. N. Yang *et al.*, “Potassium Bromide Surface Passivation on CsPbI3-xBrx Nanocrystals for Efficient and Stable Pure Red Perovskite Light-Emitting Diodes,” *J. Am. Chem. Soc.*, vol. 142, no. 6, pp. 2956–2967, 2020, doi: 10.1021/jacs.9b11719.

[156] F. Yang *et al.*, “Efficient and Spectrally Stable Blue Perovskite Light-Emitting Diodes Based on Potassium Passivated Nanocrystals,” *Adv. Funct. Mater.*, vol. 30, no. 10, p. 1908760, 2020, doi: 10.1002/adfm.201908760.

[157] D. Ma *et al.*, “Chloride Insertion-Immobilization Enables Bright, Narrowband, and Stable Blue-Emitting Perovskite Diodes,” *ACS Appl. Mater. Interfaces*, 2020, doi: 10.1021/jacs.9b12323.

[158] S. Hou, M. K. Gangishetty, Q. Quan, and D. N. Congreve, “Efficient Blue and White Perovskite Light-Emitting Diodes via Manganese Doping,” *Joule*, 2018, doi: 10.1016/j.joule.2018.08.005.

[159] E. P. Yao *et al.*, “High-Brightness Blue and White LEDs based on Inorganic Perovskite Nanocrystals and their Composites,” *Adv. Mater.*, 2017, doi: 10.1002/adma.201606859.

[160] J. Xing *et al.*, “Color-stable highly luminescent sky-blue perovskite light-emitting diodes,” *Nat. Commun.*, 2018, doi: 10.1038/s41467-018-05909-8.

[161] Y. Liu *et al.*, “Considerably enhanced exciton emission of CsPbCl3 perovskite quantum dots by the introduction of potassium and lanthanide ions,” *Nanoscale*, 2018, doi: 10.1039/c8nr03581d.

[162] W. J. Mir, T. Sheikh, H. Arfin, Z. Xia, and A. Nag, “Lanthanide doping in metal halide perovskite nanocrystals: spectral shifting, quantum cutting and optoelectronic applications,” *NPG Asia Materials*. 2020, doi: 10.1038/s41427-019-0192-0.

[163] W. Liu *et al.*, “Mn2+-Doped Lead Halide Perovskite Nanocrystals with Dual-Color Emission Controlled by Halide Content,” *J. Am. Chem. Soc.*, 2016, doi:

10.1021/jacs.6b08085.

[164] L. Xu *et al.*, “A perovskite solar cell textile that works at-40 to 160 °c,” *J. Mater. Chem. A*, vol. 8, no. 11, pp. 5476–5483, 2020, doi: 10.1039/c9ta13785h.

[165] Y. Wang, D. Li, L. Chao, T. Niu, and Y. Chen, “Perovskite photodetectors for flexible electronics : Recent advances and perspectives,” *Appl. Mater. Today*, vol. 28, no. April, 2022, doi: 10.1016/j.apmt.2022.101509.

[166] S. T. Ha, R. Su, J. Xing, Q. Zhang, and Q. Xiong, “Metal halide perovskite nanomaterials: synthesis and applications,” *Chem. Sci.*, vol. 8, no. 4, 2017, doi: 10.1039/c6sc04474c.

[167] A. Kojima, K. Teshima, Y. Shirai, and T. Miyasaka, “Organometal halide perovskites as visible-light sensitizers for photovoltaic cells,” *J. Am. Chem. Soc.*, vol. 131, no. 17, 2009, doi: 10.1021/ja809598r.

[168] M. H. Kumar, N. Yantara, S. Dharani, M. Graetzel, P. P. Boix, and N. Mathews, “Flexible, low-temperature, solution processed ZnO-based perovskite solid state solar cells,” *Chem. Commun.*, vol. 49, no. 94, 2013, doi: 10.1039/c3cc46534a.

[169] L. Yang *et al.*, “Artemisinin-passivated mixed-cation perovskite films for durable flexible perovskite solar cells with over 21% efficiency,” *J. Mater. Chem. A*, vol. 9, no. 3, 2021, doi: 10.1039/d0ta10717d.

[170] P. Jia *et al.*, “Recent Advances in Flexible Perovskite Light-Emitting Diodes,” *Advanced Materials Interfaces*, vol. 8, no. 17. 2021, doi: 10.1002/admi.202100441.

[171] Y. Shen *et al.*, “Rational Interface Engineering for Efficient Flexible Perovskite Light-Emitting Diodes,” *ACS Nano*, vol. 14, no. 5, 2020, doi: 10.1021/acsnano.0c01908.

[172] X. Hu *et al.*, “High-performance flexible broadband photodetector based on organolead halide perovskite,” *Adv. Funct. Mater.*, vol. 24, no. 46, 2014, doi: 10.1002/adfm.201402020.

[173] H. Chen *et al.*, “Flexible optoelectronic devices based on metal halide perovskites,” *Nano Research*, vol. 13, no. 8. 2020, doi: 10.1007/s12274-020-2805-x.

[174] R. Zhao, Z. Gu, P. Li, Y. Zhang, and Y. Song, “Flexible and Wearable Optoelectronic Devices Based on Perovskites,” *Advanced Materials Technologies*, vol. 7, no. 3. 2022, doi: 10.1002/admt.202101124.

[175] K. Li *et al.*, “An efficient, flexible perovskite solar module exceeding 8% prepared with an ultrafast PbI2 deposition rate,” *Sci. Rep.*, vol. 8, no. 1, 2018, doi: 10.1038/s41598-017-18970-y.

[176] B. W. Gao and J. Meng, “Large area and flexible CH3NH3PbI3 perovskite solar cell fabricated by all ink jet printing,” *Wuli Xuebao/Acta Phys. Sin.*, vol. 70, no. 20, 2021, doi: 10.7498/aps.70.20210788.

[177] B. Gao and J. Meng, “Flexible CH3NH3PbI3 perovskite solar cells with high stability based on all inkjet printing,” *Sol. Energy*, vol. 230, 2021, doi: 10.1016/j.solener.2021.10.072.

[178] Y. Y. Kim *et al.*, “Roll-to-roll gravure-printed flexible perovskite solar cells using eco-friendly antisolvent bathing with wide processing window,” *Nat. Commun.*, vol. 11, no. 1, 2020, doi: 10.1038/s41467-020-18940-5.

[179] X. L. Ou, M. Xu, J. Feng, and H. B. Sun, “Flexible and efficient ITO-free semitransparent perovskite solar cells,” *Sol. Energy Mater. Sol. Cells*, vol. 157, 2016, doi: 10.1016/j.solmat.2016.07.010.

[180] F. Qin *et al.*, “Indium tin oxide (ITO)-free, top-illuminated, flexible perovskite solar cells,” *J. Mater. Chem. A*, vol. 4, no. 36, 2016, doi: 10.1039/c6ta06657g.

[181] Y. Li *et al.*, “High-efficiency robust perovskite solar cells on ultrathin flexible substrates,” *Nat. Commun.*, vol. 7, 2016, doi: 10.1038/ncomms10214.

[182] L. Hou *et al.*, “18.0% efficiency flexible perovskite solar cells based on double hole

transport layers and CH3NH3PbI3-xClx with dual additives," *J. Mater. Chem. C*, vol. 6, no. 32, 2018, doi: 10.1039/c8tc02906g.

[183] F. De Rossi *et al.*, "Neutron irradiated perovskite films and solar cells on PET substrates," *Nano Energy*, vol. 93, 2022, doi: 10.1016/j.nanoen.2021.106879.

[184] M. Clark, *Handbook of Textile and Industrial Dyeing*, vol. 2. 2011.

[185] Y. Xu, Z. Lin, W. Wei, Y. Hao, and S. Liu, "Recent Progress of Electrode Materials for Flexible Perovskite Solar Cells," *Nano-Micro Lett.*, no. 0123456789, pp. 1–30, 2022, doi: 10.1007/s40820-022-00859-9.

[186] G. Tang and F. Yan, "Recent progress of flexible perovskite solar cells," *Nano Today*, vol. 39. 2021, doi: 10.1016/j.nantod.2021.101155.

[187] D. Yang, R. Yang, S. Priya, and S. (Frank) Liu, "Recent Advances in Flexible Perovskite Solar Cells: Fabrication and Applications," *Angewandte Chemie - International Edition*, vol. 58, no. 14. 2019, doi: 10.1002/anie.201809781.

[188] X. Liang *et al.*, "Flexible Perovskite Solar Cells: Progress and Prospects," *Frontiers in Materials*, vol. 8. 2021, doi: 10.3389/fmats.2021.634353.

[189] L. Qiu, J. Deng, X. Lu, Z. Yang, and H. Peng, "Inside Cover: Integrating Perovskite Solar Cells into a Flexible Fiber (Angew. Chem. Int. Ed. 39/2014)," *Angew. Chemie Int. Ed.*, vol. 53, no. 39, 2014, doi: 10.1002/anie.201406844.

[190] L. Qiu, J. Deng, X. Lu, Z. Yang, and H. Peng, "Innentitelbild: Integrating Perovskite Solar Cells into a Flexible Fiber (Angew. Chem. 39/2014)," *Angew. Chemie*, vol. 126, no. 39, 2014, doi: 10.1002/ange.201406844.

[191] X. Xu, L. Sun, K. Shen, and S. Zhang, "Organic and hybrid organic-inorganic flexible optoelectronics: Recent advances and perspectives," *Synthetic Metals*, vol. 256. 2019, doi: 10.1016/j.synthmet.2019.116137.

[192] I. Hussain, H. P. Tran, J. Jaksik, J. Moore, N. Islam, and M. J. Uddin, "Functional

materials, device architecture, and flexibility of perovskite solar cell," *Emergent Mater.*, vol. 1, no. 3–4, 2018, doi: 10.1007/s42247-018-0013-1.

[193] Z. Chen, Z. Li, T. R. Hopper, A. A. Bakulin, and H. L. Yip, "Materials, photophysics and device engineering of perovskite light-emitting diodes," *Reports Prog. Phys.*, vol. 84, no. 4, 2021, doi: 10.1088/1361-6633/abefba.

[194] C. Zhao, D. Zhang, and C. Qin, "Perovskite light-emitting diodes," *CCS Chem.*, vol. 2, no. 4, pp. 859–869, 2020, doi: 10.31635/ccschem.020.202000216.

[195] K. Ji, M. Anaya, A. Abfalterer, and S. D. Stranks, "Halide Perovskite Light-Emitting Diode Technologies," *Advanced Optical Materials*, vol. 9, no. 18. 2021, doi: 10.1002/adom.202002128.

[196] C. Trudeau, M. Bolduc, P. Beaupre, I. Ka, I. M. Asuo, and S. G. Cloutier, "Inkjet-Printing of Methylammonium Lead Trihalide Perovskite-Based Flexible Optoelectronic Devices," in *2018 International Flexible Electronics Technology Conference, IFETC 2018*, 2018, doi: 10.1109/IFETC.2018.8583950.

[197] G. Li, Y. Wang, L. Huang, and W. Sun, "Research Progress of High-Sensitivity Perovskite Photodetectors: A Review of Photodetectors: Noise, Structure, and Materials," *ACS Appl. Electron. Mater.*, 2022, doi: 10.1021/acsaelm.1c01349.

[198] J. J. Yoo, S. Sik Shin, and J. Seo, "Toward Efficient Perovskite Solar Cells: Progress, Strategies, and Perspectives," *ACS Energy Lett.*, vol. 7, no. 6, pp. 2084–2091, May 2022, doi: 10.1021/acsenergylett.2c00592.

[199] D. Angmo *et al.*, "A Lab-to-Fab Study toward Roll-to-Roll Fabrication of Reproducible Perovskite Solar Cells under Ambient Room Conditions," *Cell Reports Phys. Sci.*, vol. 2, no. 1, 2021, doi: 10.1016/j.xcrp.2020.100293.

[200] T. Y. Yang, Y. Y. Kim, and J. Seo, "Roll-to-roll manufacturing toward lab-to-fab-translation of perovskite solar cells," *APL Materials*, vol. 9, no. 11. 2021, doi:

10.1063/5.0064073.

[201] S. Pratap *et al.*, “Out-of-equilibrium processes in crystallization of organic-inorganic perovskites during spin coating,” *Nat. Commun.*, vol. 12, no. 1, 2021, doi: 10.1038/s41467-021-25898-5.

[202] J. A. Baker, Y. Mouhamad, K. E. A. Hooper, D. Burkitt, M. Geoghegan, and T. M. Watson, “From spin coating to roll-to-roll: Investigating the challenge of upscaling lead halide perovskite solar cells,” *IET Renew. Power Gener.*, vol. 11, no. 5, 2017, doi: 10.1049/iet-rpg.2016.0683.

[203] M. Konstantakou, D. Perganti, P. Falaras, and T. Stergiopoulos, “Anti-solvent crystallization strategies for highly efficient perovskite solar cells,” *Crystals*, vol. 7, no. 10. 2017, doi: 10.3390/cryst7100291.

[204] N. P. Indrani Coondoo, Someshwar Pola, Ed., *Perovskite and Piezoelectric Materials*. IntechOpen, 2021.

[205] J. Zhang, W. Zhang, H. M. Cheng, and S. R. P. Silva, “Critical review of recent progress of flexible perovskite solar cells,” *Mater. Today*, vol. 39, no. October, pp. 66–88, 2020, doi: 10.1016/j.mattod.2020.05.002.

[206] T. A. N. Ram K. Gupta, *Smart and Flexible Energy Devices*. CRC Press, 2022.

[207] M. Era, T. Hattori, T. Taira, and T. Tsutsui, “Self-Organized Growth of PbI-Based Layered Perovskite Quantum Well by Dual-Source Vapor Deposition,” *Chem. Mater.*, vol. 9, no. 1, 1997, doi: 10.1021/cm960434m.

[208] M. M. Tavakoli and R. Tavakoli, “All-Vacuum-Processing for Fabrication of Efficient, Large-Scale, and Flexible Inverted Perovskite Solar Cells,” *Phys. Status Solidi - Rapid Res. Lett.*, vol. 15, no. 1, 2021, doi: 10.1002/pssr.202000449.

[209] J. Li *et al.*, “All-vacuum fabrication of yellow perovskite light-emitting diodes,” *Sci. Bull.*, vol. 67, no. 2, 2022, doi: 10.1016/j.scib.2021.09.003.

[210] G. Tong *et al.*, “Dual-Phase CsPbBr3–CsPb2Br5 Perovskite Thin Films via Vapor Deposition for High-Performance Rigid and Flexible Photodetectors,” *Small*, vol. 14, no. 7, 2018, doi: 10.1002/smll.201702523.

[211] S. Tong *et al.*, “Fully-printed, flexible cesium-doped triple cation perovskite photodetector,” *Appl. Mater. Today*, vol. 15, 2019, doi: 10.1016/j.apmt.2019.03.001.

[212] D. Lee, Y. Jung, Y. Heo, S. Lee, K. Hwang, and Y. Jeon, “Slot-Die Coated Perovskite Films Using Mixed Lead Precursors for Highly Reproducible and Large-Area Solar Cells,” *ACS Appl. Mater. Interfaces*, vol. 10, pp. 16133–16139, 2018, doi: 10.1021/acsami.8b02549.

[213] Y. Diao, L. Shaw, and S. C. B. Mannsfeld, “Environmental Science Morphology control strategies for solution- processed organic semiconductor thin films,” pp. 2145–2159, 2014, doi: 10.1039/c4ee00688g.

[214] Z. Yang, S. Zhang, L. Li, and W. Chen, “Research progress on large-area perovskite thin films and solar modules,” *J Mater.*, vol. 3, no. 4, pp. 231–244, 2017, doi: 10.1016/j.jmat.2017.09.002.

[215] Y. Wang *et al.*, “Printing strategies for scaling-up perovskite solar cells,” *National Science Review*, vol. 8, no. 8. 2021, doi: 10.1093/nsr/nwab075.

[216] N. Khambunkoed *et al.*, “Fully-covered slot-die-coated ZnO thin films for reproducible carbon-based perovskite solar cells,” *Mater. Sci. Semicond. Process.*, vol. 136, 2021, doi: 10.1016/j.mssp.2021.106151.

[217] S. Razza, S. Castro-hermosa, A. Di Carlo, and T. M. Brown, “Research Update : Large-area deposition , coating , printing , and processing techniques for the upscaling of perovskite solar cell technology,” vol. 091508, 2016, doi: 10.1063/1.4962478.

[218] D. K. Mohamad, J. Griffin, C. Bracher, A. T. Barrows, and D. G. Lidzey, “Spray-Cast Multilayer Organometal Perovskite Solar Cells Fabricated in Air,” *Adv. Energy Mater.*,

2016, doi: 10.1002/aenm.201600994.

[219] S. Tong, H. Wu, C. Zhang, S. Li, C. Wang, and J. Shen, “Large-area and high-performance CH3NH3PbI3 perovskite photodetectors fabricated via doctor blading in ambient condition Large-area and high-performance CH 3 NH 3 PbI 3 perovskite photodetectors fabricated via doctor blading in ambient condition,” no. March 2018, 2017, doi: 10.1016/j.orgel.2017.07.011.

[220] K. Yuan, T. Hu, and Y. Chen, “Flexible and wearable solar cells and supercapacitors,” in *Flexible and Wearable Electronics for Smart Clothing*, 2020.

[221] S. A. Hashemi, S. Ramakrishna, and A. G. Aberle, “Recent progress in flexible-wearable solar cells for self-powered electronic devices,” *Energy and Environmental Science*, vol. 13, no. 3. 2020, doi: 10.1039/c9ee03046h.

[222] J. H. Kim *et al.*, “Flexible ITO films with atomically flat surfaces for high performance flexible perovskite solar cells,” *Nanoscale*, vol. 10, no. 44, 2018, doi: 10.1039/c8nr06586a.

[223] P. Zeng, W. Deng, and M. Liu, “Recent Advances of Device Components toward Efficient Flexible Perovskite Solar Cells,” *Solar RRL*, vol. 4, no. 3. 2020, doi: 10.1002/solr.201900485.

[224] Q. Luo *et al.*, “All-Carbon-Electrode-Based Endurable Flexible Perovskite Solar Cells,” *Adv. Funct. Mater.*, vol. 28, no. 11, 2018, doi: 10.1002/adfm.201706777.

[225] S. Albrecht *et al.*, “Monolithic perovskite/silicon-heterojunction tandem solar cells processed at low temperature,” *Energy Environ. Sci.*, vol. 9, no. 1, 2016, doi: 10.1039/c5ee02965a.

[226] M. Qin *et al.*, “Perovskite Solar Cells Based on Low-Temperature Processed Indium Oxide Electron Selective Layers,” *ACS Appl. Mater. Interfaces*, vol. 8, no. 13, 2016, doi: 10.1021/acsami.5b12849.

[227] N. Suresh Kumar and K. Chandra Babu Naidu, “A review on perovskite solar cells (PSCs), materials and applications,” *J. Mater.*, vol. 7, no. 5, 2021, doi: 10.1016/j.jmat.2021.04.002.

[228] S. He *et al.*, “Radically grown obelisk-like ZnO arrays for perovskite solar cell fibers and fabrics through a mild solution process,” *J. Mater. Chem. A*, vol. 3, no. 18, 2015, doi: 10.1039/c5ta01532d.

[229] L. Qiu, J. Deng, X. Lu, Z. Yang, and H. Peng, “Integrating Perovskite Solar Cells into a Flexible Fiber,” *Angew. Chemie Int. Ed.*, vol. 53, no. 39, 2014, doi: 10.1002/anie.201404973.

[230] J. W. Jung, J. H. Bae, J. H. Ko, and W. Lee, “Fully solution-processed indium tin oxide-free textile-based flexible solar cells made of an organic–inorganic perovskite absorber: Toward a wearable power source,” *J. Power Sources*, vol. 402, 2018, doi: 10.1016/j.jpowsour.2018.09.038.

[231] J. Y. Lam *et al.*, “A stable, efficient textile-based flexible perovskite solar cell with improved washable and deployable capabilities for wearable device applications,” *RSC Adv.*, vol. 7, no. 86, pp. 54361–54368, 2017, doi: 10.1039/c7ra10321b.

[232] B. J. Kim *et al.*, “Highly efficient and bending durable perovskite solar cells: Toward a wearable power source,” *Energy Environ. Sci.*, vol. 8, no. 3, 2015, doi: 10.1039/c4ee02441a.

[233] J. Zhai, X. Yin, L. Song, W. H. Chen, P. Du, and J. Xiong, “Preparationof fabric-like transparent electrodefor flexible perovskite solar cell,” *Thin Solid Films*, vol. 729, 2021, doi: 10.1016/j.tsf.2021.138698.

[234] S. Gholipour *et al.*, “Highly Efficient and Stable Perovskite Solar Cells based on a Low-Cost Carbon Cloth,” *Adv. Energy Mater.*, vol. 6, no. 20, 2016, doi: 10.1002/aenm.201601116.

[235] R. Li, X. Xiang, X. Tong, J. Zou, and Q. Li, “Wearable Double-Twisted Fibrous Perovskite Solar Cell,” *Adv. Mater.*, vol. 27, no. 25, 2015, doi: 10.1002/adma.201501333.

[236] D. Hao, J. Zou, and J. Huang, “Recent developments in flexible photodetectors based on metal halide perovskite,” *InfoMat*, vol. 2, no. 1, pp. 139–169, 2020, doi: 10.1002/inf2.12053.

[237] H. Jing *et al.*, “Flexible Ultrathin Single-Crystalline Perovskite Photodetector,” *Nano Lett.*, vol. 20, no. 10, 2020, doi: 10.1021/acs.nanolett.0c02468.

[238] M. Zhang *et al.*, “High-performance and stability bifacial flexible self-powered perovskite photodetector by surface plasmon resonance and hydrophobic treatments,” *Org. Electron.*, vol. 99, 2021, doi: 10.1016/j.orgel.2021.106330.

[239] F. Yu, M. Hu, F. Kang, and R. Lv, “Flexible photodetector based on large-area few-layer MoS2,” *Prog. Nat. Sci. Mater. Int.*, vol. 28, no. 5, 2018, doi: 10.1016/j.pnsc.2018.08.007.

[240] D. Ding *et al.*, “Template growth of perovskites on yarn fibers induced by capillarity for flexible photoelectric applications,” *J. Mater. Chem. C*, vol. 7, no. 31, 2019, doi: 10.1039/c9tc01879d.

[241] T. M. H. Nguyen, S. K. Lee, S. Kim, and C. W. Bark, “Practical Demonstration of Deep-Ultraviolet Detection with Wearable and Self-Powered Halide Perovskite-Based Photodetector,” *ACS Appl. Mater. Interfaces*, vol. 13, no. 48, 2021, doi: 10.1021/acsami.1c18099.

[242] S. Liu *et al.*, “Improved flexible ZnO/CsPbBr3/Graphene UV photodetectors with interface optimization by solution process,” *Mater. Res. Bull.*, vol. 130, 2020, doi: 10.1016/j.materresbull.2020.110956.

[243] H. J. Kim, H. Oh, T. Kim, D. Kim, and M. Park, “Stretchable Photodetectors Based on

Electrospun Polymer/Perovskite Composite Nanofibers," *ACS Appl. Nano Mater.*, vol. 5, no. 1, 2022, doi: 10.1021/acsanm.1c03875.

[244] Q. Dong, L. Lei, J. Mendes, and F. So, "Operational stability of perovskite light emitting diodes," *JPhys Materials*, vol. 3, no. 1. 2020, doi: 10.1088/2515-7639/ab60c4.

[245] T. Miyasaka, *Perovskite photovoltaics and optoelectronics : from fundamentals to advanced applications*. Weinheim, Germany: Wiley-VCH, 2022.

[246] Q. Shan *et al.*, "Perovskite light-emitting/detecting bifunctional fibres for wearable LiFi communication," *Light Sci. Appl.*, vol. 9, no. 1, 2020, doi: 10.1038/s41377-020-00402-8.

[247] D. H. Jiang *et al.*, "Facile Fabrication of Stretchable Touch-Responsive Perovskite Light-Emitting Diodes Using Robust Stretchable Composite Electrodes," *ACS Appl. Mater. Interfaces*, vol. 12, no. 12, 2020, doi: 10.1021/acsami.9b23291.

[248] S. Kim, H. Oh, I. Jeong, G. Kang, and M. Park, "Influence of a Solvent Trap in ITO/PEN Substrates on the Performance of Flexible Perovskite Solar Cells and Light-Emitting Diodes," *ACS Appl. Electron. Mater.*, vol. 3, no. 7, 2021, doi: 10.1021/acsaelm.1c00385.

[249] H. Kim and J. H. Ahn, "Graphene for flexible and wearable device applications," *Carbon N. Y.*, vol. 120, 2017, doi: 10.1016/j.carbon.2017.05.041.

[250] Z. Gu *et al.*, "In Situ Inkjet Printing of the Perovskite Single-Crystal Array-Embedded Polydimethylsiloxane Film for Wearable Light-Emitting Devices," *ACS Appl. Mater. Interfaces*, vol. 12, no. 19, 2020, doi: 10.1021/acsami.0c04131.

[251] R. Hosseinian Ahangharnejhad *et al.*, "Protecting Perovskite Solar Cells against Moisture-Induced Degradation with Sputtered Inorganic Barrier Layers," *ACS Appl. Energy Mater.*, vol. 4, no. 8, 2021, doi: 10.1021/acsaem.1c00816.

[252] H. Xu, "A brief review on the moisture stability for perovskite solar cells," in *IOP Conference Series: Earth and Environmental Science*, 2020, vol. 585, no. 1, doi:

10.1088/1755-1315/585/1/012027.

[253] F. Jiang *et al.*, “Stretchable, Breathable, and Stable Lead-Free Perovskite/Polymer Nanofiber Composite for Hybrid Triboelectric and Piezoelectric Energy Harvesting,” *Adv. Mater.*, vol. 34, no. 17, 2022, doi: 10.1002/adma.202200042.

[254] Y. Peng *et al.*, “Lead-Free Perovskite-Inspired Absorbers for Indoor Photovoltaics,” *Adv. Energy Mater.*, vol. 11, no. 1, 2021, doi: 10.1002/aenm.202002761.

[255] J. Shamsi, A. S. Urban, M. Imran, L. De Trizio, and L. Manna, “Metal Halide Perovskite Nanocrystals: Synthesis, Post-Synthesis Modifications, and Their Optical Properties,” *Chem. Rev.*, vol. 119, no. 5, 2019, doi: 10.1021/acs.chemrev.8b00644.

[256] S. H. Kim, K. D. Park, and H. S. Lee, “Growth kinetics and optical properties of cspbbr3 perovskite nanocrystals,” *Energies*, vol. 14, no. 2, 2021, doi: 10.3390/en14020275.

[257] L. C. Schmidt *et al.*, “Nontemplate synthesis of CH3NH3PbBr3 perovskite nanoparticles,” *J. Am. Chem. Soc.*, vol. 136, no. 3, pp. 850–853, 2014, doi: 10.1021/ja4109209.

[258] M. Tabassum, Q. Zia, Y. Zhou, M. J. Reece, and L. Su, “A review on advances in doping with alkali metals in halide perovskite materials,” *SN Appl. Sci.*, vol. 3, no. 12, 2021, doi: 10.1007/s42452-021-04877-x.

[259] F. Ye *et al.*, “High-Quality MAPbBr3 Cuboid Film with Promising Optoelectronic Properties Prepared by a Hot Methylamine Precursor Approach,” *ACS Appl. Mater. Interfaces*, vol. 12, no. 21, 2020, doi: 10.1021/acsami.0c04516.

[260] K. H. Wang, L. C. Li, M. Shellaiah, and K. W. Sun, “Structural and Photophysical Properties of Methylammonium Lead Tribromide (MAPbBr3) Single Crystals,” *Sci. Rep.*, vol. 7, no. 1, 2017, doi: 10.1038/s41598-017-13571-1.

[261] A. Hashmi, B. Jain, J. Singh, M. Aleksandrova, and A. Kumar Singh, “Facile Synthesis of Bismuth-Based Perovskite and Solvent Engineering for Improving the Crystallinity

of Lead-Free Perovskite Material: A Microstructural Exploration," in *Proceedings of the 2021 6th International Symposium on Environment-Friendly Energies and Applications, EFEA 2021*, 2021, doi: 10.1109/EFEA49713.2021.9406228.

[262] S. Gull, M. H. Jamil, X. Zhang, H. sing Kwok, and G. Li, "Stokes Shift in Inorganic Lead Halide Perovskites: Current Status and Perspective," *ChemistryOpen*, vol. 11, no. 3. 2022, doi: 10.1002/open.202100285.

[263] F. Zhang *et al.*, "Colloidal Synthesis of Air-Stable CH3NH3PbI3 Quantum Dots by Gaining Chemical Insight into the Solvent Effects," *Chem. Mater.*, vol. 29, no. 8, pp. 3793–3799, 2017, doi: 10.1021/acs.chemmater.7b01100.

[264] Y. Hassan *et al.*, "Facile Synthesis of Stable and Highly Luminescent Methylammonium Lead Halide Nanocrystals for Efficient Light Emitting Devices Figure S 1 : TEM of the CH 3 NH 3 PbI 3 NCs prepared at 60 ° C for 30 seconds exhibit 10 nm in," pp. 1–13.

[265] J. Pan *et al.*, "Highly Efficient Perovskite-Quantum-Dot Light-Emitting Diodes by Surface Engineering," *Adv. Mater.*, vol. 28, no. 39, pp. 8718–8725, 2016, doi: 10.1002/adma.201600784.

[266] D. R. Yoder-Short, U. Debska, and J. K. Furdyna, "Lattice parameters of Zn1−xMnxSe and tetrahedral bond lengths in AII1−xMnxBVI alloys," *J. Appl. Phys.*, vol. 58, no. 11, pp. 4056–4060, 1985, doi: 10.1063/1.335585.

[267] A. Perumal *et al.*, "High brightness formamidinium lead bromide perovskite nanocrystal light emitting devices," *Sci. Rep.*, vol. 6, no. 6, pp. 1–10, 2016, doi: 10.1038/srep36733.

[268] Y. Zu *et al.*, "High-Brightness and Color-Tunable FAPbBr3 Perovskite Nanocrystals 2.0 Enable Ultrapure Green Luminescence for Achieving Recommendation 2020 Displays," *ACS Appl. Mater. Interfaces*, vol. 12, no. 2, pp. 2835–2841, 2020, doi: 10.1021/acsami.9b18140.

[269] Q. A. Akkerman, G. Rainò, M. V. Kovalenko, and L. Manna, "Genesis, challenges and

opportunities for colloidal lead halide perovskite nanocrystals," *Nat. Mater.*, vol. 17, no. 5, pp. 394–405, 2018, doi: 10.1038/s41563-018-0018-4.

[270] C. Shen *et al.*, "Transition metal ion doping perovskite nanocrystals for high luminescence quantum yield," *Chem. Eng. J.*, vol. 382, p. 122868, 2020, doi: 10.1016/j.cej.2019.122868.

[271] B. J. Moon *et al.*, "Rare-Earth-Element-Ytterbium-Substituted Lead-Free Inorganic Perovskite Nanocrystals for Optoelectronic Applications," *Adv. Mater.*, vol. 31, no. 33, p. 1901716, 2019, doi: 10.1002/adma.201901716.

[272] C. Zhang *et al.*, "Core/Shell Metal Halide Perovskite Nanocrystals for Optoelectronic Applications," *Adv. Funct. Mater.*, vol. 31, no. 19, p. 2100438, 2021, doi: 10.1002/adfm.202100438.

[273] S. Tian *et al.*, "Thermally Stable Red-Emitting Mixed Halide Perovskite Nanocrystals Enabled by Solid Reaction and Co-Doping Process," *Adv. Opt. Mater.*, vol. 10, no. 17, p. 2200751, 2022, doi: 10.1002/adom.202200751.

[274] C. Chen *et al.*, "Passivation Layer of Potassium Iodide Yielding High Efficiency and Stable Deep Red Perovskite Light-Emitting Diodes," *ACS Appl. Mater. & Interfaces*, vol. 14, no. 14, pp. 16404–16412, Mar. 2022, doi: 10.1021/acsami.2c00621.

[275] Y. Chu *et al.*, "Unveiling the photoluminescence regulation of colloidal perovskite quantum dots via defect passivation and lattice distortion by potassium cations doping: Not the more the better," *J. Colloid Interface Sci.*, vol. 596, pp. 199–205, 2021, doi: 10.1016/j.jcis.2021.03.128.

[276] J. Li *et al.*, "Rubidium Doping to Enhance Carrier Transport in CsPbBr3 Single Crystals for High-Performance X-Ray Detection," *ACS Appl. Mater. Interfaces*, vol. 12, no. 1, pp. 989–996, 2020, doi: 10.1021/acsami.9b14772.

[277] H. Chen *et al.*, "High-Efficiency Formamidinium Lead Bromide Perovskite

Nanocrystal-Based Light-Emitting Diodes Fabricated via a Surface Defect Self-Passivation Strategy," *Adv. Opt. Mater.*, vol. 8, no. 6, p. 1901390, 2020, doi: 10.1002/adom.201901390.

[278] J. Zhang *et al.*, "Growth mechanism of CsPbBr3 perovskite nanocrystals by a co-precipitation method in a CSTR system," *Nano Res.*, vol. 12, no. 1, pp. 121–127, 2019, doi: 10.1007/s12274-018-2190-x.

[279] Q. Li *et al.*, "Solid Ligand-Assisted Storage of Air-Stable Formamidinium Lead Halide Quantum Dots via Restraining the Highly Dynamic Surface toward Brightly Luminescent Light-Emitting Diodes," *ACS Photonics*, vol. 4, no. 10, pp. 2504–2512, 2017, doi: 10.1021/acsphotonics.7b00743.

[280] L. Protesescu *et al.*, "Monodisperse Formamidinium Lead Bromide Nanocrystals with Bright and Stable Green Photoluminescence," *J. Am. Chem. Soc.*, vol. 138, no. 43, pp. 14202–14205, 2016, doi: 10.1021/jacs.6b08900.

[281] B. Tang *et al.*, "An All-Inorganic Perovskite-Phase Rubidium Lead Bromide Nanolaser," *Angew. Chemie - Int. Ed.*, vol. 58, no. 45, pp. 16134–16140, 2019, doi: 10.1002/anie.201910617.

[282] C. Zhang, S. Wang, X. Li, M. Yuan, L. Turyanska, and X. Yang, "Core/Shell Perovskite Nanocrystals: Synthesis of Highly Efficient and Environmentally Stable FAPbBr3/CsPbBr3 for LED Applications," *Adv. Funct. Mater.*, vol. 30, no. 31, p. 1910582, 2020, doi: 10.1002/adfm.201910582.

[283] M. Abdi-Jalebi *et al.*, "Potassium-and rubidium-passivated alloyed perovskite films: Optoelectronic properties and moisture stability," *ACS Energy Lett.*, vol. 3, no. 11, pp. 2671–2678, 2018, doi: 10.1021/acsenergylett.8b01504.

[284] D. Han *et al.*, "Efficient light-emitting diodes based on in situ fabricated FAPbBr3 nanocrystals: The enhancing role of the ligand-assisted reprecipitation process," *ACS*

Nano, vol. 12, no. 8, 2018, doi: 10.1021/acsnano.8b05172.

[285] N. Yantara *et al.*, "Designing Efficient Energy Funneling Kinetics in Ruddlesden–Popper Perovskites for High-Performance Light-Emitting Diodes," *Adv. Mater.*, 2018, doi: 10.1002/adma.201800818.

[286] L. Protesescu *et al.*, "Monodisperse Formamidinium Lead Bromide Nanocrystals with Bright and Stable Green Photoluminescence," *J. Am. Chem. Soc.*, 2016, doi: 10.1021/jacs.6b08900.

[287] J. Hai, H. Li, Y. Zhao, F. Chen, Y. Peng, and B. Wang, "Designing of blue, green, and red CsPbX3 perovskite-codoped flexible films with water resistant property and elimination of anion-exchange for tunable white light emission," *Chem. Commun.*, vol. 53, no. 39, 2017, doi: 10.1039/c7cc01152k.

[288] H. Fang *et al.*, "Few-layer formamidinium lead bromide nanoplatelets for ultrapure-green and high-efficiency light-emitting diodes," *Nano Res.*, vol. 12, no. 1, pp. 171–176, 2018, doi: 10.1007/s12274-018-2197-3.

[289] M. Imran *et al.*, "Switchable Anion Exchange in Polymer-Encapsulated APbX3Nanocrystals Delivers Stable All-Perovskite White Emitters," *ACS Energy Lett.*, vol. 6, no. 8, 2021, doi: 10.1021/acsenergylett.1c01232.

[290] F. Liu *et al.*, "Colloidal Synthesis of Air-Stable Alloyed CsSn1-xPbxI3 Perovskite Nanocrystals for Use in Solar Cells," *J. Am. Chem. Soc.*, vol. 139, no. 46, 2017, doi: 10.1021/jacs.7b08628.

[291] P. M. Talianov *et al.*, "Halide Perovskite Nanocrystals with Enhanced Water Stability for Upconversion Imaging in a Living Cell," *J. Phys. Chem. Lett.*, vol. 12, no. 37, 2021, doi: 10.1021/acs.jpclett.1c01968.

[292] S. Bhaumik *et al.*, "Highly stable, luminescent core-shell type methylammonium-octylammonium lead bromide layered perovskite nanoparticles," *Chem. Commun.*, vol.

52, no. 44, pp. 7118–7121, 2016, doi: 10.1039/c6cc01056c.

[293] H. Zhou *et al.*, "Water Passivation of Perovskite Nanocrystals Enables Air-Stable Intrinsically Stretchable Color-Conversion Layers for Stretchable Displays," *Adv. Mater.*, vol. 32, no. 37, 2020, doi: 10.1002/adma.202001989.

[294] S. N. Raja *et al.*, "Encapsulation of Perovskite Nanocrystals into Macroscale Polymer Matrices: Enhanced Stability and Polarization," *ACS Appl. Mater. Interfaces*, vol. 8, no. 51, 2016, doi: 10.1021/acsami.6b09443.

[295] W. Cai *et al.*, "Polymer-Assisted in Situ Growth of All-Inorganic Perovskite Nanocrystal Film for Efficient and Stable Pure-Red Light-Emitting Devices," *ACS Appl. Mater. Interfaces*, vol. 10, no. 49, 2018, doi: 10.1021/acsami.8b13418.

[296] S. Hou, Y. Guo, Y. Tang, and Q. Quan, "Synthesis and Stabilization of Colloidal Perovskite Nanocrystals by Multidentate Polymer Micelles," *ACS Appl. Mater. Interfaces*, vol. 9, no. 22, 2017, doi: 10.1021/acsami.7b03445.

[297] S. M. Jafari, *Handbook of Food Nanotechnology: Applications and Approaches*. 2020.

[298] T. Chen *et al.*, "Blinking CsPbBr3 perovskite nanocrystals for the nanoscopic imaging of electrospun nanofibers," *Nano Res.*, vol. 14, no. 5, 2021, doi: 10.1007/s12274-020-3189-7.

[299] Z. Wang *et al.*, "Air Stable Organic–Inorganic Perovskite Nanocrystals@Polymer Nanofibers and Waveguide Lasing," *Small*, vol. 16, no. 43, 2020, doi: 10.1002/smll.202004409.

[300] P. C. Tsai, J. Y. Chen, E. Ercan, C. C. Chueh, S. H. Tung, and W. C. Chen, "Uniform Luminous Perovskite Nanofibers with Color-Tunability and Improved Stability Prepared by One-Step Core/Shell Electrospinning," *Small*, vol. 14, no. 22, 2018, doi: 10.1002/smll.201704379.

[301] F. E. Ahmed, B. S. Lalia, and R. Hashaikeh, "A review on electrospinning for membrane

fabrication: Challenges and applications," *Desalination*, vol. 356. 2015, doi: 10.1016/j.desal.2014.09.033.

[302] Y. Shao *et al.*, " Designable and highly stable emissive CsPbI 3 perovskite quantum dots/polyvinylidene fluoride nanofiber composites ," *Opt. Mater. Express*, vol. 12, no. 1, p. 109, 2022, doi: 10.1364/ome.448282.

[303] Q. Zia *et al.*, "Porous poly(L–lactic acid)/chitosan nanofibres for copper ion adsorption," *Carbohydr. Polym.*, vol. 227, 2020, doi: 10.1016/j.carbpol.2019.115343.

[304] Y. Duan, G. Z. Yin, D. Y. Wang, and R. D. Costa, "In Situ Ambient Preparation of Perovskite-Poly(l -lactic acid) Phosphors for Highly Stable and Efficient Hybrid Light-Emitting Diodes," *ACS Appl. Mater. Interfaces*, vol. 13, no. 18, 2021, doi: 10.1021/acsami.1c04025.

[305] C. Geng, S. Xu, H. Zhong, A. L. Rogach, and W. Bi, "Aqueous Synthesis of Methylammonium Lead Halide Perovskite Nanocrystals," *Angew. Chemie - Int. Ed.*, vol. 57, no. 31, 2018, doi: 10.1002/anie.201802670.

[306] Q. F. Li, J. T. Wang, B. Tian, S. Kong, T. Wang, and Z. Wang, "Hybridization of CsPbBr3 Perovskite Nanocrystals with Polymer Nanofiber to Improve their Luminescence Stability," *Eur. J. Inorg. Chem.*, vol. 2018, no. 38, pp. 4215–4220, 2018, doi: 10.1002/ejic.201800669.

[307] J. Hai, H. Li, Y. Zhao, F. Chen, Y. Peng, and B. Wang, "Designing of blue, green, and red CsPbX3 perovskite-codoped flexible films with water resistant property and elimination of anion-exchange for tunable white light emission," *Chem. Commun.*, vol. 53, no. 39, pp. 5400–5403, 2017, doi: 10.1039/c7cc01152k.

[308] K. Hills-Kimball, Y. Nagaoka, C. Cao, E. Chaykovsky, and O. Chen, "Synthesis of formamidinium lead halide perovskite nanocrystals through solid-liquid-solid cation exchange," *J. Mater. Chem. C*, vol. 5, no. 23, 2017, doi: 10.1039/c7tc00598a.

[309] S. Liang *et al.*, “Recent Advances in Synthesis, Properties, and Applications of Metal Halide Perovskite Nanocrystals/Polymer Nanocomposites,” *Advanced Materials*, vol. 33, no. 50. 2021, doi: 10.1002/adma.202005888.

[310] X. Hu, Y. Xu, J. Wang, J. Ma, L. Wang, and W. Jiang, “In Situ Fabrication of Superfine Perovskite Composite Nanofibers with Ultrahigh Stability by One-Step Electrospinning Toward White Light-Emitting Diode,” *Adv. Fiber Mater.*, vol. 5, no. 1, pp. 183–197, 2022, doi: 10.1007/s42765-022-00207-x.

[311] D. H. Jiang *et al.*, “Novel ultra-stable and highly luminescent white light-emitting diodes from perovskite quantum dots - Polymer nanofibers through biaxial electrospinning,” *APL Mater.*, vol. 7, no. 11, 2019, doi: 10.1063/1.5124880.

[312] R. Cheng, Z.-B. Liang, H. Shen, J. Guo, C.-F. Wang, and S. Chen, “In-situ synthesis of stable perovskite quantum dots in core-shell nanofibers via microfluidic electrospinning,” *Chinese Chem. Lett.*, vol. 34, no. 3, p. 107384, 2023, doi: 10.1016/j.cclet.2022.03.107.

[313] Y. Lee *et al.*, “Lead-Free Inorganic Nanoparticles of Perovskite Embedded within Waterproof Nanofiber Films for White Color Emission,” *ACS Appl. Nano Mater.*, vol. 5, no. 12, pp. 18409–18416, Dec. 2022, doi: 10.1021/acsanm.2c04261.

[314] M. Tabassum, Q. Zia, Y. Zhou, Y. Wang, M. J. Reece, and L. Su, “A Review of Recent Developments in Smart Textiles Based on Perovskite Materials,” pp. 447–463, 2022.

[315] M. Tabassum, Q. Zia, J. Li, M. T. Khawar, S. Aslam, and L. Su, “FAPbBr 3 Perovskite Nanocrystals Embedded in Poly (L – Lactic Acid) Nanofibrous Membranes for Enhanced Air and Water Stability,” *Membranes (Basel).*, pp. 1–13, 2023.

List of publications

- **Tabassum, M**., Zia, Q., Su, L. (2023). Fabrication of Potassium- and Rubidium-doped Formamidinium Lead Bromide Nanocrystals for Surface Defects Passivation and Improved Photoluminescence Stability, *ACS Applied Electronic Materials*, 6 (1), 550-558.
- **Tabassum, M**., Zia, Q., Li, J., Khawar, M. T., Aslam, S., & Su, L. (2023). $FAPbBr_3$ Perovskite Nanocrystals Embedded in Poly (L–lactic acid) Nanofibrous Membranes for Enhanced Air and Water Stability. *Membranes*, *13*(3), 279.

- **Tabassum, M**., Zia, Q., Aslam, S., Wang, Y., Zhang, J., Reece, M. J., & Su, L. (2022). Tuning the Optical Properties of $MAPbBr_3$ Perovskite Nanocrystals via Alkali Metal Ions Doping. Advanced Materials proceedings, 5480.1003.

- **Tabassum, M**., Zia, Q., Zhou, Y., Wang, Y., Reece, M. J., & Su, L. (2022). A Review of Recent Developments in Smart Textiles Based on Perovskite Materials. *Textiles*, *2*(3), 447-463.

- **Tabassum, M**., Zia, Q., Zhou, Y., Reece, M. J., & Su, L. (2021). A review on advances in doping with alkali metals in halide perovskite materials. *SN Applied Sciences*, *3*, 1-15.

- Zhang, J., Zhao, J., Zhou, Y., Wang, Y., Blankenagel, K. S., Wang, X., **Tabassum, M**., & Su, L. (2021). Polarization-sensitive photodetector using patterned perovskite single-crystalline thin films. *Advanced Optical Materials*, *9*(17), 2100524.

- **Tabassum, M**., Zia, Q., Su, L. (2024). Fabrication of Potassium- and Rubidium-Doped Formamidinium Lead Bromide Nanocrystals for Surface Defect Passivation and Improved Photoluminescence Stability. *ACS Applied Electronic Materials*, 6, 1, 550–558.